



HAL
open science

Advanced modulation formats and nonlinear mitigation for spectral efficient optical transmission systems

Ivan Fernandez de Jauregui Ruiz

► **To cite this version:**

Ivan Fernandez de Jauregui Ruiz. Advanced modulation formats and nonlinear mitigation for spectral efficient optical transmission systems. Networking and Internet Architecture [cs.NI]. Institut National des Télécommunications, 2018. English. NNT : 2018TELE0009 . tel-01810324

HAL Id: tel-01810324

<https://theses.hal.science/tel-01810324>

Submitted on 7 Jun 2018

HAL is a multi-disciplinary open access archive for the deposit and dissemination of scientific research documents, whether they are published or not. The documents may come from teaching and research institutions in France or abroad, or from public or private research centers.

L'archive ouverte pluridisciplinaire **HAL**, est destinée au dépôt et à la diffusion de documents scientifiques de niveau recherche, publiés ou non, émanant des établissements d'enseignement et de recherche français ou étrangers, des laboratoires publics ou privés.



Spécialité : Électronique et Communications

Ecole doctorale : Informatique, Télécommunications et Electronique de Paris

Présentée par

Ivan Fernandez de Jauregui Ruiz

**Pour obtenir le grade de
DOCTEUR DE TELECOM SUDPARIS**

Advanced modulation formats and nonlinear mitigation for spectral efficient optical transmission systems

Soutenue le 12 Avril 2018

Devant le jury composé de :

Directeur de thèse

Prof. Badr-Eddine Benkelfat (*Telecom SudParis*)

Rapporteurs

Prof. Alberto Bononi (*University of Parma*)

Prof. Magnus Karlsson (*Chalmers University*)

Examineurs

Prof. Didier Erasme (*Télécom ParisTech*)

Dr. Nicolas Dubreuil (*Institute d'Optique Graduate School*)

Dr. Anne-Laure Billabert (*Conservatoire National des Arts et Métiers*)

Encadrants

Dr. Amirhossein Ghazisaeidi (*Nokia Bell-Labs France*)

Prof. Yann Frignac (*Telecom SudParis*)

NNT. <2018TELE0009>

"I have heard articulate speech by sunlight! I have heard a ray of the sun laugh and cough and sing! I have been able to hear a shadow and I have even perceived by ear the passage of a cloud across the sun's disk. You are the grandfather of the Photophone and I want to share my delight at my success".

— Alexander Graham Bell, *in a letter to his father Alexander Melville Bell, dated February 26, 1880*

ACKNOWLEDGEMENTS

I would like to start by thanking all the members of the jury for the precious time they have taken to read and evaluate my report, as well as for their fruitful advices and comments.

It gives me immense pleasure to thank Amirhossein Ghazisaeidi for all his support and continuous guidance during the practical phase of this thesis. I thank him for his astute criticism and for encouraging me to always give my best to present high-quality and meaningful results. I thank him for his patience and for transmitting me part of his immense knowledge.

I would also like to express my sincere gratitude to Gabriel Charlet for encouraging me to perform this thesis after my Master's internship. I thank him for all the practical discussions and for teaching me how to present results in an original and relevant way. I thank him for his guidance, for his trust, and for all his support.

I thank Jeremie Renaudier for all his suggestions and help during the final part of this thesis, and which who I would have liked to work more closely since the beginning of my work. I also thank Patrice Tran, Patrick Brindel, Dylan LeGac and Christian Simonneau for having introduced me to the various techniques and tricks in the lab, but specially for your infinite patience on all those hours setting-up, optimizing, and performing all the experiments. I thank also Christian Doriz for all the fruitful discussions and work during the Optoplan project.

I specially thank Alexis Carbo, Elie Awwad, Rafael Rios-Müller and Kaoutar Benyahya for all their support, for their friendship, and for their motivation. I thank all my colleagues in the department for their help, and for making my stay at Bell Labs a very pleasant one. It has been a honor and pleasure to be part of this great team.

This acknowledge would not be complete without thanking all my family, specially my parents and brothers for all their support, and for encouraging me to always move forward and to search for new limits. I thank them for having educated me with social sense where my work and wellness cannot come at the expense of others. I thank them and my political family for their constant love, encouragement, and moral support.

I also thank my friends Ruben Hernandez and Uriel Esparza for their lifetime friendship. Liliana Beltran, Jessica Martinez, Jose Luis Martinez, Daniel Villavicencio,... It would be impossible to tell all the new experiences and good moments that we have lived together. I thank all their support and for always being there for me.

Last but not least, I leave these last lines to the most important person in my life, my wife Viridiana. None of this would have been possible without you. You have always been there by my side, encouraging me, motivating me, pushing me. You have not given up in our future no matter how long and difficult the road has been. I thank you for always showing me that good things come with sacrifice, and better do those sacrifices next to the person you love.

CONTENTS

ACKNOWLEDGEMENTS	5
CONTENTS	7
ABSTRACT	9
RESUME	11
LIST OF ACRONYMS AND SYMBOLS	15
LIST OF ACRONYMS	15
LIST OF SYMBOLS	18
1 COHERENT OPTICAL FIBER TELECOMMUNICATIONS SYSTEMS	21
1.1 TRANSOCEANIC SUBMARINE OPTICAL FIBER SYSTEMS STATUS AND TRENDS	21
1.2 DIGITAL TELECOMMUNICATION SYSTEMS	25
1.2.1 <i>Achievable Information Rates</i>	26
1.2.2 <i>Forward Error Correction Codes</i>	29
1.2.3 <i>Modulation Formats</i>	30
1.2.4 <i>Pulse Shaping</i>	35
1.3 COHERENT OPTICAL COMMUNICATIONS SYSTEMS	36
1.3.1 <i>Optical Transmitter</i>	37
1.3.2 <i>Optical Link</i>	38
1.3.3 <i>Optical Coherent Receiver</i>	50
1.3.4 <i>Standard Digital Signal Processing Blocks</i>	52
1.3.5 <i>Nonlinear Digital Signal Processing</i>	56
1.4 PERFORMANCE ANALYSIS	60
1.4.1 <i>AWGN Channel</i>	60
1.4.2 <i>Back-to-back (B2B) Penalties</i>	61
1.4.3 <i>Nonlinear Variance</i>	62
1.4.4 <i>Theory of Nonlinear Channel</i>	63
1.4.5 <i>Theoretical Limits to Nonlinear Compensation</i>	64
1.5 SUMMARY	66

2	LOW-COMPLEXITY DIGITAL NONLINEAR COMPENSATION	67
2.1	FILTERED DIGITAL BACKPROPAGATION OPTIMIZATION	67
2.1.1	<i>FDBP Parameter Optimization</i>	68
2.1.2	<i>Experimental Validation</i>	74
2.2	IMPACT OF STOCHASTIC POLARIZATION EFFECTS ON NLC ALGORITHMS	77
2.2.1	<i>Experimental Results</i>	77
2.2.2	<i>Simulation Results</i>	85
2.3	PRACTICAL LIMITS OF NLC ALGORITHMS	87
2.3.1	<i>Simulation Set-up</i>	87
2.3.2	<i>Numerical Results</i>	89
2.4	SUMMARY	97
3	HIGH-CAPACITY MODULATION FORMATS	99
3.1	MODULATION FORMATS COMPARISON	100
3.1.1	<i>Theoretical Performance</i>	100
3.1.2	<i>Experimental Performance</i>	105
3.2	TRUNCATED PROBABILISTIC CONSTELLATION SHAPING	110
3.3	SUMMARY	114
4	TRANSOCEANIC TRANSMISSION RECORDS	115
4.1	25.4 TB/S OVER TRANS-PACIFIC DISTANCES USING TPCS-64QAM	115
4.2	HIGH SYMBOL-RATE TRANSOCEANIC TRANSMISSION	121
4.2.1	<i>Single-carrier Experiments</i>	122
4.2.2	<i>Dual-carrier Experiments</i>	125
4.3	65 TB/S LEVERAGED BY PCS-64QAM	128
4.3.1	<i>Experimental Set-up</i>	128
4.3.2	<i>Experimental Results</i>	129
4.4	SUMMARY	130
5	CONCLUSIONS AND PERSPECTIVES	133
	REFERENCES	137
	PUBLICATIONS	145
	AS FIRST AUTHOR	145
	AS CO-AUTHOR	145

ABSTRACT

Global data traffic is expected to reach up to 4.3 ZB per year by 2020. This growth will be driven by the rise of two main technological fields: the creation of a new cloud integrated network of seemingly infinite capacity, and the Internet of Things (IoT) that will lead to a massive digitization and connection of devices. By 2021, the number of IP connected devices is expected to be more than three times the global population.

This amount of data traffic will challenge the core IP/optical infrastructure over which these services will flow. With most of the global communications being eventually transported on submarine point-to-point fiber-optic systems, different cutting-edge technologies have been under research during the past years to cope with the exponential increase of the global network-traffic.

With fiber Kerr nonlinear effects limiting the performance of current fiber-optic transmission systems, intense research has been done in the development of techniques searching to mitigate their effects. Approaches based on advanced digital signal processing (DSP) algorithms have taken the lead over optical techniques, as they can be more easily implemented in already deployed systems. In this sense, two main algorithms have been proposed in the literature: digital backpropagation (DBP), which is the most efficient algorithm in terms of performance improvement although its high computational complexity; and perturbative nonlinear compensation (PNLC), which presents a reduced complexity at the expense of lower achievable gains. Although, nonlinear compensation (NLC) is still not present in commercial systems due to its high complexity, it has been used in most of the recent “hero experiments” for distances above 6,000 km. However, with the continuous increase of processing capabilities of integrated circuits, DSP-based NLC techniques will be most likely implemented in future generation systems.

Besides nonlinear compensation techniques, the use of multi-level modulation formats beyond 16QAM and high symbol-rates have gained momentum in the last years. One of the

breakthroughs has been the introduction of QAM-based probabilistic constellation shaping (PCS-QAM), which has proven to outperform regular QAM formats. Not only the achievable rates approach the linear Shannon capacity as the constellation adopts a Gaussian like distribution, but rate adaptation is also possible while keeping the low complexity non-iterative decoding bit interleaved coded modulation scheme.

This thesis focuses on the evaluation of performance and achievable benefits of advanced modulation formats as PCS-QAM and digital nonlinear equalization techniques to increase the performance and throughput of long-haul optical fiber systems.

In the first part, the performance and achievable gains of low complexity nonlinear compensation techniques based on filtered DBP (FDBP), and PNLC are evaluated for long-haul submarine optical fiber systems. First, semi-analytical formulae are obtained for the optimization of the parameters involved in the FDBP algorithm, making complex and time-consuming exhaustive optimization unnecessary. Second, the impact of polarization mode dispersion (PMD) and polarization dependent loss (PDL) on the performance of FDBP and PNLC is experimentally addressed. Finally, a numerical study showing the practical limits of single channel nonlinear compensation versus algorithm complexity is carried out for transoceanic fiber-optic transmission systems

In the second part, the design and achievable rate increase brought by PCS-QAM over regular formats is addressed. First, the performance comparison of four advanced modulation formats for transoceanic coherent systems, i.e., 32QAM, 64QAM, 64APSK, and PCS-64QAM, is performed experimentally and numerically considering the theoretical gap to the linear Shannon capacity, nonlinear performance, back-to-back implementation penalties, and DSP challenges. Then, the design and optimization of a truncated-PCS (TPCS) to maximize the throughput of trans-Pacific optical fiber links is presented.

In the third part, PCS-QAM and NLC techniques are combined to demonstrate several transoceanic transmission records. First, the highest spectral efficiency for distances above 10,000 km using C-band EDFA only amplification is demonstrated. Then, cutting-edge CMOS digital-to-analog convertor's technology and wideband receivers together with PCS-QAM and NLC are used to achieve the highest per channel bit-rate up to date for trans-Atlantic and trans-Pacific distances. Finally, a record 65 Tb/s using C+L bands EDFA only amplification over 6,600 km employing PCS-64QAM, multi-rate FECs, and NLC is shown.

The final part of this thesis is devoted to the conclusions.

RESUME

Il est estimé que d'ici 2021 le trafic mondial de données atteindra 4.3 ZB par an, et que le nombre d'appareils IP connectés sera plus de trois fois supérieur à la population mondiale. Cette quantité de trafic de données mettra au défi l'infrastructure des réseaux IP/optiques qui représente l'épine dorsale des systèmes de télécommunications. En effet, la majeure partie des communications mondiales est transportée par des systèmes transocéaniques à fibre optique. Afin de faire face à cette demande croissante du trafic de données, différentes technologies sont actuellement étudiées pour augmenter la capacité de ces systèmes de transmission très longue distance.

La capacité des systèmes de transmission optiques modernes est fortement limitée par les effets non-linéaires de type Kerr dans la fibre. Dans ce contexte, différentes techniques de traitement de signal numérique (DSP) à complexité relativement élevée ont été proposées pour mitiger ces effets, notamment la rétropropagation numérique filtrée (FDBP), et la compensation non linéaire perturbative (PNLC). Avec le développement rapide des circuits intégrés à haute vitesse, les techniques de compensation non linéaire (NLC) basées sur DSP seront très probablement mises en œuvre dans les systèmes de future génération.

En outre, l'utilisation des formats de modulation multi-niveaux à haute efficacité spectrale au-delà de 16QAM a pris de l'ampleur pour augmenter la capacité de transmission de ces systèmes optiques. En particulier l'introduction du format QAM avec mise en forme probabiliste (PCS-QAM), démontré plus performant que les formats QAM classiques, a permis non seulement de s'approcher de la limite fondamentale de Shannon en régime linéaire, car la constellation adopte une distribution de type Gaussien, mais aussi d'adapter le débit du canal tout en conservant un schéma de codage à faible complexité basé sur la modulation codée avec entrelacement de bits (BICM).

Dans ce contexte, ce travail de thèse est axé sur l'étude de la performance et des gains réalisables par des techniques DSP à faible complexité pour mitiger les effets non-linéaires de type monocanal, ainsi que l'évaluation de la performances et mise en œuvre des formats PCS-QAM pour augmenter l'efficacité spectrale (SE) des systèmes pour les distances transocéaniques.

Dans le premier chapitre, les principaux aspects d'un système de communication numérique et des systèmes cohérents optiques longue distance basés sur le multiplexage en longueur d'onde (WDM) sont traités. D'abord, nous décrivons les principaux éléments de base de la transmission numérique, tels que : les taux réalisables dans les systèmes BICM, les codes de correction d'erreurs (FEC), les formats de modulation de cardinalité élevée incluant PCS-QAM, et la mise en forme des impulsions. Ensuite, nous décrivons les différents blocs d'un système cohérent optique long-distance, incluant : l'émetteur optique, les principaux phénomènes physiques affectant un signal optique pendant la propagation, l'architecture du récepteur cohérent, suivi par les principaux blocs DSP utilisés pour la récupération de données transmises. Enfin, nous abordons l'évaluation de la performance du système en termes du rapport signal à bruit (SNR), y compris toutes les sources de bruit comme : le bruit des amplificateurs optiques, le bruit lié au transmetteur et au récepteur, et le bruit non-linéaire lié à l'effet Kerr. Ce dernier est calculé à partir des modèles analytiques basés sur la théorie de perturbation de premier ordre.

Le deuxième chapitre est basé sur l'évaluation de la performance des algorithmes FDBP et PNLC utilisés pour mitiger les effets non-linéaires de type monocanal. Dans la première partie, nous étudions la dépendance des paramètres impliqués dans l'algorithme FDBP avec les différents paramètres du système, tels que : nombre de canaux WDM, puissance optique transmise, débit de modulation symbole et coefficients physiques de la fibre. Nous montrons numériquement et expérimentalement que les paramètres FDBP dépendent principalement de l'élargissement temporel des impulsions par étape FDBP, ce qui nous permet d'obtenir des formules semi-analytiques simples pour leur calcul, et d'éviter une optimisation exhaustive complexe. Dans la deuxième partie, nous étudions expérimentalement l'impact des effets de dispersion modale de polarisation (PMD) et de pertes dépendant de la polarisation (PDL) sur la performance des algorithmes FDBP et PNLC. Nous montrons que des valeurs de PMD aussi grandes que 5 fois la durée du symbole conduisent à une dégradation maximale observable de seulement ~ 0.1 dB dans le gain réalisable par la FDBP et la PNLC; tandis que la dégradation du gain correspondant à des valeurs PDL jusqu'à 9dB est de seulement ~ 0.2 dB. Ces observations expérimentales montrent la robustesse de ces algorithmes contre les effets PDL et PMD. Enfin, dans la troisième partie, nous évaluons numériquement les gains pratiques réalisables par la FDBP et la PNLC en relation avec la complexité liée à son implémentation. Nous montrons que dans le cas idéal sans bruit linéaire d'amplification, la FDBP travaillant à une étape par tronçon de fibre peut atteindre 90% du gain maximum théorique, tandis que pour la PNLC il est réduit à $\sim 75\%$. En considérant le bruit linéaire d'amplification, ces gains réalisables sont encore diminués, avec une dégradation plus élevée pour les distances de

transmission plus longues. Le bruit linéaire dégrade la performance de la FDBP et de la PNLC en même proportion indépendamment de la complexité de l'algorithme. Pour les régimes OSNR des systèmes transatlantiques, la PNLC peut atteindre des gains compris entre 0.5dB et 0.7dB pour les systèmes utilisant des canaux modulés à 32GBd, tandis que pour les systèmes avec des canaux modulés à 64GBd, les gains augmentent de 0.7 dB jusqu'à 1.1 dB.

Le troisième chapitre est basé sur la conception et l'évaluation de la performance du format PCS-QAM par rapport aux formats de modulation réguliers en amplitude et en quadrature (QAM). Dans la première partie, nous comparons théoriquement et expérimentalement le débit de données atteignable par PCS-64QAM, 64APSK, 64QAM et 32QAM, en considérant des pénalités linéaires et non linéaires après 6600 km. Nous montrons que les formats PCS-64QAM et 64APSK présentent de nouveaux défis pour l'implémentation des algorithmes DSP, en nécessitant l'utilisation de symboles pilotes. En ce qui concerne le 64APSK, nous montrons expérimentalement que sa performance se dégrade rapidement à de faibles valeurs de SNR, ayant besoin d'un taux de pilotes plus élevé dans la chaîne DSP. En tenant en compte les dégradations linéaires, non linéaires et les défis d'implémentation du DSP, le PCS-64QAM atteint des SE plus élevées par rapport à 32QAM, 64QAM et 64APSK pour les distances transocéaniques. Dans la deuxième partie, nous montrons la conception d'une version de PCS-64QAM nommée *PCS-64QAM tronqué* (TPCS-6AQAM) optimisée pour maximiser la SE des liens optiques transpacifiques. Le TPCS-64QAM proposé maximise la capacité sur la région de SNR entre 7 et 11.5 dB, tout en prenant en compte les pénalités liées au FEC.

Dans le quatrième chapitre, nous combinons la NLC avec les formats PCS-64QAM et TPCS-64QAM pour démontrer différents records de transmission transocéaniques. Dans la première partie, nous utilisons le TPCS-64QAM, la FDBP et des codes FEC basés sur la technologie SC-LDPC pour atteindre un record de 25.4 Tb/s avec une SE de 6.06 b/s/Hz après 10285 km. Nous montrons que le TPCS-64QAM apporte un gain de 0.25 b/symb/pol par rapport au 64QAM. De plus, nous montrons que l'augmentation de débit due à la FDBP est limitée à ~ 4% à cause de la puissance de sortie limitée de nos amplificateurs optiques. Dans la deuxième partie, nous présentons des nouveaux records de débit de données par canal pour les distances transocéaniques. Grâce à l'utilisation d'un DAC à haute vitesse, à un récepteur large bande, au PCS-64QAM et à la NLC, nous démontrons 550Gb/s par canal sur 6600km et 430 Gb/s sur 13200km. De plus, nous démontrons également 850 Gb/s à double porteuse sur 6600 km et 1Tb/s sur 3960 km. Enfin, dans la troisième partie, nous utilisons PCS-64QAM, ainsi que des codes SC-LDPC et la NLC pour atteindre un débit net de 65Tb/s sur 6600 km, avec une SE de 7.3 b/s/Hz. Toutes les démonstrations ci-dessus correspondaient à des records de transmission au moment de leurs réalisations.

La dernière partie de cette thèse est consacrée aux conclusions.

LIST OF ACRONYMS AND SYMBOLS

LIST OF ACRONYMS

ADC	analog to digital converter
AO	acousto-optic
APSK	amplitude phase shift-keying
ASE	amplified spontaneous emission
ASIC	application specific integrated circuit
AWGN	additive white Gaussian noise
B2B	back-to-back
BER	bit error rate
BICM	bit interleaving coded modulation
BMD	bit metric decoding
BPS	blind phase search
BPSK	binary phase shift keying
CD	chromatic dispersion
CMA	constant modulus algorithm
CMOS	complementary metal oxide semiconductor
COI	channel of interest
CPE	carrier phase estimation
CSF	coherent submarine fiber
DAC	digital to analog converter
DBP	digital backpropagation
DC	dual carrier
DCU	dispersion compensation unit
DEMUX	demultiplexer
DFB	distributed feedback laser
DGD	differential group delay
DM	dispersion managed
DSP	digital signal processing
DU	dispersion unmanaged
ECL	external cavity laser
EDFA	erbium doped fiber amplifier
EML	electro absorption modulator
ENOB	effective number of bits
FDBP	filtered digital backpropagation
FEC	forward error correction
FFT	fast Fourier transform
FIR	finite impulse response
FWM	four wave mixing
GMI	generalized mutual information
GN	Gaussian noise
GVD	group velocity dispersion
HD	hard decision
ISI	inter-symbol interference
LMS	least mean square

LO	local oscillator
LPF	low-pass filter
LUT	look-up table
MCI	multi-channel interference
ML	maximum likelihood
MMA	multi-modulus algorithm
MSE	minimum square error
MUX	multiplexer
MZM	Mach-Zendher modulator
NF	noise figure
NLC	nonlinear compensation
NLI	nonlinear interference
NLT	nonlinear threshold
NOB	number of bits
NSNI	nonlinear signal-noise interaction'
OPC	optical phase conjugation
OSA	optical spectrum analyzer
OSNR	optical signal to noise ratio
PBC	polarization beam coupler
PBS	polarization beam splitter
PCS	probabilistic constellation shaping
PCTW	phase-conjugated twin waves
PDL	polarization dependent loss
PM	polarization multiplexing
PMD	polarization mode dispersion
PMF	polarization maintaining fiber
PNLC	perturbative nonlinear compensation
PPN	phase and polarization noise
PSA	phase-conjugated amplification
PSD	power spectral density
QAM	quadrature amplitude modulation
QPSK	quaternary phase shift keying
RC	raised cosine
ROADM	reconfigurable optical add-drop multiplexer
RP1	first order regular perturbation
RRC	root raised cosine
RX	receiver
SC	single carrier
SCI	self channel interference
SC-LDPC	spatially coupled low density parity check
SD	soft decision
SE	spectral efficiency
SER	symbol error ratio
SG	super-Gaussian
SNR	signal to noise ratio
SOA	semiconductor optical amplifier
SOP	state of polarization
SPM	self-phase modulation
SSF	split-step Fourier method
SSMF	standard single mode fiber
TLS	tunable laser source
TPCS	truncated probabilistic constellation shaping

TX	transmitter
WDM	wavelength division multiplexing
WSS	wavelength selective switch
XCI	cross-channel interference
XPM	cross-phase modulation

LIST OF SYMBOLS

A_{LO}	local oscillator amplitude
A_{eff}	fiber effective area
A	input constellation alphabet
a	complex points in constellation alphabet A
α	fiber attenuation coefficient
a_{NLI}	normalized nonlinear variance
B_{FDBP}	FDBP low-pass filter bandwidth
B_{ref}	optical spectrum analyzer reference bandwidth
β_2	group velocity dispersion
β_3	group velocity dispersion slope
β	propagation constant
C	Shannon capacity
c	speed of light
C_{mn}	perturbative nonlinear coefficients
\hat{D}_z	dispersion operator
D	fiber dispersion coefficient
δT_s	time offset
ε	pulse energy
F	amplifier noise factor
f	frequency
G	amplifier gain
γ	fiber nonlinear coefficient
Γ	PDL coefficient
H	horizontal polarization
h_{eff}	SSFM effective step size
\hbar	Plank's constant divided by 2π
h	SSFM step size
η	DSP B2B penalty factor
I	in-phase component
\mathbb{I}	mutual information
K_p	pilot symbol block length
κ	FDBP/PNLC/DBP scaling factor
κ_{TRX}	TX-RX impairments
L_d	dispersion length
L_{eff}	effective span length
L	link length
L_{span}	span length
λ_0	channel of interest central wavelength
λ	wavelength
M	modulation order
μ_n	n 'th constellation moment
m	bits per symbol
N_0	noise power spectral-density
N_{ASE}	power spectral density of ASE noise
N_p	number of pilot symbols within a block
N_{span}	optical link number of spans

N_{steps}	DBP/FDBP steps per span
N_t	adaptive equalizer number of taps
n	fiber refractive index
n_2	fiber nonlinear Kerr coefficient
n_{sp}	amplifier spontaneous emission factor
ν	Maxwell-Boltzman distribution free parameter
ν_p	phase velocity
P_{ASE}	ASE noise power
P_{ch}	WDM channel power
P	average power
ρ	RRC roll-off factor
Q	quadrature component
R_s	symbol-rate
\hat{r}	constellation amplitudes
r_c	code rate
\mathcal{R}	detector responsivity
R	information rate
σ_{ASE}^2	ASE noise variance
σ_{NLI}^2	nonlinear variance
T_s	symbol duration
τ_{DGD}	differential group delay
t	time
φ_s	phase offset
V	vertical polarization
W	WDM channel bandwidth
ω	angular frequency
x	transmitted symbols
\hat{x}	estimated symbols
y	received symbols
z	distance
Ω_s	frequency offset

1 COHERENT OPTICAL FIBER TELECOMMUNICATIONS SYSTEMS

In this chapter, we first discuss the current status and trends of transoceanic submarine optical fiber systems. Then, we present the fundamental notions of digital communications and information theory over the linear Gaussian channel. Finally, we present the operation principles of coherent optical fiber systems, where linear and nonlinear impairments of signal transmission and the different techniques for their mitigation are also discussed.

1.1 TRANSOCEANIC SUBMARINE OPTICAL FIBER SYSTEMS STATUS AND TRENDS

The first deployment of a trans-Atlantic cable was done in 1858 relying North America and Europe. It consisted of several copper wires and was used for telegraph communications. Even though the cable only served for three weeks, it represents an heroic event in the history of the human technical revolution. Almost a century later, in 1956, the first transatlantic telephone cable system (TAT-1) was inaugurated, initially carrying 36 telephone channels. The evolution of submarine cables was slow in the following 38 years, and by 1994, the maximum number of voice channels was increased to 10,500 [1-3].

On the other hand, the first erbium doped fiber amplifier (EDFA) for optical fiber systems was shown in 1987, where optical gains up to 26 dB at a wavelength of 1530 nm were demonstrated [4, 5]. This experiment led to a worldwide effort on developing high gain EDFAs. In 1989, an experimental demonstration using EDFAs to amplify multiple wavelength signals

without cross-talk paved the way to amplified wavelength division multiplexing (WDM) systems [6]. The advent of WDM with optical amplification started a revolution for the development of high-capacity optical fiber systems. In 1996, the first trans-Atlantic optical cable making use of EDFA amplification and WDM technology (TAT-12/13) was deployed, initially carrying 2 WDM channels modulated at 5 Gb/s [4] using intensity modulation with direct detection (IM-DD).

The advances in high speed analog-to-digital converters (ADC), digital-to-analog converters (DAC), and high-speed application-specific integrated circuits (ASIC) in the early 2000s, together with the increased demand on data traffic renewed the interest for coherent technologies which were extensively studied during the 1980s. Since then, coherent detection has been the milestone technology for long haul optical fiber transmission systems. Its adoption has not only allowed the use of more complex higher order modulation formats, but has also enabled the use of advance digital signal processing (DSP) techniques enabling electronic equalization of deterministic system impairments. Coherent detection has become the *de-facto* standard for current commercial long-haul optical fiber systems. Modern commercial transoceanic cables can carry up to 20 Tb/s, equivalent to 312 million voice channels.

The transmission rates allowed by submarine optical cables are several tens of thousands of times more than can be achieved by satellites. In consequence, transoceanic optical fiber systems have become the backbone of international communications. It is commonly said that 99% of the total voice and data traffic is at present carried worldwide by submarine cables [3]. Fig. 1.1 shows the map of optical submarine cables laid worldwide by 2017, stretching over 1.1 million km [7].

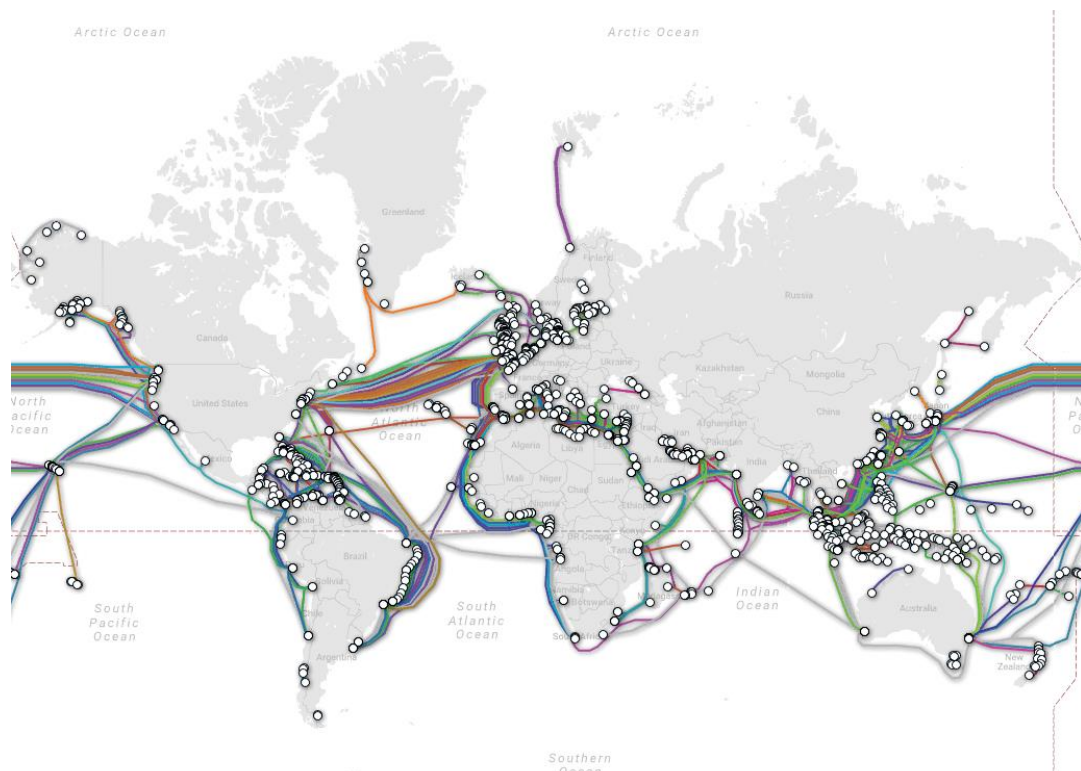


Fig. 1.1: Submarine cable map in 2017. Source Telegeography website [7].

The evolution of system throughput, spectral efficiency (SE), and channel bit-rate in research lab demonstrations for trans-Atlantic distances ($> 6,000$ km) since 1999 is shown in Fig. 1.2 [8-24]. Before the arrival of coherent detection, the maximum achievable system throughput was 6 Tb/s using WDM channels modulated at 10 Gb/s reaching SEs of 0.8 b/s/Hz. After 2008, a non-stopping increase have been made possible thanks to the synergy of different cutting-edge technological advances.

Great advances in CMOS technology have led to high speed DACs and ADCs. Their sampling rates have increased from 22 GSamples/s in 2006 [25] to 100 GSamples/s in 2016 [26]. These great improvements have allowed the use of Nyquist pulse shaping techniques to further increase the SE. Together with coherent detection, they have also allowed the possibility to use powerful DSP algorithms to compensate for system impairments. Compensation of chromatic dispersion (CD), polarization mode dispersion (PMD), as well as transmitter/receiver imperfections such as time skew and imbalances of quadrature components and polarization tributaries are common practices in current coherent optical systems.

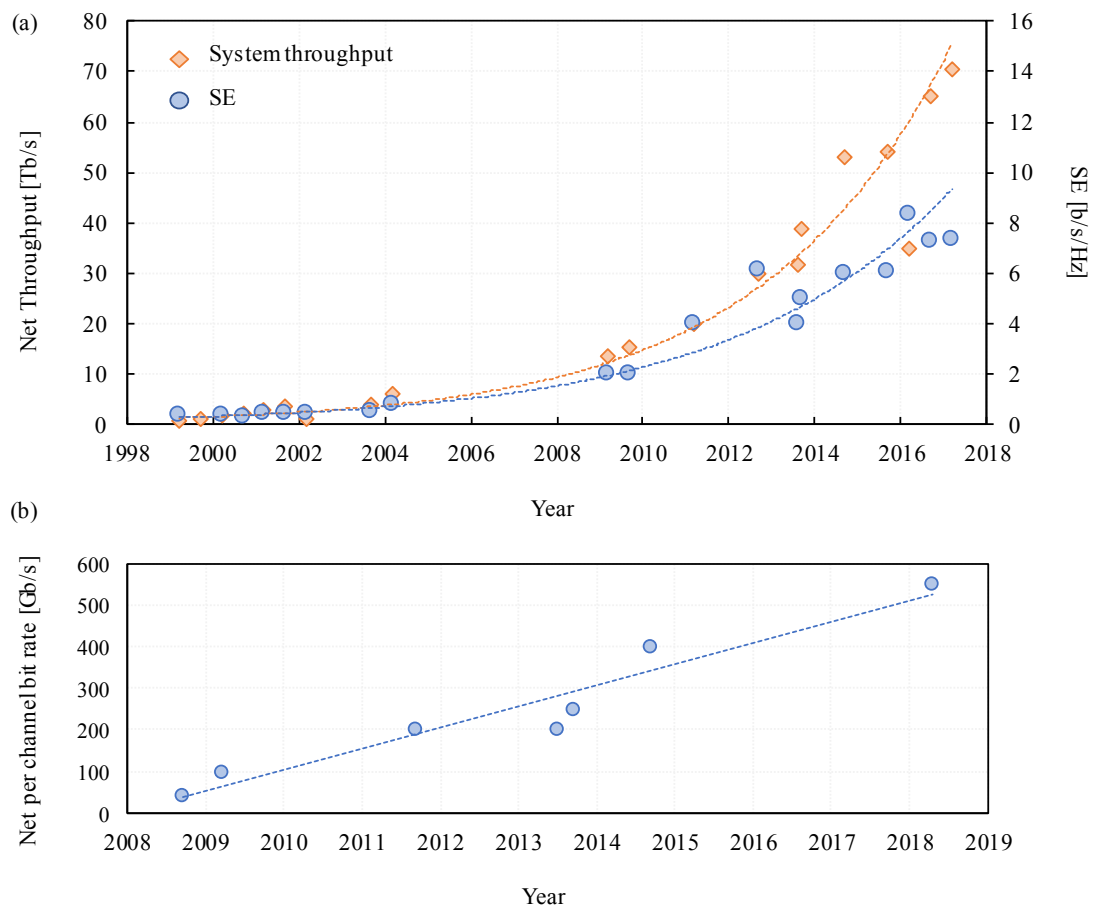


Fig. 1.2: (a) Net system throughput and spectral efficiency (SE) evolution in main research experiments over the years, (b) increase in channel bit rate since the arrival of coherent detection.

Moreover, a great increase in the system SE has been possible by the use of multi-level modulation formats and high symbol-rate channels. Systems working at 40 Gb/s with binary phase shift keying (BPSK) were rapidly updated to 100 Gb/s by the use of quadrature phase shift keying (QPSK) [14, 15], and to 200 Gb/s – 400 Gb/s using 16-quadrature amplitude modulation (16QAM) [23, 27, 28]. The net system throughput passed from 15 Tb/s in 2009, to 54,2 Tb/s by 2016, [15, 29]. Higher order modulation formats beyond 16QAM have gained momentum in the last couple of years. Experimental demonstrations using 32QAM and 64QAM have been presented [20, 21, 30, 31]. However, one of the recent breakthroughs has been the introduction of constellation shaping techniques, which have proven to outperform regular QAM formats. Geometric constellation shaping based on *64-amplitude phase shift keying* (64PSK) was used in [20] to achieve a record C-band SE of 8.3 b/s/Hz (net 34.9 Tb/s) after 6,375 km, while 4D-PS-9/12-56APSK was used in [22] to achieve 7.2 b/s/Hz (net 70.4Tb/s) over 7,600 km, using C+L bands EDFA-only amplification. Similarly, probabilistic constellation shaping (PCS) based on 64QAM constellation (PCS-64QAM) was used in [30] to demonstrate a SE of 7.3 b/s/Hz (net 65 Tb/s) over 6,600 km with C+L-band EDFA-only amplification. Beyond laboratory experiments, PCS-64QAM has also been successfully demonstrated in field-trials, achieving a SE of 7.46 b/s/Hz over a 5,523 km in service EDFA-only trans-Atlantic Facebook cable [32].

Hard-decision forward error correction codes (HD-FEC) have been replaced with the more powerful soft-decision FECs (SD-FEC). Specially, high performance FEC codes based on spatially-coupled low-density parity-check (SC-LDPC) have been introduced [33-35]. Adaptive multi-rate FEC was used in [18, 19, 29, 30], to achieve up to 20% capacity increase over trans-Atlantic and trans-Pacific distances with respect a single FEC code rate.

With fiber Kerr nonlinear effects limiting the performance of current fiber-optic transmission systems, different digital nonlinear compensation (NLC) techniques have been proposed. The most efficient algorithm in terms of performance improvement is digital backpropagation (DBP) [36, 37]; however, its hardware implementation is challenging due to its high computational complexity. Different approaches to reduce the complexity of NLC have been proposed, as the low-pass filter DBP (FDBP) [38, 39], or perturbative nonlinear compensation (PNLC) [40]. DSP-based NLC has been used in all recent transmission experiments for distances above 6,000 km [18-20, 22, 29, 30, 41].

Finally, novel optical components as optical fibers with ultra-low loss (<0.16 dB/km), large effective area ($\geq 150\mu\text{m}^2$), and high chromatic dispersion ($>20\text{ps/nm/km}$), together with wide-band amplification based on C+L bands ($\sim 70\text{nm}$) have been commonly adopted in laboratory experiments; increasing the SE by reducing the span loss, increasing tolerance to fiber nonlinearities, and practically doubling the useful bandwidth per optical cable [18-22, 29-31]. While high performance optical fibers are starting to be commercially deployed, C+L band amplification is likely to be adopted by the industry in the foreseeable future.

Compared to optical components, novel DSP techniques present an advantage for increasing the throughput of optical cables. With the wet plant lying on the seabed with twenty-five years' life span and almost no possible upgrade capability [3,141], new optical components can only be adopted for optical cables to be laid in the future, and are not viable for already deployed systems. On the contrary, novel DSP techniques can be relatively easily implemented in the submarine line terminal equipment, leading to a simpler and smoother upgrade of already deployed systems.

In this work, we focus on the evaluation of novel DSP techniques to increase the throughput and spectral efficiency of transoceanic optical fiber systems. In particular DSP techniques for the mitigation of fiber nonlinear distortions will be investigated, as well as on the use of capacity approaching modulation formats for next generation optical fiber systems.

1.2 DIGITAL TELECOMMUNICATION SYSTEMS

The main objective of a digital transmission system is to transmit information from a given source to a given destination without errors despite the presence of noise and other signal perturbations. Fig. 1.3 shows a schematic representation of the main building blocks of a digital telecommunication system. The process of transmitting information can be described as follows.

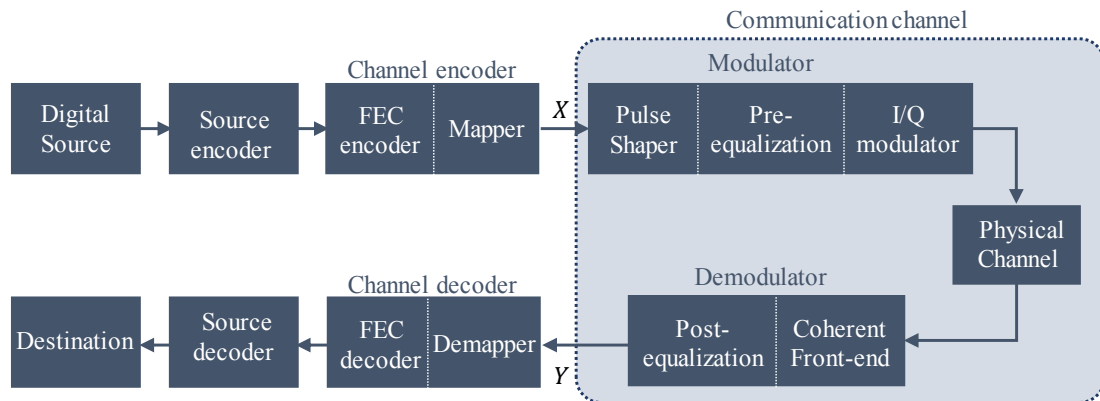


Fig. 1.3: Basic elements of a digital communication system.

The digital source generates information bits (0s and 1s) representing the message to be transmitted. A process known as *source encoding* compresses the data in order to remove redundancy, such that the information can be efficiently represented by the smallest number of bits possible. At the output of the source encoder, the binary data can be represented by a sequence of i.i.d bits. The resulting binary sequence is then passed to the *channel encoder*,

which introduces, in a controlled manner, some redundancy to increase robustness to noise. This error control scheme process is also known as *forward error correction* (FEC).

The resulting coded bits are then mapped to *symbols* drawn from a given *constellation alphabet*, also referred as a *modulation format*. The module which maps coded bits to symbols is called the *mapper*. For an equiprobable alphabet of size M , the number of coded bits per symbol is $m = \log_2(M)$. For example, let A be the constellation alphabet with complex constellation points, such that $A = \{a_1, a_2, \dots, a_M\}$. The mapper will map m -bit blocks at the output of the FEC, to a unique member of A . This process will generate a symbol sequence represented by $\mathbf{x} = (x_1, x_2, \dots, x_k, \dots)$ with $x_k \in A$.

In practice, information is transmitted over a physical medium in the form of an electromagnetic wave. Therefore, the discrete symbols at the mapper output have to be transformed to a signal waveform appropriate for transmission. This process is known as *pulse-shaping*. In this sense, while the modulation format determines the maximum information each symbol can carry, pulse shaping determines the spectral width occupied by the signal.

After pulse shaping, different kind of equalization techniques to compensate for channel impairments can be applied. Thanks to the availability of high resolution DACs, equalization can be performed at the transmitter side in the digital domain by means of DSP. This is referred as *pre-equalization*.

The resulting signal is then modulated into a carrier wave and transmitted through the physical channel. In the case of an optical fiber system, the signal is modulated into a laser source by means of an electro-optic IQ-modulator (see Sec. 1.3.1). After transmission, the received-signal coherently detected (see Sec. 1.3.3). Digital *post-equalization* can also be performed by means of DSP.

After *post-equalization*, the received symbols $\mathbf{y} = (y_1, y_2, \dots, y_k, \dots)$ have to be converted back to a sequence of bits. To do so, a module called the *channel decoder* estimates the transmitted coded bits and performs error correction. Finally, the information bits are decompressed and the message is recovered.

We recall that in the frame of information theory, all elements between the channel encoder and the channel decoder are referred as the *communication channel*. That is to say, all elements working at the *symbol* level as shown in Fig. 1.3.

1.2.1 Achievable Information Rates

1.2.1.1 Channel Capacity

The maximum information rate that can be transmitted over a given communication channel was first formulated by Shannon in [42], and is referred as the *channel capacity*, C . Therefore,

reliable communication can be achieved only if the information rate, R , is smaller than or equal to the channel capacity, i.e., $R \leq C$.

The channel capacity is determined by the statistical properties of the channel. The simplest additive white Gaussian noise (AWGN) channel is given by:

$$Y = X + Z \quad (1.1)$$

where X and Y are complex random variables representing the channel input and output respectively, and Z is a complex Gaussian random variable of zero mean accounting for noise. In this case, the AWGN channel will transform X into Y following the channel conditional probability:

$$p_{Y|X}(y|x) = \frac{1}{\pi N_0} e^{-\frac{|y-x|^2}{N_0}} \quad (1.2)$$

with x and y realizations of X and Y , and N_0 the complex noise variance. The quantity that measures the maximum amount of information that can be transported over the channel is referred as the *mutual information*, \mathbb{I} , and is obtained by [43]:

$$\begin{aligned} \mathbb{I}(X; Y) &= \iint p_{XY}(x, y) \cdot \log_2 \frac{p_{Y|X}(y|x)}{p_Y(y)} dx dy \\ &= \iint p_{XY}(x, y) \cdot \log_2 \frac{p_{XY}(x, y)}{p_X(x) \cdot p_Y(y)} dx dy \end{aligned} \quad (1.3)$$

where $p_{XY}(x, y)$ is the joint probability, and $p_X(x)$ and $p_Y(y)$ are the marginal probability density functions of X and Y . The channel capacity is the maximum mutual information, where the maximization is performed over all possible input distributions $p_X(x)$, i.e., $C = \max_{p_X(\cdot)} \mathbb{I}(X; Y)$.

Shannon showed in [42] that for the AWGN channel, the optimum source distribution that maximizes C is itself complex and Gaussian, of the form:

$$p_X(x) = \frac{1}{\pi P} e^{-\frac{|x|^2}{P}} \quad (1.4)$$

with P the signal power. The channel capacity is therefore given by the celebrated Shannon capacity formula:

$$C = \log_2(1 + SNR) \quad (1.5)$$

and is measured in bits per channel use, where $SNR = P/N_0$ is the signal to noise ratio. The channel capacity can be seen as the maximum achievable information rate at which information can be transmitted over the channel for a given SNR.

1.2.1.2 Constrained Capacity

The above formulation has been obtained considering that the input and output alphabets A , and B have an infinite number of elements, such that the input and output distributions $p_X(x)$ and $p_Y(y)$ are continuous Gaussian functions. In practical systems, A and B are finite, and their distributions are typically not Gaussian. The resulting information rates are denoted as *modulation constrained capacity* and are bounded away from the Shannon capacity.

Considering a finite constellation alphabet $A = \{a_1, a_2, \dots, a_i, \dots, a_M\}$ of size M , the constrained capacity can be estimated by Monte-Carlo time averaging for long-enough N as:

$$\hat{I}(X; Y) = \frac{1}{N} \sum_{k=1}^N \log_2 \frac{p(y_k|x_k)}{\sum_{x \in A} p(y_k|x)p_X(x)} \quad (1.6)$$

where x_k and y_k are the k -th symbol of the transmitted and received symbol sequence of size N . We define the *source entropy* $H(X)$ as:

$$H(X) = H = \sum_{x \in A} -p_X(x) \cdot \log_2 p_X(x) \quad (1.7)$$

Eq. (1.6) corresponds to the maximum information rate that can be achieved for a given constellation. In practice, this limit is only attainable in systems where the channel coding and the mapper are jointly designed. This scheme is referred as *coded modulation*.

1.2.1.3 Generalized Mutual Information

In order to reduce system complexity associated to coded modulation, another coding scheme referred as *bit-interleaved coded modulation* (BICM) is typically preferred.

BICM allows to separate coding and mapping, resulting in a higher flexibility in system design. Within this scheme, the generated coded bits at the output of the FEC are interleaved to sparse possible burst errors during transmission. The resulting coded interleaved bits are then partitioned into blocks of length $m = \log_2(M)$, and mapped to modulation symbols. At the receiver side, soft information about the coded bits is propagated from the demodulator to the decoder in the form of bit-wise a posteriori probabilities or log-likelihood ratios. This decoding scheme is known as bit-metric decoding (BMD).

Due to the interleaving, the BICM system can be regarded as m parallel memoryless and independent binary channels. The maximum information rate of BICM is usually referred as the *generalized mutual information* (GMI) defined by [44,45]:

$$GMI \approx H(X) - \frac{1}{N} \sum_{k=1}^N \sum_{i=1}^m \log_2 \frac{\sum_{x \in A} q_{Y|X}(y_k|x)p_X(x)}{\sum_{x \in A_{b_{k,i}}} q_{Y|X}(y_k|x)p_X(x)} \quad (1.8)$$

where $q_{Y|X}$ is the auxiliary channel conditional probability, $b_{k,i}$ is the i -th bit of the k -th transmitted symbol, and $A_{b_{k,i}}$ is the set of the constellation symbols whose i -th bit is $b_{k,i}$.

Employing a BICM scheme results in a capacity loss with respect to the coded modulation constrained capacity. However, this loss is very small assuming Gray-mapping.

1.2.2 Forward Error Correction Codes

As already mentioned, the main goal of channel coding, or FEC, is to add redundancy to the binary information sequence at the output of the source encoder. After transmission over the noisy channel, the FEC decoder exploits this redundancy to fully recover the source information. In general, the binary channel encoder will introduce redundancy bits in form of *parity checks*. The *code rate*, r_c , is defined by:

$$r_c = \frac{K_c}{N_c} \quad (1.9)$$

The FEC encoder takes a block of K_c information bits, and adds $N_c - K_c$ redundant bits. The *FEC overhead* is defined by:

$$OH = \frac{N_c - K_c}{K_c} = \frac{1 - r_c}{r_c} \quad (1.10)$$

The Shannon capacity and the GMI derivations in Seq. 1.2.1 assumed ideal FEC codes with block lengths N_c tending to infinity. The information rates of real systems with practical FEC codes will be bounded away from capacity.

A useful metric to quantify the performance of digital communication system is the bit-error-rate (BER), defined as the ratio between the number of received erroneous bits and the total number of transmitted bits. FEC coding schemes are usually characterized by their *coding gain*, which measures the difference of the required SNR between coded and uncoded transmission to achieve a given BER. In actual optical communication systems, the required BER after FEC decoding (*post-FEC BER*) is typically $<10^{-15}$.

Over the years, different coding schemes have been introduced; *i.e.*, Hamming codes, Reed-Solomon (RS) codes, Bose–Chaudhuri–Hocquenghem (BCH) codes, Block Turbo Codes (BTC), etc. Today high-capacity optical transmission systems beyond 100 Gb/s typically use *Low-Density Parity-Check* (LDPC) codes with $OH \sim 20\%$. A new type of LDPC code referred to as spatially coupled LDPC codes (SC-LDPC) is an emerging channel coding scheme enabling virtually arbitrary long block lengths with manageable complexity [34,46]. SC-LDPC codes can achieve net coding gains close to theoretical limits, operating with less than 1 dB SNR gap to capacity. SC-LDPC will be use as the chosen coding scheme within this work.

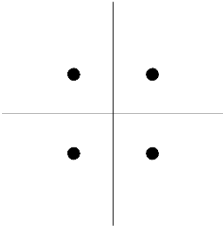
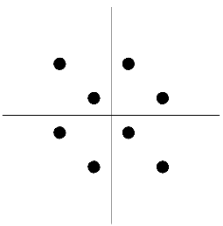
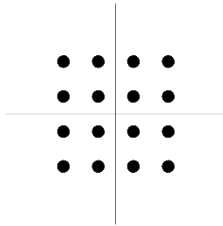
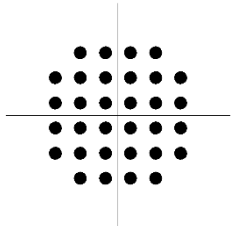
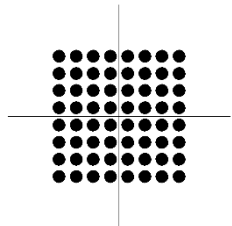
1.2.3 Modulation Formats

A constellation alphabet having M points can carry a maximum of $m = \log_2(M)$ bits per symbol. This maximum is achieved only when the probability of occurrence of the constellation points is uniform, i.e., $P_X(X = a_k) = 1/M$, such that the constellation entropy is defined as:

$$H(X) = m = \log_2(M) \quad (1.11)$$

The two real-valued components of the constellation symbols $\text{Re}(a_k)$, and $\text{Im}(a_k)$ are referred as the *in-phase* (I) and *quadrature* (Q) components respectively, with Re and Im standing for real and imaginary parts. The most well-known modulation formats for coherent optical systems (sketched in Table 1) are: quadrature phase shift keying: (QPSK), and M - *quadrature amplitude modulation* (QAM), i.e., 8QAM, 16QAM, 32QAM, 64QAM.

Table 1: Some modulation formats used for in coherent optical fiber systems.

QPSK	8QAM	16QAM
$(M = 4, m = 2)$	$(M = 8, m = 3)$	$(M = 16, m = 4)$
		
32QAM	64QAM	
$(M = 32, m = 5)$	$(M = 64, m = 6)$	
		

The average power associated with a constellation is given by:

$$P = \frac{1}{M} \sum_{k=1}^M |a_k|^2 \quad (1.12)$$

For a constant output power of the modulator, constellations with higher values of M will have their points more closely packed together, leading to higher BER for the same SNR, and therefore requiring stronger FECs, i.e., lower code rates. For a given modulation format, BER can be minimized by the use of a proper bit-to-symbol mapping. In general, the probability of symbol error is higher for adjacent symbols, such that the minimum BER is found when adjacent symbols have only one bit difference. The mapping having this property is called Gray mapping.

As observed in Table 1, the distribution of the discrete constellations points is not Gaussian, and therefore suboptimal for the AWGN channel. The resulting achievable information rates will be bounded away from the Shannon capacity. Fig. 1.4 shows the GMI in b/channel use for different formats, as well as the Shannon capacity.

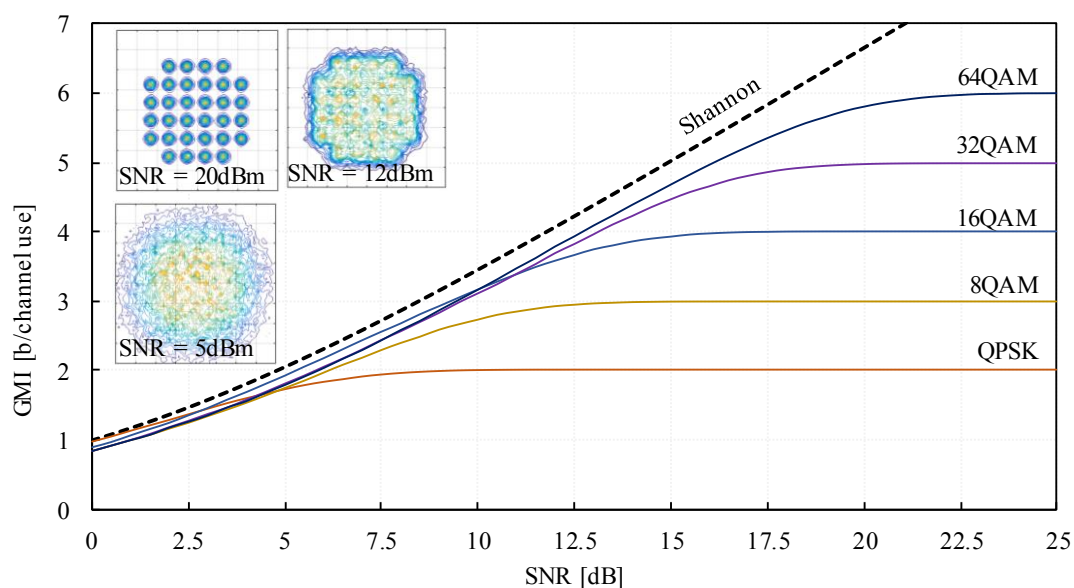


Fig. 1.4: Soft-decision generalized mutual information for QPSK, 8/16/32/64QAM. Insets: 32QAM constellation for different SNR values.

At high SNR, all formats saturate at their corresponding entropies H . The insets of Fig. 1.4 show a 32QAM constellation at different values of SNR. For low values of SNR, the constellation resembles more a Gaussian distribution as the signal is highly impaired by AWGN.

Modulation formats with “*Gaussian-like*” distributions can be used to approach capacity. These formats rely on applying some kind of shaping to a constellation with a discrete number of points. The shaping technique can either be geometrical, where equiprobable constellation points are arranged in the complex plane to make the constellation to appear Gaussian, it can be probabilistic, where the constellation points are visited with nonuniform probability densities approximating the Gaussian distribution; or it can be a combination of both geometrical and probabilistic techniques. These techniques are well known in the literature [47-49], but have

been recently introduced for fiber-optic telecommunications systems, and have shown to outperform regular square QAM formats [20-22, 30, 41, 50-52].

A type of PCS based on QAM constellation was recently proposed in [50], presenting two main design advantages. First, it can be applied to any square QAM constellation which are desirable due to their simplicity, and for which the BICM scheme can be employed with almost no penalty thanks to the use of symbol Gray mapping; and second, FEC implementation is independent of shaping, such that no change in FEC engine is required for different shaping modes, allowing for rate adaptation with fine granularity [51]. In terms of performance, PCS based on 64QAM was shown to achieve higher shaping gains compared to geometric shaping based on 64-*amplitude phase shift-keying* (64APSK) [30], while at the same time being more tolerant to frequency offsets and phase noise resulting in lower implementation penalties for low operating signal-to-noise ratio (SNR) regimes [53]. For the above reasons, PCS-QAM has become one of the main subjects of research and is becoming an interesting candidate for implementation in future coherent optical commercial systems.

In PCS-QAM, the probability mass function (PMF) of the QAM constellation points are set according to a discrete Maxwell-Boltzmann distribution with free parameter $\nu \geq 0$, according to:

$$P_X(x) = \frac{\exp(-\nu|x|^2)}{\sum_{x \in A} \exp(-\nu|x|^2)} \quad (1.13)$$

The free parameter ν can be optimized to change the source distribution and minimize the gap to the Shannon capacity for a given target SNR. The entropy, H , of the resulting constellation can then be obtained as per (1.7). Considering a given FEC code rate, r_c , the ideal transmission rate, R , is calculated by [51]:

$$R = H - (1 - r_c) \cdot m \quad (1.14)$$

where m is the number of bits per symbol of the QAM constellation at which PCS is applied, i.e. $m = 6$ for 64QAM.

In practice, the DSP module which sets the PMF of the constellation points for a given ν is called the *distribution matcher* (DM). At the transmitter, the DM is concatenated with a systematic binary encoder for FEC. This scheme is referred to as probabilistic amplitude shaping (PAS). At the receiver side, an inverse DM is placed after the de-mapper and the FEC decoder. Please note that the de-mapper should be modified to account for the symbols prior probabilities. The design of the DMs is an actual research topic and it is out of the scope of this work. The PCS-QAM can be seen as an instance of BICM with bit-metric mismatched decoding, for which the correct metric to measure the achievable rates is the GMI. A detail description of the PAS scheme is found in [50]. Fig. 1.5a and Fig. 1.5b show the constellations and the PMFs of the in-phase or quadrature components for the standard 64QAM and PCS based on 64QAM with an arbitrary value of ν .

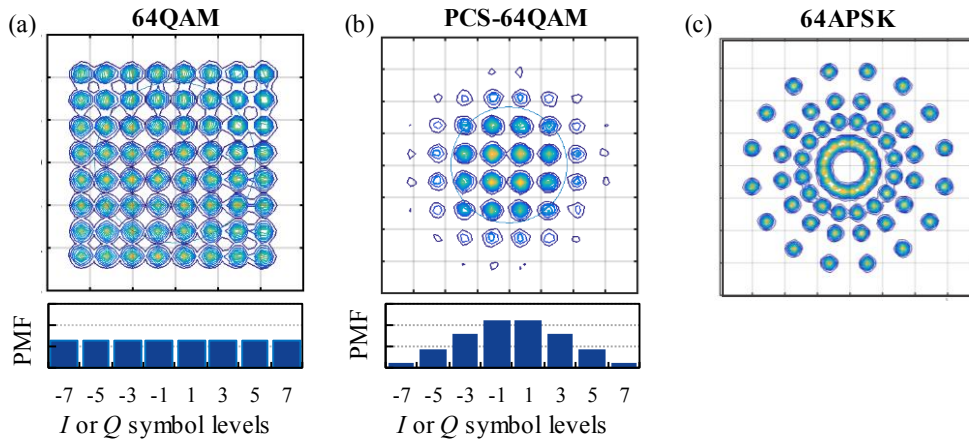


Fig. 1.5: Constellations and PMFs of I or Q components for (a) 64QAM and (b) PCS-64QAM formats. (c) 64APSK constellation.

Unlike QAM constellations, APSK constellations usually do not support Gray mapping and require complex iterative FEC decoding. In [52], a 64APSK constellation supporting Gray mapping was introduced, and further used in [20] for transoceanic distances, and it was shown to outperform regular QAM. In particular, 64APSK is composed of 4 concentric rings, each with 16 uniformly spaced PSK points as shown in Fig. 1.5c. On the other hand, hybrid constellations make use of coded modulation with complex iterative decoding, being unattractive for practical implementation in commercial systems and will not be considered in this work.

Fig. 1.6 shows the GMI for 64QAM, 64APSK and PCS-64QAM, where the last one is optimized for a SNR value of 12 dB. It is observed that PCS outperforms other formats and approaches the Shannon capacity. A performance comparison between regular QAM formats, 64APSK, and PCS-64QAM is presented in Sec. 3.1.

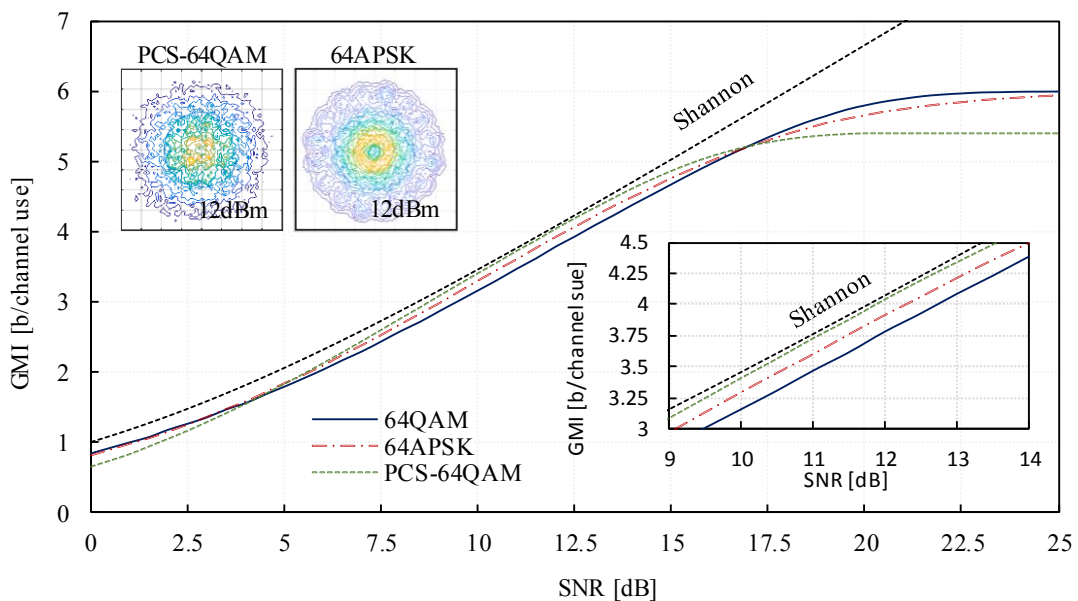


Fig. 1.6: GMI for 64QAM, 64APSK and PCS-64QAM optimized for a SNR value of 12 dB.

1.2.3.1 System Performance Metrics

As already mentioned, the *post-FEC* BER in actual coherent optical communication systems is typically $<10^{-15}$. In general, such low values make post-FEC BER evaluation practically impossible by means of numerical simulations and experimental off-line processing.

In order to relax this requirement, another performance metric referred as the *FEC limit* is typically used. It is defined as the maximum BER at the input of the FEC decoder for which the decoder successfully decodes the received block. In general, this approach works well when employing HD-FECs, however, for SD-FECs it is less accurate [54]. In this sense, it has been recently shown that for BICM systems the GMI can be used to make a more robust prediction of the post-FEC BER when QAM formats are used [55-58].

In this work, we focus on three main performance metrics, i.e., SNR, pre-FEC BER (pre-FEC Q^2 -factor), and the GMI. The pre-FEC BER can be calculated from the transmitted and decided received symbols as:

$$BER = \frac{1}{N \cdot H} \sum_{k=1}^N d_H(\mathcal{M}(x_k), \mathcal{M}(\hat{x}_k)) \quad (1.15)$$

where x_k is the k 'th transmitted symbol, N is the sequence length, $\mathcal{M}(\cdot)$ accounts for symbol-to-bit mapping, $d_H(\cdot)$ is the Hamming distance, and \hat{x}_k is the k 'th decided symbol obtained using maximum a posteriori (MAP) detection as:

$$\hat{x}_k = \underset{x \in A}{\operatorname{argmin}} \left[|y_k - x|^2 - \frac{p_X(x)}{SNR} \right] \quad (1.16)$$

BER is usually converted to another performance metric called Q^2 -factor by:

$$Q^2 = 20 \log_{10} [\sqrt{2} \cdot \operatorname{erfc}^{-1}(2 \cdot BER)] \quad (1.17)$$

with erfc^{-1} the inverse complementary error function.

While the GMI and the pre-FEC Q^2 -factor are performance metrics of a digital communication system depending on the modulation format and decoding schemes, the SNR is a direct measure of signal distortions. As it will be pointed out in Sec. 1.4, in modern optical long-haul optical fiber systems as the ones considered in this work, all sources of noise can be well approximated by Gaussian noise statistics, and can be correctly accounted for by SNR calculation. It can be analytically shown that the SNR can be estimated from the transmitted and received symbol sequences as:

$$\widehat{SNR} = \left[\frac{|\mathbf{x}|^2 |\mathbf{y}|^2}{|\mathbf{x} \mathbf{y}^\dagger|^2} - 1 \right]^{-1} \quad (1.18)$$

where \dagger is the Hermitian conjugate.

1.2.4 Pulse Shaping

After choosing the modulation format, the signal has to be adapted to cope with the physical properties of the medium. Rectangular pulses are not suitable for transmitting data over band limited channels, as they will require infinite bandwidth to avoid distortion. However, limiting the signal bandwidth will produce pulses to spread over time, such that overlapping between different pulses will occur. At the receiver, the waveform will be converted back to the digital domain by means of the ADC. This process is realized by sampling the received waveform with a given sampling frequency. Without proper sampling and proper pulse shape, the sampled signal will suffer from inter-symbol interference (ISI).

The signal waveform can be written as:

$$x(t) = \sum_k x_k g(t) \quad (1.19)$$

where x_k corresponds to the k 'th transmitted constellation symbol. Each symbol will be multiplied by a given pulse shape, $g(t)$. For a given symbol-rate, the pulse shape $g(t)$ that minimizes the signal bandwidth is the *sinc* function, as its Fourier transform is the rectangular function such that:

$$g(t) = \text{sinc}(t) \quad (1.20)$$

$$\mathcal{F}\{g(t)\} = \tilde{g}(f) = \text{rect}(f \cdot T_s) \quad (1.21)$$

where T_s is the symbol duration. The bandwidth of the resulting complex signal is therefore $W = R_s$, where $R_s = 1/T_s$ is the symbol-rate. One particular property of the *sinc* function is that it is zero at all sampling instants $t = kT_s$ except for $k = 0$, i.e:

$$g(kT) = \begin{cases} 1; & k = 0 \\ 0; & k \neq 0 \end{cases} \quad (1.22)$$

such that perfect sampling at instances kT_s allows recovering the transmitted data symbols without ISI. However, the main disadvantage of sinc pulses is that the amplitude decays slowly such that unperfect sampling will lead to significant ISI.

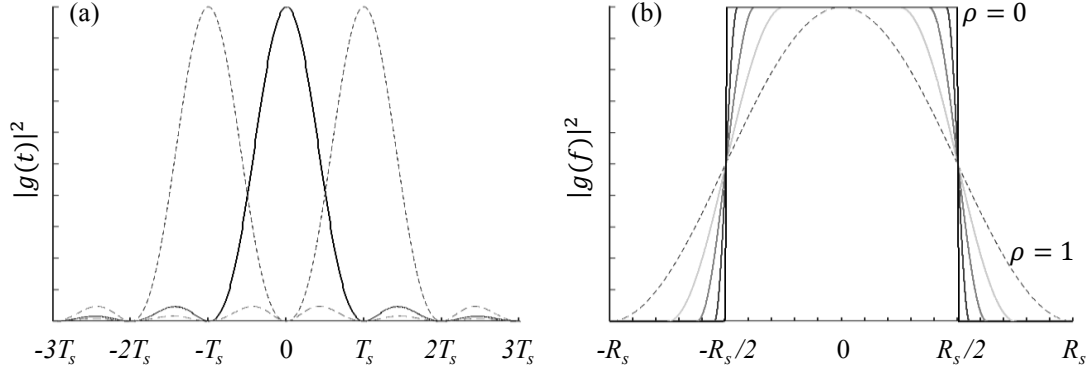


Fig. 1.7: (a) Sinc pulses in time domain, and (b) raised cosine spectrum with various roll-offs factors.

Another pulse shape which satisfies (1.22) is the raise-cosine (RC) pulse defined as:

$$\tilde{g}(f) = \begin{cases} 1, & |f| \leq \frac{(1-\rho)}{2T_s} \\ \frac{1}{2} \left[1 + \cos \left(\frac{\pi T_s}{\rho} \left[|f| - \frac{(1-\rho)}{2T_s} \right] \right) \right], & \frac{(1-\rho)}{2T_s} < |f| \leq \frac{(1+\rho)}{2T_s} \\ 0, & \text{otherwise} \end{cases} \quad (1.23)$$

where ρ is the *roll-off* factor. RC pulses decay faster than the *sinc* pulses when $\rho > 0$, and are therefore more tolerant to imperfect sampling. However, the required spectrum is increased to $W = R_s(1 + \rho)$.

Another and most commonly used pulse shape is the root-raised cosine (RRC), which is obtained by applying the square root to the frequency domain version of (1.23). A priori, RRC pulses do not satisfy (1.22) and therefore exhibit ISI. However, when the received signal is corrupted by noise, the optimum receiver that maximizes the SNR for AWGN channels is called the matched-filter receiver. The match filter function equals $g(t)$, such that having an RRC pulse and an RRC matched filter will lead to an overall pulse shape with RC spectrum. Throughout this work we will focus only on RRC pulse shaping.

1.3 COHERENT OPTICAL COMMUNICATIONS SYSTEMS

Up to now, an overview of a general digital telecommunication system, where information is transmitted from source to destination using a given physical channel, has been presented. For the particular case of transoceanic optical systems, the signal has to be adapted to the fiber channel. Fig. 1.8 shows the main structure of a coherent long-haul optical communication system based on WDM technology, consisting of three main blocks: the optical transmitter, the

optical link, and the coherent optical receiver. In the following, an overview of each of the main blocks is presented.

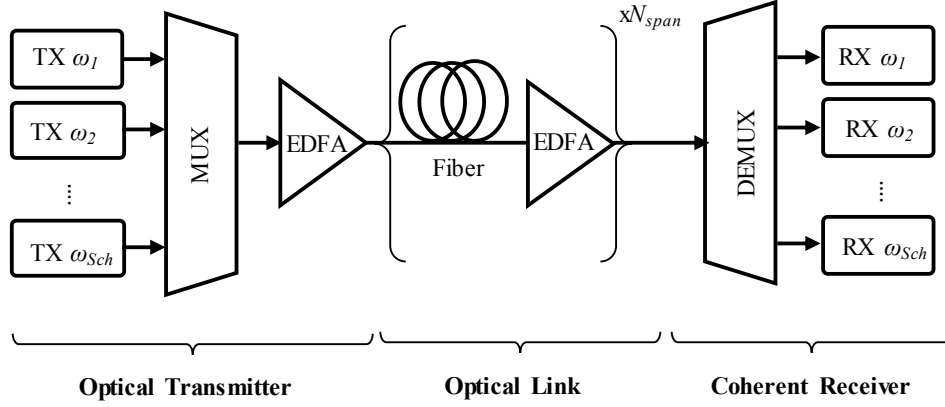


Fig. 1.8: General block diagram of long haul optical transmission systems.

1.3.1 Optical Transmitter

The main function of the optical transmitter is to convert an electrical waveform into the optical domain for further transmission through the optical link. For typical high-speed systems, this process is achieved by modulating the light of a laser source with an external optical modulator, which is driven by an electrical signal containing the data to be transmitted.

To maximize the spectral efficiency, all possible physical degrees of freedom of light should be considered. Modern coherent systems make use of amplitude, phase and polarization for data modulation. Therefore, any kind of multi-level modulation formats as the ones presented in Sec. 1.2.3 can be employed. The main structure of a WDM amplitude, phase and polarization diversity transmitter is sketched in Fig. 1.9.

After pulse shaping and pre-equalization, the two discrete waveforms to be transmitted over the two orthogonal polarizations H and V of light are divided into their real and imaginary parts (I and Q components), and transformed to an electrical analog waveform by means of four DACs. The four resulting signals are denoted as x^{VI} , x^{VQ} , x^{HI} , and x^{HQ} .

An optical carrier with central frequency ω_s is splitted into its two orthogonal polarizations, each of them feeding two nested Mach-Zehnder (MZ) modulators with $\pi/2$ shift between their outputs. Each MZ is driven by the aforementioned electrical waveform signals. After modulation, the two orthogonal polarizations are recombined by the use of a polarization beam coupler (PBC). In the case of WDM transmission, the same process is performed for the rest $S_{ch} - 1$ optical channels, which outputs are then optically multiplexed by means of a WDM

multiplexer. The resulting field is finally amplified and sent to the fiber link. Throughout this work all modulation formats are considered to be dual polarization.

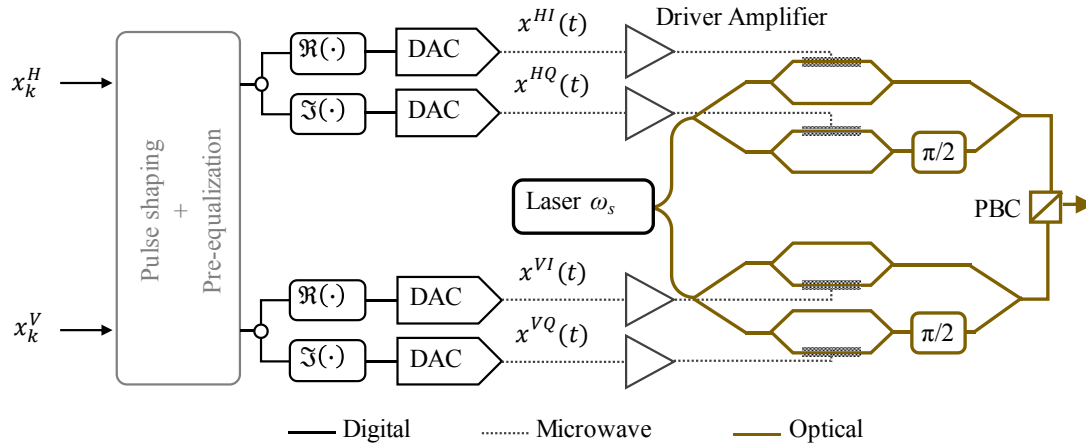


Fig. 1.9: Polarization division multiplexing IQ (PM-IQ) WDM transmitter.

In practice, the bandwidth and resolution of DACs are the key factors to achieve higher data rate transmissions. High-speed state-of-the-art DACs based on 28nm CMOS technology allowing sampling rates of 92 GS/s are commercially available [59], while DACs based on BiCMOS technology working at 100 GS/s have been demonstrated [26].

For high-speed long-haul transmission, MZ modulators are preferred over electro-absorption modulators (EML) due to their higher electro-optical bandwidth (~ 40 GHz), small insertion losses (≤ 4 dB), high extinction ratio (≥ 20 dB), and lower wavelength dependency.

1.3.2 Optical Link

The WDM signal at the output of the transmitter is then propagated through the optical link. For long haul applications, the link consists of a concatenation of single mode fiber spans, and optical amplifiers as sketched in Fig. 1.8.

The most common type of amplification is the erbium doped fiber amplifier (EDFA). The output power of an EDFA can exceed 25 dBm, they present relative flat gain spectrum, can achieve noise figures (NF) below 5 dB, and amplification bandwidths of ~ 35 nm. Moreover, they can be designed to work on C or L bands, such that WDM systems with a useful bandwidth of ~ 9.7 THz have been demonstrated [22]. Other amplification schemes based on Raman amplification, or hybrid Raman/EDFA also exist. However, due to their high pump power requiring high electrical power feeding, their use have been limited to terrestrial systems. Recently, large bandwidth amplification covering continuous 100 nm optical bandwidth using

semiconductor optical amplifiers (SOA) has also been demonstrated for terrestrial distances [60].

In legacy WDM systems, fiber CD was compensated either by introducing optical dispersion compensation units (DCU) in the link, or by the combination of fiber spans with positive and negative dispersion coefficients. These systems are typically referred as *dispersion managed* (DM). CD is now compensated in the digital domain thanks to the use of coherent detection and DSP, avoiding the use of the highly lossy DCUs, and simplifying the design of optical links. These systems are referred as *dispersion unmanaged* (DU) and have become the standard for current optical coherent systems. In this work, we focus only in DU long-haul transmission systems based on EDFA amplification (Fig. 1.8). Furthermore, we consider the case where all spans are identical (homogeneous spans).

During propagation, the signal will be impaired by fiber linear and nonlinear effects, as well as by amplified spontaneous emission (ASE) noise introduced at each EDFA stage. These impairments can be analytically represented as following.

Let's consider the scalar optical field of a given WDM channel labeled by s , and with central carrier angular frequency ω_s , be defined by:

$$E_s(z, t) = \sum_k x_k g_{k,s}(z, t) \exp(-i\omega_s t + i\beta(\omega)z) \quad (1.24)$$

where z represents distance, t represents time, x_k correspond to the k 'th complex dimensionless modulation format symbols defining the message (Sec. 1.2.3), $g_s(0, t)$ is the pulse shape of the s 'th optical channel waveform (Sec. 1.2.4), and β is the propagation constant. The total optical field considering all WDM channels can then be expressed as:

$$E(z, t) = E_0(z, t) + \sum_s E_s(z, t) \quad (1.25)$$

where the channel of interest (COI) corresponding to $s = 0$ has been singled out from the summation. In this work, we suppose that $g_0(0, t) = g_s(0, t)$ for all s , such that all channels have the same pulse shaping.

We define the pulse energy as:

$$\varepsilon = \int_{-\infty}^{\infty} |g_0(0, t)|^2 dt \quad (1.26)$$

and the normalized optical field $U(z, t)$ at a given propagation distance z as:

$$U(z, t) = \frac{E(z, t)}{f(z)\sqrt{\varepsilon}} \quad (1.27)$$

where $f(z)$ is the normalized power profile along z of the system shown in Fig. 1.8. The evolution of the scalar optical field along the optical fiber can be described by a normalized version of the nonlinear Schrödinger equation expressed by [61, 62]:

$$\frac{\partial U}{\partial z} = \underbrace{-i \frac{\beta_2}{2} \frac{\partial^2 U}{\partial t^2} + \frac{\beta_3}{6} \frac{\partial^3 U}{\partial t^3}}_{\text{dispersion}} + \underbrace{i \gamma \varepsilon f(z) |U|^2 U}_{\text{Kerr nonlinearities}} + \underbrace{\frac{n(z, t)}{\sqrt{\varepsilon f(z)}}}_{\text{ASE noise}} \quad (1.28)$$

where β_2 is the group velocity dispersion (GVD) corresponding to the acceleration of the spectral components of the pulse, β_3 is the GVD slope accounting for the variation of GVD as a function of the angular frequency, $\gamma = 2\pi n_2 / \lambda_0 A_{eff}$ is the nonlinear coefficient, n_2 is the fiber nonlinear Kerr refractive index, A_{eff} is the effective area, λ_0 is the COI wavelength, and $n(z, t)$ is the ASE noise source. Please note that we assume β_2 , β_3 and γ to be z independent, such that all spans are made of the same fiber. For lumped amplification, and considering that the EDFA exactly compensates for the span loss, $f(z)$ can be expressed as:

$$f(z) = \exp(-\alpha(z - z_{n-1})) \quad \begin{matrix} z_{n-1} \leq z \leq z_n \\ n=1 \dots N_{span} \end{matrix} \quad (1.29)$$

where α is the attenuation coefficient of the fiber.

In the case of dual polarization, (1.28) is divided into two coupled NLSE equations for which the Manakov approximation is commonly used to account for the random birefringence along the optical fiber. The normalized Manakov equation is expressed by:

$$\frac{\partial \mathbf{U}}{\partial z} = -i \frac{\beta_2}{2} \frac{\partial^2 \mathbf{U}}{\partial t^2} + \frac{\beta_3}{6} \frac{\partial^3 \mathbf{U}}{\partial t^3} + \frac{8}{9} \gamma \bar{\varepsilon} f(z) \mathbf{U}^\dagger \mathbf{U} \mathbf{U} + \frac{\mathbf{n}(z, t)}{\sqrt{\bar{\varepsilon} f(z)}} \quad (1.30)$$

where $\mathbf{U} = [U_V(z, t), U_H(z, t)]^T$, $\mathbf{n}(z, t) = [n_V(z, t), n_H(z, t)]^T$, and $\bar{\varepsilon} = \varepsilon/2$. The superscript T stands for matrix transpose operation and the superscript \dagger stands for Hermitian conjugation. In the following we assume a scalar field for simplicity of explanation.

1.3.2.1 Fiber Dispersion

When light propagates through a dielectric medium as the fiber, its speed will be decreased proportional to the dielectric constant of the medium. For an optical fiber, the phase velocity, v_p , is:

$$v_p = \frac{c}{n(\omega)} \quad (1.31)$$

where c is the speed of light in vacuum, and $n(\omega)$ is the refractive index of the fiber which is in general frequency dependent. The propagation constant β is related to v_p by the following expression:

$$\beta(\omega) = \frac{\omega}{v_p} \quad (1.32)$$

The frequency dependence of β means that different spectral components of the field will travel with different velocities during propagation. For normal dispersive fibers, this leads to a temporal broadening of the optical pulses within each channel, and a walk-off between pulses belonging to different WDM channels.

Eq. (1.32) can be expanded in a Taylor series with respect to the COI central frequency as:

$$\beta(\omega) = \beta_0 + \beta_1(\omega - \omega_0) + \frac{1}{2}\beta_2(\omega - \omega_0)^2 + \frac{1}{6}\beta_3(\omega - \omega_0)^3 + \dots \quad (1.33)$$

where β_i is the i 'th derivative of β with respect to ω . For a perfectly cylindrical fiber, β_0 and β_1 do not lead to any direct signal degradation during transmission. On the other hand, the group velocity dispersion β_2 is responsible for pulse broadening, and is linked to the dispersion coefficient D through the following expression:

$$D = -\frac{2\pi c}{\lambda^2}\beta_2 \quad (1.34)$$

The third order dispersion β_3 is related to the dispersion slope parameter S , by:

$$S = \frac{4\pi c}{\lambda^3}\left(\beta_2 + \frac{\pi c}{\lambda}\beta_3\right) \quad (1.35)$$

For DU systems working away from the zeroth dispersion point as the ones considered in this work, β_3 is very small compared to β_2 and can be neglected¹. In this case, considering only the group velocity dispersion β_2 , and neglecting fiber nonlinearities (i.e., $\gamma = 0$), (1.28) can be solved straightforward, leading to:

$$u(z, t) = \hat{D}_z[u(0, t) + u_{ASE}(z, t)] \quad (1.36)$$

where

$$\hat{D}_z[u(0, t)] = \mathcal{F}^{-1}\left\{\exp\left(-i\frac{\beta_2}{2}\omega^2 z\right)\mathcal{F}\{u(0, t)\}\right\} \quad (1.37)$$

¹ When working with high symbol-rate channels this approximation is less accurate, such that β_3 has to be considered for CD compensation.

is the dispersion operator, $u(0, t)$ is the optical field at the input of the link, and $u_{ASE}(z, t)$ accounts for the accumulated ASE noise at a given distance z . As fiber dispersion is deterministic, it can be efficiently compensated for in the digital domain by applying the adjoint of the operator \widehat{D}_z to the received signal. This technique will be addressed in Sec.1.3.4.2.

Consider a DU system composed of an optical fiber with dispersion coefficient $D = 20.6$ ps/nm·km (i.e., Corning Vascade EX3000), after 6,000 km transmission, the accumulated dispersion reaches 1.23×10^5 ps/nm. An optical pulse corresponding to a WDM channel modulated at 32 GBd will broaden almost 1000 times its width.

1.3.2.2 Fiber Kerr Nonlinearities

The last term in (1.28) corresponds to nonlinear interactions due to the Kerr effect, which causes variations of the refractive index of the fiber proportional to the power of the optical field. Fiber nonlinearities have been widely studied over the years, and their effects on optical pulse propagation have been commonly described within the frame of DM systems, where the pulses do not drastically change their shape during propagation. Within this frame, nonlinear effects were divided into categories depending on their specific way of impacting the optical signal, *self-phase modulation (SPM)*, *cross-phase modulation (XPM)*, *non-degenerated four-wave mixing (FWM)*, and *degenerated FWM*.

In this frame, since 2010 intense research has been made on developing analytical models to describe nonlinear interactions in PM WDM coherent systems. These models have proved by means of numerical simulations and experiments to be quite accurate on predicting system performance for DU links working in the pseudolinear regime. The majority of these models rely on solving (1.28) by applying first order regular perturbation (RP1) theory.

The first group of these models rely on a frequency domain approach, where the optical spectrum is sliced into spectral components and nonlinear interactions are analytically expressed similar to classical four wave mixing (FWM) formulation. The most well-known model is called the Gaussian Noise (GN) model and was formally introduced in [63-66]. The key underlying hypothesis of the GN model is that the transmitted signal statistically behaves as a stationary random Gaussian process, and that fiber nonlinearities lead to a nonlinear interference (NLI) which manifest itself as an additive white Gaussian noise (AWGN). These assumptions seem to hold in long-haul DU systems, where large values of accumulated dispersion make the power spectral density (PSD) of the signal tend to a circular complex Gaussian distribution independently of the modulation format. It is important to note that early attempts of the “GN model” tend back to 1993 [67], however the signal Gaussianity assumption didn’t hold for the DM systems used at that time and thus preventing widespread research.

The second group of these models utilize a time-domain analysis, where fiber nonlinearities are modeled by the FWM interaction between signal pulses at different time instances. The first study was introduced in [68] and retaken in [62] where a rigorous analysis of the RP1 method was carried out considering a multi span amplified link with coherent detection. Contrary to the frequency domain analysis, no signal Gaussianity has to be assumed. In [69-72], a proper formulation considering modulation format dependency was developed, leading also to an updated version of the GN model called enhanced-GN (EGN) [73]. Later on, a rigorous theory based on [62, 70], but including nonlinear signal-noise interactions (NSNI) as first proposed in [76], was developed in [61].

Finally, a third approach also in time domain was developed in [74, 75], where the autocorrelation function of the nonlinear distortions was propagated along the link in a similar way as the split step Fourier (SSFM) method. However, contrary to the SSFM where the link is modeled by a single path composed of a concatenation of linear (\hat{D}) and nonlinear (\hat{N}) blocks, this method used several parallel paths each of them containing only one \hat{N} element, such that parallel computing could be performed.

For a suitable explanation to describe the different types of nonlinear interactions, we make use the first kind of models, where nonlinear interactions are modeled as a FWM process between four frequency components of the optical spectrum [77]. Let's assume for the moment the propagation through an optical fiber of only one WDM channel with a given spectral bandwidth W . The FWM approach consists of slicing up its spectrum into an infinitesimal number of spectral components as shown in Fig. 1.10, and then to analyze their nonlinear beating using classical FWM formulation.

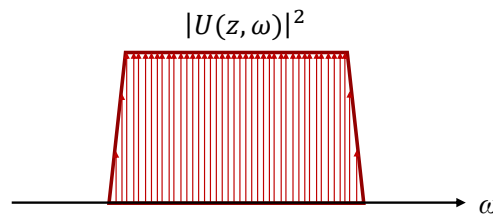


Fig. 1.10: WDM channel decomposed on a finite number of spectral tones.

Let the single WDM channel be represented as the sum of different discrete spectral tones of the form:

$$U(z, t) = \sum_i \zeta_i(z) \exp(-i\omega_i t) \quad (1.38)$$

where $\zeta_i(z)$ represents the spectrum of the spectral tone ω_i , and is considered to be a zero-mean random variable whose statistics depends on the transmitted symbols [69]. Inserting (1.38) into the nonlinear term of (1.28), leads to:

$$i\gamma\epsilon f(z)|U|^2U = i\gamma\epsilon f(z) \sum_i \sum_j \sum_k \zeta_i \zeta_j^* \zeta_k \exp(-i(\omega_i - \omega_j + \omega_k)) \quad (1.39)$$

From (1.39) the fiber nonlinearities produce nonlinear beatings between any three spectral components of the optical field, giving rise to a nonlinear interference (NLI) tone located at $\omega_l = \omega_i - \omega_j + \omega_k$. The strength of the NLI will depend on system parameters as: modulation format, link power profile, dispersion coefficient, etc. The above process can be generalized to multiple WDM channels, and nonlinear distortions can be classified depending on the spectral position of the interfering frequency tones ω as shown in Fig. 1.11.

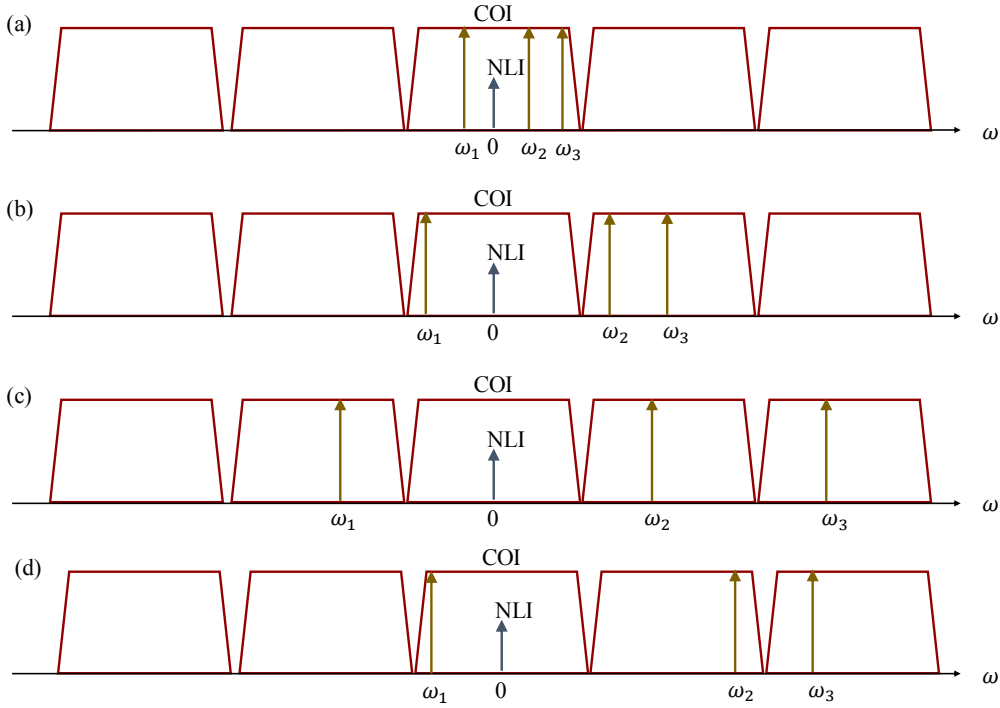


Fig. 1.11: Different types of FWM nonlinear interactions inducing a NLI tone at the channel of interest.

The first type of nonlinear interactions corresponds to the case where all spectral tones rely within the COI. This process can be cataloged as self-channel interference (SCI). It induces phase variations which are proportional to the instantaneous power of the COI itself, and which are transformed into amplitude variations by the coupling between dispersion and nonlinearities.

The second type can be classified as cross channel interference (XCI), which corresponds to the case where NLI arises from the interaction of the COI with only one any other channel.

XCI induces a phase shift on the COI proportional to the instantaneous power of the interfering channels, which will also be translated into amplitude variations by the interplay with fiber dispersion. Moreover, a polarization dependent NLI will induce a different phase-shift onto each polarization component of the field. As the change on SOP will depend on the instantaneous power of the co-propagating channels, it results in a noise-like SOP scattering and, hence, depolarization.

The third and fourth type can be classified as multi-channel interference (MCI), which arise from the interaction between the COI and two or three other channels. The strength of MCI in most relevant fibers with channel symbol-rates above 25 GBd, is of second importance and can be safely neglected.

The previous types of NLI can be further classified into two general groups: *intra-channel* nonlinearities containing SCI only, and *inter-channel* nonlinearities containing XCI and MCI. A priori, nonlinear interactions are deterministic and can be compensated for in the digital domain, if the information of all WDM channels is available. However, since joint processing of multiple WDM channels is currently considered to be prohibitively complex for commercial systems, inter-channel NLI is commonly treated as noise.

For the rest of this work, we will follow the time-domain analysis of [61] and [62] to describe NLI, as this method will be used to evaluate the NLI variance for performance analysis in Sec. 1.4.3, and to calculate the inter-channel NLI for DSP compensation in Sec. 1.3.5.2.

Eq. (1.28) can be solved using RP1 theory assuming that fiber nonlinearity acts as a small perturbation to the field. In the following, a fast description of the derivation of nonlinear distortions is presented. For a detail derivation, the reader is invited to [61], and [62]. In the frame of RP1 theory, we can expand U with respect to γ as:

$$U(z, t) = u^{(0)}(z, t) + \Delta u_{NL} \quad (1.40)$$

where $\Delta u_{NL}(z, t) = \gamma u^{(1)}(z, t)$, and $u^{(n)}(z, t)$ is the n 'th order perturbation of the normalized field $U(z, t)$. By substituting (1.40) into (1.28), and neglecting β_3 we obtain the zeroth and first order terms of the form:

$$\frac{\partial u^{(0)}(z, t)}{\partial z} = -i \frac{\beta_2}{2} \frac{\partial^2 u^{(0)}(z, t)}{\partial t^2} + \frac{n(z, t)}{\sqrt{\varepsilon f(z)}} \quad (1.41)$$

$$\frac{\partial \Delta u_{NL}(z, t)}{\partial z} = -i \frac{\beta_2}{2} \frac{\partial^2 \Delta u_{NL}(z, t)}{\partial t^2} + i \gamma \varepsilon f(z) |u^{(0)}(z, t)|^2 u^{(0)}(z, t) \quad (1.42)$$

Whose solutions are:

$$u^0(z, t) = \widehat{D}_z [u^0(0, t) + u_{ASE}(z, t)] \quad (1.43)$$

$$\Delta u_{NL}(z, t) = i\gamma\varepsilon\widehat{D}_z \int_0^z f(z')dz' \times \widehat{D}_{z'}^\dagger \left[|u^{(0)}(z', t)|^2 u^{(0)}(z', t) \right] \quad (1.44)$$

where \widehat{D}_z^\dagger is the adjoint of \widehat{D}_z . For an optical link of length L , the total field before detection ($z = L$) may be conveniently written as:

$$u(L, t) = \widehat{D}_L[u^{(0)}(0, t) + u_{ASE}(L, t)] + \Delta u_{NL}(L, t) \quad (1.45)$$

The resulting signal is the sum of the dispersed transmitted pulses and ASE noise, plus nonlinear distortions coming from the Kerr effect. At the receiver, the signal is first filtered to extract the COI, and then mixed with a local oscillator (LO) to perform balanced coherent detection (Seq. 1.3.3). Assuming the total modulated WDM waveform at the input be expressed by:

$$s(0, t) = \sum_k x_k u_k^{(0)}(0, t) + \sum_{k,s \neq 0} x_{k,s} u_{k,s}^{(0)}(0, t - \delta T_s) \exp(-i\Omega_s t + i\phi_s(0)) \quad (1.46)$$

where Ω_s , ϕ_s , and δT_s are the frequency, phase and time offsets of the s 'th channel with respect to the COI. After sampling and match filtering, the sampled photocurrent can be expressed as:

$$I_k = A_{L0}^* [x_k + \Delta x_{k,ASE} + \Delta x_{k,NL}] \quad (1.47)$$

where A_{L0}^* is the amplitude of the LO, x_k are the transmitted symbols on the COI, $\Delta x_{k,ASE}$ is a linear perturbation due to ASE noise, and $\Delta x_{k,NL}$ is a nonlinear perturbation term of the form:

$$\Delta x_{k,NL} = i\gamma\varepsilon \int_0^L dz f(z) |u^{(0)}(z, t)|^2 u^{(0)}(z, t) u_k^{(0)*}(z, t) \quad (1.48)$$

The previous equation represents the total nonlinear distortions using RP1 theory. By inserting (1.46) into (1.48) and neglecting NSNI, $\Delta x_{k,NL}$ can be written as:

$$\begin{aligned} \Delta x_{k,NL} = & \sum_{m,n,p} x_{m+k} x_{n+k} x_{p+k}^* C_{m,n,p}^{(0,0)} \\ & + 2 \sum_s \sum_{m,n,p} x_{m+k} x_{n+k,s} x_{p+k,s}^* C_{m,n,p}^{(0,s)} \\ & + \sum_{\substack{s,s' \\ s \neq s'}} \sum_{m,n,p} x_{m+k,s} x_{n+k,s'} x_{p+k,s+s'}^* C_{m,n,p}^{(s,s')} \end{aligned} \quad (1.49)$$

where the term $C_{m,n,p}$ corresponds to the system kernel weighting the nonlinear interactions between different signal symbols, and is expressed as:

$$C_{m,n,p}^{(s,s')} = i\gamma\varepsilon \int_0^L dz f(z) e^{i[\phi_s(z) + \phi_{s'}(z) - \phi_{s+s'}(z)]} \\ \times \int dt u_0^{(0)*}(z, t) u_{m,s}^{(0)}(z, t - t_s) u_{n,s'}^{(0)}(z, t - t_{s'}) u_p^{(0)*}(z, t - t_{s+s'}) \quad (1.50)$$

The first, second and third sums in (1.49) correspond to intra-channel (SCI), degenerate inter-channel (XCI) and non-degenerate inter-channel (MCI) FWM terms. As stated before, for long-haul DU links with channel symbol-rates above 25 GBd, the MCI term is much smaller than SCI and XCI, and can be safely neglected.

1.3.2.3 ASE Noise

The second term of (1.47) corresponds to ASE noise added to the k 'th symbol of the COI, and can be modeled as a zero-mean Gaussian random variable of variance σ_{ASE}^2 . For an EDFA, the PSD of ASE over the two signal polarizations is given by:

$$N_{ASE} = 2n_{sp}\hbar\omega_0(G - 1) \quad (1.51)$$

where n_{sp} is the spontaneous emission factor, \hbar is the Plank's constant divided by 2π , ω_0 is the reference angular frequency, and G is the gain of the amplifier. It is more practical to link the quantity n_{sp} to the most commonly used noise factor, F , defined as the ratio between the optical signal-to-noise ratio (OSNR) at the input and at the output of the amplifier by:

$$F = \frac{OSNR_{in}}{OSNR_{out}} = \frac{1}{G} + \frac{2n_{sp}(G - 1)}{G} \quad (1.52)$$

In this case, N_{ASE} can be expressed as:

$$N_{ASE} = \hbar\omega_0(GF - 1) \quad (1.53)$$

The ASE PSD is assumed constant over a given reference bandwidth B_{ref} , which is conventionally chosen to be 0.1 nm (12.5 GHz). In the case of homogeneous spans, the total ASE power over the reference bandwidth can be simply defined as:

$$P_{ASE} = N_{ASE}B_{ref}N_{spans} \quad (1.54)$$

For a wavelength around 1550 nm and assuming that optical amplifiers completely compensate for span loss, (1.54) can be approximated to:

$$P_{ASE_{dBm}} \approx -58_{dBm} + NF + 10\log_{10}(N_{spans}) + \alpha L_{span} \quad (1.55)$$

where NF is the amplifier noise figure in dB, i.e., $NF = 10\log_{10}(F)$.

1.3.2.4 Polarization Mode Dispersion

Real optical fibers present unintentional variations in the core shape due to stresses or deformations during the manufacturing process. This circular asymmetry leads to fiber birefringence. Therefore, an input pulse to the fiber will split into two orthogonal fast and slow polarization modes, which will acquire a relative time delay due to a difference in their group velocities. This relative time delay is referred as differential group delay (DGD), and is expressed by:

$$\Delta t = \tau_{DGD} = L \cdot \Delta\beta \quad (1.56)$$

where $\Delta\beta$ is the difference in group velocity between the fast and slow modes, and L is the propagation distance. DGD is sketched in Fig. 1.12a.

However, fiber birefringence is not constant but changes randomly along the fiber. These random variations will cause coupling between the two signal polarizations, as the fast and slow polarization modes from one segment decompose into both the fast and slow modes of the next segment. It can be shown that DGD accumulates as a random walk process [78], following a Maxwellian distribution. The mean value of the DGD is called the polarization mode dispersion (PMD). In the case of long-haul systems, PMD scales with the root-mean-square of the transmission distance. Due to PMD, a linearly polarized signal propagating through the fiber quickly reaches a state of arbitrary polarization

Moreover, DGD varies with optical angular frequency, due to the frequency dependence of the group velocity. Therefore, different frequency components of a pulse acquire different polarization states, resulting in pulse broadening.

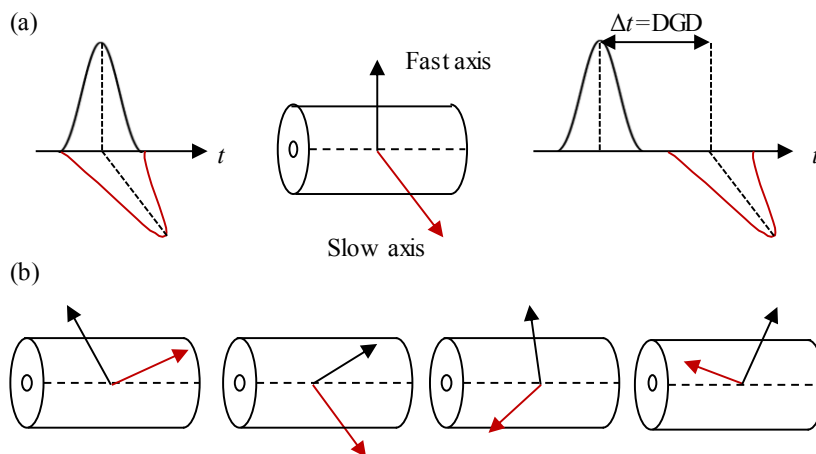


Fig. 1.12: (a) DGD over a fiber section with constant birefringence, and (b) schematic representation of a real fiber as a concatenation of infinitesimal birefringent sections randomly coupled.

PMD can be modeled by the concatenation of independent randomly oriented birefringent components given by:

$$H_{PMD} = \prod_{i=1}^N R_i D_i R_i^{-1} \quad (1.57)$$

$$R_i = \begin{bmatrix} \cos(\alpha_i) & \sin(\alpha_i) \\ -\sin(\alpha_i) & \cos(\alpha_i) \end{bmatrix} \quad (1.58)$$

$$D_i = \begin{bmatrix} \exp(-i(\omega\Delta t_i + \theta_i)/2) & 0 \\ 0 & \exp(i(\omega\Delta t_i + \theta_i)/2) \end{bmatrix} \quad (1.59)$$

Each birefringent element D_i introduces a constant phase shift. The rotation matrix R_i accounts for the random axes orientation of each PMD element.

In PM WDM systems, PMD leads to coherent crosstalk between the two orthogonal multiplexed polarizations (H, V), and to changes in the relative polarization state of the different wavelength channels as they propagate along the optical fiber. When operating in the linear regime, the first effect can be efficiently compensated by adaptive equalization algorithms as the one described in Sec. 1.3.4.3, while the second is of no importance.

Considering the fiber nonlinear regime, stochastic nonlinear interactions will take place due to the random polarization changes between different spectral components. In this case, the variance of the NLI term in (1.47) is not constant, and has been shown to statistically follow a Gaussian distribution [79]. While the effects of PMD on system performance in DU systems are very small due to the large accumulated CD, it becomes a fundamental limitation for nonlinear compensation techniques.

1.3.2.5 Polarization Dependent Loss

Besides PMD, another polarization effect is polarization dependent loss (PDL). It results from the asymmetry in the insertion loss or gain of an optical element (i.e., amplifiers, isolators, re-configurable optical add-drop multiplexers (ROADMs), etc.).

The transfer function of a PDL element can be modeled as:

$$\mathbf{H}_{PDL} = \begin{bmatrix} \cos(\alpha) & \sin(\alpha) \\ -\sin(\alpha) & \cos(\alpha) \end{bmatrix} \begin{bmatrix} 1 & 0 \\ 0 & \sqrt{\Gamma} \end{bmatrix} \begin{bmatrix} \cos(\alpha) & -\sin(\alpha) \\ \sin(\alpha) & \cos(\alpha) \end{bmatrix} \quad (1.60)$$

$$\Gamma_{dB} = -10 \log_{10}(\Gamma) \quad (1.61)$$

where $\Gamma_{dB} \geq 0$ is the PDL coefficient in dB, and α corresponds to a mismatch between the polarization states of the incident signal and the principal polarization states (PPS) of the PDL component.

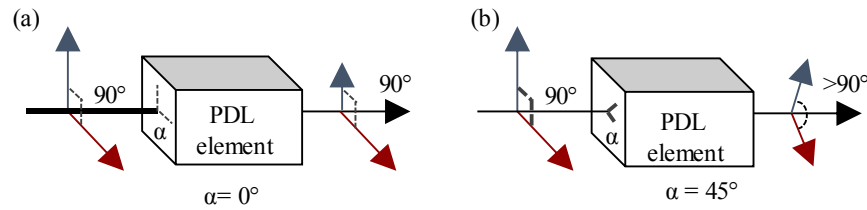


Fig. 1.13: PDL effect: the reference signal without PDL propagates through a PDL element aligned with (a) its polarization axes, and (b) at an angle of $\theta=45^\circ$ with respect to its polarization axes.

Due to fiber birefringence, PDL translates into signal power fluctuations depending on the random evolution of the states of polarization (SOP), leading to OSNR penalty and break of the orthogonality between the polarization tributaries. Similar to PMD, PDL is a random process whose statistics follow a Maxwellian distribution when expressed in dB as shown in [80].

Contrary to the unitary processes as CD or PMD, the power fluctuations caused by PDL cannot be undone by digital equalization. System margins are typically considered in order to account for PDL-induced penalties. Other techniques aiming to mitigate PDL effects as Polarization-Time coding [81], or Pairwise coding [82] have been suggested.

1.3.3 Optical Coherent Receiver

After transmission, the COI is optically filtered and detected. The main function of the coherent receiver is to convert the incoming optical signal back to the electrical domain. Assuming intradyne coherent detection, the optical signal is coherently combined with the optical field of a continuous wave free-running LO before optical-electrical conversion. Fig. 1.14 shows the structure of a full coherent polarization diverse receiver.

At its input, the signal is divided into its two orthogonal polarizations components by the use of polarization beam splitters (PBS). Each polarization enters a free-space mixer structure whose second input is fed by the unmodulated light coming from a LO tuned at the same wavelength of the signal. Within each mixer, the LO is separated into two 90° - phase shifted parts that interfere with the incident signal. This process produces two pairs of outputs in quadrature for each polarization. The 8 resulting optical fields are then detected individually using *PIN* photodiodes. Balanced detection is used to suppress the DC components corresponding to direct detection.

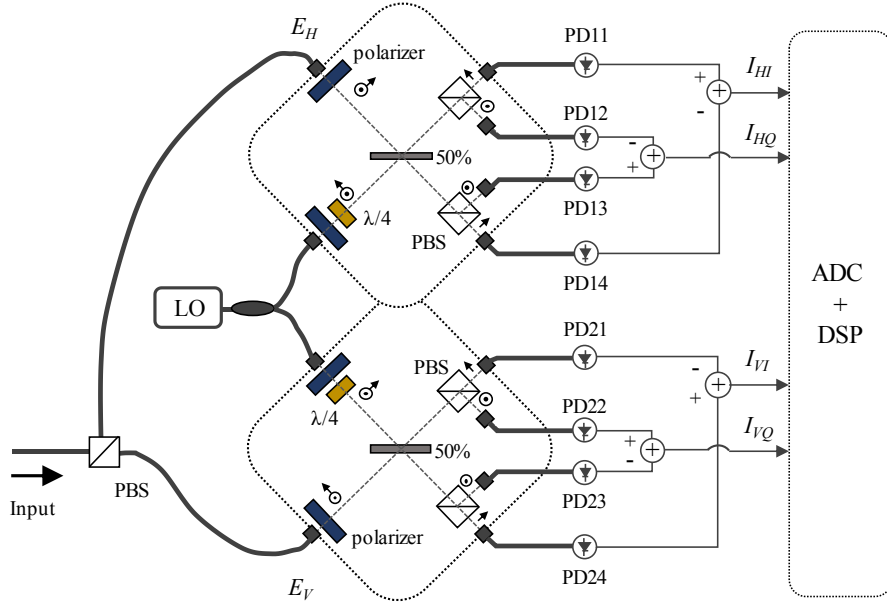


Fig. 1.14: Full coherent polarization diverse coherent detection. PBS: polarization beam splitter, PD: photodiode.

The photocurrents after balanced detection are described as:

$$\begin{pmatrix} I_{HI} \\ I_{HQ} \\ I_{VI} \\ I_{VQ} \end{pmatrix} = \mathcal{R} \begin{pmatrix} \text{Re}\{u_{COI}^H A_{LO}^*\} \cos(\Omega_{LO} t + \phi_{LO}) \\ \text{Im}\{u_{COI}^H A_{LO}^*\} \sin(\Omega_{LO} t + \phi_{LO}) \\ \text{Re}\{u_{COI}^V A_{LO}^*\} \cos(\Omega_{LO} t + \phi_{LO}) \\ \text{Im}\{u_{COI}^V A_{LO}^*\} \sin(\Omega_{LO} t + \phi_{LO}) \end{pmatrix} \quad (1.62)$$

where \mathcal{R} is the detector responsivity, u_{COI} is the COI optical signal, A_{LO} is the LO amplitude, and Ω_{LO} , and ϕ_{LO} , are frequency and phase offsets between the LO and the COI. Please note that ϕ_{LO} is a time-varying function due to the nonzero COI and LO laser linewidths. The frequency and phase offsets between the signal and LO can be compensated in the digital domain by means of DSP (Sec. 1.3.4.4).

The main advantage of coherent detection is evident from (1.62). First, as the generated photocurrents are proportional to A_{LO} , by making the power of the LO higher than that of the signal, the receiver sensitivity can be greatly improved. Moreover, I and Q signal components can be fully recovered; thus, a complete reconstruction of the field can be made and advanced post-processing algorithms can be applied to compensate for system impairments. Finally, the two orthogonal polarizations are detected independently, such that information can be coded into each polarization.

1.3.4 Standard Digital Signal Processing Blocks

The effects that are compensated for in the digital domain by means of DSP in current coherent optical systems are: CD, PMD, frequency and phase time-varying offsets, and transmitter/receiver IQ imbalances. The main DSP clocks compensating for these effects are sketched in Fig. 1.15, and will be discussed in the following.

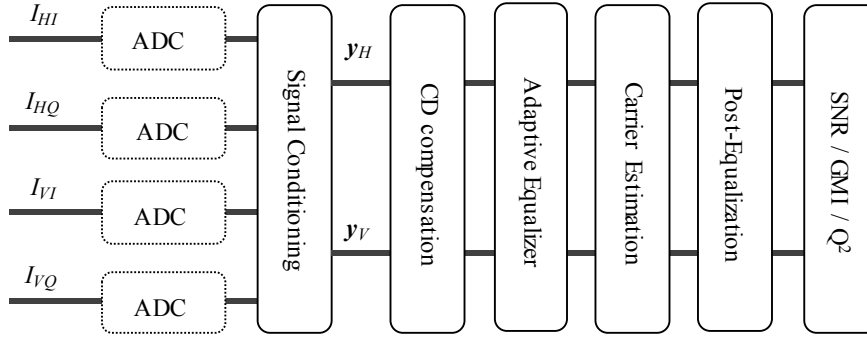


Fig. 1.15: Standard DSP blocks for linear impairments mitigation.

1.3.4.1 Signal Conditioning

According to the Shannon-Nyquist criterion, the received signal has to be sampled at a rate of at least twice its bandwidth. The first step of DSP is to resample the signal at 2 samples per symbol (sps), followed by a digital filter to suppress out-of-band noise.

At this stage, any residual DC component of the signal can also be removed to compensate for signal components that are artifacts of the receiver structure and not present in the optical spectrum. The signals are also normalized in power, removing any power imbalance within the receiver, and simplifying much of the signal processing performed later.

1.3.4.2 Chromatic Dispersion Compensation

As presented in Sec. 1.3.2, mitigation of fiber CD can be performed by applying the adjoint of the dispersion operator \hat{D}_z . For a total propagation distance L , CD compensation can be written as:

$$\hat{\mathbf{y}}^H = \hat{D}_L^\dagger[\mathbf{y}^H] \quad (1.63)$$

$$\hat{\mathbf{y}}^V = \hat{D}_L^\dagger[\mathbf{y}^V] \quad (1.64)$$

The operator \widehat{D}_L^\dagger can be efficiently implemented using overlap-and-save methods and fast Fourier transforms (FFT) [83].

1.3.4.3 Adaptive Equalization

A key aspect of a polarization diversity coherent receiver is to recover the two orthogonal polarization tributaries. Due to fiber birefringence, the two polarizations will be coupled and ISI will occur. As presented in Sec. 1.3.2.4, fiber birefringence can be modeled as a concatenation of birefringent sections whose axes change randomly along the fiber.

The total concatenation of birefringent sections can be modelled into an equivalent channel impulse response. The task of the equalizer is to estimate the inverse of the impulse response to reverse the effects of polarization coupling and PMD. The equalizer performs the following matrix operation:

$$\begin{bmatrix} \hat{y}_k^H \\ \hat{y}_k^V \end{bmatrix} = \begin{bmatrix} \mathbf{h}_k^{HH} & \mathbf{h}_k^{VH} \\ \mathbf{h}_k^{HV} & \mathbf{h}_k^{VV} \end{bmatrix} \begin{bmatrix} \mathbf{y}_k^H \\ \mathbf{y}_k^V \end{bmatrix} \quad (1.65)$$

where y_k and \hat{y}_k are the k -th symbols at the input and output of the equalizer respectively. We define \mathbf{y}_k as a $2N_t+1$ long vector ($\mathbf{y}_k = (y_{k-N_t}, \dots, y_k, \dots, y_{k+N_t})^T$), and the N_t -tap equalizer filters $\mathbf{h}_k = (h_{k,-N_t}, \dots, h_k, \dots, h_{k,N_t})$. The problem of adaptive equalization is finding the equalizer filters \mathbf{h} as a function of time (k). A common algorithm for constant amplitude signals is the *constant modulus algorithm* (CMA) which tries to minimize the following error function:

$$\begin{aligned} \varepsilon_k^H &= 1 - |\hat{y}_k^H|^2 \\ \varepsilon_k^V &= 1 - |\hat{y}_k^V|^2 \end{aligned} \quad (1.66)$$

In the case of multi-level modulation formats, another algorithm referred as *multi-modulus algorithm* (MMA) can be used. In this case, the error function takes the form

$$\begin{aligned} \varepsilon_k^H &= \hat{r}^2 - |\hat{y}_k^H|^2 \\ \varepsilon_k^V &= \hat{r}^2 - |\hat{y}_k^V|^2 \end{aligned} \quad (1.67)$$

where \hat{r} is the closest constellation amplitude to the received symbol. The estimation can be improved by sending a periodic sequence of known pilot symbols. In this case, the error function can be modified to:

$$\begin{aligned} \varepsilon_k^H &= (1 - p_k) \cdot \hat{r}^2 + p_k \cdot |x_k^H|^2 - |\hat{y}_k^H|^2 \\ \varepsilon_k^V &= (1 - p_k) \cdot \hat{r}^2 + p_k \cdot |x_k^V|^2 - |\hat{y}_k^V|^2 \end{aligned} \quad (1.68)$$

where x_k is the k -th transmitted pilot symbol, and p_k is k -th element of a binary gating function indicating the position of the pilot symbols ($p_k \in \{0,1\}$). Considering a pilot rate $r_p = N_p/K_p$ (i.e., sending N_p consecutive pilot symbols at the beginning of a sequence block of length K_p), the gating function is:

$$p(k) = \text{rec}\left(\frac{k}{N_p}\right) \otimes \sum_{n=1}^{(2N+1)/K_p} \delta(k - (n-1)K_p - 1) \quad (1.69)$$

where $\text{rec}(\cdot)$ is the rectangular function, and $\delta(\cdot)$ the Dirac-delta function. The equalizer filters \mathbf{h} can then be updated by stochastic gradient descent [84]. In addition to polarization dependent impairments, this adaptive equalizer can also be used to implement the matched filter, find the optimal sampling instant and compensate residual CD [85].

1.3.4.4 Carrier Estimation

As seen in Seq. 1.3.3, the use of a free running LO will lead to frequency and time-varying phase offsets. Therefore, the problem of carrier estimation can be divided into a coarse estimation of the frequency offset, followed by a fine estimation of the slowly varying phase and residual frequency offset.

Assuming that CD, DGD, and polarization demultiplexing have been completely compensated for, and ignoring for NL effects, the signal of one of the polarization tributaries at the output of the equalizer can be written as:

$$y_k = x_k \exp(i\zeta_k k + i\xi_k) + n_k \quad (1.70)$$

where x_k are the transmitted symbols, ζ_k is the time-discrete frequency offset between the COI and the LO defined as $\zeta = \Omega_{LO} T_s$, with T_s the symbol period, ξ_k is a discrete time-varying phase, and n_k is an additive zero-mean circularly-symmetric complex-valued Gaussian noise.

Frequency estimation can be performed based on the maximization of periodogram as [86]:

$$\hat{\zeta}_k = \frac{1}{4} \arg \max_{\zeta} \left| \frac{1}{N} \sum_{n=-N}^N (y_{k+n})^4 \cdot e^{-i\zeta k} \right|^2 \quad (1.71)$$

with $2N + 1$ the number of available samples. If N is a factor of 2, the maximization can be efficiently done through the computation of FFT.

Once the frequency estimation is done, the estimation of the phase ξ has to be performed. The time-varying phase can be modeled as a Wiener process in which $\xi_{k+1} = \xi_k + b_k$, where b_k is a random variable with zero mean and variance $2W_p T_s$, and W_p is the sum of linewidths of

the signal and LO lasers. Phase estimation can be done using the well-known Blind Phase Search (BPS) algorithm as:

$$\hat{\xi}_k = \arg \min_{\xi} \sum_{n=-N}^N \frac{|y_{k+n} - \hat{x}_{k+n} e^{-i\xi}|^2}{N_0} - \log_{10}(P(\hat{x}_{k+n})) \quad (1.72)$$

where N is the averaging length, \hat{x}_k is the decided symbol, and $P(\hat{x}_k)$ corresponds to the prior probabilities. Please note that for equiprobable constellations (1.72) is reduced to:

$$\hat{\xi}_k = \arg \min_{\xi} \sum_{n=-N}^N |y_{k+n} - \hat{x}_{k+n} e^{-i\xi}|^2 \quad (1.73)$$

As the phase varies typically much slowly that the symbol duration, phase estimation can be performed by averaging over many symbol intervals N . Increasing N will improve the estimation by averaging out Gaussian noise, however fast variations of the phase will be not able to be tracked. On the contrary, choosing low values of N will allowed tracking fast phase variations, but the estimation will be poor as additive noise is not sufficiently averaged. Therefore, N has to be optimized depending on the system SNR and on the phase variation speed. Typical linewidth values of external cavity lasers (ECL) are around 100 kHz and can go up to a few MHz for distributed feedback (DFB) lasers.

The minimization in (1.72) cannot be performed analytically, and there is typically more than one phase that minimizes this metric depending on the rotational symmetry of the constellation, S . Therefore, (1.72) can be solved by testing equally spaced candidate phases, evaluate the metric and choose the phase that minimizes it. However, the metric has ambiguities over the range between 0 to 2π , such that we can test phases between 0 and $2\pi/S$, and then apply a phase unwrapper that removes discontinuities.

After phase estimation, the phase ambiguity has to be corrected for. This can be performed using a pilot-aided approach similar to the one described in Sec. 1.3.4.3, where N_p pilot symbols are sent within a block length K_p . The phase ambiguity is calculated and averaged over the N_p pilots within each symbol block, and the resulting estimated phase ambiguity is then applied to the entire block. This process is known as pilot-aided cycle slip removal.

1.3.4.5 Post Equalization

The last DSP stage is a post-equalizer which compensates for any phase/gain mismatch between I and Q components of the received signal. These IQ imbalances may arise from an improper biasing of the PM-IQ modulator, imperfections in the coherent receiver front-end, or timing mismatches (delay skew) due to different physical path lengths in the circuit trace. The

penalties associated to IQ imbalances grow as the order of the modulation and symbol-rate increases [87].

1.3.5 Nonlinear Digital Signal Processing

After efficient mitigation of the previous impairments, the performance of actual coherent long-haul transmission systems is limited by fiber nonlinearities. As seen in Sec. 1.3.2, *signal-signal* fiber nonlinear interactions arising from the Kerr effect are a priori deterministic and could be compensated by DSP. Different DSP based nonlinear compensation (NLC) techniques have been under research during the past years.

Optical NLC techniques have also been studied. The main interest behind optical NLC techniques is their large processing bandwidth capabilities that are forbidden by DSP. Two main approaches have been proposed in the literature: mid-link optical phase conjugation (OPC), and coherent superposition in phase sensitive amplification (PSA). Both techniques are based on transmitting a phase-conjugated version of the signal to cancel out fiber nonlinearities (NL). In OPC the propagating signal is phase-conjugated at the middle of the optical link, such that transmission of the conjugated signal through the second half of the link cancels out CD and NL. However, to be efficient, this approach requires a fully symmetric transmission line which is difficult to achieve in practical systems. In addition, it requires the transmission link to be modified by the insertion of one or several optical phase conjugator elements [88-90]. On the other hand, coherent superposition in PSA is based on co-propagating two phase-conjugated waves (signal and idler), and then coherently superimposing them at the receiver side by means of a PSA. This process can also be implemented in the digital domain, which is better known as phase-conjugated twin waves (PCTW). The main drawback of PSA and PCTW is the reduction by half of the SE, making them incompatible with high capacity optical transmission systems [91-94]. In contrast to the idea of having large processing bandwidth capabilities, both OPC and PSA have been only demonstrated for a reduced number of optical channels with relative low gains. Optical NLC techniques are deemed to be too expensive and complex to be adopted by the industry at least in the near future.

The main advantage of DSP-based NLC is that it does not require the transmission link to be modified, making it more flexible and less costly for implementation in already deployed systems. In this sense, the most well-known technique is digital backpropagation (DBP) [36, 37], which is the most efficient algorithm in terms of performance improvement, and it is often used as a reference for all other nonlinear compensation techniques. The main drawback of DBP is its high computational complexity, making its hardware implementation unfeasible. Different approaches to reduce its complexity have been proposed [38, 95-98], specially filtered DBP (FDBP). Besides DBP, another novel approach based on perturbation theory called perturbative nonlinear compensation (PNLC) has proven to achieve considerable NLC gains

with reduced complexity [40, 99, 100]. Approaches based on 3rd order frequency domain Volterra series have also been studied [140]. In combination with the continuous increase of processing capabilities and lower power consumptions of integrated circuits, DSP-based NLC techniques are the most promising candidates for implementation in future generation systems.

In this work, we center our study on the performance of FDBP and PNLC. In the following, we briefly describe their implementation principles.

1.3.5.1 Digital Backpropagation

DBP involves calculating a numerical solution of (1.28) by means of the split step Fourier method (SSFM), where the fiber is treated as a series of linear and nonlinear sections, assuming that their joint interaction is independent within a small fiber section h . The linear DBP step is based on applying the adjoint dispersion operator \hat{D}_h^\dagger over the length $z = h$, while the DBP nonlinear step is defined by the nonlinear operator based on the Manakov equation by:

$$\hat{N}_{h_{eff}}^H[\mathbf{y}^H] = \mathbf{y}^H \cdot e^{iP\frac{8}{9}\gamma\kappa h_{eff}(|\mathbf{y}^H|^2 + |\mathbf{y}^V|^2)} \quad (1.74)$$

$$\hat{N}_{h_{eff}}^V[\mathbf{y}^V] = \mathbf{y}^V \cdot e^{iP\frac{8}{9}\gamma\kappa h_{eff}(|\mathbf{y}^H|^2 + |\mathbf{y}^V|^2)} \quad (1.75)$$

where the parameter κ is a constant of proportionality that has to be optimized, \mathbf{y}^V and \mathbf{y}^H are DBP input signal samples over H and V polarizations, $|\mathbf{y}^H|^2 + |\mathbf{y}^V|^2$ is the normalized received signal power such that its mean equals the unity, and P is the optical power per polarization at the position of the fiber where \hat{N} is applied. For DBP steps equal or higher than the span length L_{span} , the effective DBP step length is defined as: $h_{eff} = L_{eff}/N_{stps}$, with $L_{eff} = 1 - \exp(-\alpha L_{span})/\alpha$ being the effective span length, α the fiber attenuation coefficient, and $N_{stps} = L_{span}/h$ the number of DBP steps per span.

In order to decrease the complexity of the standard DBP, it has been shown that low-pass filtering $|\mathbf{y}^H|^2 + |\mathbf{y}^V|^2$ helps decreasing N_{stps} without sacrificing performance, this technique is known as FDBP [38]. In this case, \hat{N} can be expressed by:

$$\hat{N}_{h_{eff}}^H[\mathbf{y}^H] = \mathbf{y}^H \cdot e^{iP\frac{8}{9}\gamma\kappa h_{eff}(\mathcal{F}^{-1}\{\mathcal{F}\{|\mathbf{y}^H|^2 + |\mathbf{y}^V|^2\} \cdot H(f)\})} \quad (1.76)$$

$$\hat{N}_{h_{eff}}^V[\mathbf{y}^V] = \mathbf{y}^V \cdot e^{iP\frac{8}{9}\gamma\kappa h_{eff}(\mathcal{F}^{-1}\{\mathcal{F}\{|\mathbf{y}^H|^2 + |\mathbf{y}^V|^2\} \cdot H(f)\})} \quad (1.77)$$

where $\mathcal{F}\{\cdot\}$ and $\mathcal{F}^{-1}\{\cdot\}$ stand for Fourier and inverse Fourier transform, and $H(f)$ is the frequency response of the nonlinear phase correction filter. DBP/FDBP outputs after each step ρ can be expressed by:

$$\mathbf{y}_{\rho+1}^H = \widehat{N}_{\text{eff}}^H \left[\widehat{D}_h^\dagger [\mathbf{y}_\rho^H] \right] \quad (1.78)$$

$$\mathbf{y}_{\rho+1}^V = \widehat{N}_{\text{eff}}^V \left[\widehat{D}_h^\dagger [\mathbf{y}_\rho^V] \right] \quad (1.79)$$

In general, the computational complexity of FDBP per step is higher than that of standard DBP, requiring two extra n -point real number FFT, and one extra real number multiplication. However, FDBP allows reducing the total number of steps per link, resulting in an overall reduced complexity. As mentioned, the linear step is performed in the frequency domain by means of FFT, while the nonlinear step is performed in the time domain, both working typically at 2 samples per symbol.

1.3.5.2 Perturbative Nonlinear Compensation

As presented in Seq. 1.3.2.2, (1.28) can be solved using a time-domain RP1 theory, where fiber NL is treated as a small perturbation to the optical field. Expressions for the nonlinear distortion $\Delta x_{k,NL}$ can be obtained following (1.49). The idea behind PNLC is to pre-calculate these distortions and subtract them from the signal. Contrary to DBP, PNLC operates at the symbol level and requires a single compensation stage per link. Therefore, its complexity is greatly reduced compared to DBP.

Considering the simplest scheme where the transmitter and receiver have only access to the COI, the information of other WDM channels is unknown and cannot be used for NLC. Therefore, assuming only intra-channel NLC, the compensated k 'th symbol in H and V polarizations of the received noisy signals \hat{y}_k^H and \hat{y}_k^V after PNLC can be written as [40]:

$$\begin{aligned} \hat{y}_k^H &= y_k^H \\ &- \kappa \sum_{\substack{m=-B \\ m \neq 0}}^B \sum_{\substack{n=-B \\ n \neq 0}}^B [y_{m+k}^H y_{n+k}^H (y_{m+n+k}^H)^* + y_{m+k}^H y_{n+k}^V (y_{m+n+k}^V)^*] \cdot C_{m,n} \end{aligned} \quad (1.80)$$

$$\begin{aligned} \hat{y}_k^V &= y_k^V \\ &- \kappa \sum_{\substack{m=-B \\ m \neq 0}}^B \sum_{\substack{n=-B \\ n \neq 0}}^B [y_{m+k}^V y_{n+k}^V (y_{m+n+k}^V)^* + y_{m+k}^V y_{n+k}^H (y_{m+n+k}^H)^*] \cdot C_{m,n} \end{aligned} \quad (1.81)$$

where κ is a scaling parameter to account for channel power uncertainty that has to be optimized, and $C_{m,n}$ is a complex matrix of size $2B \times 2B$ containing all the pre-calculated intra-channel perturbative coefficients. The second terms of (1.80) and (1.81) are similar to (1.49) when only intra-channel nonlinearities are considered, and where $p = m + n$. The $C_{m,n}$ coefficients are functions of the power profile, dispersion map and pulse shape. For the special

case of Nyquist pulses DU systems, they can be expressed as [40]:

$$C_{m,n} = i \frac{8}{9} \gamma P_0 L_d \int_{\frac{|m|+|n|}{2\pi}}^{L_{tot}/L_d} d\eta f(\eta) \frac{\exp(imn/\eta)}{2\pi\eta} \times \left(1 - \frac{|m| + |n|}{2\pi\eta}\right) \quad (1.82)$$

where γ is the fiber nonlinear coefficient, P_0 is the transmitted channel optical power, L_d is the dispersion length defined by $L_d = \beta_2/T_s^2$, L_{tot} is the total link length, η is the normalized propagation distance with respect to L_d , and $f(\cdot)$ is the power profile. Considering homogeneous spans with EDFA-only amplification compensating completely for the span loss, $f(\cdot)$ is expressed as:

$$f(\eta) = \exp\left(-\alpha \text{mod}(L_d \eta, L_{span})\right) \quad (1.83)$$

with α the fiber attenuation coefficient and $\text{mod}(\cdot)$ the modulus operator. The term $m = n = 0$ is excluded from (1.82). The complexity and performance of PNLC are determined by the size of the $C_{m,n}$ matrix. When more terms are considered, a higher performance is achieved at the cost of a higher complexity. In general, the optimum size of the $C_{m,n}$ matrix will depend on the channel memory induced by chromatic dispersion. Fig. 1.16 shows an example of the normalized amplitude in dB of the $C_{m,n}$ coefficients, i.e. $20 \log_{10}(C_{m,n}/C_{0,0})$, for an arbitrary system. An approach to reduce the complexity of PNLC is simply to discard all terms below a given amplitude threshold ξ_{th} , while keeping B fix [99].

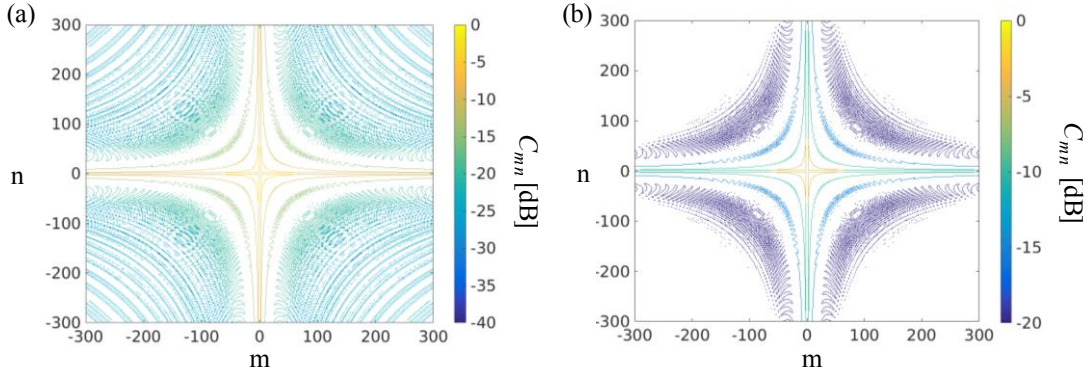


Fig. 1.16: Magnitude of the (a) complete and (b) truncated $C_{m,n}$ look-up-table (LUT) for an arbitrary system normalized to $C_{0,0}$. For the truncated case, all valued below -20 dB have been discarded.

Note that contrary to DBP/FDBP where fiber CD and NL are jointly compensated, PNLC compensates only for fiber NL. Therefore, the CD equalization DSP block is still required.

1.4 PERFORMANCE ANALYSIS

As mentioned in Sec. 1.2, different metrics for system performance evaluation are generally used, among which we find the MI, GMI, pre-FEC BER, and Q²-factor. For an AWGN channel, all the above metrics are functions of the SNR. While the first are metrics of performance of a digital system depending on the modulation format and decoding schemes, the SNR is the conventional physical measure of transmission. It is the reciprocal of the normalized mean squared error between the transmitted and received symbols, and therefore is a suitable measure of signal distortions independent of the modulation format. All impairments following Gaussian statistics can be accurately accounted for by SNR evaluation. In the following, system performance evaluation in terms of SNR is described.

1.4.1 AWGN Channel

As mentioned in Sec. 1.3.2, the use of several optical amplifiers in the link will degrade the OSNR of the system due to accumulation of ASE noise. The definition of OSNR is:

$$OSNR = \frac{P_{ch}}{P_{ASE}} \quad (1.84)$$

where P_{ch} is the total average channel signal power over the two polarizations, and P_{ASE} is the power of ASE noise as per (1.55). ASE noise is defined over a reference bandwidth, B_{ref} , which is commonly taken to be 12.5 GHz or equivalently 0.1 nm. Contrary to the OSNR, the SNR accounts only for the noise inside the bandwidth of the signal, inside which the PSD of ASE is assumed to be locally white. Under this assumption, the OSNR and SNR for a polarization-multiplexed signal are related by:

$$OSNR = \frac{R_s}{B_{ref}} SNR \quad (1.85)$$

The SNR accounting for ASE noise can then be expressed as:

$$SNR = \frac{P_{ch}}{\sigma_{ASE}^2} \quad (1.86)$$

where the ASE variance σ_{ASE}^2 over the COI is expressed as:

$$\sigma_{ASE}^2 = P_{ASE} \frac{R_s}{B_{ref}} \quad (1.87)$$

The above definition of SNR corresponds exactly to the SNR that can be measured on the received electrical signal constellation at the input of the FEC.

1.4.2 Back-to-back (B2B) Penalties

An ideal ADC presents a perfectly linear response and simply quantizes the incoming signal by 2^{NOB} number of discrete levels, where NOB corresponds to the number of bits associated with the ADC. Therefore, an 8-bit ADC will have 256 quantization levels. Considering a noiseless sinusoidal wave at the input of an ideal ADC, the SNR at its output is obtained by:

$$SNR_{dB} = 6.02 \cdot NOB + 1.76 \quad (1.88)$$

However, a real ADC will add some extra noise and distortions to the signal that will contribute to further degrade the SNR. We can then define the effective number of bits (ENOB), as the resolution of an ideal ADC that would have the same SNR as the real ADC under study. The ENOB of state-of-the-art 8 bit-ADC/DACs is <6 bits. The limited resolution of ADC/DACs will limit the maximum achievable SNR of the system.

Additional SNR penalties will arise from high signal pre-emphasis to overcome IQ modulator limited bandwidth, from an increased peak-to-average power ratio (PAPR) due to the use higher order modulation formats, from added ASE noise due to optical amplification of the signal at the transmitter and receiver side, and DSP penalties due to imperfect signal equalization.

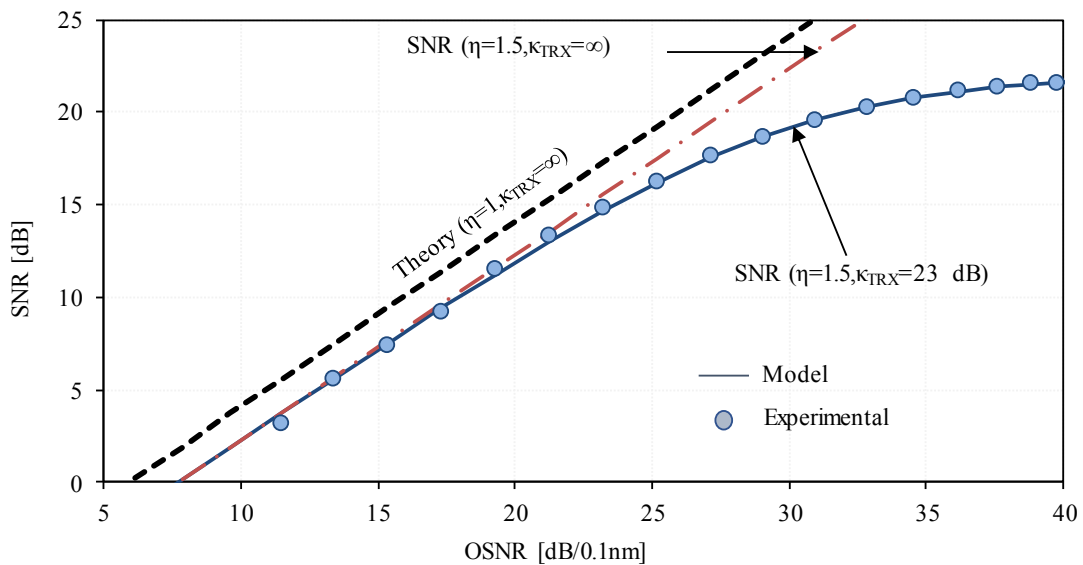


Fig. 1.17: Typical B2B performance showing implementation penalties.

Fig. 1.17 shows a typical experimental back-to-back (B2B) performance of an arbitrary system in terms of SNR vs OSNR. The theoretical relation between SNR and OSNR following (1.85) is also shown for comparison.

In this work, we model B2B penalties by introducing two variables into (1.86), κ_{TRX} accounting for TX-RX impairments, and η accounting for DSP penalties. The presence of κ_{TRX} will impose a maximum achievable SNR independent on signal power, while η will be translated into a horizontal translation of the curve. Under these constraints, (1.86) can be rewritten as:

$$SNR = \frac{P_{ch}}{\eta\sigma_{ASE}^2 + \kappa_{TRX}P_{ch}} \quad (1.89)$$

The proposed modeling of B2B SNR is also depicted in Fig. 1.17 showing to be sufficient to match experimental results. In practice, the values of η and κ_{TRX} have to be obtained from experimental curves.

1.4.3 Nonlinear Variance

All the three types of perturbative models described in Seq. 1.3.2.2 can be used to calculate the variance of NLI distortions. It is important to notice that all three approaches converge to similar results, and can be used to *accurately* predict the performance of modern DU long haul optical coherent systems. In this work, the time-domain model of [61] is preferred due to its reduced computational complexity. The impact of NSNI on the overall performance for fully loaded WDM systems has been shown to be negligible. Moreover, when NLC is applied, its impact is only important for a large number of compensated WDM [61]. Therefore, NSNI will not be considered in this work.

The nonlinear distortions are treated as a NLI noise term. For *signal-signal* interactions, its variance is given by:

$$\sigma_{NLI}^2 = a_{NLI}P_{ch}^3 \quad (1.90)$$

where a_{NLI} is a proportionality coefficient independent of signal power accounting for both intra-channel and inter-channel nonlinear distortions, i.e.

$$a_{NLI} = a_{NLI-intra} + a_{NLI-inter} \quad (1.91)$$

In general, a_{NLI} is a function of all system parameters, i.e., modulation format, symbol-rate, fiber type, propagation distance, channel count, etc. The estimation of a_{NLI} is reduced to calculate:

$$a_{NLI} = Var(\Delta x_{k,NL})/P_{ch}^3 \quad (1.92)$$

Following [61], $a_{NLI-intra}$ and $a_{NLI-inter}$ can be expressed as are given by:

$$a_{NLI-intra} = \frac{16}{81} \gamma^2 \left[3\mathcal{X}_1 + \left(\frac{\mu_4}{\mu_2^2} - 2 \right) [\mathcal{X}_2 + 5\mathcal{X}_3 + 4\mathcal{X}_4] + \left(\frac{\mu_6}{\mu_2^3} - 9 \frac{\mu_4}{\mu_2^2} + 12 \right) \mathcal{X}_5 \right] \quad (1.93)$$

$$a_{NLI-inter} = \frac{16}{81} \gamma^2 \left[5 \sum_s \left[\mathcal{X}_{1,s} + \left(\frac{\mu_4}{\mu_2^2} - 2 \right) \mathcal{X}_{3,s} \right] + 2 \sum_{s,s'} \mathcal{X}_{1,s,s'} \right] \quad (1.94)$$

where μ_n the n 'th moment of the constellation with symbols a_k defined by:

$$\mu_n = \langle |a_k|^n \rangle \quad (1.95)$$

and where the various coefficients \mathcal{X} are functions of the power profile, pulse shaping and dispersion map (see Appendix of [61]) for a given WDM channel denoted by s . The COI corresponds to the case of $s = 0$ and is dropped from the notation.

1.4.4 Theory of Nonlinear Channel

Considering all three sources of noise (ASE, B2B, and NLI) to be uncorrelated, the total system SNR can finally be written as:

$$SNR = \frac{P_{ch}}{\eta \sigma_{ASE}^2 + \kappa_{trx} P_{ch} + a_{NLI} P_{ch}^3} \quad (1.96)$$

The power which maximizes the SNR, also known as nonlinear threshold (NLT), can be obtained by finding the P satisfying $dSNR/dP = 0$, and is given by:

$$P_{NLT} = \left(\frac{\eta \sigma_{ASE}^2}{2a_{NLI}} \right)^{1/3} \quad (1.97)$$

and the corresponding optimum SNR can be then expressed as:

$$SNR_{NLT} = \frac{1}{(\eta \sigma_{ASE}^2)^{2/3} \left(\frac{27}{4} a_{NLI} \right)^{1/3} + \kappa_{trx}} \quad (1.98)$$

Fig. 1.18 shows the performance of an arbitrary system in terms of channel power versus SNR generated as per (1.96), where P_{NLT} and SNR_{NLT} are also shown.

In [72], the dynamics of inter-channel NLI was studied following a pulse collision approach. It was interestingly pointed out that inter-channel NLI has two types of noise contributions: phase and polarization noise (PPN), and circular noise. For long haul WDM systems based on lumped amplification as the ones studied in this work, the circular NLI component dominates over PPN contributions, such that the overall NLI variance distribution is mostly circular

Gaussian. Therefore, the SNR calculated by (1.96) can be directly translated to GMI following the GMI vs SNR curve for each modulation format as shown in Fig. 1.4.

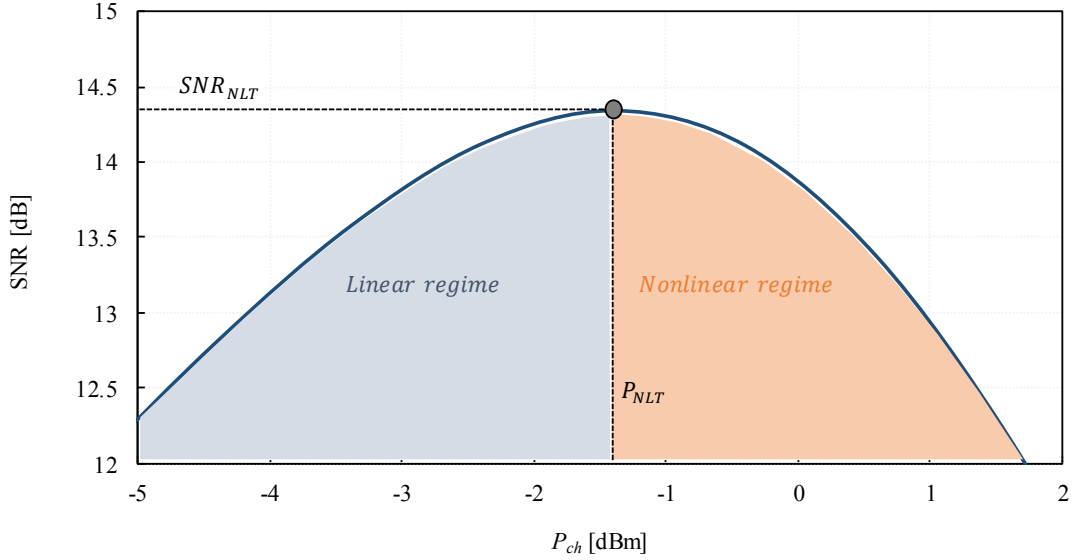


Fig. 1.18: SNR versus average channel launched power for an arbitrary system.

1.4.5 Theoretical Limits to Nonlinear Compensation

The possibility to analytically evaluate the nonlinear variance have not only served to address system performance evaluation, but also to estimate the ultimate potential benefits of NLC. The evaluation of NLC benefit is typically made in terms of the improvement in the peak SNR described by (1.98). A typical system performance with and without NLC is shown in Fig. 1.19. A reduction in a_{NLI} is translated into an improvement on the maximum SNR by:

$$\Delta SNR_{NLT} [dB] = \frac{1}{3} \Delta a_{NLI} [dB] \quad (1.99)$$

Meaning that a 3 dB improvement in a_{NLI} will only be translated into 1 dB improvement in system SNR. As mentioned in Sec. 1.4.3, the total nonlinear variance a_{NLI} is composed of two terms, accounting for intra-channel ($a_{NLI-intra}$) and inter-channel ($a_{NLI-inter}$) nonlinear distortions. A reduction in a_{NLI} will therefore depend on the number of considered WDM channels for NLC, which will depend on the electronic processing bandwidth of the TX or RX, and the corresponding complexity on DSP.

Usually, the bandwidth of the state-of-the-art RX technology takes a lead on the TX technology, such that more than one WDM channel can be detected by a single wideband receiver. Therefore, multi-channel NLC could be in principle accomplished either by DBP or

PNLC. In practice, multichannel NLC is challenging and limited success has been demonstrated experimentally.

The computational complexity of multi-channel NLC is too high compared to single channel NLC techniques. In the case of DBP, increasing the back-propagated bandwidth requires an increase on the number of DPB steps applied to maintain the same accuracy [101]. In the case of PNLC, besides the intra-channel $C_{m,n}$ matrix, one inter-channel $K_{m,n}$ matrix must be computed for each compensated channel. Multichannel PNLC has been recently experimentally demonstrated [102].

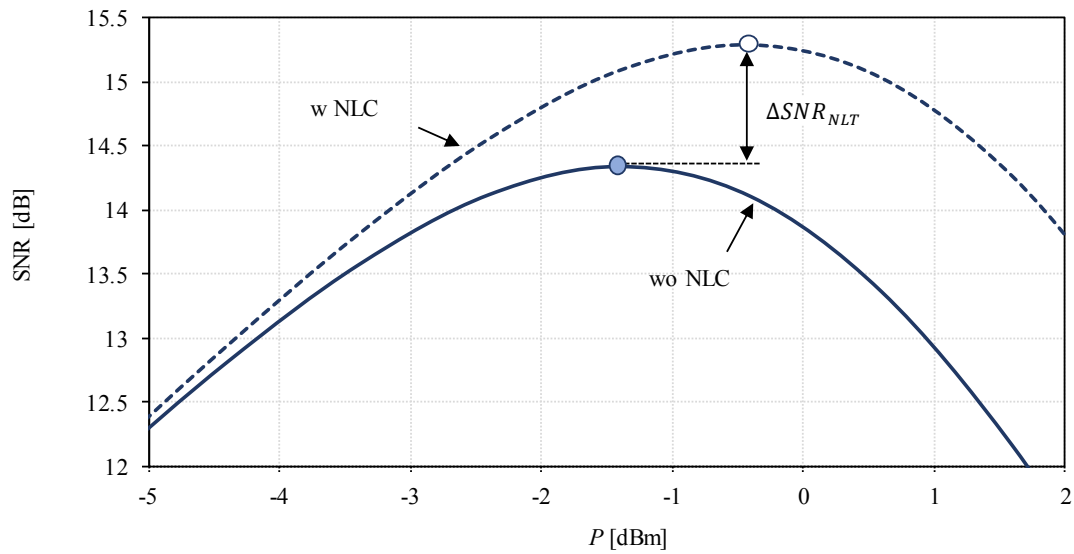


Fig. 1.19: SNR versus average channel launched power for an arbitrary system.

In this work we mainly focus on single channel NLC². Therefore, considering only intra-channel NLC, the maximum achievable gain is given by:

$$\Delta SNR_{NLT} [dB] < 10 \log_{10} \left(\frac{(a_{NLI-Intra} + a_{NLI-Inter})^{1/3} + \xi}{a_{NLI-Inter}^{1/3} + \xi} \right) \quad (1.100)$$

where ξ is defined by:

$$\xi = \frac{\kappa_{trx}}{(\eta \sigma_{ASE}^2)^{2/3} \left(\frac{27}{4}\right)^{1/3}} \quad (1.101)$$

² An experimental demonstration using multi-channel NLC based on DBP is presented in Sec. 4.2

1.5 SUMMARY

This chapter dealt with the main aspects of a digital communication system, and optical long-haul coherent systems based on wavelength division multiplexing. We first described the main building blocks and key aspects of digital transmission, such as: achievable rates in BICM systems, forward error correction codes, higher order modulation formats including novel probabilistic constellation shaping, and pulse-shaping.

We then described the different blocks of an optical long-haul coherent system. We reviewed the architecture of an optical transmitter capable of generating arbitrary modulation formats for data transmission. We reviewed the key physical phenomena impairing an optical signal during propagation as: amplifier noise, chromatic dispersion, fiber nonlinearities, polarization mode dispersion, and polarization dependent loss. We also presented the architecture of a coherent receiver able to map the optical field into the electrical domain, followed by all the digital signal processing blocks for mitigation of linear and nonlinear impairments.

Moreover, we described the metrics for performance evaluation as the generalized mutual information, and the signal to noise ratio. We addressed the system performance in terms of SNR including all sources of noise as: optical amplifier noise, back-to-back noise, and nonlinear noise. Finally, we presented analytical models based on perturbation theory to evaluate the maximum nonlinear gain provided by nonlinear compensation algorithms.

All these concepts will be used in the following chapters. Chapter 2 will be on the performance evaluation of the nonlinear digital signal processing algorithms based on digital-back propagation and perturbative nonlinear compensation. Chapter 3 will deal with the design and performance evaluation of probabilistic constellation shaping versus regular modulation formats. Finally, Chapter 4 will present some transmission here experiments using the techniques described before.

2 LOW-COMPLEXITY DIGITAL NONLINEAR COMPENSATION

In this chapter, we evaluate the performance and gain benefits of low-complexity nonlinear compensation algorithms, i.e., filtered digital-backpropagation (FDBP) and perturbative nonlinear compensation (PNLC). In the first part, we derive by means of numerical simulations semi-analytical formulae to calculate the parameters involved within the FDBP algorithm avoiding complex exhaustive optimization. In the second part, we investigate the impact of PMD and PDL on the performance of FDBP and PNLC to assess their robustness to these effects when used to compensate single channel nonlinear distortions. Finally, we show the practical achievable gains of FDBP and PNLC for different algorithm complexities for transoceanic distances.

2.1 FILTERED DIGITAL BACKPROPAGATION OPTIMIZATION

As stated in Sec. 1.3.5.1, DBP relies on solving the inverse NLSE or Manakov equation using the well-known SSFM. In a real fiber, interaction between dispersion and nonlinearities takes place during propagation. However, within the frame of the SSFM, the dispersive and nonlinear effects alternate over a small propagation step h . This approximation leads to an error term dependent on the size of h [103]. For the SSFM to approach the exact solution of the NLSE or Manakov equations, the step size should tend to zero. A large step size leads to the creation of numerical artifacts reducing the accuracy of the numerical solution [104-106]. Different criteria to properly choose the value h for fiber transmission simulations can be found

in the literature [103].

While choosing small step values leads to a higher accuracy, it also leads to high computational requirements, as the number of computations grows proportional to the number of steps applied. For practical NLC, choosing small step sizes is unattractive as it makes high-resolution DBP too complex for commercial implementation. In general, increasing h will lead to an overestimation of nonlinear distortions, as the nonlinearity of each step is lumped at a single point and the phase mismatch between different frequency components induced by CD is ignored within each step. Overestimation of fiber nonlinearities will then lead to the creation of spurious frequency components [38,106]. The constant of proportionality, κ , (also referred as nonlinear scaling factor) present in (1.74) and (1.75), has been introduced to overcome this overestimation when large values of h are used. Typically, it has to be optimized depending on system parameters and DBP step sizes [36,39,107].

In [38], a modification of the standard DBP was proposed, where the intensity waveform within the nonlinear step was low-pass filtered to reduce overestimation arising from high frequency components. As mentioned in Sec. 1.3.5.1, this technique is referred as FDBP, and it allows reducing the number of SSFM steps per span, N_{steps} , without sacrificing performance. This approach requires first choosing the nonlinear phase correction low-pass filter (LPF) type, and then the joint optimization of κ , and the 3-dB LPF bandwidth B_{FDBP} . This joint optimization is a complex problem since, a priori, both B_{FDBP} and κ are functions of eight independent variables, i.e., N_{steps} , fiber dispersion coefficient D , Kerr nonlinear coefficient γ , attenuation coefficient α , channel launched power P_{ch} , symbol-rate R_s , span length L_{span} , and channel count S_{ch} . The joint optimization of B_{FDBP} and κ has to be in principle performed for every system configuration under study [38, 39].

In the following, we study the dependency of B_{FDBP} and κ on all the above-mentioned variables by means of numerical simulations, and we provide semi-analytical formulae to estimate them in the case of DU systems.

2.1.1 FDBP Parameter Optimization

Fig. 2.1a shows the position of the FDBP block in the DSP chain. As fiber CD is also compensated within FDBP, it replaces the CD compensation block. Fig. 2.1b shows the schematic representation of FDBP based on (1.78) and (1.79).

It consists of a first linear sub-step compensating for CD, followed by a nonlinear sub-step compensating for fiber nonlinearities. For a given link composed of N_{spans} , this process is repeated a total of M_{tot} times depending on the applied FDBP N_{steps} as $M_{total} = N_{spans} \cdot N_{steps}$. To reduce complexity, we are interested in $N_{steps} \leq 1$.

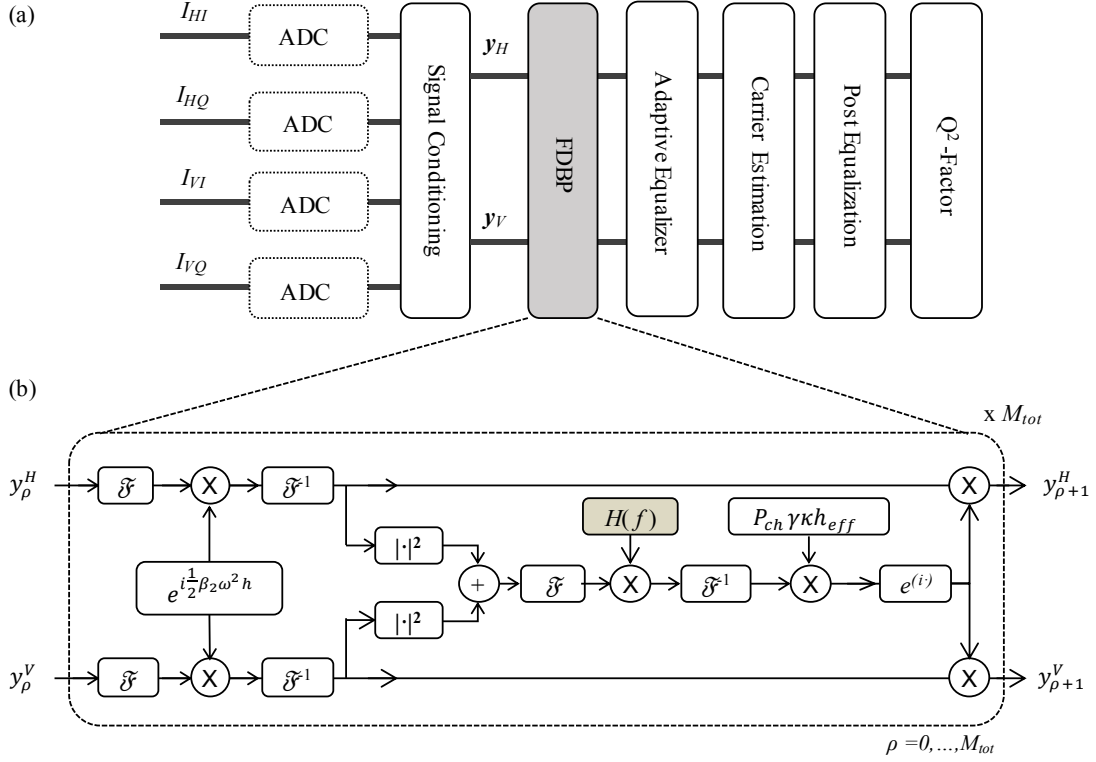


Fig. 2.1: (a) FDBP position in DSP chain, and (b) FDBP block-diagram.

$H(f)$ corresponds to the frequency response of the LPF involved in the nonlinear sub-step. In [108], several filters types were investigated leading to similar performances, although the performance of a Gaussian LPF was marginally better, which was then used in [39] and [109]. Therefore, in the following we assume a super-Gaussian (SG) LPF with transfer function:

$$H(f) = \exp \left[-\ln(2) \left| \frac{f}{B_{FDBP}} \right|^{2n} \right] \quad (2.1)$$

where n is the SG order. The filter is normalized such that: $\int |H(f)|^2 df = 1/dt$ and $H(B_{FDBP}) = 0.5 \cdot H(0)$, where $dt = 1/(sps \cdot R_s)$. Moreover, we assume that the signal processed by FDBP algorithm has been sampled at 2 sps.

For numerical simulations, de-correlated binary de Bruijn sequences of length 2^{13} are used to generate 49 GBd PM-16QAM symbols. The signal is then digitally shaped using a frequency-domain RRC filter with roll-off factor 0.01. We do both single-channel and WDM 7-channel simulations. Laser linewidths are set to zero. In order to correctly account for nonlinear distortions, the total simulated bandwidth is three times the WDM signal bandwidth.

The transmission line consists of 30 spans of 100 km standard single mode fiber (SSMF) with $D = 16.54$ [ps/nm/km], $\gamma = 1.3$ [1/W/km] and $\alpha = 0.2$ [dB/km]. Span loss is perfectly compensated at the span end by a noiseless EDFA, while the total noise is loaded at the receiver side. Fiber propagation is simulated by SSFM, where the step size is updated using

the nonlinear phase-rotation method to keep the nonlinear phase within each step below 1 mrad. No change in results were observed for lower values.

At the receiver side, the COI corresponding to the center channel is matched filtered and sampled at 2 sps. These samples are then processed either by CD compensation block or by FDBP block. Finally, carrier phase estimation is performed using BPS algorithm. We do not consider any polarization effect as PMD or PDL. Therefore, adaptive equalization is not performed

In this section, we measure the system performance in terms of Q^2 -factor. The FDBP gain is then defined as the difference between the Q^2 -factor when using FDBP and when using CD compensation at a given power. Q^2 -factor is calculated from BER using Monte Carlo where 40 different random noise seeds were applied for noise loading to count at least 2000 errors for each simulated point. Under this configuration, the uncertainty of the estimated Q^2 -factor is found to be ± 0.06 dB assuming a confidence interval of 99%.

In a first instance, we show the joint optimization of B_{FDBP} and κ . To do so, we perform single channel simulations and we set the channel optical power to $P_{ch} = 2$ dBm, which corresponds to the NLT when no NLC is applied. For FDBP, we set $N_{stps} = 0.5$, which corresponds to performing one FDBP step every 2 spans, while the SG LPF order is set to $n = 0.5$. The FDBP parameters κ and B_{FDBP} are independently swept in steps of 0.025 and 0.2 GHz respectively. The uncertainty on Q^2 -factor translates to equivalent uncertainties in κ and B_{FDBP} of ± 0.025 and ± 0.6 GHz respectively. Fig. 2.2a illustrates the contour plot of FDBP-compensated Q^2 -factor showing that κ and B_{FDBP} should be jointly optimized to achieve the maximum FDBP gain. This joint optimization will be performed in the following for each system parameter under study.

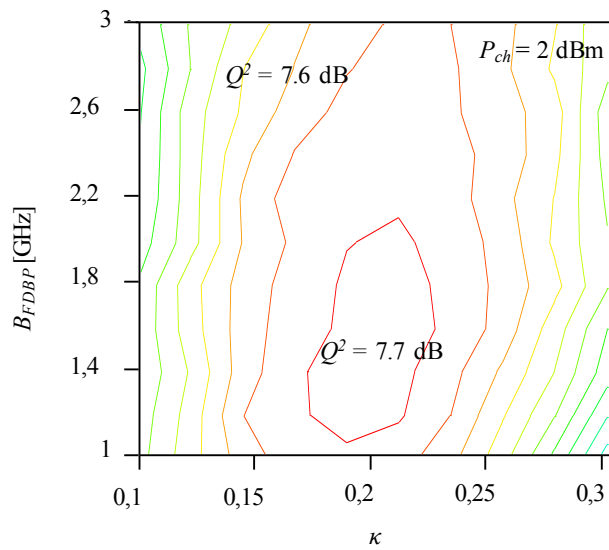


Fig. 2.2: Joint optimization of κ and B_{FDBP} for single channel transmission considering FDBP with $N_{stps} = 0.5$ and SG LPF order $n = 0.5$.

Following the above joint optimization procedure, we now study the dependency of the FDBP gain on the SG LPF order. For the same system configuration, we sweep n according to $n = \{0.125, 0.25, 0.5, 1, 2, 3\}$. The corresponding FDBP gains are shown in Fig. 2.3a using the optimal values of κ and B_{FDBP} for each case. It is observed that the FDBP gain dependence on n is weak but an optimum point is found when $n = 0.5$. This agrees with [108], where the FDBP gain depended slightly for different LPF functions. From now on we fix $n = 0.5$.

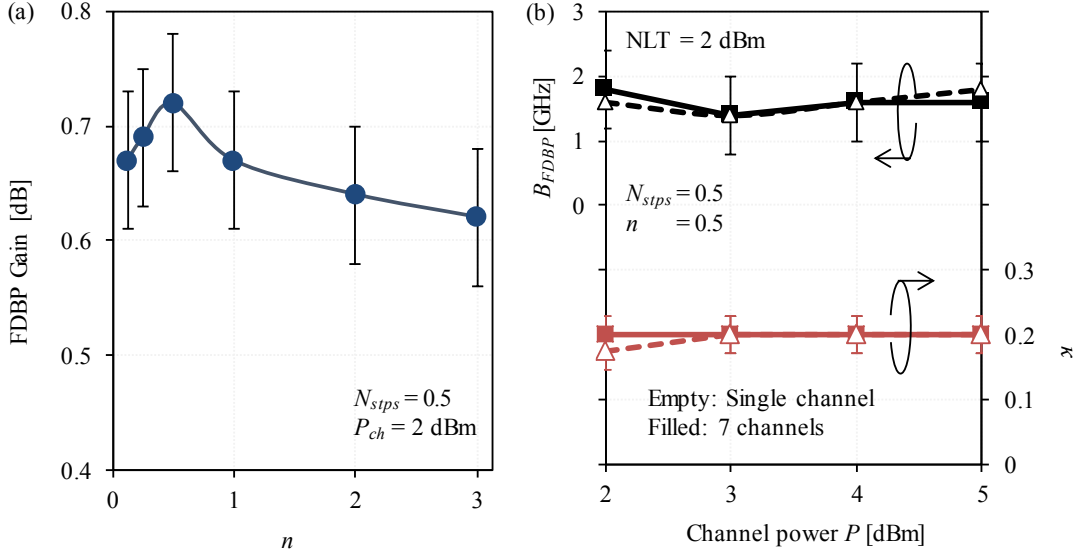


Fig. 2.3: (a) FDBP gain vs SG LPF order, and (b) optimum values of κ and B_{FDBP} for different optical powers considering single and 7 channels propagation.

We now investigate the dependency of κ and B_{FDBP} with channel optical power and number of WDM channels. We consider channel optical powers ranging from 2 dBm to 5 dBm, which corresponds to NLT to NLT+3dBm, and we consider 1-channel or 7-channels spaced at 50 GHz. At the transmitter side, each channel is decorrelated by applying random time delays and random polarization rotations with respect to the COI. The results are presented in Fig. 2.3b. It is observed that neither channel count nor launched power have an impact on optimizing κ and B_{FDBP} .

In previous works, [38, 39, 109], it has been shown that κ and B_{FDBP} depend strongly on the value of N_{stps} . Changing N_{stps} translates into changing the accumulated dispersion per step ($\beta_2 h$) and the nonlinear phase rotation ($\gamma h_{eff} P_{ch}$), implying that the dependency of κ and B_{FDBP} on system parameters might be uniquely through these products. To test this hypothesis, we do exhaustive joint optimization considering two cases:

- 1) we perform 30x100 km SSMF simulation and optimize κ and B_{FDBP} for different values of N_{stps} , and

2) we fix $N_{steps} = 1$ and perform propagation simulations using hypothetical fiber parameters where β_2 and γ are modified such that the products $\beta_2 h$ and $\gamma h_{eff} P_{ch}$ coincide with those in the first case for various values N_{steps} .

We recall that the dispersion coefficient D is related to β_2 by (1.34). In the following we use D instead of β_2 as it has more practical meaning. The results of these two previous cases are presented in Fig. 2.4, confirming that the optimum values of κ and B_{FDBP} are equal for both cases. This allows us to fix N_{steps} and modify the fiber coefficients (D, α, γ) to study their individual impact on κ and B_{FDBP} .

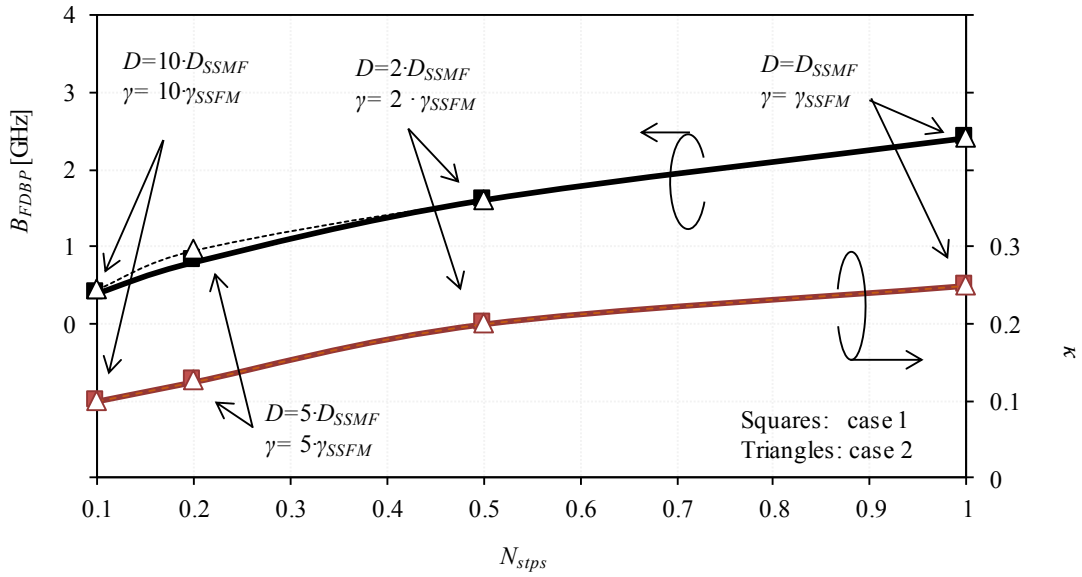


Fig. 2.4: Dependency of κ and B_{FDBP} with N_{steps} (squares) and $\beta_2 h, \gamma h_{eff} P$ products (triangles) fixing $N_{steps} = 1$, for 1 channel with $n = 0.5, P_{ch} = 2$ dBm.

We now investigate on the individual dependency of κ and B_{FDBP} on fiber parameters. To reduce computation time, we fix $N_{steps} = 0.5$, and sweep D, α and γ in the range: $D = \{2, 5, 7, 11, 15, 17, 20\}$ ps/nm/km, $\gamma = \{0.5, 0.8, 1.3, 1.5\}$ 1/W/km and $\alpha = \{0.16, 0.18, 0.20, 0.22\}$ dB/km, which are in the range of actual fiber parameters. For each of the resulting 112 combinations, κ and B_{FDBP} are jointly optimized by exhaustive search as previously presented, and their optimum values are obtained.

Fig. 2.5a shows the optimum values of B_{FDBP} versus α for the particular case of $\gamma = 1.3$ [1/W/km] for different values of D , while Fig. 2.5b shows B_{FDBP} versus γ for $\alpha = 0.2$ [dB/km] also for different values of D . It is observed that the optimum B_{FDBP} presents negligible dependency on γ and α , but strongly depend on the value of D . The same behavior was observed for all possible combinations of D, α and γ , as well as for the optimum κ . These results agree with Fig. 2.3b, where κ and B_{FDBP} did not present any variation when changing the channel power, implying that the product $\gamma h_{eff} P_{ch}$ does not play a role in the determination

of the FDBP parameters. Therefore, it is only the product $\beta_2 h$ which has to be taken into account.

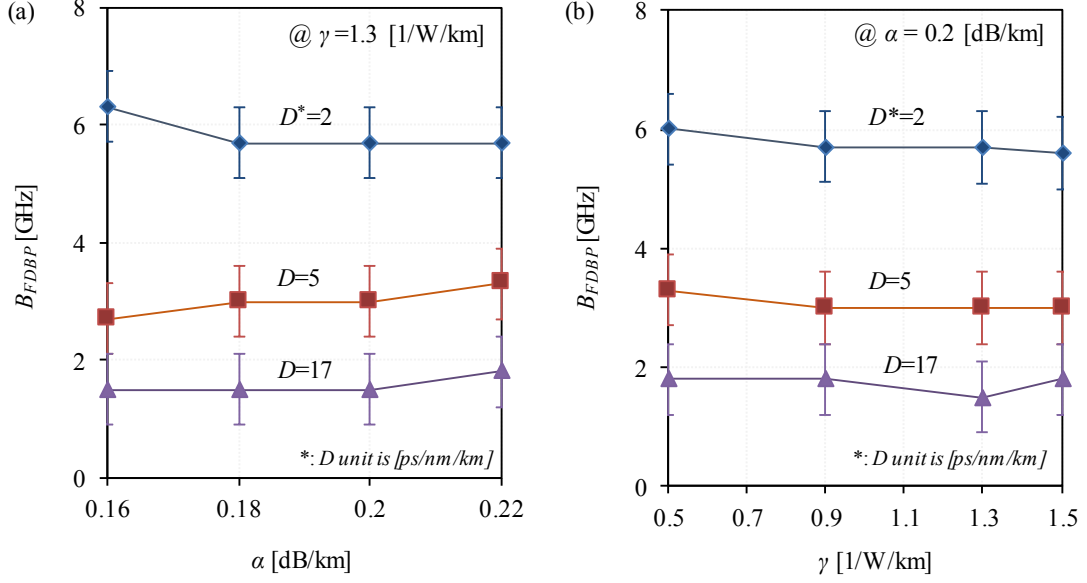


Fig. 2.5: (a) B_{FDBP} dependency on α and D for $\gamma = 1.3$ 1/W/km, and (b) B_{FDBP} dependency on γ and D for $\alpha = 0.2$ dB/km.

Considering the unique dependency of κ and B_{FDBP} on D , we fix $\gamma = 1.3$ 1/W/km and $\alpha = 0.22$ dB/km, and study their dependency with D for different symbol-rates. The results are presented in Fig. 2.6. Instead of showing the dependency of κ and B_{FDBP} with D , we use the dispersion-induced pulse broadening per FDBP step defined as:

$$\Delta T = \frac{2Dh\lambda_0 R_s}{c} \quad (2.2)$$

which takes into consideration D , h and the channel symbol-rate R_s . λ_0 is the COI central wavelength, and c is the speed of light. We consider symbol-rates of $R_s = \{24, 32, 43, 49\}$ GBd and PM-16QAM signals.

It is observed that the optimum values of κ and B_{FDBP} depend mainly on ΔT , for which the following expressions can be found by numerical fitting.

$$B_{FDBP} = \frac{1.48}{\Delta T} \quad (2.3)$$

$$\kappa = \sqrt{\frac{44.9 \times 10^{-12}}{\Delta T}} \quad (2.4)$$

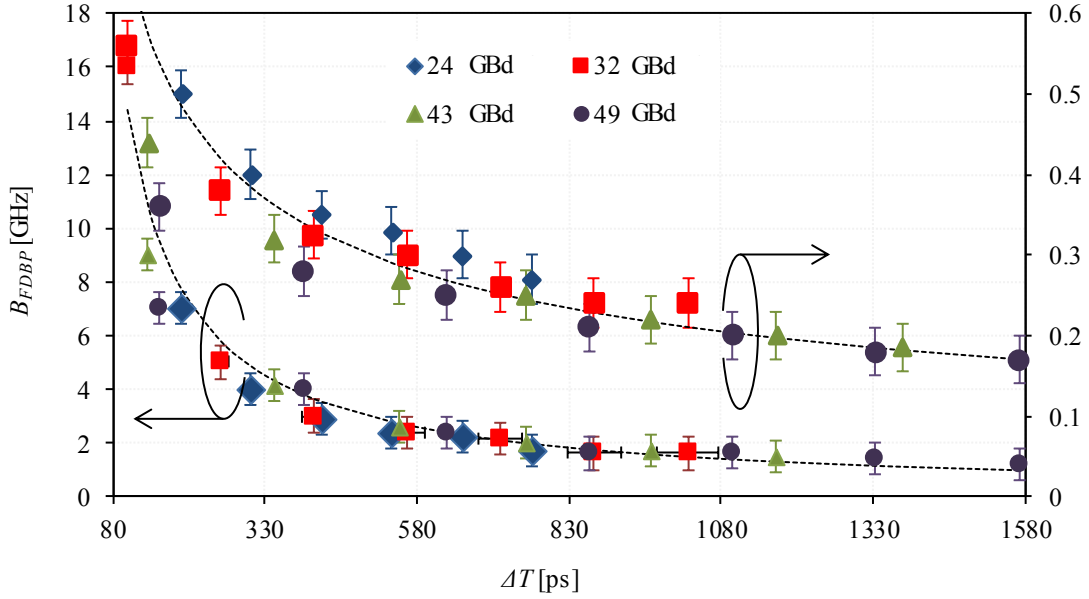


Fig. 2.6: κ and B_{FDBP} dependency on the pulse broadening per FDBP step at 24, 32, 43 and 49 GBd, and for $n = 0.5$.

These expressions are the main results of this section. The dimension of the numerator in (2.4) is [s], such that κ is dimensionless. Please note that these expressions are only valid when considering a SG LPF of order $n = 0.5$ normalized such that: $\int |H(f)|^2 df = 1/dt$ and $H(B_{FDBP}) = 0.5 \cdot H(0)$, and working at 2 sps. However, the above results show that simple expressions can be obtained for a given filter type depending mainly on the dispersion-induced pulse broadening per FDBP step.

2.1.2 Experimental Validation

In order to validate the above formulae, we perform experimental measurements using the test-bed shown in Fig. 2.7. The transmitter consists of 64 C-Band DFB lasers spaced at 50 GHz which are modulated with a PM IQ-mod driven by a 65 GS/s DAC. Each DAC generates two 24.5 GBd PM-16QAM subcarriers with RRC 0.01 for every laser source, leading to a total of 128 WDM channels with 25 GHz spacing. For measurement channels, four DFB lasers at mid C-band are replaced by 8 interleaved tunable-laser sources (TLS) spaced at 25 GHz. Odd and even TLS sources are modulated with separate PM IQ-MODs driven by DACs generating single-carrier 24.5 GBd PM-16QAM. The link consists of a recirculation loop of 12x50 km spans, each composed of 25 km of Corning Vascade EX3000 fiber ($D=20$ ps/nm/km, $\gamma=0.62$ 1/W/km and $\alpha=0.16$ dB/km) followed by 25 km of EX2000 fiber ($D =20$ ps/nm/km, $\gamma =0.84$ 1/W/km and $\alpha =0.16$ dB/km). Span loss is compensated by in-line EDFAs. One channel at $\lambda=1549.01$ nm is measured. A coherent receiver with a 33 GHz real-time scope working at 80 GS/s is used. Sampled waveforms are processed off-line by standard coherent receiver DSP blocks described in Sec. 1.3.4.

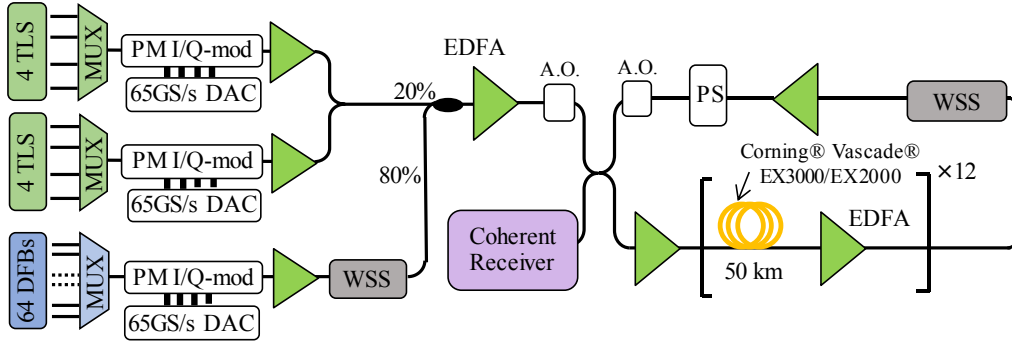


Fig. 2.7: Experimental set-up. DAC: digital-to-analog convertor, PM I/Q-mod: polarization multiplexing I/Q modulator, TLS: tunable laser source, DFB: distributed feedback laser, MUX: multiplexer, AO: acousto-optic switch, WSS: wavelength selective switch, PS: synchronous polarization scrambler.

FDBP is optionally applied to the received waveforms instead of CD compensation, where κ and B_{FDBP} are optimized by exhaustive search for $N_{steps} = 1, 0.5$ and 0.25 using $n = 0.5$ for the LPF SG order. Fig. 2.8 shows the optimum values of κ and B_{FDBP} found by exhaustive search in dashed, as well as the optimum values found by (2.3) and (2.4) in solid lines. The error bars associated with the experimental values correspond to the range where the FDBP gain variation is less than 0.05 dB. We conclude the proposed analytical formulas give an excellent estimation of κ and B_{FDBP} under the range of parameters studied in this work.

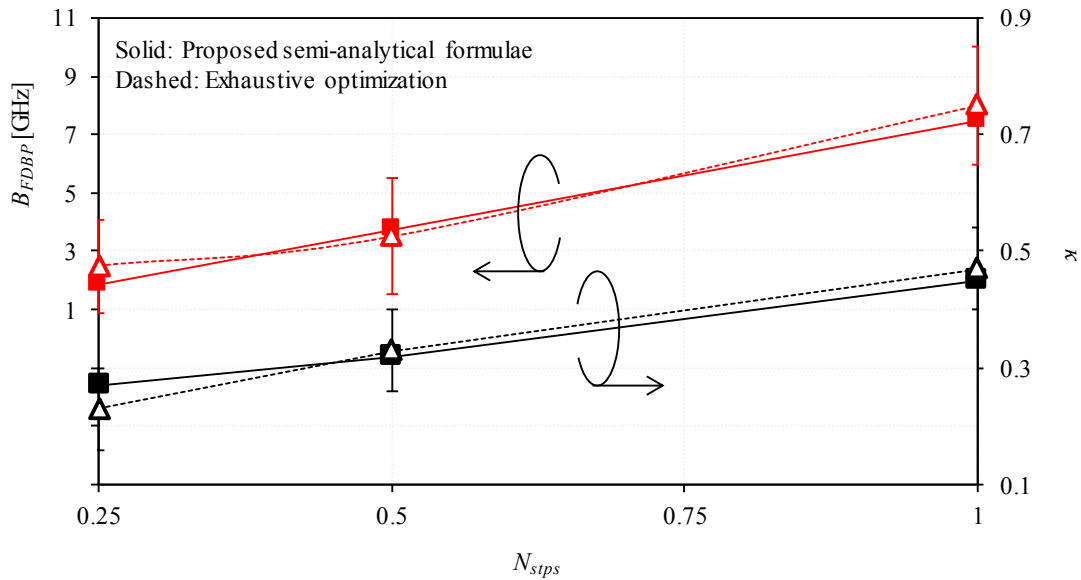


Fig. 2.8: Exhaustively optimized (dashed) and analytically optimized per (2.3) and (2.4) (solid) values of κ and B_{FDBP} as a function of N_{steps} .

Fig. 2.9 shows the Q^2 -factor vs. power curves after 4,800 km transmission both with and without FDBP compensation. In the case of FDBP compensation, three values of N_{steps} are examined: 0.25, 0.5 and 1, and κ and B_{FDBP} are found as per (2.3) and (2.4).

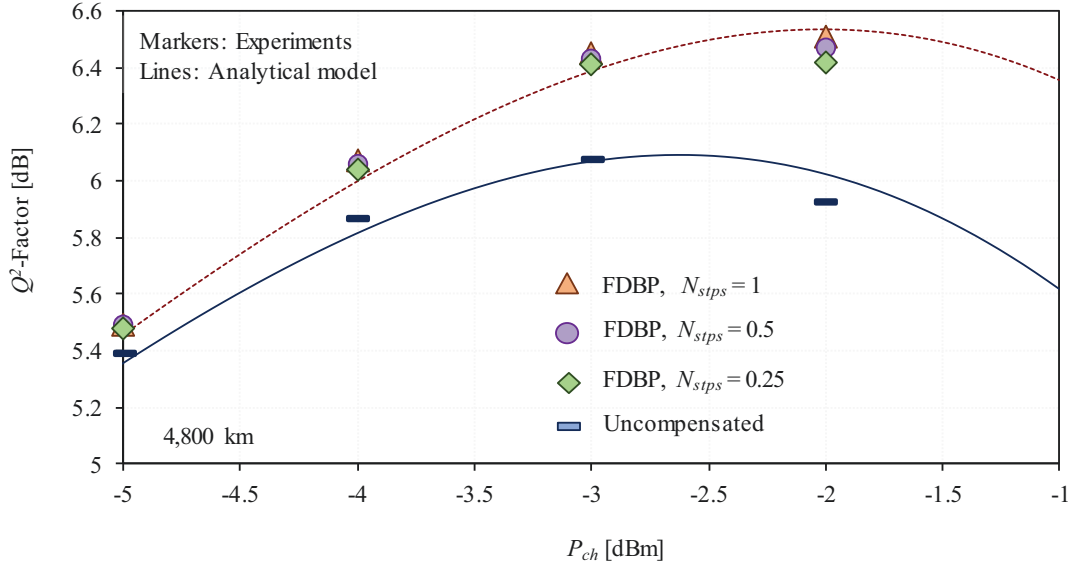


Fig. 2.9: Measured and theoretical predicted Q^2 -factor vs. channel optical power after 4,800 km transmission.

Measurements are reported by markers, while lines correspond to the analytical model described by (1.96). The nonlinear noise variance is calculated following (1.93) and (1.94) derived in [61], while the B2B coefficients (κ_{trx} and η) are obtained by fitting B2B curves. The solid line corresponds to the analytical model performance prediction of the uncompensated system, whereas the dashed line curve is the prediction assuming that self-channel nonlinearity ($a_{NLI-Intra}$) is perfectly compensated (cf. Seq. 1.4.5). We observed a good match between FDBP gain and the theoretical expected gain when single channel nonlinearity is removed.

Following the above results, we can conclude that it is possible to derive simple analytical formulae describing the dependency of κ and B_{FDBP} with the pulse broadening per FDBP step, avoiding their complex exhaustive optimization.

We put emphasis that the above results have been obtained by numerical simulations and experiments, however, a more detailed theoretical study has to be performed to obtain the ideal LPF transfer function and to understand the relationship of κ and B_{FDBP} with system parameters.

From now on Eqs. (2.3) and (2.4) will be used all along this work when FDBP is used to compensate for nonlinear distortions, and in some cases their validity has been further verified by exhaustive optimization.

2.2 IMPACT OF STOCHASTIC POLARIZATION EFFECTS ON NLC ALGORITHMS

In the absence of any stochastic effect, the NLSE or the Manakov equation governing the propagation of light in the optical fiber are fully reversible by zero forcing equalization. In this case, applying full-field high-resolution DBP with a large number of N_{steps} will fully compensate fiber nonlinearities. However, in the presence of stochastic effects as NSNI, PMD, and/or PDL, the fiber channel is not fully reversible as the stochastic interplay between these effects and nonlinearity is not taken into account for NLC. The presence of these stochastic effects becomes a fundamental limitation to completely mitigate fiber nonlinear effects.

The impact of PMD in the case of ideal high-resolution DBP has been extensively analyzed in [101, 107, 110-112]. It was shown that the penalty on the DBP achievable gain grows as the backpropagated bandwidth is increased. This degradation is explained by the fact that frequency components located far from each other will suffer from a higher induced depolarization due to PMD, leading to a higher mismatch between the true nonlinear interactions and the ones considered within the DBP algorithm. To this extent, different modified DBP algorithms trying to take into account PMD have been recently proposed [113-115]. The impact of PDL on NLC has never been addressed to the best of our knowledge.

From a practical point of view, performing high-resolution and multi-channel DBP is still extremely challenging and not yet viable for commercial implementation. If NLC techniques are to be adopted in the near future, they will be limited to single channel compensation and low complexity architectures (as PNLC with reduced LUT sizes or FDBP with low N_{steps}). In this case, the impact of PMD/PDL on NLC will be greatly reduced. First, because the backpropagated bandwidth is decreased, and second, because the penalty brought by the low complexity NLC implementation will dominate the achievable performance.

With this practical implementation of NLC in mind, we investigate the impact brought by PMD and PDL on the performance of FDBP and PNLC in the special case of transoceanic DU systems. We focus on PM-16QAM WDM channels modulated at 32 GBd and 50 GHz spacing corresponding to a practical study case.

2.2.1 Experimental Results

We start by performing transmission experiments for which the experimental set-up is depicted in Fig. 2.10. On the transmitter side, a WDM loading comb of 63 C-band DFB lasers is modulated with a PM IQ-MOD driven by an 88 GSamples/s DAC. The modulated DFB lasers are then passed through a WSS who cuts a spectral band of 50 GHz exactly at the middle of the DFB comb (1545.72 nm). A single TLS used as measurement channel at 1545.72 nm is modulated by a second PM IQ-MOD and coupled to the rest of the WDM channels. All channels

are synthesized by decorrelated binary De Bruijn sequences of length 2^{15} with RRC pulse shaping and 0.01 with roll-off. An optical fiber piece with 80 ps of chromatic dispersion is added after the loading channels for further decorrelation of about 3 symbols between adjacent channels.

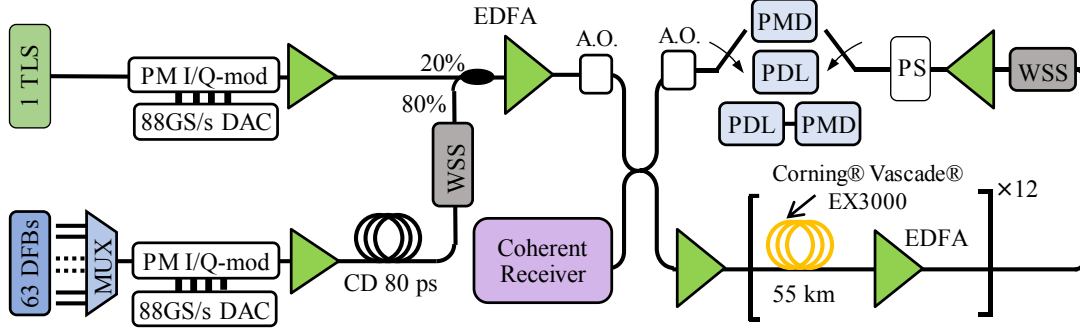


Fig. 2.10 : Experimental set-up. DAC: digital-to-analog convertor, PM I/Q-mod: polarization multiplexing I/Q modulator, TLS: tunable laser source, DFB: distributed feedback laser, MUX: multiplexer, AO: acousto-optic switch, WSS: wavelength selective switch, PS: synchronous polarization scrambler.

The recirculating loop consists of 12 spans of 55 km Corning® Vascade® EX3000 fiber ($D=20$ ps/nm/km, $\gamma=0.62$ 1/W/km and $\alpha=0.16$ dB/km), with EDFAs exactly compensating for span loss, leading to a total transmission distance of 6,600 km. At the receiver side, the COI is filtered and detected by a standard coherent receiver with a 33 GHz real-time scope working at 80 GS/s. Sampled waveforms are processed off-line by standard coherent receiver DSP blocks described in Sec. 1.3.4. NLC is optionally applied to the received waveforms either by FDBP or PNLC.

In general, PMD is an effect that is distributed along the optical fiber. While legacy deployed fibers can have large amounts of PMD, modern fibers used for long haul applications have a very small PMD coefficient typically below 0.05 ps/ $\sqrt{\text{km}}$. This is the case of our Corning Vascade EX3000 fiber used in our laboratory, such that an external PMD element must be introduced in the link to emulate PMD effects. In [116], it was shown that the correct emulation of PMD depends on the characteristics of the PMD emulator, and on its position in the experimental setup to correctly account for PMD-nonlinear interactions. For DU systems, it was shown that placing a polarization maintaining fiber (PMF) section at the transmitter side was enough to correctly emulate the effects of PMD; while for DM systems, at least one PMF section was required at each recirculating-loop round trip. In this sense, in order to emulate PMD in our experimental set-up, a PMF fiber of $\tau_{e\text{DGD}} = 20$ ps was inserted at the end of each loop and should be enough to correctly account for PMD-nonlinear interactions.

Contrary to PMD, PDL is a lumped effect introduced by optical elements. The major contribution is done by optical WSS used for channel equalization and add/drop capabilities, and which are typically placed after sever fiber spans. Therefore, PDL emulation is performed

by inserting a PDL element of $\Gamma_{e\text{ dB}}=1.6$ dB at the end of each loop. In order to randomize the states of polarization at each round-trip, a low speed polarization scrambler is placed just before the PDL/PMD elements. Therefore, the relative orientation of the channels and the PDL/PMD elements polarization axes are changed at each round-trip. After 10 loops (6,600 km) the setup behaves as a ten-section ($N_{sec} = 10$) all-order PDL/PMD emulator, for which the expected PDL/PMD values can be obtained by [80, 117]:

$$\mathbb{E}[\Gamma_{dB}] = \sqrt{\frac{8 \cdot N_{sec}}{3\pi}} \Gamma_{i\text{ dB}} \quad (2.5)$$

$$\mathbb{E}[\tau_{DGD}] = \sqrt{\frac{8 \cdot N_{sec}}{3\pi}} \tau_{i\text{ DGD}} \quad (2.6)$$

such that $\mathbb{E}[\Gamma_{dB}] = 4.6$ dB, and $\mathbb{E}[\tau_{DGD}] = 58$ ps.

We first address the system performance when no additional PMD or PDL are added to the link. Fig. 2.11 shows the Q^2 -factor vs. launched power after propagation. Mitigation of single channel nonlinearities is performed either by PNLC or FDBP. In the case of FDBP, we apply $N_{steps}=10, 1$ and 0.25 with optimized coefficients as shown in Sec. 2.1. For PNLC, a 300×300 look-up-table is used as no further gain was found for larger sizes, while the PNLC parameter κ in (1.80) and (1.81) has been optimized by an exhaustive search to achieve maximum gain. We include the theoretical performance using (1.96), where the nonlinear noise variance is calculated following (1.93) and (1.94) derived in [61], and the B2B coefficients (κ_{trx} and η) are obtained by fitting B2B curves.

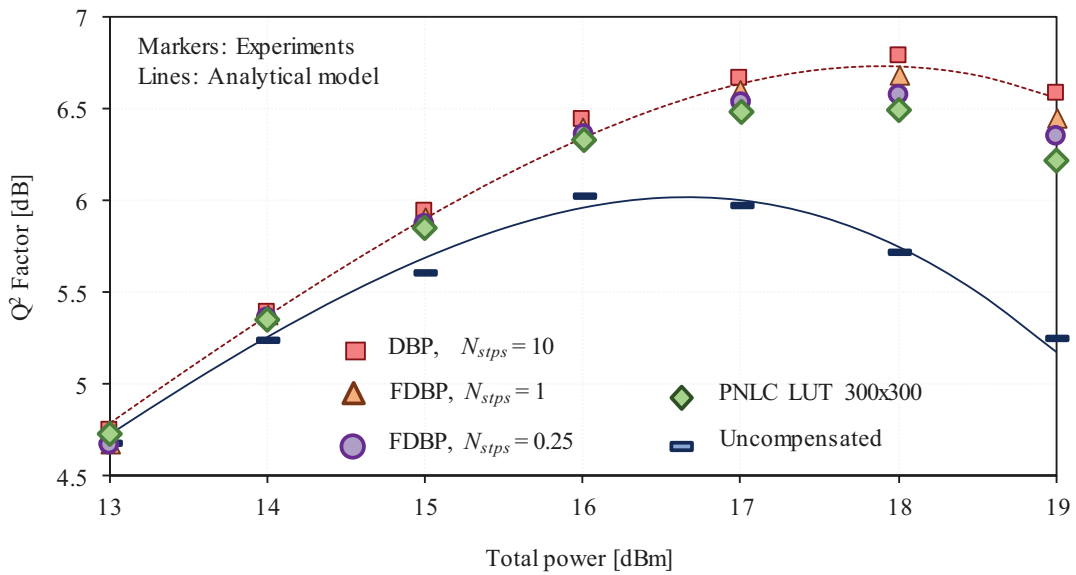


Fig. 2.11: Q^2 -Factor versus launched power after 6,600 km.

High-resolution DBP with $N_{steps} = 10$ achieves a maximum gain of 0.8 dB in optimum Q^2 -factor, which is in line with the value predicted by the theoretical model. On the other hand, FDBP with $N_{steps} = 1$, $N_{steps} = 0.25$ and PNLC provide a gain in optimum Q^2 -factor of 0.7 dB, 0.55 dB and 0.45 dB respectively.

In order to study the impact of PDL and PMD on NLC gain, we fix the optical power to 18 dBm which corresponds to the optimum Q^2 -factor when NLC is applied. Moreover, we focus only on FDBP with $N_{steps} = 1$, $N_{steps} = 0.25$, and PNLC, as we are only interested in low complexity NLC architectures. At 18 dBm, FDBP $N_{steps} = 1$, $N_{steps} = 0.25$, and PNLC provide 1 dB, 0.8 dB and 0.7 dB of gain respectively.

The characterization of the nonlinear gain provided by FDBP and PNLC is done under four different scenarios:

- 1) *No PDL - No PMD*,
- 2) *PMD only*,
- 3) *PDL only, and*
- 4) *PDL + PMD*.

For each case, we record 600 different waveforms and processed them offline. The PDL and PMD values can be estimated based on the adaptive equalizer butterfly filter coefficients \mathbf{h} [85, 118], whose transfer function is:

$$\mathbf{H}(f) = \begin{bmatrix} \mathfrak{F}\{\mathbf{h}^{HH}(t)\} & \mathfrak{F}\{\mathbf{h}^{VH}(t)\} \\ \mathfrak{F}\{\mathbf{h}^{HV}(t)\} & \mathfrak{F}\{\mathbf{h}^{VV}(t)\} \end{bmatrix} \quad (2.7)$$

Normalizing $\mathbf{H}(f)$ by the square root of its determinant gives:

$$\mathbf{U}(f) = \frac{\mathbf{H}(f)}{\det(\sqrt{\mathbf{H}(f)})} \quad (2.8)$$

where $\mathbf{U}(f)$ is a unitary matrix accounting for the inverse channel DGD, which can be obtained by [85]:

$$\hat{t}_{DGD} = 2 \sqrt{\det\left(\frac{1}{2\pi} \frac{d\mathbf{U}(f)}{df}\right)} \Bigg|_{f=0} \quad (2.9)$$

whereas PDL can be estimated as [118]:

$$\hat{I}_{dB} = \left| 10 \log_{10} \left(\frac{\lambda_1(f)}{\lambda_2(f)} \right) \right|_{f=0} \quad (2.10)$$

with λ_1 and λ_2 the eigenvalues of $\mathbf{H}^\dagger(f) \cdot \mathbf{H}(f)$.

Fig. 2.12a shows the probability distribution $\Pr(\hat{\tau}_{DGD})$ of the estimated DGD ($\hat{\tau}_{DGD}$) for the PMD-only and PDL+PMD cases obtained as per (2.9). As expected, they follow Maxwellian distributions with a mean value of 55 ps, in good agreement with the theoretical expected value of 58 ps. By using (2.10), Fig. 2.12b shows the probability distribution $\Pr(\hat{I}_{dB})$ of the estimated PDL (\hat{I}_{dB}) for the PDL-only and PDL+PMD cases. In the same manner, they follow Maxwellian distributions with a mean value of ~ 4 dB, in close agreement with the theoretical expected value of 4.6 dB. Please note that (2.10) tends to underestimate the true PDL value, as the equalizer response depends on the SNR [85].

From Fig. 2.12 it is observed that the maximum PDL value corresponds to ~ 9 dB, while the maximum DGD is ~ 160 ps, corresponding to ~ 5 times the symbol duration. Both values well in excess of the ones found in current commercial systems.

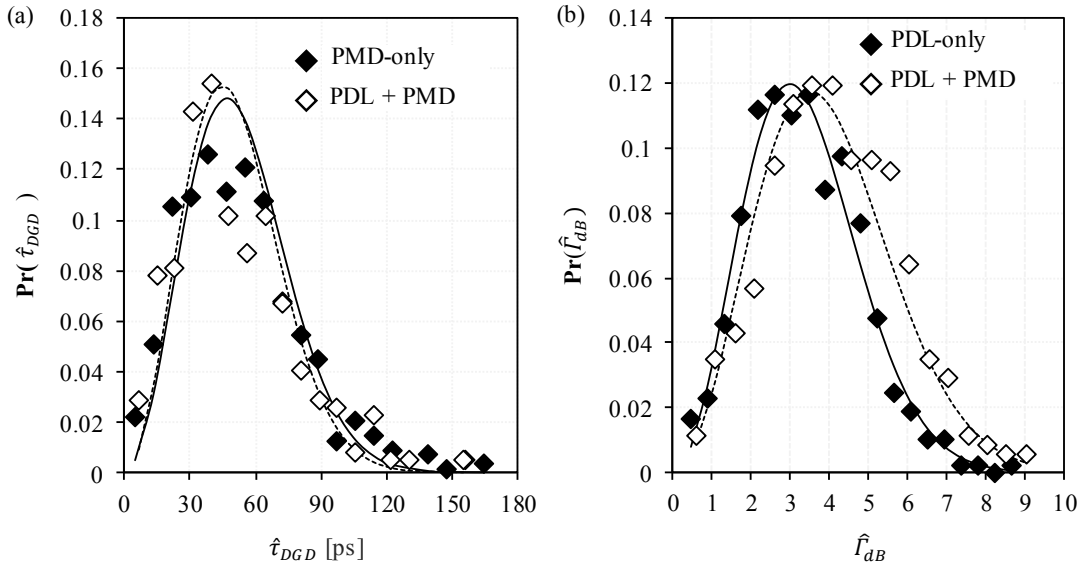


Fig. 2.12: (a) Probability distribution of the estimated PDL. (b) Probability distribution of the estimated DGD. Markers: experiments, lines: Maxwellian fit.

We now characterize the system performance without NLC. For each of the four cases, Fig. 2.13a shows the Q^2 -factor probability density $\Pr(Q^2)$, while Fig. 2.13b shows the probability of the Q^2 -factor loss (QL) defined as $QL = Q_{max}^2 - Q^2$ [dB]. We observe that system performance is unaffected in case of PMD-only, as observed in [119]. On the other hand, in the case of PDL-only the mean Q^2 -factor decreases by ~ 0.5 dB, while the maximum observable QL is increased by ~ 1.4 dB. Adding PMD to PDL helps to decrease QL by 0.3 dB compared to the PDL-only case, while the mean value is unchanged. Similar results were obtained by means of numerical simulations in [120].

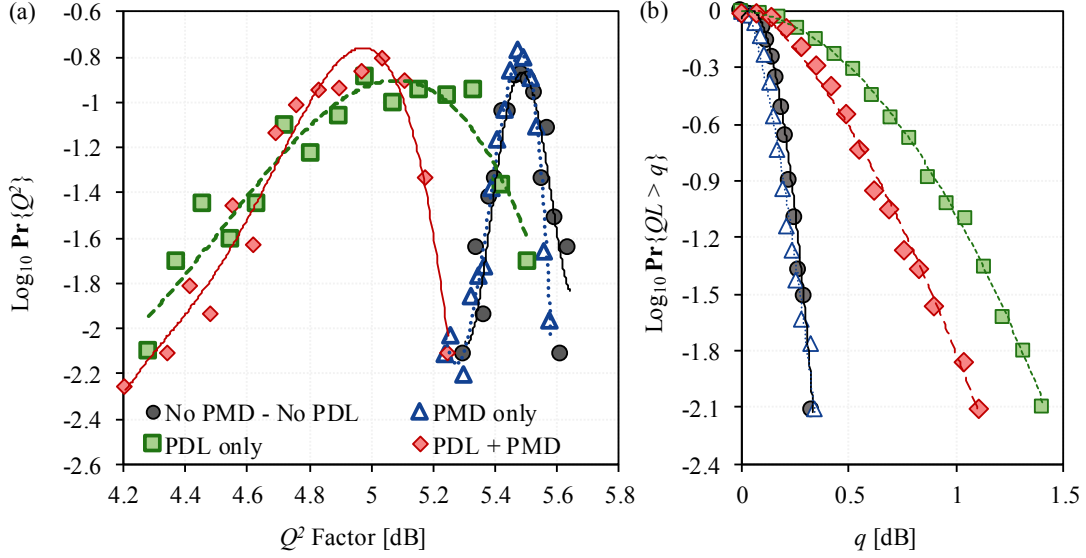


Fig. 2.13: (a) Uncompensated Q^2 -factor probability density and (b) Q^2 -factor loss (QL) probability for each study case.

The previous results are in agreement with other works studying the impact of PMD and PDL on the performance of coherent optical fiber systems. In the linear regime, the PMD-induced effects can be effectively compensated by digital adaptive equalization, such that even high values of PMD cause no system penalty as long as a sufficiently large impulse response of the butterfly filters is considered. Contrary to PMD, PDL is a non-unitary linear transformation and its effects cannot be compensated by DSP. PDL induces fluctuations on the system SNR by random polarization dependent OSNR degradation, an effect that cannot be compensated for by any means [121, 122].

In the nonlinear regime, PMD reduces intra-channel nonlinear distortions due to the induced depolarization and decorrelation between the signal tributaries, leading to an improvement in system performance. However, this improvement is almost negligible in DU systems, as decorrelation due to large values of CD dominates over PMD [119, 123, 124]. In the case of PDL, the loss of orthogonality induces instantaneous peak-to-peak optical power variations that will lead to an increase in nonlinear signal distortions. However, in DU systems, the large values of accumulated CD induces strong signal fluctuations that dominate over those induced by PDL [125-129].

We now investigate on the impact of PMD and PDL on NLC. We apply FDBP with $N_{stps} = 1$, $N_{stps} = 0.25$ and PNLC for each of the four different study cases. For the special case of *PMD-only*, Fig. 2.14 shows the uncompensated Q^2 -factor and the NLC gain (ΔQ_{NLC}^2) versus the estimated DGD. As observed previously, the uncompensated Q^2 -factor remains constant for all values of DGD. On the other hand, the gain provided by FDBP with $N_{stps} = 1$ and $N_{stps} = 0.25$ remains basically constant, while PNLC shows a higher degradation

A possible explanation of the higher sensitivity of PNLC to DGD compared to FDBP is the following. While FDBP and PNLC are based on different approaches to compensate for fiber nonlinear distortions, another characteristic which distinguishes them is their relative position within the DSP chain. While FDBP is placed at the very input, PNLC is placed after all other compensating blocks. A time delay between the two signal polarizations due to DGD will be compensated by the CMA, such that the relative position between the two polarizations after propagation is lost for PNLC. On the contrary, for FDBP the backpropagated signals are still impaired by DGD. Therefore, as DGD increases a higher impact on PNLC with respect to FDBP is expected. Even though, the decrease in PNLC achievable gain due to PMD is kept below 0.1 dB for values up to 150 ps of DGD.

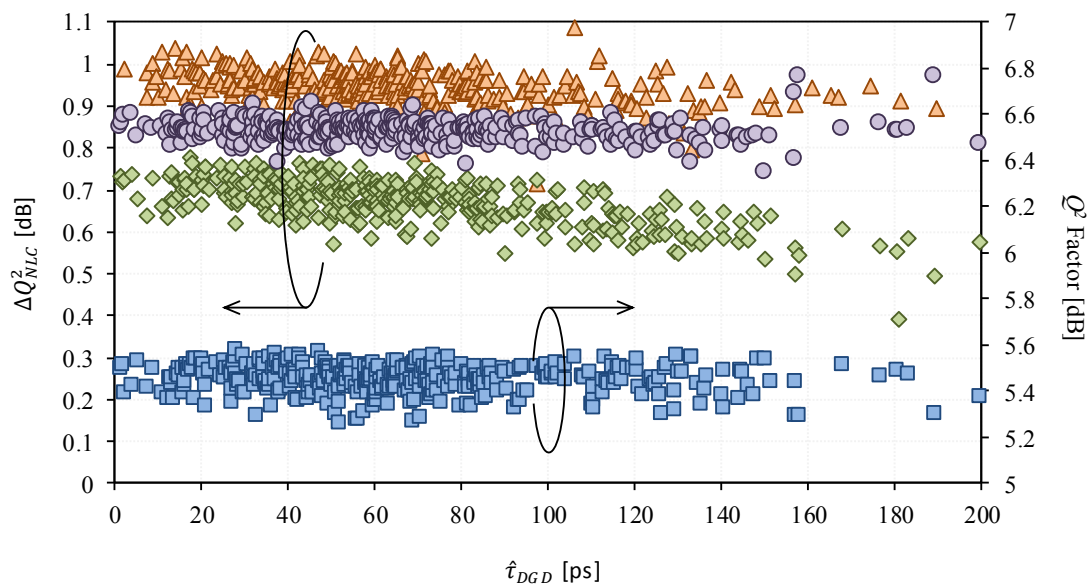


Fig. 2.14: Experimental Q^2 -factor and nonlinear compensation gain (ΔQ_{NLC}^2) vs estimated DGD.

Fig. 2.15 shows the probability density of ΔQ_{NLC}^2 , and the probability of the ΔQ_{NLC}^2 loss (ΔQL_{NLC}), defined as $\Delta QL_{NLC} = \Delta Q_{NLC}^2_{max} - \Delta Q_{NLC}^2$ [dB], that is, the ΔQL_{NLC} degradation with respect to the best observed NLC gain. Fig. 2.15a corresponds to the *No PDL-No PMD* case. The maximum observable ΔQL_{NLC} is kept below 0.15 dB for both PNLC and FDBP. When PMD is added to the link (Fig. 2.15b) the maximum ΔQL_{NLC} is basically unchanged for both cases of FDBP, while for PNLC is increased by 0.1 dB as stated previously.

Removing the PMD element and introducing PDL into the link (Fig. 2.15c) shows no further decrease on the mean ΔQ_{NLC}^2 for all algorithms types. However, ΔQL_{NLC} is greatly increased, being FDBP the most affected one with values $\sim 3x$ higher than when no PDL/PMD is perturbing the system. On the contrary, PNLC shows to be more robust with only $\sim 2x$ ΔQL_{NLC} increases

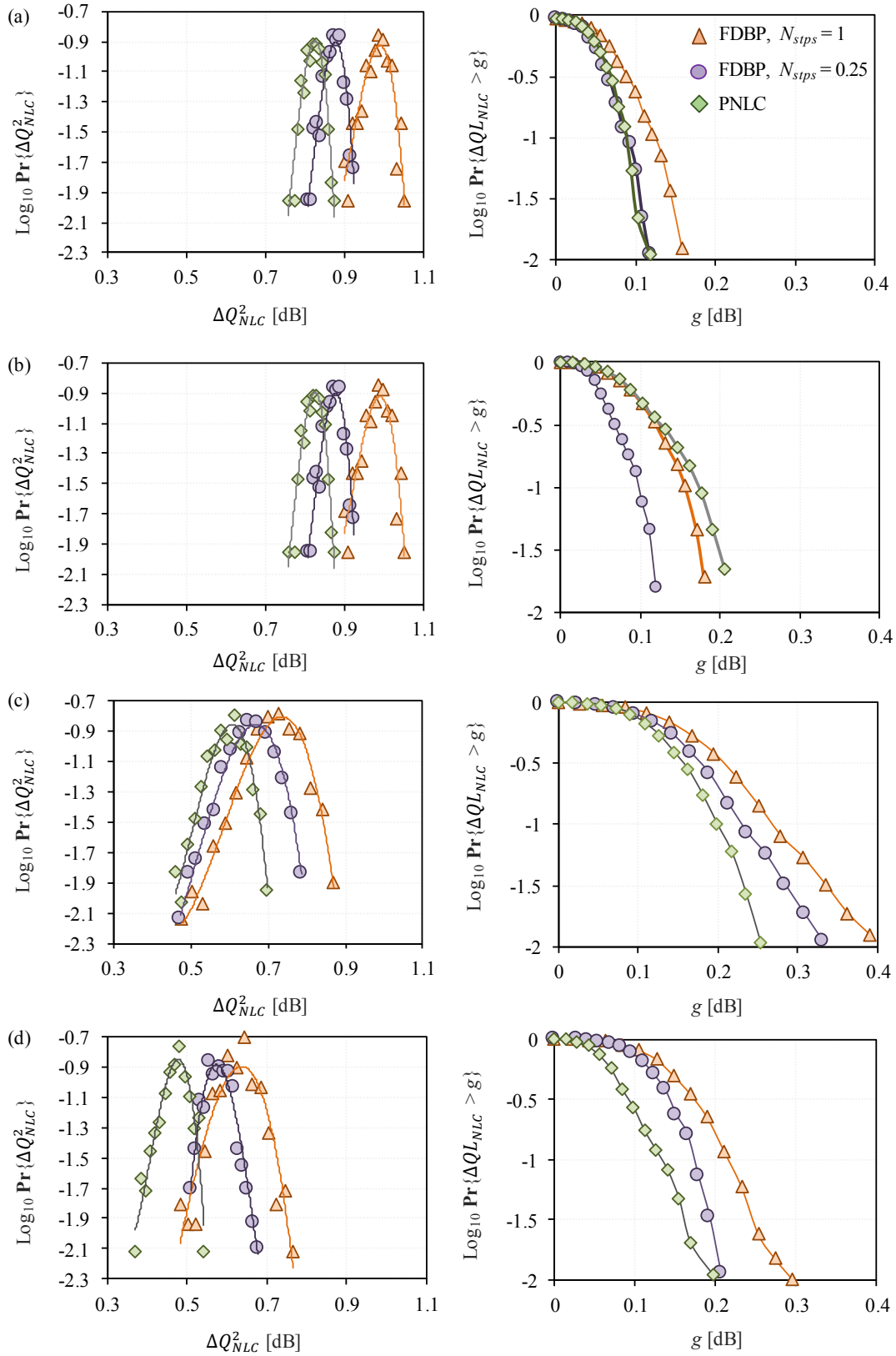


Fig. 2.15: Experimental nonlinear gain (ΔQ_{NLC}^2) probability distribution and nonlinear gain loss (ΔQ_{NLC}) for (a) No PDL nor PMD, (b) PMD-only, (c) PDL-only, and (d) PDL + PMD.

Finally, when both PDL and PMD are added into the link (Fig. 2.15d) the mean ΔQ_{NLC}^2 is further decreased by ~ 0.1 dB for all algorithms, while the maximum observable ΔQ_{NLC} is reduced by ~ 0.1 dB compared to the *PDL-only* case.

Results presented in Fig. 2.15 show that PNLC seems to be more sensitive to PMD than FDBP. On the contrary, PNLC is more robust than FDBP to PDL, as ΔQ_{NLC} is increased by ~ 0.15 dB in comparison to 0.25 dB for FDBP. Furthermore, in the presence of both PDL and PMD, while the overall ΔQ_{NLC} is reduced, PNLC is still more robust than FDBP.

The reason of the apparent higher robustness of PNLC to PDL compared to FDBP is still an open problem which must be further studied.

2.2.2 Simulation Results

In order to validate the results shown experimentally, we now evaluate the impact of PMD and PDL on FDBP and PNLC by means of numerical simulations.

At the transmitter side, de-correlated binary de Bruijn sequences of length 2^{13} are used to generate 49 GBd PM-16QAM symbols. We use RRC pulses with roll-off factor 0.01. Laser linewidths are set to zero. In order to reduce computation time, we consider only 3 WDM channels. The channel power is set to 0 dB corresponding to optimum power when NLC is applied. The transmission line is equal to the experimental one, where a PMD ($\tau_{e\ DGD} = 20$ ps) and/or PDL ($\Gamma_{e\ dB} = 1.6$ dB) element are placed after each 12 fiber spans (equivalent of 1 loop). The polarization of the signal at the input and output of both elements is randomly rotated following (1.57) and (1.60). The amplifier NF is set such that the uncompensated Q^2 -factor is ~ 5 dB to match the experimental performance working regime. Noise is loaded at the receiver side.

The DSP blocks consist on match filtering, CD compensation, polarization demultiplexing based on CMA using 35 taps, and carrier phase correction based on BPS. BER is computed from 20-seed ASE noise loading, and transformed into Q^2 -factor. FDBP and PNLC are optionally applied.

For each of the studied experimental cases (*PMD-only*, *PDL-only*, and *PMD+PDL*) we perform 600 different transmission simulations using NVIDIA Tesla K80 GPU cards, where the SSFM algorithm has been optimized for GPU compatibility. For each loading noise seed, we apply FDBP $N_{steps} = 1$, $N_{steps} = 0.25$, PNLC with a 300x300 LUT, and only CD compensation (uncompensated). Then the gain of FDBP and PNLC is calculated and averaged over all noise seeds. The process is repeated for all 600 transmitted waveforms and all studied cases.

Fig. 2.16 shows $\Pr\{\Delta Q_{NLC}^2\}$ and $\Pr\{\Delta Q_{NLC}\}$ for the above cases. Please note that the NLC achievable gains are higher due to the reduced number of transmitted channels, and so the fluctuations in the gain due to PMD and PDL.

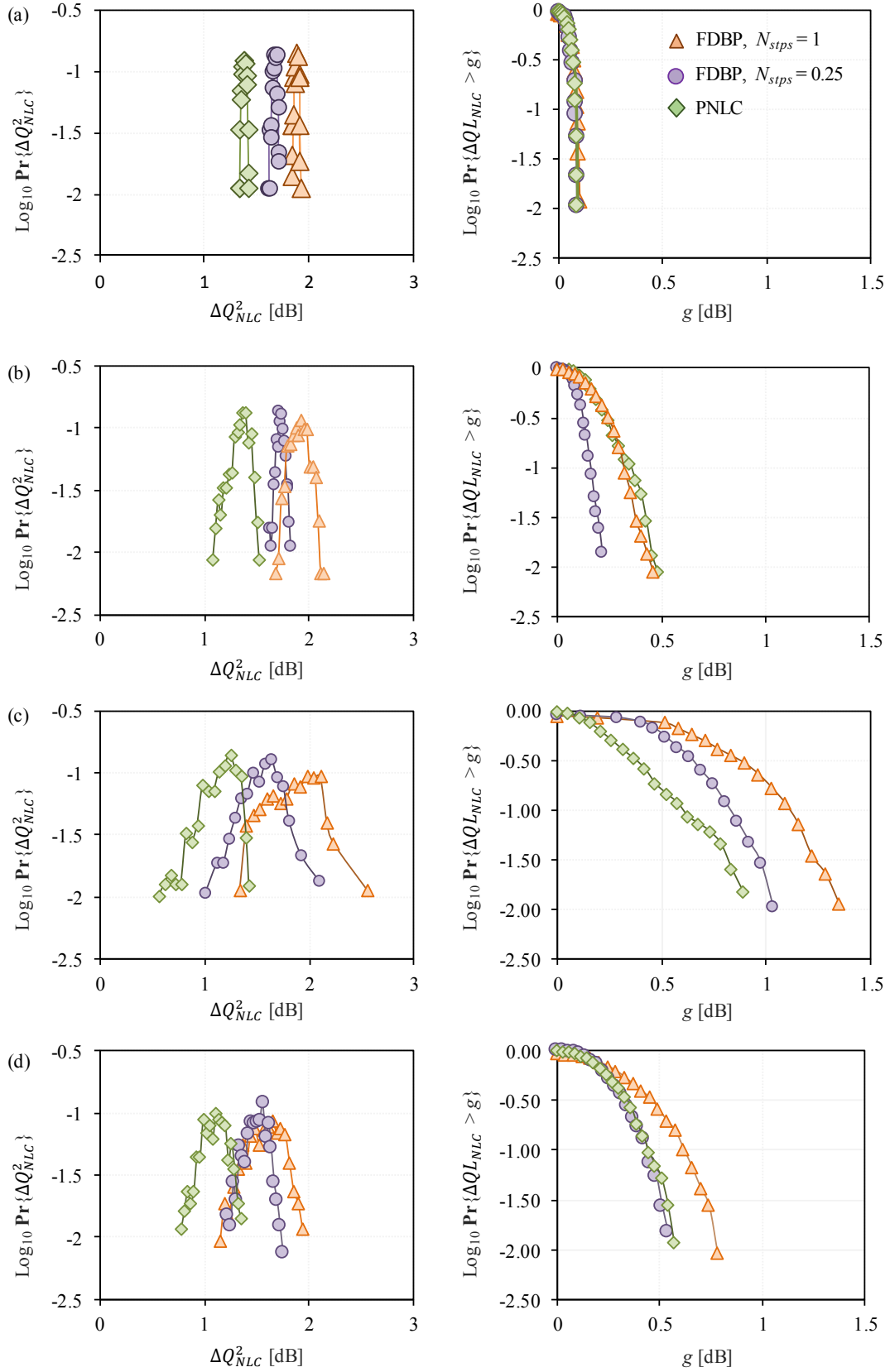


Fig. 2.16: Numerical nonlinear gain (ΔQ_{NLC}^2) probability distribution and nonlinear gain loss (ΔQ_{NLC}) for (a) No PDL nor PMD, (b) PMD-only, (c) PDL-only, and (d) PDL + PMD.

It is observed that when only PMD is applied both FDBP with $N_{steps} = 1$ and PNLC are equally impacted. When only PDL is added to the link, PNLC shows to be more robust compared to FDBP as found experimentally, while adding PMD+PDL reduces the gain fluctuations compared to the PDL-only case. The trends found numerically are closed in line to the experimental observations.

Considering the experimental results, both FDBP and PNLC show to be robust against PMD and PDL impairments for full C-band transoceanic systems when only intra-channel nonlinearities are compensated for.

2.3 PRACTICAL LIMITS OF NLC ALGORITHMS

The availability of analytical models predicting the performance of optical fiber transmission systems have also led to evaluate the ultimate upper bounds limits of NLC [65, 71, 76, 130, 131]. Theoretically speaking, these upper bounds are only attainable with ideal NLC which completely cancels out the NLI generated by all frequency components inside the considered compensated bandwidth.

From the practical point of view, NLC algorithms with low computational complexity as FDBP and PNLC are preferred due to their lower requirements on DSP. However, this reduction in algorithm complexity is accompanied by a decrease in their efficiency to cancel out NLI, and therefore to a decrease in achievable NLC gain.

In this section we investigate the practical limits of single-channel NLC based on FDBP and PNLC versus different algorithm complexities in fully-loaded C-band submarine systems³.

2.3.1 Simulation Set-up

We focus our study on DU systems with homogeneous spans employing lumped EDFA amplification. The link under study corresponds to a typical high-capacity submarine system composed of 55 km Corning Vascade EX3000 fiber spans ($D = 20.6$ ps/nm/km, $\gamma = 0.62$ 1/W/km, $\alpha = 0.157$ dB/km), where the full C-band is filled with WDM channels (~ 4.1 THz signal bandwidth). We consider two system configurations:

1. 111 WDM channels at 32 GBd spaced at 37.5 GHz, and
2. 55 WDM channel at 64 GBd spaced at 75 GHz.

³ This is an ongoing and unpublished work.

The first case corresponds to a typical current system configuration, while the second reflects the industry trend to continue increasing the per-channel bit rate using high symbol-rate signals. The modulation format is PM-16QAM.

At the transmitter side, the COI is synthesized using binary de Bruijn sequences of length 2^{14} . In order to avoid sequence correlations, all adjacent WDM channels are generated using independent random sequences also of length 2^{14} . To correctly account for the spectral broadening due to fiber nonlinearities, the total simulated bandwidth is three times the WDM signal bandwidth (i.e., 3×4.1 THz). The generated signal for each channel is then digitally shaped using a frequency-domain RRC filter with roll-off factor 0.01. Adjacent channels with respect to the COI are further decorrelated by randomly rotating their input state of polarization. All laser linewidths are set to 0 Hz, and we assume equal optical power for all channels.

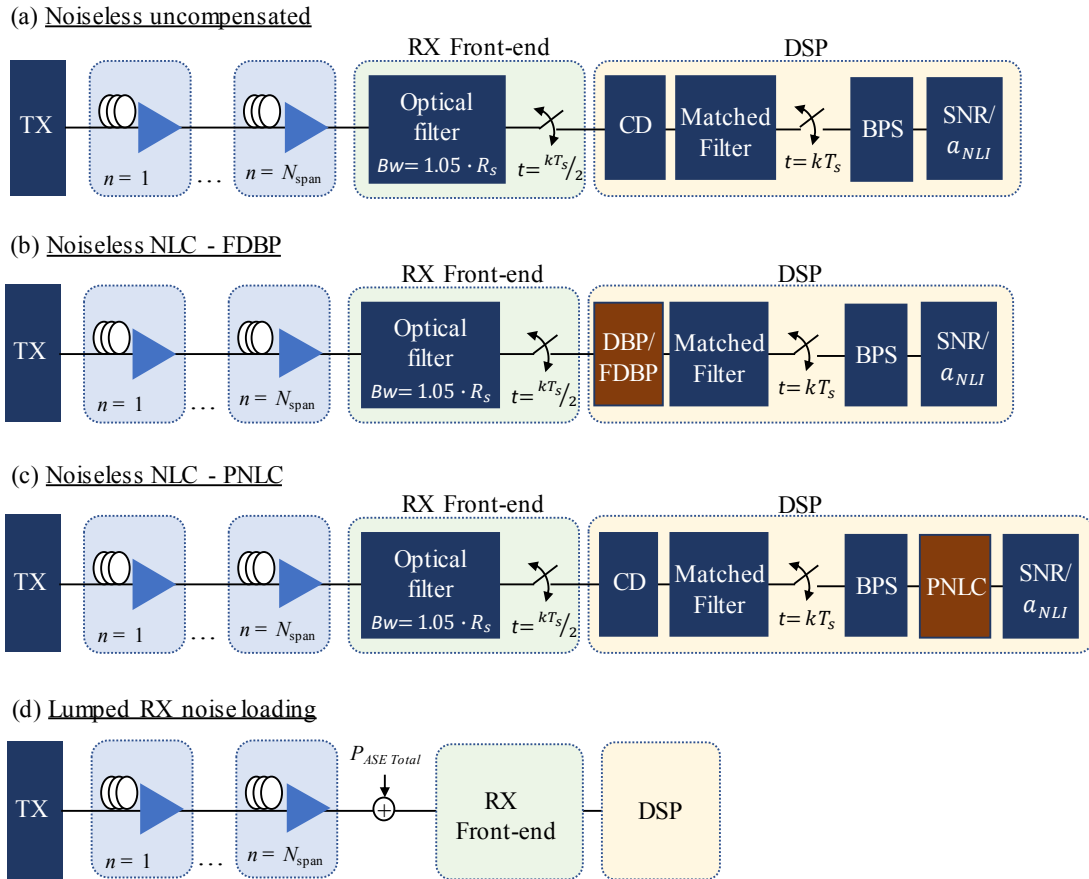


Fig. 2.17: Numerical set-up for a WDM system composed $55 \times N_{span}$ identical fiber spans of Corning EX3000 fiber for (a) an uncompensated system, (b) FDBP based post-NLC, and (c) PNLC based post-NLC. (d) Lumped RX noise loading scheme.

Fiber transmission is simulated using the SSFM applied to the Manakov equation and executed using NVIDIA Tesla K80 GPU cards. Lumped amplification at the end of each span completely compensates for span loss, while noise loading is performed at the receiver side

as shown in Fig. 2.17d. Amplifiers are set in gain mode; therefore, signal depletion by ASE is not considered. The amplifiers NF is set to 5 dB.

At the receiver side, the COI is optically filtered with an ideal rectangular filter with $1.05 \times R_s$ bandwidth, and sampled at 2 sps. After CD compensation, a block performing match filtering is applied. Then, carrier phase estimation based on BPS is performed, with the averaging length chosen to equal the sequence length such that only the global phase is compensated for. Finally, SNR is calculated following (1.18).

NLC is performed either by DBP/FDBP or by PNLC. In the first case, the CD compensation block is replaced by the DBF/FDBP block Fig. 2.17b. In the case of PNLC, it is applied between the phase estimation block and SNR calculation. The different simulation set-up as well as the DSP blocks are sketched in Fig. 2.17.

2.3.2 Numerical Results

When evaluating the gain of NLC techniques by means of numerical simulations it is common to calculate the gain from the well-known *bell-curves* (cf. Fig. 2.18), where the transmitted optical power is swept over a given value range and the performance is obtained for each point with and without NLC. As nonlinear transmission simulations and NLC processing have to be performed for each optical power, this technique requires high computational resources when the total simulated bandwidth is high.

As seen in Sec. 1.4.3, in the frame of RP1 theory, fiber nonlinearities are treated as an AWGN process whose variance is completely characterized by: $P_{NLI} = a_{NLI} P^3$, and where the NLI term a_{NLI} is independent on signal power. Under this assumption, the optimum SNR gain brought by NLC is given by the difference in the NLI term before and after NLC as per (1.99). Therefore, as long as the system operates within the validity of RP1 theory, it is sufficient to calculate the a_{NLI} term with and without NLC to obtain the NLC gain indifferently of the optical power of the transmitted signal.

This approach is simpler as only one numerical simulation has to be performed at a fixed optical power. As all other sources of noise apart from nonlinearities are exactly known, the a_{NLI} term after SNR calculation can be obtained by:

$$\widehat{a_{NLI}} = \left(\frac{P}{\widehat{SNR}} - P_{ASE\ Total} \frac{R_s}{B_{ref}} \right) / P^3 \quad (2.11)$$

where \widehat{SNR} is the estimated SNR calculated from the transmitted and received symbols as per (1.18), and where we have assumed a perfect transmitter and receiver. $P_{ASE\ Total}$ corresponds to the total equivalent ASE noise accumulated over all fiber spans calculated as per (1.55). In the absence of ASE noise (i.e., $P_{ASE\ Total} = 0$), a_{NLI} can be computed straightforward from (2.11) avoiding the numerical uncertainty in P_{ASE} .

We perform a preliminary set of numerical simulations to validate the system performance prediction and NLC gain using the a_{NLI} approach. In order to reduce computation time, we consider 5 channels modulated at 64 GBd with 75 GHz spacing.

In the first set, we perform SSFM simulations for different optical transmitted powers ranging from 0 to 3 dBm. Noise loading is performed at the receiver side, and \widehat{SNR} is computed with and without NLC averaged over 15-seed ASE noise loadings. When NLC is applied, noise loading is performed after the DBP block to avoid degradation of the gain due to self-induced NSNI within the algorithm.

In the second set, a single SSFM simulation is performed for a fixed transmitted power corresponding to the system NLT. Without adding ASE noise, a_{NLI} is obtained as per (2.11) with and without NLC. Then, SNR vs optical power curves are obtained analytically following (1.96) using $\widehat{a_{NLI}}$.

Fig. 2.18 shows the SNR vs channel optical power for the two previous described cases after 7,150 km, where the theoretical performance based on the perturbative model of [61] is also included. NLC is performed by high resolution DBP with $N_{steps} = 20$, and with FDBP with $N_{steps} = 1$. A good match between analytical model and SSFM simulations is found with and without NLC. High resolution DBP achieves the maximum achievable gain, while it is reduced for FDBP. As expected, obtaining the system performance from the SSFM computation of $\widehat{a_{NLI}}$ gives the same results as performing independent SSFM for varying optical powers. From now on, system performance and NLC gains are obtained from SSFM computation of a_{NLI} .

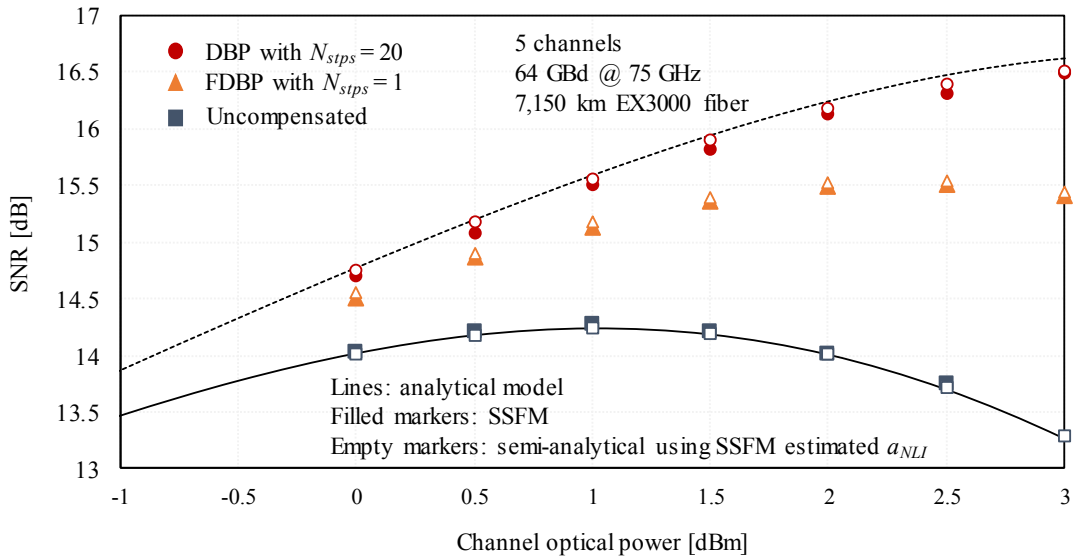


Fig. 2.18: System performance with and without NLC for a 5x32 GBd WDM channels spaced at 75 GHz after 7,150 km EX3000 transmission. (Lines) complete analytical model, (filled markers) SSFM simulations, and (blanked markers), semi-analytical model using SSFM estimated a_{NLI} .

2.3.2.1 Filtered Digital Backpropagation

We now move to full C-band simulation. We start by evaluating the NLC gain versus FDBP algorithm complexity. At a first instance, we neglect ASE noise, such that the signal entering the FDBP algorithm is only impacted by deterministic fiber nonlinearities. This case can be seen as the upper limits of FDBP, where the achievable gain is only due to the associated algorithm accuracy. Considering the case of 32 GBd channels at 37.5 GHz spacing, Fig. 2.19a shows the FDBP gain vs transmission distance for different values of N_{stps} . The FDBP coefficients κ and B_{FDBP} have been obtained following (2.3) and (2.4), where exhaustive optimization has been performed for a few points to further verify their validity. The maximum gain obtained by high resolution DBP is also shown for comparison.

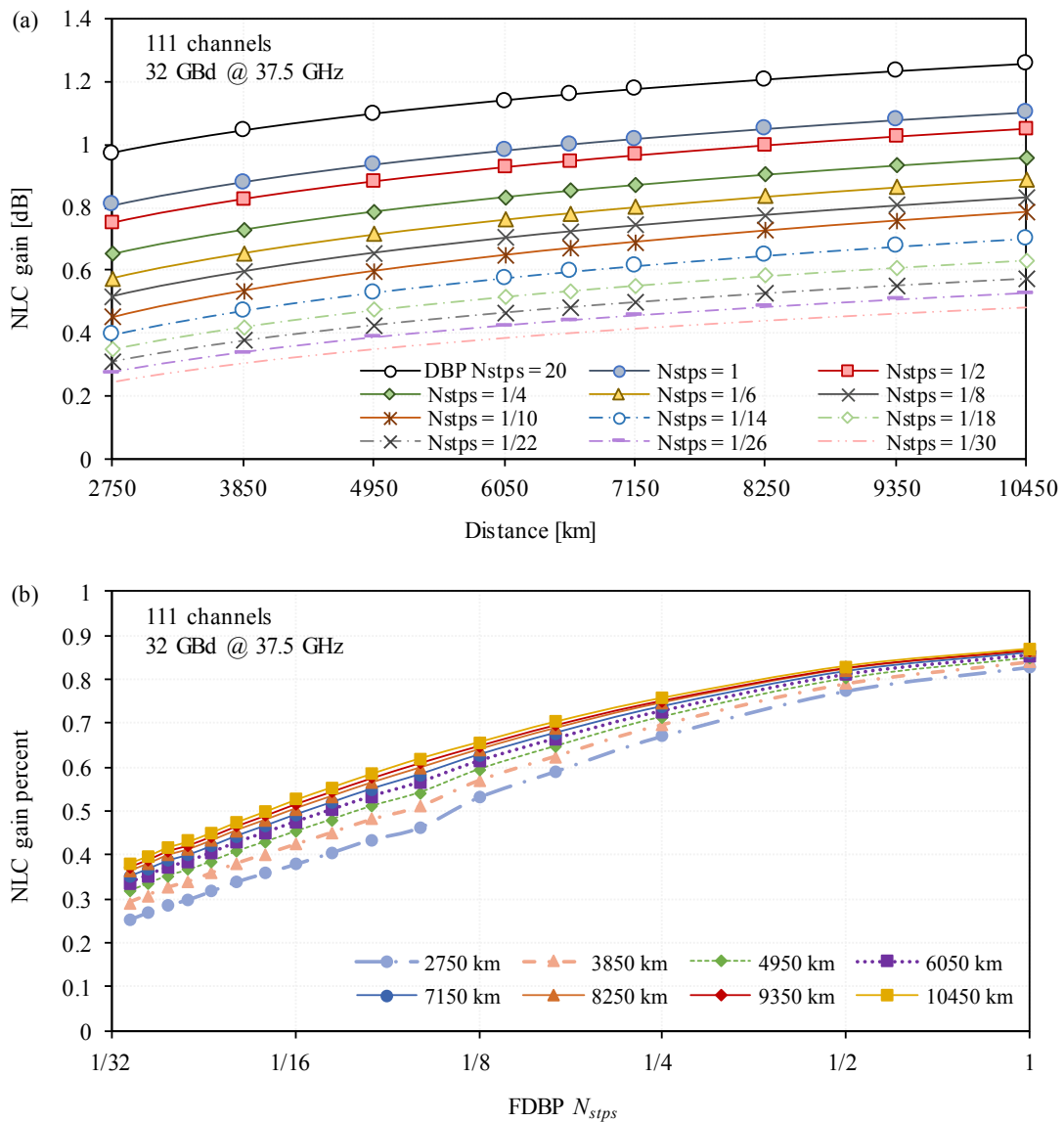


Fig. 2.19: (a) Noiseless FDBP gain versus propagation distance for different N_{stps} values. (b) Noiseless FDBP gain percent relative to high resolution DBP versus N_{stps} for different propagation distances for a system composed of 111 channels at 32 GBd and 37.5 GHz spacing.

We note that the DBP/FDBP gain keeps growing with the transmitted distance, as the intra-channel nonlinear variance accumulates much faster along distance with respect to inter-channel nonlinearities [71]. The maximum achievable gain provided by high resolution DBP lies in the region between 1 to 1.2 dB for all considered distances. Performing FDBP with $N_{stps} = 1$ leads to a reduction of ~ 0.2 dB in achievable gain, which is further decreased for lower N_{stps} values. For distances above 6,000 km, considerable gains above 0.6 dB are attainable with FDBP steps as low as $N_{stps} = 1/10$. To better compare the achievable gain vs FDBP complexity, Fig. 2.19b shows the FDBP gain percent with respect to high resolution DBP vs N_{stps} . Performing FDBP with $N_{stps} = 1$ achieves almost 90% of the maximum gain. For transoceanic distances, 50% of the maximum gain can be achieved with $N_{stps} = 1/16$.

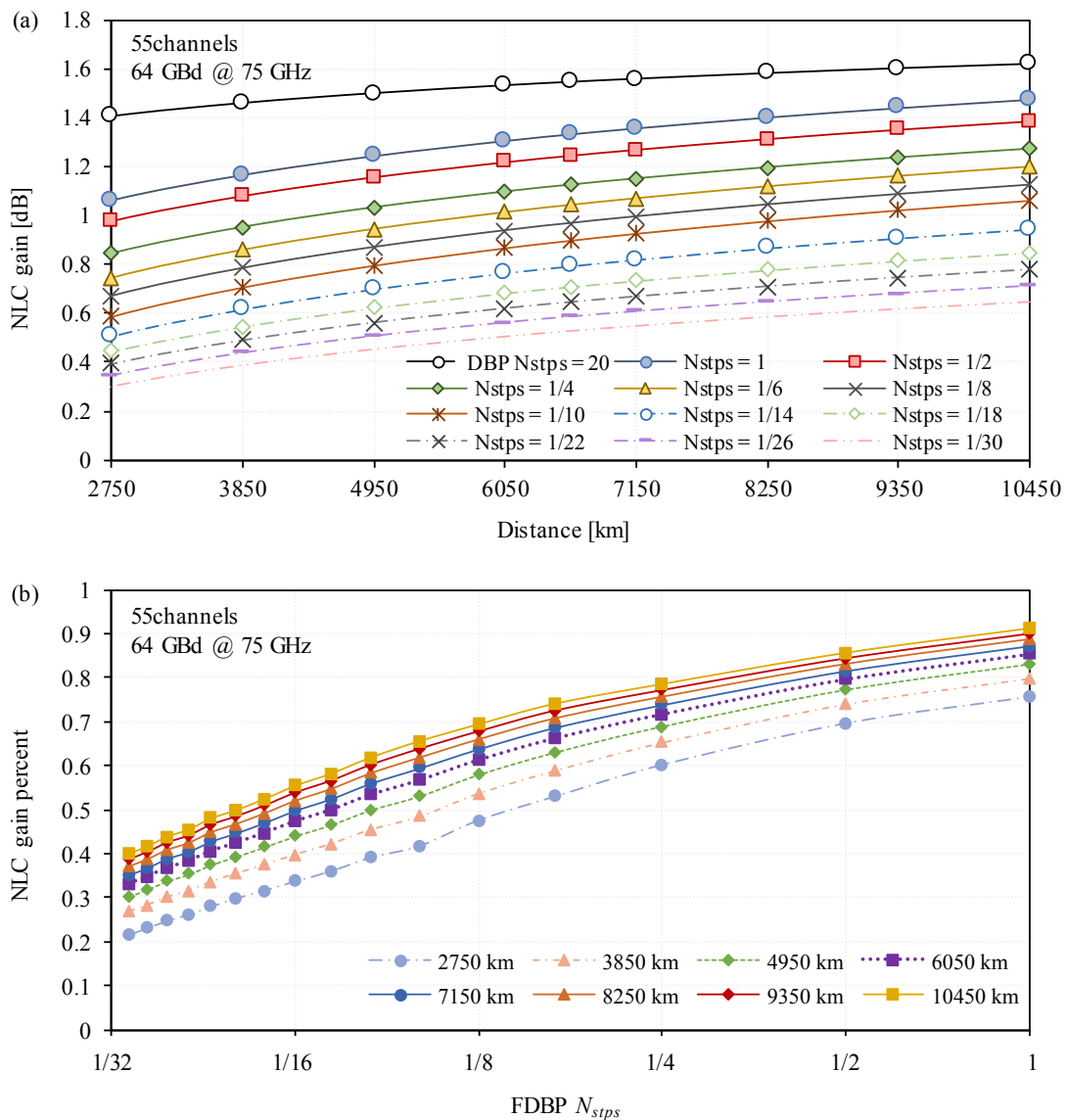


Fig. 2.20: (a) Noiseless FDBP gain versus propagation distance for different N_{stps} values. (b) Noiseless FDBP gain percent relative to high resolution DBP versus N_{stps} for different propagation distances for a system composed of 55 channels at 64 GBd and 75 GHz spacing.

Fig. 2.20 shows the same curves but considering 64 GBd channels with 75 GHz spacing. Doubling the channel symbol-rate and reducing the number of WDM channels by half, leads to an increase of ~ 0.2 dB on the achievable gains. For transoceanic distances, the maximum achievable gain is ~ 1.5 dB, while $N_{steps} = 1/30$ is enough to achieve gains above 0.5 dB. These results show that increasing the channel symbol-rate not only leads to an increase in the achievable NLC gain, but that N_{steps} can be greatly reduced while still achieving considerable gains.

FDBP with $N_{steps} = 1$ leads to 90% of the maximum achievable gain, while lower values of N_{steps} lead to similar results compared to the 32 GBd case. From Fig. 2.19 and Fig. 2.20, it is observed that lower gains are achieved for decreasing propagation distances, with a larger impact for the 64 GBd system. This can be due to the use of not optimum values of FDBP coefficients. However, performing exhaustive optimization of κ and B_{FDBP} leads to the same results. This behavior needs to be further verified. However, the achievable gain percent is relatively the same for transoceanic distances.

The above results were obtained considering a noiseless system, such that the FDBP algorithm only deals with the deterministic nonlinear impairments and is not affected by ASE noise. However, in real systems ASE noise is added at each amplification point, leading to NSNI during propagation. NSNI not only impacts the system performance, but also the effectiveness of a nonlinear equalizer placed at the receiver side. First because NSNI taking place during propagation is not compensated due to its stochastic nature, and also because self-induced NSIN will take place within the NLC algorithms [61, 76, 132, 133]. A type of DBP referred as stochastic DBP taking into account ASE noise have also been proposed [134]. However, due to its increased complexity it is not considered in this work.

To study the impact of noise in the effectiveness of FDBP, we now load ASE noise at the receiver side. Thus, NSNI taking place during forward propagation is neglected. The FDBP gain is obtained for different values of loaded ASE noise. We take as a reference a system with amplifiers having $NF = 5$ dB, for which the reference OSNR is computed ($OSNR_{ref}$). Then we degrade the received OSNR by a given value $\Delta OSNR = \{1, 2, 3, 4, 5\}$ dB. The resulting system OSNR is therefore $OSNR = OSNR_{ref} - \Delta OSNR$

Fig. 2.21a shows the FDBP gain vs distance for $N_{steps} = 1$, and different values of $\Delta OSNR$ considering the system configuration at 32GBd. The maximum achievable gain with noiseless high resolution DBP and noiseless FDBP are also shown for comparison. As found in [76], after a certain distance the FDBP gain decreases due to NSNI. Therefore, there exists an optimal link length for which DBP is maximally effective. The penalty in FDBP gain increases for lower values of received OSNR. For a fixed distance of 6,600 km, Fig. 2.21b shows the FDBP gain vs $\Delta OSNR$ for different values of N_{steps} . It is observed that the gain is equally degraded for all values of N_{steps} , where similar results were found for other distances. Therefore, the impact brought by NSIN within the FDBP algorithm is independent on N_{steps} .

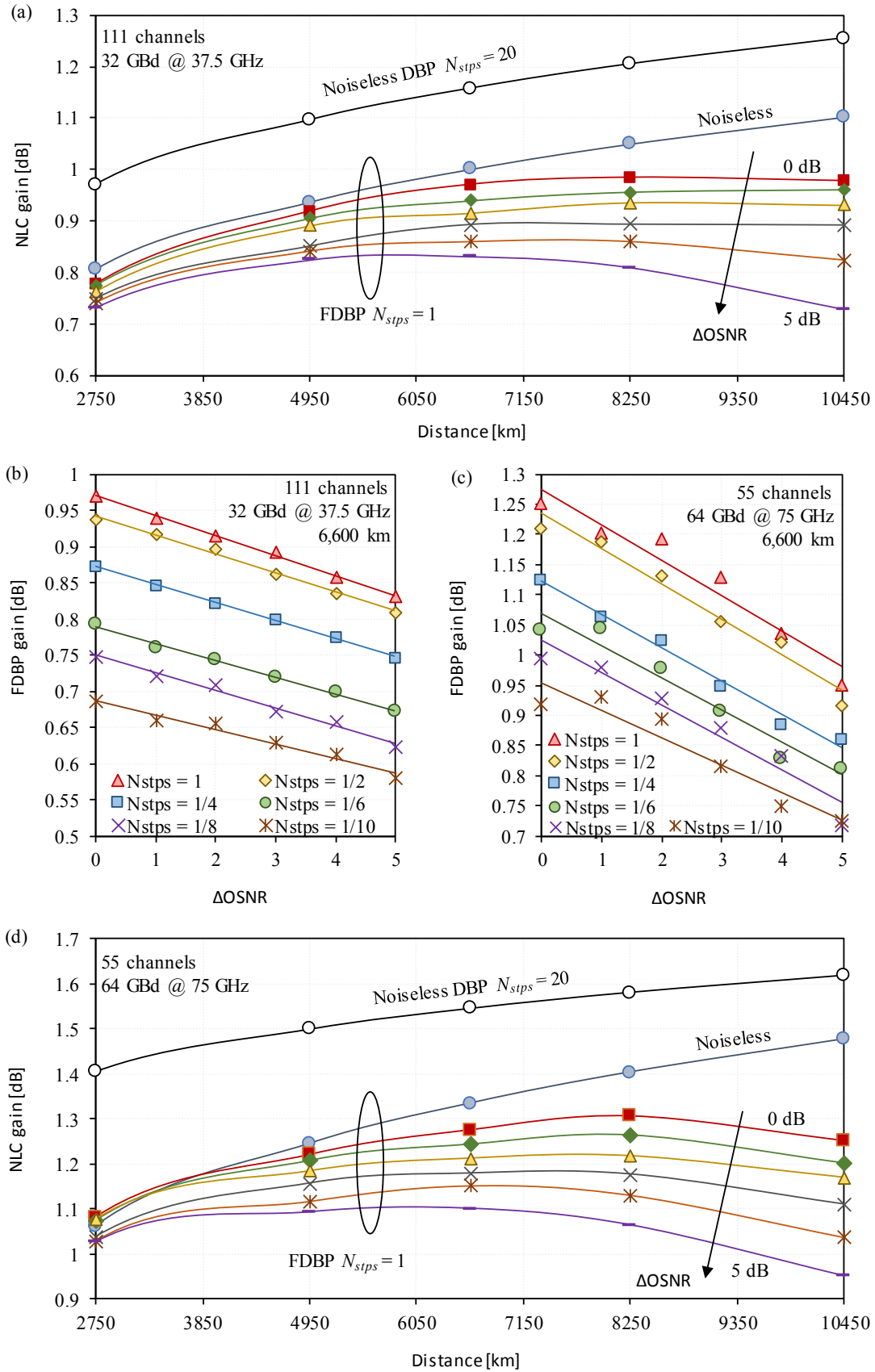


Fig. 2.21: (a),(d) NLC gain versus propagation distance for noiseless DBP with $N_{stps} = 20$, noiseless FDBP with $N_{stps} = 1$, and FDBP with $N_{stps} = 1$ for different received OSNR regimes. (b),(c) FDBP gain versus OSNR penalty for different N_{stps} .

Similar results for the 64GBd system configuration are shown in Fig. 2.21c and Fig. 2.21d., However, it is observed that the NLC gain degradation due to linear noise is higher than that of the 32GBd case. This is explained by the fact that doubling the symbol-rate will also double the in-band noise entering the FDBP algorithm, leading to higher induced NSNI.

2.3.2.2 Perturbative Nonlinear Compensation

We now evaluate the achievable gains provided by PNLC. A noiseless system is considered first as in the previous section, such that the achievable PNLC gains are only due to the efficiency in inverting deterministic nonlinear distortions. The complexity of the algorithm comes from the number of $C_{m,n}$ coefficients considered for nonlinear compensation, where the optimum value depends on the channel memory induced by chromatic dispersion.

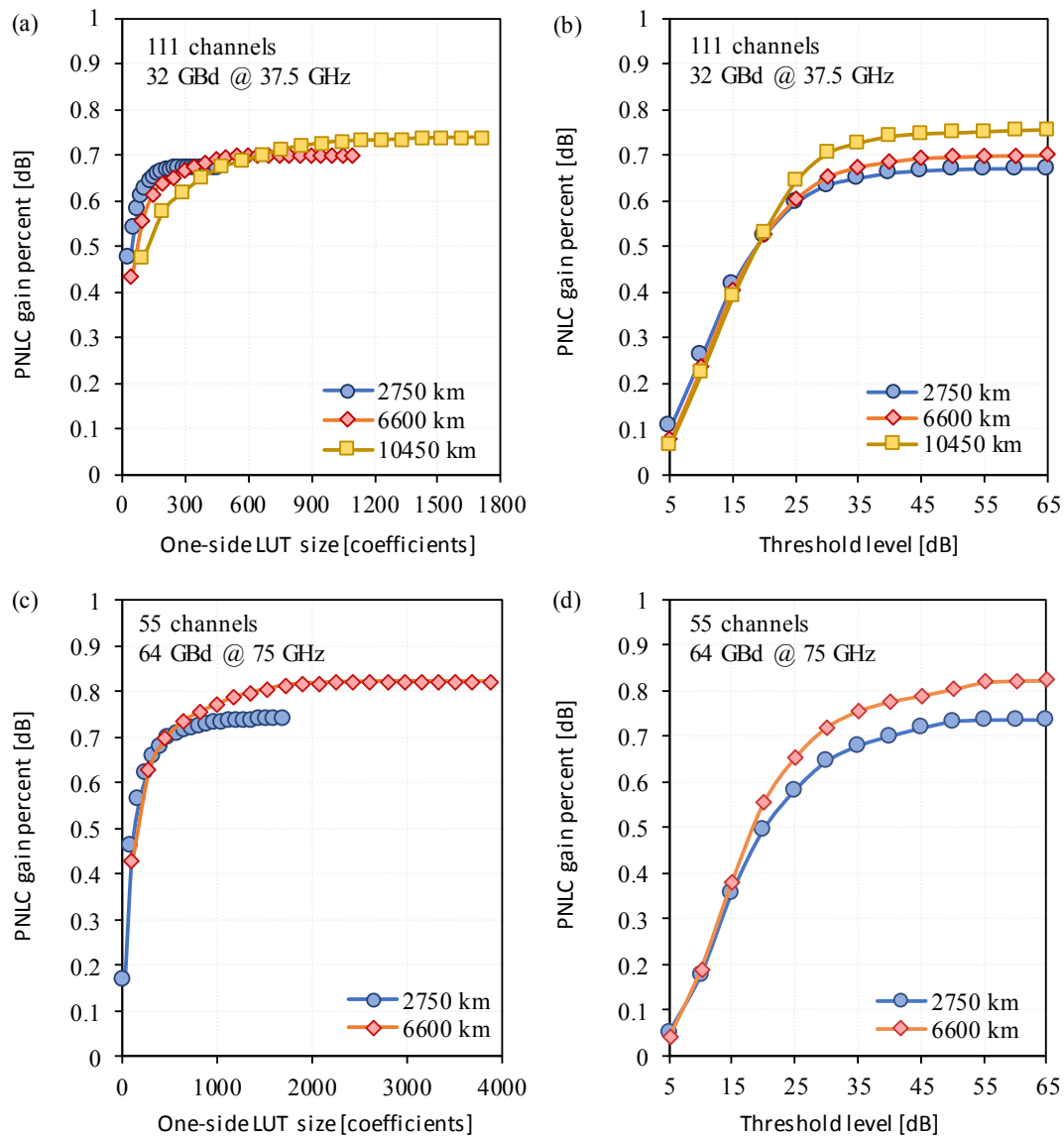


Fig. 2.22: PNLC gain percent versus (a),(c) C_{mn} LUT size, and (b),(d) C_{mn} discard threshold.

For the 32 GBd configuration, Fig. 2.22 shows the PNLC gain percent with respect to the maximum achievable gain provided by high resolution DBP versus the one-sided C_{mn} LUT size for three propagation distances. The scaling parameter present in (1.80) and (1.81) has been optimized for each point. It is observed that the maximum gain provided by PNLC is around 70% of the maximum achievable gain. Moreover, the gain saturates at $\sim 50\%$ of the ideal LUT size depending on the channel memory. In order to further reduce complexity, all C_{mn} terms below a given threshold with respect to $C_{0,0}$ can be discarded. Fig. 2.22b shows the PNLC gain percent considering a 50% LUT versus the threshold value used to discard terms. The maximum gain percent corresponds to the ones of Fig. 2.22a, where saturation is achieved for threshold values above 35 dB.

Similarly, Fig. 2.22c and Fig. 2.22d shows the achievable PNLC gain percent for the 64 GBd configuration. Contrary to the previous case, we only consider a maximum propagation distance of 6,600 km, as the number of C_{mn} elements grows quadratically with the channel symbol-rate. Therefore, for each distance, the optimum LUT size for the 64 GBd configuration is 4 times bigger than the 32 GBd case. The achievable gains are $\sim 80\%$ of the maximum achievable gain provided by high resolution DBP. As for 32 GBd channels, the optimum C_{mn} coefficient discard threshold at which the gain saturates is ~ 35 dB.

Now we investigate on the impact of noise on the performance of PNLC. As it was done for FDBP, the OSNR at the receiver side is degraded from its reference value by a given amount $\Delta OSNR$, and PNLC is applied. Shows the PNLC gain versus LUT size for a fixed distance of 6,600 km, where the maximum gain achievable gain for noiseless DBB and PNLC are also shown for comparison.

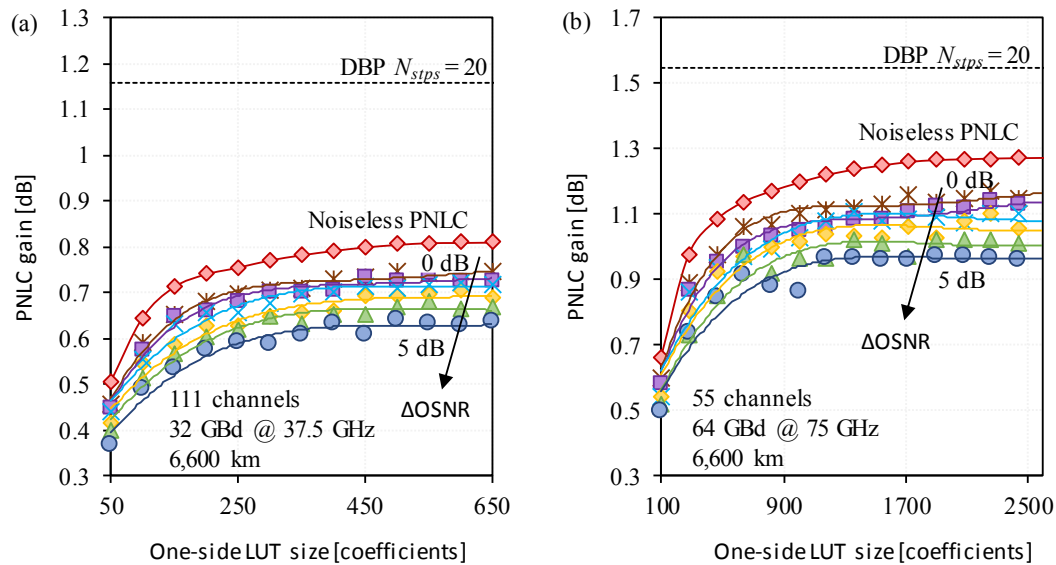


Fig. 2.23: PNLC gain versus C_{mn} LUT size for different working OSNR regimes at 6,600 km for (a) 32 GBd and (b) 64 GBd system configurations.

As observed in Fig. 2.23, the impact of noise on PNLC gain does not depend on the considered LUT size. This was the same findings as for FDBP, where noise impact was independent with the applied N_{steps} . From Fig. 2.23a, it is observed that increasing $\Delta OSNR$ from 0 dB to 5 dB leads to a gain degradation of ~ 0.1 dB. This is the same degradation found at 6,600km for FDBP as shown in Fig. 2.21b. The above process has been repeated for the other distances considered in Fig. 2.22, (i.e., 2750 km, 10450 km for 32GBd, and 2750 km for 64 GBd). It was found that the degradation in PNLC gain versus OSNR penalty closely match the gain degradation of the FDBP. Therefore, we can conclude that both FDBP and PNLC are equally affected by linear noise, and the gain degradation is independent of the algorithm complexity.

Besides the NLC degradation due to a decreased algorithm complexity and linear noise impact, both FDBP and PNLC can achieve gains above 0.5 dB for transoceanic distances with low-complexity architectures for the two studied system configurations

2.4 SUMMARY

In this chapter we evaluated the performance and practical achievable gains of low-complexity single-channel NLC algorithms. In the first part, we studied the dependency of the parameters involved within the FDBP algorithm on different system parameters as: channel count, launched power, symbol-rate, and fiber coefficients. We showed numerically and experimentally that the FDBP parameters depend mainly on the pulse broadening per FDBP step, allowing us to derive simple semi-analytical formulae for their computation, and avoiding complex exhaustive optimization.

In the second part, we experimentally addressed the impact of PMD and PDL on the performance of FDBP and PNLC. We showed that PMD values as large as 5 times the symbol duration lead to a maximum observable degradation of only ~ 0.1 dB in the achievable gain of FDBP and PNLC; while the corresponding gain degradation due to PDL values as large as 9 dB is only ~ 0.2 dB. These experimental observations show the robustness of these algorithms to PDL and PMD.

Finally, in the third part, we numerically evaluated the practical achievable gains provided by FDBP and PNLC for different algorithm complexities for two transoceanic system configurations, i.e., 32 GBd channels at 37.5 GHz spacing and 64 GBd channels at 75 GHz spacing. For an ideal noiseless case, the maximum achievable gain provided by high-resolution DBP is above 1 dB for distances above 6,000 km. FDBP working at one step per span can achieve 90% of this maximum gain, while for PNLC with optimum LUT size it is

reduced to ~75%. For the noisy case, these attainable gains are further decreased, with a higher degradation for longer transmission distances, leading to an optimal link length for which NLC is maximum. Linear noise equally affects both FDBP and PNLC, independently of the algorithm complexity. For practical OSNR working regimes and trans-Atlantic distances, PNLC can achieve gains between 0.5dB and 0.7 dB for systems employing 32GBd channels, while for 64 Gbd systems it is increased to 0.7dB up to 1.1 dB.

3 HIGH-CAPACITY MODULATION FORMATS

The great advances in high-speed high-resolution DAC/ADC's have not only allowed the use of powerful DSP algorithms to compensate for system impairments in coherent optical fiber systems, but also the possibility to generate higher spectral efficiency signals using higher order modulation formats with arbitrary pulse shaping.

Modulation formats beyond 16QAM have been recently explored by a few research groups to significantly increase the SE of submarine systems [20, 31]. In [20], 32QAM was used to achieve 7.9 b/s/Hz over 6,800 km, while in [31], a SE of 7.1 b/s/Hz was achieved after 5,380 km using 64QAM with coded modulation and iterative decoding.

Other formats besides regular QAM have also been explored. As presented in Sec. 1.2.3, according to Shannon channel coding theorem, the optimum source distribution for the AWGN channel is complex-circular and Gaussian. In practice, one can use formats with a discrete number of constellation points, and then apply some kind of constellation shaping to make the source distribution closer to Gaussian, which helps decrease the gap between the constrained and the linear Shannon capacity. Ref. [20] showed a record C-band SE of 8.3 b/s/Hz by using geometric constellation shaped 64APSK. Later on, in [30], the novel probabilistic constellation shaping based on 64QAM constellation (PCS-64QAM) was employed for the first time over 6,600 km to achieve a SE of 7.3 b/s/Hz employing C+L bands with EDFA only amplification. This experiment was followed by a field trial over a 5,523 km in service C-band EDFA-only trans-Atlantic Facebook cable to demonstrate a SE of 7.46 b/s/Hz [32].

Finally, hybrid formats employing both geometrical and probabilistic shaping have also been experimentally demonstrated. The 4D-PS-9/12-56APSK was used in [22] to achieve 7.2 b/s/Hz

over 7,600 km, using C+L bands EDFA-only amplification, while 4D-PS-7/12-40APSK was demonstrated in [41] to achieve 5.29 b/s/Hz after 17,107 km. However, these hybrid formats are based on coded modulation with complex iterative decoding, therefore unattractive from the industry point of view.

In the first part of this chapter, we experimentally compare the performance and achievable rates of different higher order modulation formats employing low complexity BICM with BM decoding (i.e. 32QAM, 64QAM, 64APSK, PCS-64QAM) for transoceanic distances, together with some DSP challenges associated with their practical implementation. Then, we focus on the design of a truncated version of PCS-64QAM (TPCS-6AQAM) optimized to maximize the SE of trans-Pacific optical links.

3.1 MODULATION FORMATS COMPARISON

As seen in Sec. 1.2.3 ,“Gaussian-like” constellations decrease the gap between the constrained and the linear Shannon capacity, outperforming regular QAM formats. However, in the nonlinear regime, the fourth and sixth moments of the constellation become important in computing the total noise variance as presented in Sec. 1.3.2.2. Moreover, the constellation shaping naturally results in more circular symmetric constellation patterns, which imposes some challenges in the DSP chain, and might lead to additional implementation penalties. Moreover, generating and receiving complex constellations requires higher resolution of DAC and ADC’s.

Therefore, a fair comparison of the performance of higher order formats for coherent optics requires addressing at least four issues: theoretical gap to the linear Shannon capacity, nonlinear performance at optimum launch power, B2B implementation penalties due to limited DAC and ADC resolutions, and DSP challenges.

In this section, we experimentally compare the performance of four modulation formats for transoceanic distances, *i.e.*, 32QAM, 64QAM, 64APSK, and PCS-64QAM, addressing all the above-mentioned issues.

3.1.1 Theoretical Performance

We start by evaluating the theoretical performance of the four mentioned formats. We adopt two performance metrics: the SNR, and the GMI, which is the correct measure to be used for systems employing BICM as presented in Sec. 1.2.1.3. We consider a PCS-64QAM with a source entropy, H , of 5.4 b/symb/pol, which was shown in [30] to minimize the gap to the linear Shannon capacity for a SNR target of 12 dB. Fig. 3.1 shows the GMI for all the above formats over the SNR region of interest.

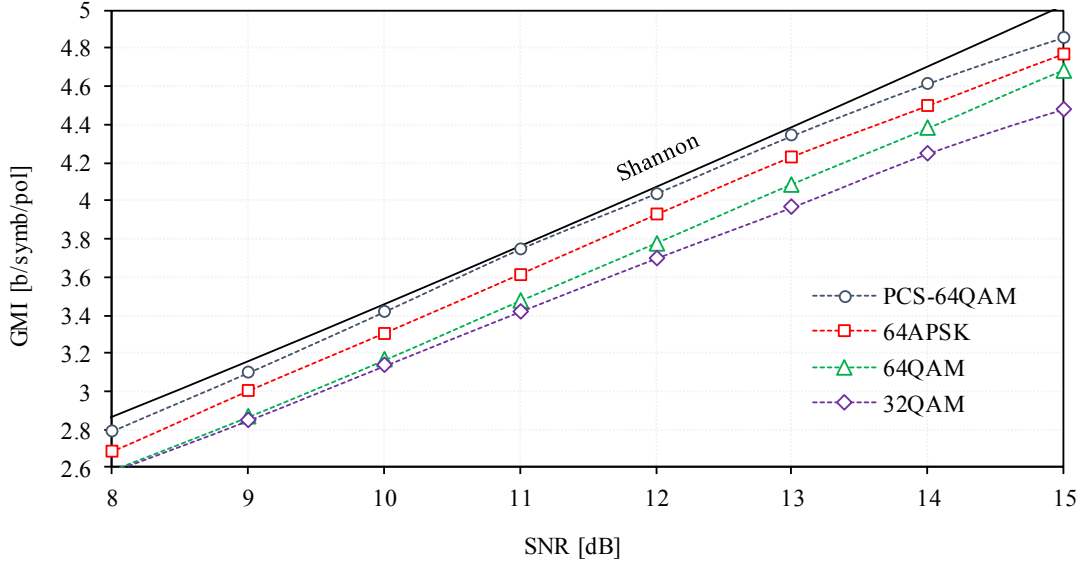


Fig. 3.1: GMI for 32QAM, 64QAM, 64APSK, and PCS-64QAM with $H = 5.4$ bi/symb/pol.

From Fig. 3.1 it is clear that PCS-64QAM outperforms all other considered formats. The second place belongs to 64APSK, which outperforms 64QAM by its geometric-shaping gain. For a SNR of 12 dB, the gain provided by PCS-64QAM over 64APSK is 0.1 b/symb/pol, while with respect to 32QAM and 64QAM is 0.34 b/symb/pol and 0.26 b/symb/pol respectively.

According to (1.96), the total SNR after transmission through the optical fiber is inversely proportional to the nonlinear noise variance arising from the fiber Kerr nonlinear effects, with the nonlinear noise variance being directly proportional to 4th, μ_4 , and 6th, μ_6 , constellation moments according to (1.93) and (1.94). As observed in Fig. 3.2a, μ_4 and μ_6 increase with the constellation order, with the Gaussian constellation maximizing both coefficients. Therefore, it is expected that Gaussian-like constellations will present a higher nonlinear penalty after fiber transmission.

Fig. 3.2b shows the theoretical SNR vs optical power obtained as per (1.96) for a system composed of 61 channels at 49 GBd with 50 GHz spacing, where the nonlinear variance is calculated following (1.93) and (1.94). The transmission distance is set to 6,600 km composed of 55 km EX3000 fiber spans, and we consider the same B2B penalties for all formats. The SNR is then transformed to GMI following the curves of Fig. 3.1.

It is observed that in terms of SNR, both PCS-64QAM and 64APSK are more nonlinear than 32QAM and 64QAM, with a penalty of ~ 0.25 dB at NLT. Despite this nonlinear penalty, PCS-64QAM still outperforms all other formats in terms of GMI, with a net gain of 0.09 b/symb/pol with respect to 64APSK, 0.26 b/symb/pol with respect to 32QAM, and 0.18 b/symb/pol against 64QAM.

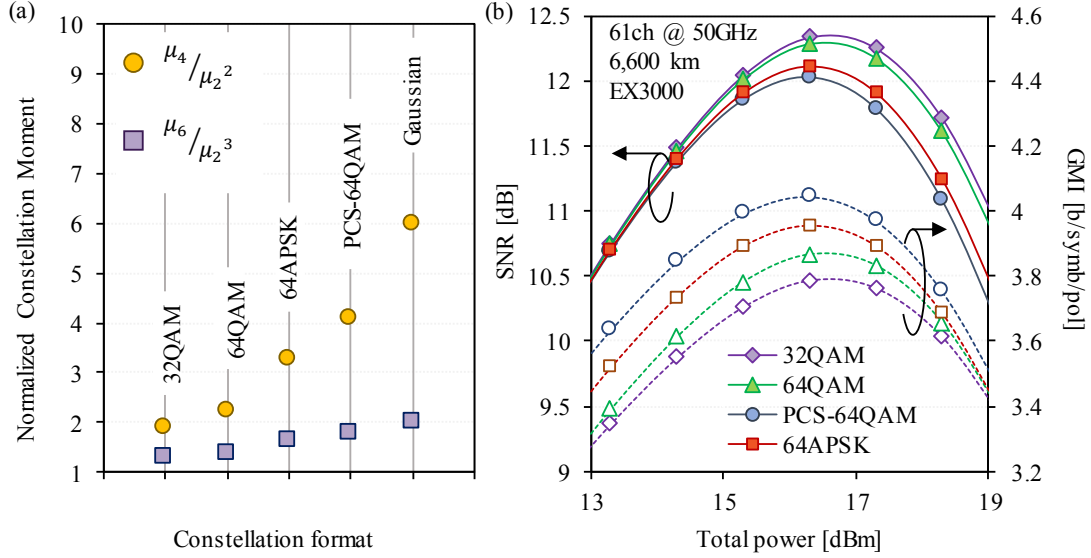


Fig. 3.2: (a) Normalized 4th and 6th constellation moment, and (b) theoretical SNR/GMI vs optical power for 32QAM, 64QAM, 64APSK, and PCS-64QAM.

From the above results, it is clear that PCS-64QAM outperforms all other formats in terms of achievable GMI assuming all formats have the same B2B SNR performance. However, the combination of high symbol-rate, Gaussian-like constellations, and low SNR working regimes will lead to DSP challenges, which if are not well addressed will lead to extra implementation penalties.

The first of these challenges was addressed in [30], where it was experimentally shown that the Gaussian-like constellation associated to PCS-64QAM and 64APSK cause the polarization demultiplexer to converge more difficulty, such that a pilot-assisted MMA has to be used after pre-convergence by a CMA block. In order to address this issue⁴, we can study the polarization demultiplexer performance dependency on modulation format by considering a simple fiber channel model of the form:

$$\begin{bmatrix} y_k^H \\ y_k^V \end{bmatrix} = \begin{bmatrix} \cos(\alpha) & \sin(\alpha) \\ -\sin(\alpha) & \cos(\alpha) \end{bmatrix} \begin{bmatrix} x_k^H \\ x_k^V \end{bmatrix} + \begin{bmatrix} n_k^H \\ n_k^V \end{bmatrix} \quad (3.1)$$

where x_k is the k 'th sent symbol over H and V polarizations, n is an AWGN of variance $N_0/2$, α is a random polarization rotation angle, and y_k is the k 'th received corrupted symbol. The polarization demultiplexer can be modeled as a ML estimator of α of the form:

$$\hat{\alpha}_k = \underset{\alpha_b}{\operatorname{argmax}} \prod_{n=-N}^N P(|y_{k+n}^H| | \alpha_b) \quad (3.2)$$

⁴ The theoretical study of the convergence of the polarization demultiplexer for different modulation formats is an unpublished and ongoing work.

where we have considered only one signal polarization for simplicity. Following (3.2), the estimator will choose the angle $\hat{\alpha}$ that maximizes the probability distribution function $P(|y_{k+n}^H||\alpha_b)$ between all possible test angles α_b . For a complex-circular AWGN channel, the signal amplitude probability follows a Rice distribution, such that $P(|y_{k+n}^H||\alpha_b)$ can be written as:

$$P(|y_{k+n}^H||\alpha_b) = \sum_{m=1}^M \left(\frac{2 \cdot |\tilde{y}_{k+n}^H|}{N_0} \right) \exp\left(-\frac{(|\tilde{y}_{k+n}^H|^2 + |a_m|^2)}{N_0} \right) I_0\left(\frac{2 \cdot |\tilde{y}_{k+n}^H|^2 \cdot |a_m|^2}{N_0} \right) P(a_m) \quad (3.3)$$

where a_m is the m 'th complex constellation point, $P(a_m)$ is its corresponding a priori probability, $I_0(\cdot)$ is the modified Bessel function of the first kind with order zero, and $\tilde{y}_{k+n}^H = y_{k+n}^H \cdot \cos \alpha_b + y_{k+n}^V \cdot \sin \alpha_b$. Following (3.2) and (3.3), we can calculate the minimum square error (MSE) between the estimated polarization rotation angle, $\hat{\alpha}$, and the real one, α , by:

$$MSE = \mathbb{E}[(\hat{\alpha} - \alpha)^2] \quad (3.4)$$

For theoretical analysis we focus only on QAM formats, as 64APSK is less attractive for commercial implementation and is less performant than PCS-64QAM. We also include 16QAM for better comparison.

For simplicity, we assume a constant polarization rotation angle over the whole sequence length. Fig. 3.3 shows the MSE of the ML estimation versus the observation window size N , for two different SNR working regimes, (i.e., 16 dB and 12 dB).

Due to the constant rotation angle, the MSE continuously decrease versus the averaging length as AWGN is averaged out from the estimation. However, it is observed that the ML estimation converges more slowly for PCS-64QAM, with a higher penalty when passing from 16 dB to 12 dB compared to the other QAM formats. This simple analysis shows that the polarization tracking speed of the polarization demultiplexer is greatly reduced for PCS-64QAM, leading to a poor channel estimation and to possible performance degradation.

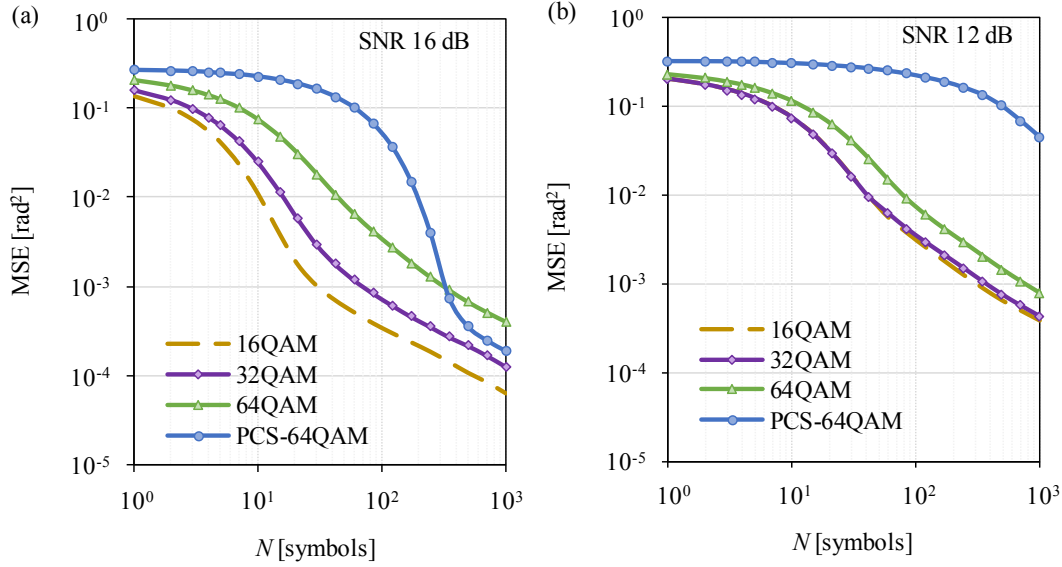


Fig. 3.3: MSE of the ML polarization rotation angle estimation for 32QAM, 64QAM, 64APSK, and PCS-64QAM at (a) 15 dB and (b) 12 dB SNR.

A similar analysis can also be performed for the carrier phase estimation DSP block⁵ [135]. Considering a channel model as per (1.70) where the time-varying phase is modeled as a Wiener process, and assuming a zero-residual frequency offset, the ML phase estimation can be performed following the BPS algorithm based on (1.72). For the case of QAM formats which present a rotational symmetry of $\pi/2$, it is sufficient to test equally spaced phases between 0 and $\pi/2$, followed by unwrapping. For all formats, we test 64 phases and perform fully data aided cycle slip removal for MSE calculation.

Fig. 3.4 top row shows the MSE of the phase estimation angle considering no laser linewidth, and a 100 kHz linewidth for a SNR of 16 dB. When the laser linewidth is set to 0, the MSE continuously decreases for increasing values of N , as AWGN is averaged out from the estimation. When a 100 kHz laser linewidth is considered, an optimum value of N is found, as low values of N are not enough to average out AWGN noise, while high values of N are not able to track the time-varying phase. It is observed that PCS-64QAM behaves similar to 32QAM, with 64QAM being the format that converges more slowly.

When the SNR decreases to 12 dB (Fig. 3.4 bottom row), 64QAM behaves better than 32QAM and PCS-64QAM. Please note that in the case of QAM constellations, the constellation points with the highest energy contribute the most to the ML estimation. These points are not present in the case of 32QAM, and they have the lowest probability of occurrence in the case of PCS-64QAM. Therefore, it is well expected that the phase estimation of the two last mentioned formats will be degraded.

⁵ The theoretical study of the convergence of the phase estimation for different modulation formats is also an unpublished and ongoing work.

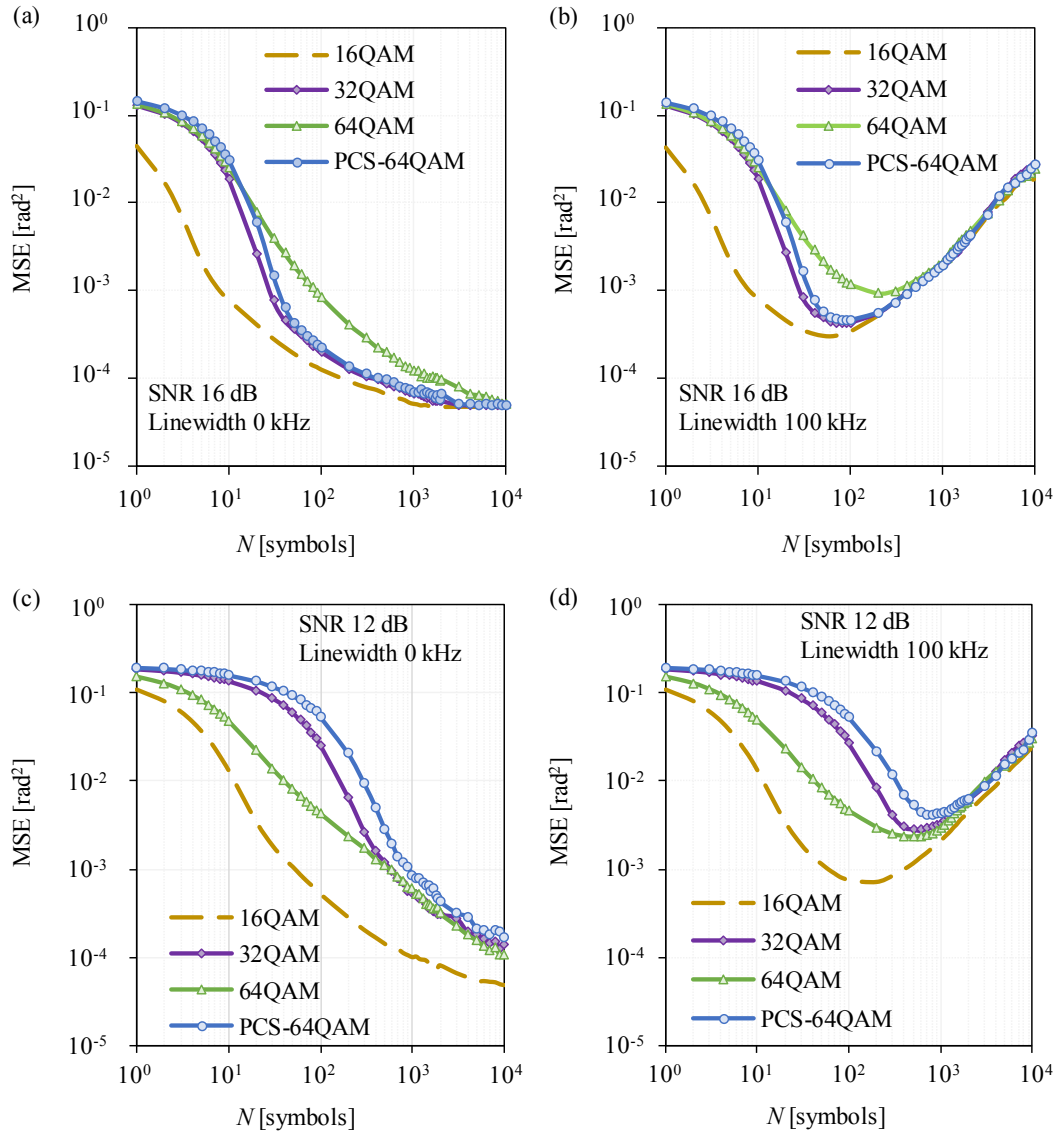


Fig. 3.4: MSE of the ML phase estimation for 16QAM, 32QAM, 64QAM, 64APSK, and PCS-64QAM considering a zero, and a 100 kHz laser linewidth, for two working SNR regimes.

From Fig. 3.4 we can conclude that for low SNR regimes, PCS-64QAM requires higher averaging window lengths compared to the other considered formats, being more sensitive to phase noise.

3.1.2 Experimental Performance

After comparing the theoretical performance of all formats, and the challenges associated to some DSP blocks, we now proceed to compare them experimentally. We start by comparing the performance in B2B configuration. To do so, for each format we generate random signal sequences of length 2^{15} with 49 GBd RRC pulses with roll-off 0.01. The generation is performed offline using the standard random number generator MatLab function, which in the case of PCS-

64QAM also serves to emulate the DM. The generated sequences are loaded to an 88 GSamples/s DAC, which drives a PM IQ-MOD modulating a single TLS. The generated optical signal is passed through a double stage EDFA, where a variable optical attenuator (VOA) is placed in the middle to achieve a desired OSNR. The signal is then filtered and detected by an 80 GSamples/s scope receiver with 33 GHz electrical bandwidth. Sampled waveforms are then processed off-line by standard DSP blocks. For 32QAM and 64QAM formats, DSP blocks consisting of polarization de-multiplexing using CMA, carrier frequency and phase recovery using BPS, pilot-based cycle-slip removal using 1% pilots followed by LMSE adaptive post-equalization. Finally, SNR and GMI corrected for pilot use are computed for each waveform following (1.8) and (1.18).

As found theoretically, for low SNR regimes the performance of PCS-64QAM and 64APSK is degraded due to a poor channel estimation. As shown in [30], this degradation can be overcome by the use of pilot symbols for DSP convergence. Increasing the pilot rate will lead to an improvement of the signal SNR, but will reduce the effective GMI as the pilot rate should be subtracted from the net information rate. Therefore, the optimum pilot rate is the one that maximizes the effective GMI. Fig. 3.5 shows the pilot-aided DSP blocks used for 64APSK and PCS-64QAM.

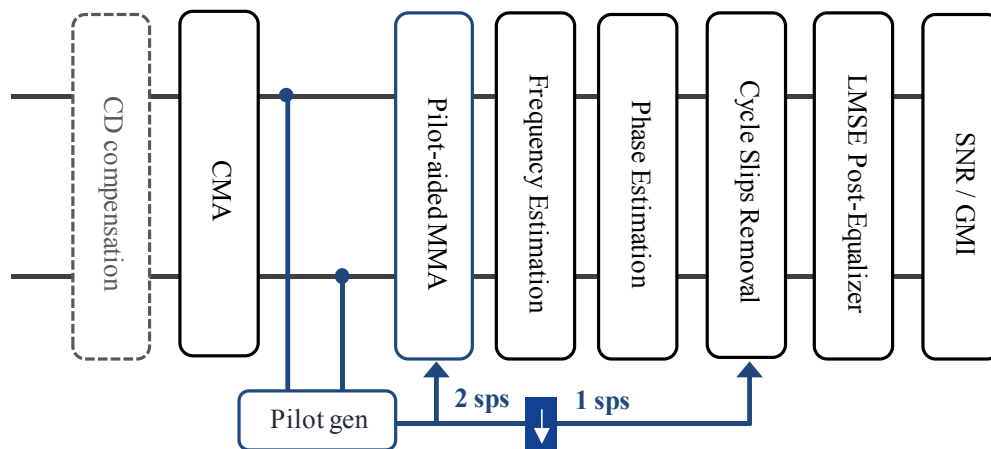


Fig. 3.5: Pilot-aided DSP for PCS-64QAM and 64APSK.

Fig. 3.6 shows the GMI and SNR versus the pilot percentage for the two last mentioned formats for a B2B OSNR of 19 dB corresponding to the end-of-link OSNR of our transmission line after 6,600 km. An optimum value of 1% is found for PCS-64QAM, while it is increased to 2% for 64APSK. In terms of SNR performance, PCS-64QAM and 64APSK working at optimum pilot rate present a degradation of ~ 0.3 compared to the achievable SNR using 100% pilots.

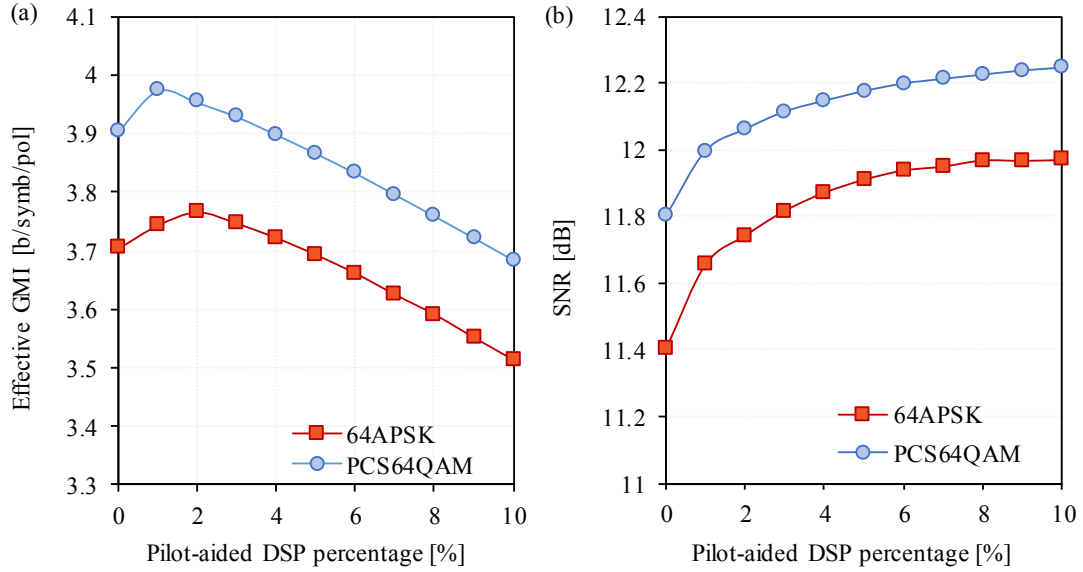


Fig. 3.6: (a) GMI and (b) SNR vs DSP pilot percent for 64APSK and PCS-64QAM.

Fig. 3.7a shows the experimental B2B SNR using the optimized DSP pilot rates. At an OSNR of 19 dB, 32QAM has the lowest implementation penalty of 0.5 dB in SNR, followed by 64QAM and PCS-64QAM with 0.8 dB, and finally 64APSK with 1.2 dB. In the case of 64APSK, there is a manifest degradation of performance for low OSNRs, such that OSNRs below 17 dB cannot be processed with a 2% pilot rate.

The implementation penalties shown in Fig. 3.7a will be translated into penalties in GMI. Fig. 3.7b shows the experimental GMI corrected for pilot use versus OSNR curves for all formats (solid markers), where the ideal curves are also shown for comparison (blank markers). The implementation penalties of 64QAM shown in Fig. 3.7a annihilate its superior theoretical SE with respect to 32QAM, making both formats having the same performance over the OSNR region of interest. This is the same case for 64APSK, which due to its poor performance for low OSNR values and the higher DSP pilot-aided rate, the achievable SE is the same as that of 32QAM, and 64QAM. Therefore, PCS-64QAM achieves a gain of ~ 0.3 bits/symbol/polar with respect to all other formats at 19 dB OSNR.

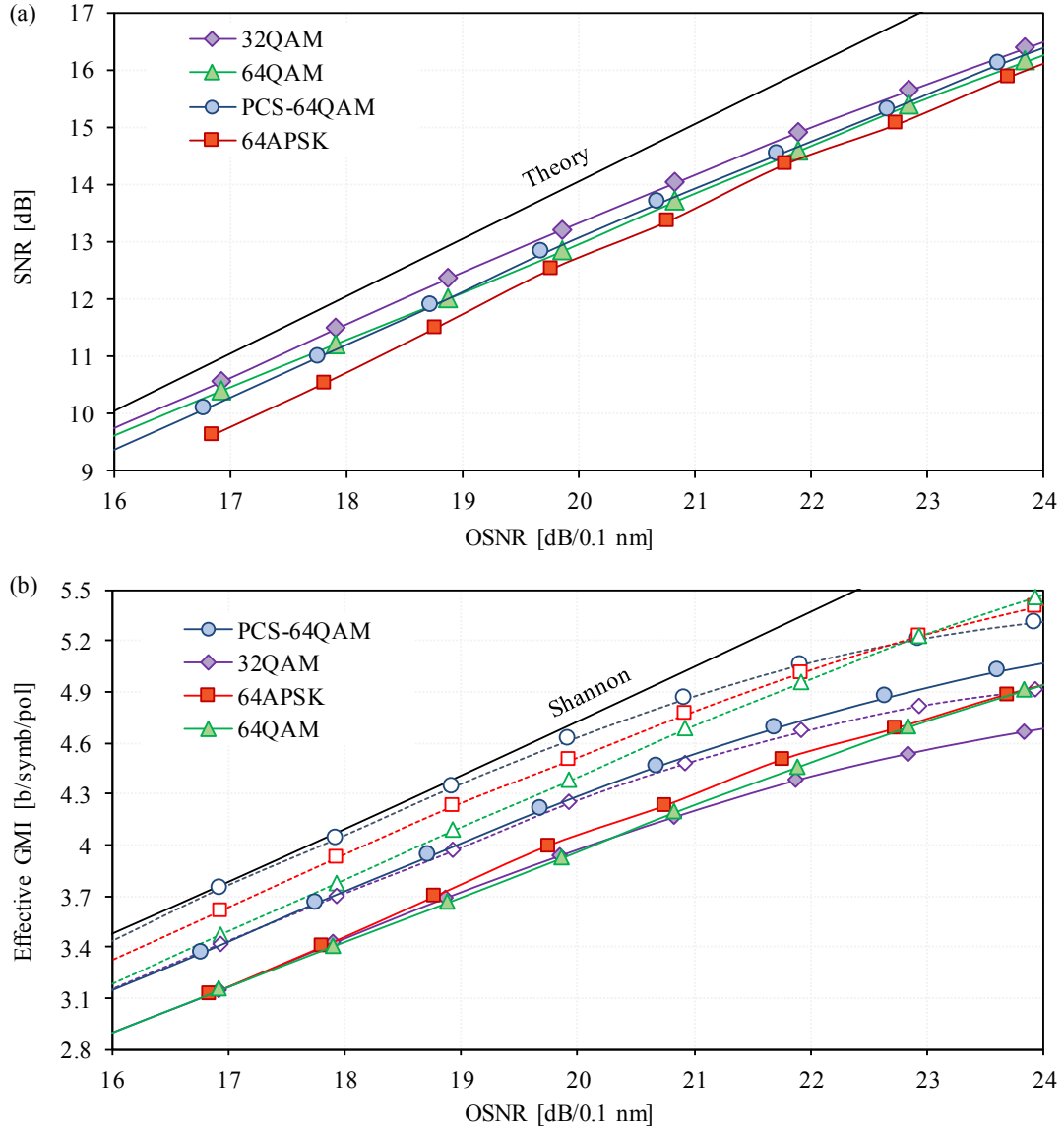


Fig. 3.7: Experimental (a) SNR and (b) effective GMI performance in B2B for 32QAM, 64QAM, PCS-64QAM, and 64APSK.

We now compare the performance of all formats after 6,600 km transmission. The recirculating loop corresponds to the one shown in Fig. 2.10 without any extra polarization element in the link. The transmitter consists of 60 WDM loading channels divided into even and odd rails distributed over the C-band with 50 GHz spacing. Each rail is modulated with a different PM IQ-MOD. Odd and even loading channels are coupled through a WSS and further combined to the measured channel consisting of a single TLS modulated with an independent PM IQ-MOD. The multiplexed signal is then transmitted over 10 recirculating loops of 55 km long spans of Corning Vascade fiber, and EDFA-only amplification, for a total transmitted distance of 6,600 km. The receiver configuration and DSP blocks are the same as the one used for B2B characterization.

Fig. 3.8a shows the experimental performance (markers) comparison in terms of SNR vs the total optical launched power. The theoretical predictions (lines) are also shown, where the performance in the linear regime is obtained by matching the B2B curves presented in Fig. 3.7a and by the characterization of the experimental linear noise of our test-bed.

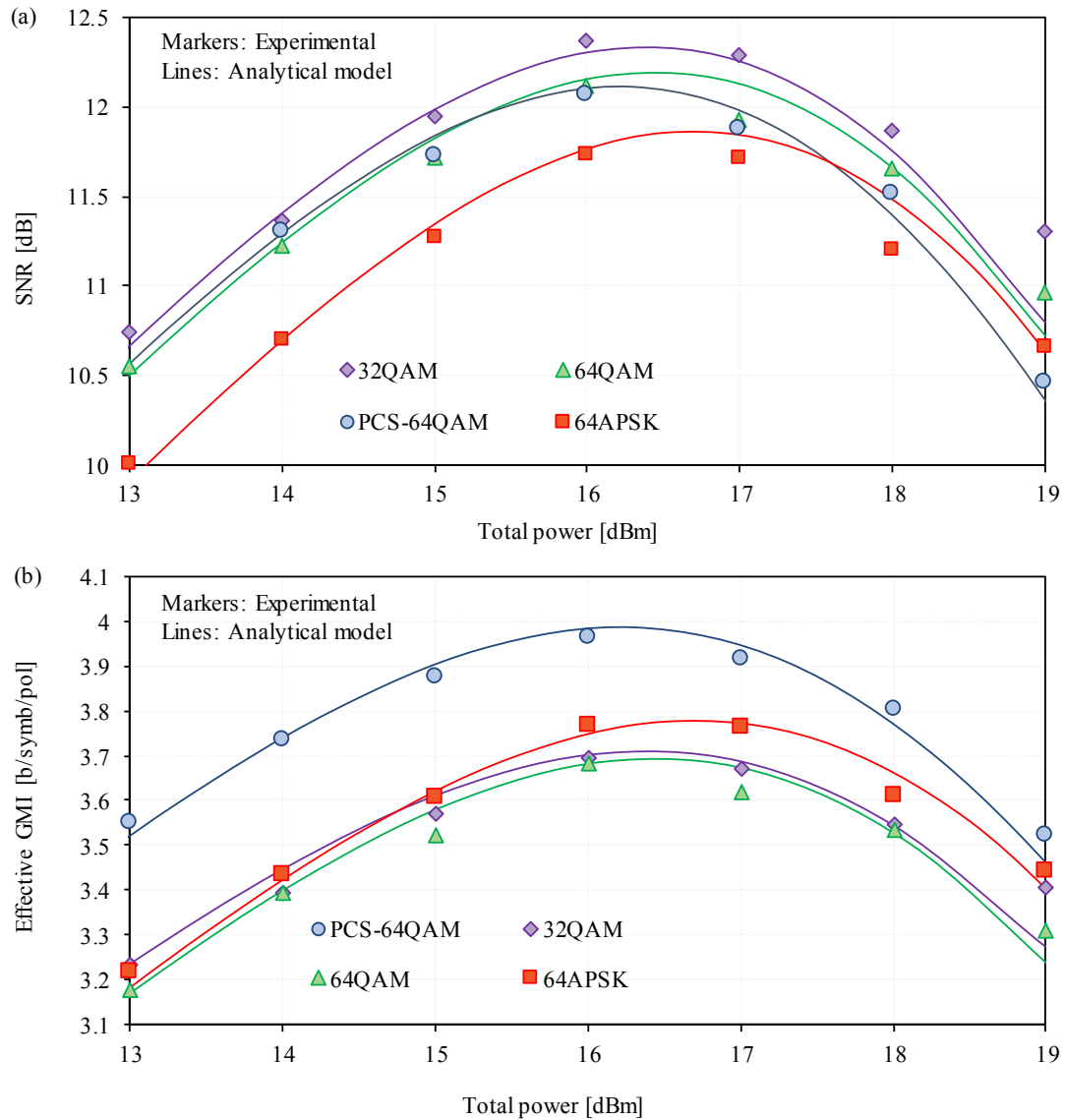


Fig. 3.8: Experimental (a) SNR and (b) effective GMI performance after 6,600 km for all studied modulation formats.

In terms of SNR, PCS-64QAM presents an increased penalty with optical power with respect to 64QAM and 32QAM. This penalty corroborates the higher nonlinear penalty due to the Gaussian-like constellation of PCS-64AM, as in the linear regime PCS-64QAM, 32QAM, and 64QAM formats have comparable performance. Regarding 64APSK, its poor linear SNR is translated into a degradation in the linear regime of Fig. 3.8a, being of ~ 0.6 dB in SNR compared to the other formats at an optical power of 13 dBm.

Fig. 3.8b shows the performance in terms of effective GMI vs total optical launched power. It is observed that 32QAM and 64QAM achieve the same maximum SE of 3.7 bits/symb/pol, showing that the use of 64QAM presents no benefit compared to 32QAM. At the optimum power, PCS-64QAM has a gain of ~ 0.25 bits/symb/pol compared to both 32QAM and 64QAM. The gain provided by 64APSK is only 0.06 bits/symb/pol compared to 32QAM and 64QAM.

From the above results, we can conclude that PCS-64QAM achieves the best performance considering all types of implementation penalties, making it a good candidate for future generation systems.

3.2 TRUNCATED PROBABILISTIC CONSTELLATION SHAPING

Due to the superior performance of PCS-64QAM over other formats, we now extend its use to trans-Pacific distances. As presented in Sec. 1.2.3, the PMF of the PCS-QAM constellation points are set according to a discrete Maxwell- Boltzmann distribution with free parameter ν . This parameter should be optimized to change the source distribution and minimize the gap to the Shannon capacity for a given target SNR. In the last section, the SNR target was around 12 dB corresponding to the SNR after a trans-Atlantic distance of 6,600 km. For trans-Pacific distances ($>10,000$ km) the source entropy of PCS-64QAM has to be re-optimized. In this section, we address the design of a truncated PCS-64QAM constellation (TPCS-64QAM), and its use for trans-Pacific distances.

The design process of PCS-64QAM is performed by means of numerical simulations and is discussed next. First, we generate random symbol sequences of length 2^{15} for different PCS-64QAM source entropies, H . Then, AWGN is added to each sequence to achieve a given SNR, for which we obtain the information rate, R , by two means: first, we consider an ideal FEC, i.e., a capacity achieving infinite block length FEC for which the correct measurement of R corresponds to the calculation of the GMI; and second, we actually apply our offline home-made FEC decoder to the noisy simulated sequences as described in [[51] Sec. VI.1]. Finally, we calculate the gap to capacity; i.e., the difference between the Shannon capacity and R for a given SNR and H .

By construction, PCS-64QAM is compatible only with FEC code rates, r , larger than or equal to $2/3$ [50]. Therefore, we have used a SC-LDPC FEC code family of 25 rates ranging from 0.67 to 0.91 with steps of 0.01. For more information about SC-LDPC codes please refer to [33-35].

As stated previously, the PCS-64QAM employed in [30] and presented in the last section, was optimized for a SNR target of 12 dB for a target distance of 6,600 km, resulting in $H = 5.4$ b/symb/pol. Considering the minimum code rate $r = 2/3$, this PCS-64QAM is not feasible below 3.4 b/symb/pol, corresponding to ~ 10.5 dB SNR including FEC penalty.

For a target distance of 10,285 km (see Sec. 4.1), the optimum operation point lies in the SNR region between 9 dB to 10 dB, such that the PCS-64QAM of [30] cannot be used. Moreover, for practical implementation concerns, SNR margins up to 1 dB accounting for system end-of-life (EOL) conditions must be considered. Therefore, the minimum required SNR supported by the system should be 8 dB. The optimum PCS-64QAM should minimize the gap to capacity over the region of interest, while still considering the minimum required SNR.

Fig. 3.9 shows the minimum supported SNR that can be decoded by FEC with minimum rate $r = 0.67$ versus PCS-64QAM source entropy, for an ideal FEC (GMI), and for our SC-LDPC codes. Considering a minimum required SNR of 8 dB, the maximum source entropy H when the ideal FEC is considered is 4.6 b/symb/pol, which is reduced to 4.6 b/symb/pol when practical SC-LDPC FEC decoding is applied. Therefore, source entropies bigger than 4.6 b/symb/pol are not supported for our system.

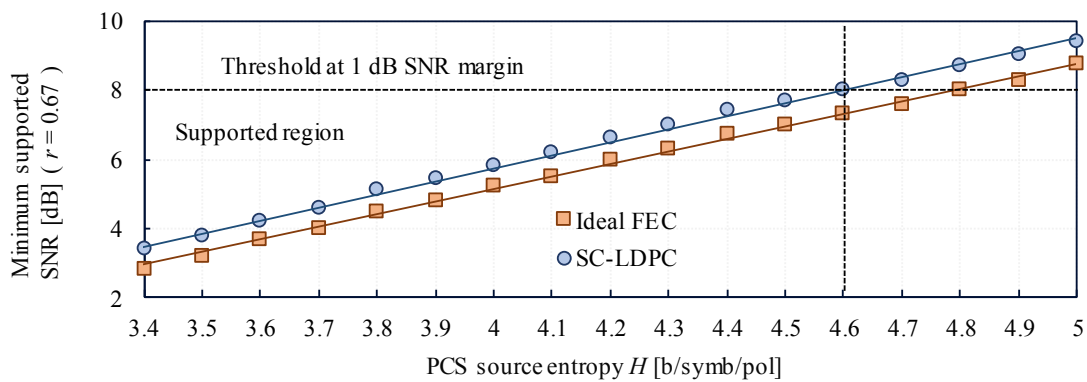


Fig. 3.9: Minimum supported SNR for a FEC rate $r = 0.67$.

Fig. 3.10a shows the gap to capacity considering a SNR of 9 dB. For the ideal FEC (square markers) the H that minimizes the gap to capacity is 4.6 b/symb/pol, however we observe a negligible difference for values between 4.3 to 5 b/symb/pol, all of them having a gap to capacity lower than 0.05 b/symb/pol. A different optimum value of H is obtained when actual SC-LDPC FEC decoding is applied (circle markers), which can be explained as follows. For higher values of H , lower FEC code rates are required to successfully decode the sequences for a SNR of 9 dB (Fig. 3.10b). The lower the code rate, our SC-LDPC codes present a higher gap to the maximum achievable rate (GMI) (cf Fig. 3.11b).

Fig. 3.10c shows the gap to capacity in the SNR range between 7 dB to 11 dB for $H = 4.6$ b/symb/pol and $H = 4.3$ b/symb/pol, for an ideal FEC and that of our SC-LDPC respectively. As found before, when an ideal FEC is considered, the optimum H is 4.6 b/symb/pol. For practical SC-LDPC codes, the optimum PCS-64QAM mode is $H = 4.3$ b/symb/pol, which minimizes the gap to capacity over the SNR region of interest, and support SNR values down to 7 dB for successfully FEC decoding.

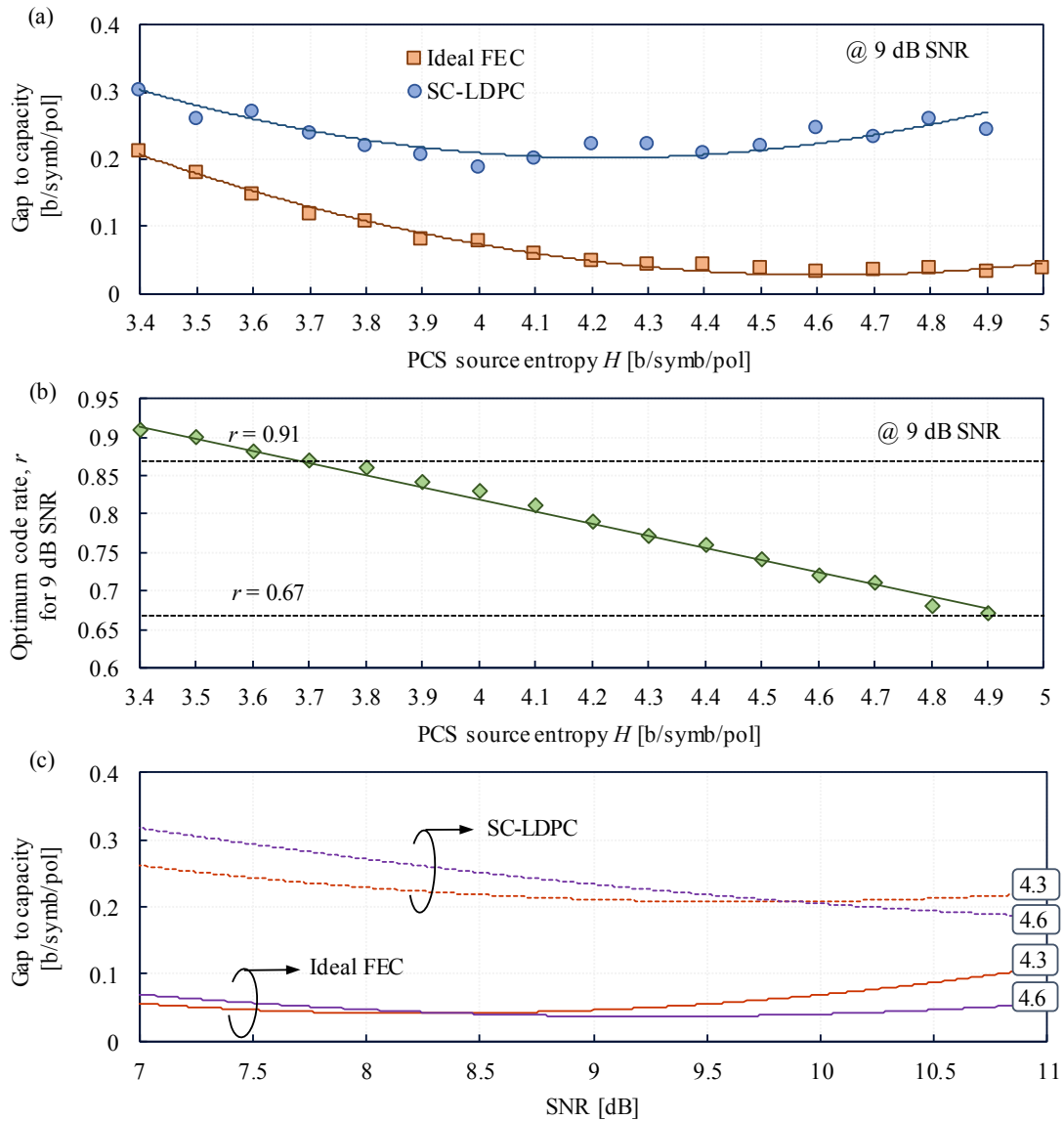


Fig. 3.10: (a) gap to Shannon capacity at SNR = 9 dB, (b) optimum r for successfully FEC decoding at SNR = 9 dB as a function of PCS source entropy, H . (c) Gap to capacity for $H = 4.3$ b/symb/pol and $H = 4.6$ b/symb/pol as a function of SNR.

For the optimized PCS-64QAM, we found that the PMF of the outer-most symbols is almost null (0.0018). Therefore, we forced the PMF of the outermost points to zero, and reoptimized the PMF such that the resulting source entropy is closer to $H = 4.3$ b/symb/Hz. The resulting process can be seen as a PCS-64QAM where the PMF has been obtained by means of a truncated Maxwell-Boltzmann distribution. We opt to call this format truncated PCS-64QAM (TPCS-64QAM), which constellation and PMF are shown in Fig. 3.11a. The exact source entropy is found to be 4.33 b/symb/pol.

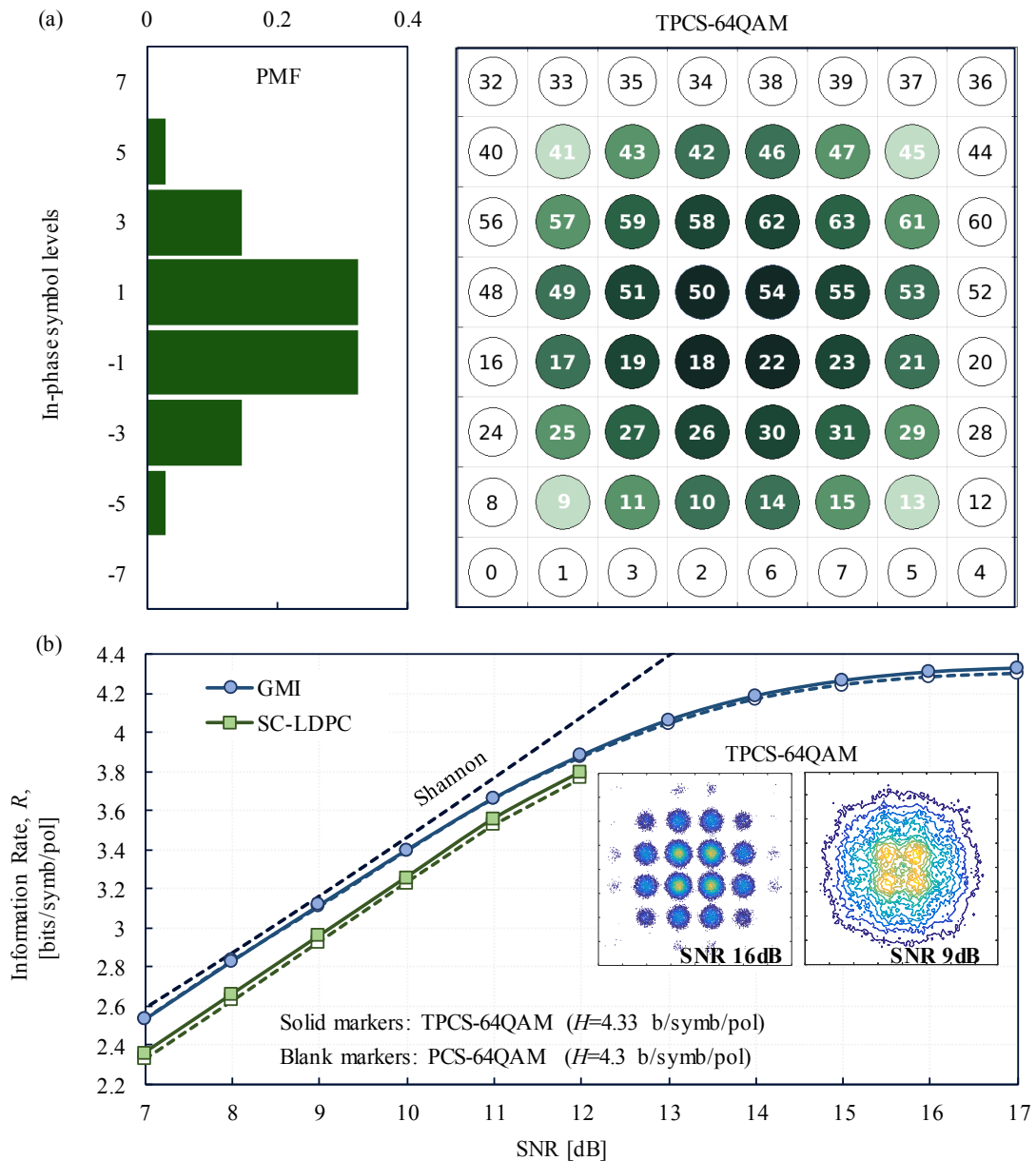


Fig. 3.11: (a) Left, probability mass function (PMF) of the in-phase symbols for the TPCS-64QAM. Right, TPCS-64QAM constellation, along with its Gray mapping. (b) Information rate, R , for the designed TPCS-64QAM and PCS-64QAM.

Fig. 3.11b illustrates R as a function of SNR for the optimized PCS-64QAM (blank markers), and TPCS-64QAM (filled markers). TPCS-64QAM does not lead to any meaningful difference compared to PCS-64QAM. At 9 dB SNR, our SC-LDPC codes present a penalty of <0.2 b/symb/pol compared to the GMI. The slight apparent improvement of TPCS-64QAM with respect to PCS-64QAM when SC-LDPC codes are applied might be to some numerical difference in signal power normalization. However, this discrepancy is less than 0.1 dB in SNR and can be neglected within the frame of this work.

Finally, Fig. 3.12 compares the GMI for the designed TPCS-64QAM with the PCS-64QAM used in [30], as well as for some standard formats, 64QAM, 32QAM and 16QAM. In the interval

from 7 dB to 10.5 dB SNR, the proposed TPCS-64QAM outperforms all other formats, having a SNR penalty below 0.2 dB with respect to the Shannon limit.

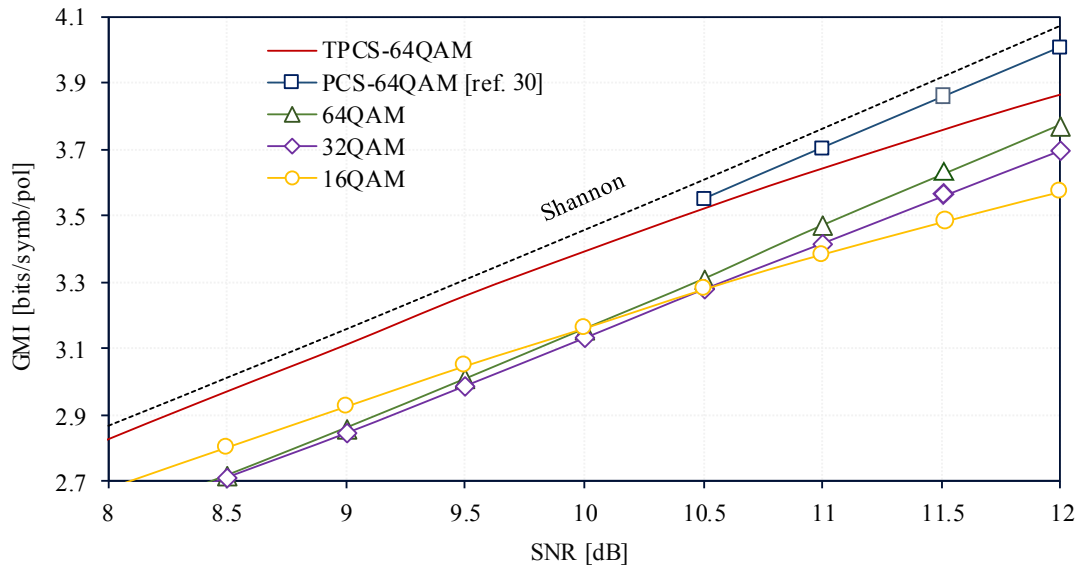


Fig. 3.12: GMI for various modulation formats.

3.3 SUMMARY

In the first part of this chapter, we theoretically and experimentally compared the performance of PCS-64QAM, 64APSK, 64QAM, and 32QAM, considering linear implementation penalties and nonlinear penalties after 6,600 km. We showed that while 32QAM and 64QAM formats are simple to generate and receive, this last one suffers from more implementation penalties, and achieves the same SE as 32QAM despite its theoretical superior performance. We also showed that both PCS-64QAM and 64APSK present new DSP challenges, and require pilot-assisted polarization demultiplexing. Regarding 64APSK, it was experimentally shown that it requires a higher pilots-aided DSP rate, and its performance degrades rapidly at low values of SNRs, making its implementation challenging. Taking into account linear, nonlinear, and DSP impairments, PCS-64QAM outperforms 32QAM, 64QAM and 64APSK for coherent transoceanic system applications.

In the second part, we showed the design of a truncated version of PCS-64QAM (TPCS-6AQAM) optimized to maximize the SE of trans-Pacific optical links. The TPCS64QAM minimizes the gap to capacity over the SNR region of 7-11.5 dB, while considering FEC implementation penalties corresponding to our SC-LDPC codes.

4 TRANSOCEANIC TRANSMISSION RECORDS

In this chapter, we show how the use of PCS-64QAM, novel DSP techniques as NLC, and multi-rate FECs, cutting-edge CMOS technology available for DACs, and advanced wideband receivers can be used to increase the throughput and channel bit-rate of submarine systems.

In the first section we employ TPCS-64QAM to demonstrate 25.4 Tb/s after 10,285 km. The gain provided by TPCS-64QAM over regular 64QAM is investigated over trans-Atlantic and trans-Pacific distances. Moreover, the potential benefits of NLC to increase the net system throughput is addressed. In the second section, we use TPCS-64QAM and PCS-64QAM together with NLC, and advanced wideband transmitters and receivers to demonstrate the following new per-channel bit-rate records: single-carrier 550 Gb/s after 6,600 km, 430 Gb/s single-carrier after 13,200 km, and 850Gb/s dual-carrier after 3,960 km. Finally, we present a trans-Atlantic transmission record using C + L band EDFA-only amplification leveraging 65 Tb/s thanks to the use of PCS-64QAM, NLC, and multi-rate FECs.

4.1 25.4 TB/S OVER TRANS-PACIFIC DISTANCES USING TPCS-64QAM

In Sec. 3.2, the TPCS-64QAM was optimized to approach capacity in the SNR region corresponding to trans-Pacific distances. In this section, we experimentally analyze its achievable benefits in terms of system throughput. To better compare the prospect TPCS-64QAM achievable gains for already deployed systems, we employ a straight-line testbed composed of coherent submarine fiber (CSF) and C-band EDFA-only amplification, which corresponds to a typical configuration of long-haul commercial submarine systems. We opt to

operate at 49 GBd with 50 GHz channel spacing to reflect the industry trend towards increasing the channel symbol-rate.

Fig. 4.1a illustrates the experimental set-up. The test channel consists of a single TLS which is modulated with a dedicated PM I/Q-mod. It is surrounded by 83 loading channels modulated by a second distinct modulator. Each modulator is driven by a dedicated DAC operating at 90 Gsamples/s, and loaded with a different randomly generated sequence of length 35680. Nyquist pulse shaping based on root-raised cosine with 0.01 roll-off is used to generate 49 GBd signals. The resulting WDM comb is amplified and a noise source is added to emulate the OSNR at the EOL conditions. The transmission line consists of a straight-line of 188 spans of $110 \mu\text{m}^2$ effective area CSF with 54.4 km average span length. Eight equalization spans using shape equalizers are used to flatten the gain shape, followed by EDFAs. In total, 197 C-band EDFAs with 34 nm bandwidth and 16.6 dBm average output power are used, for a total transmission distance of 10,285 km.

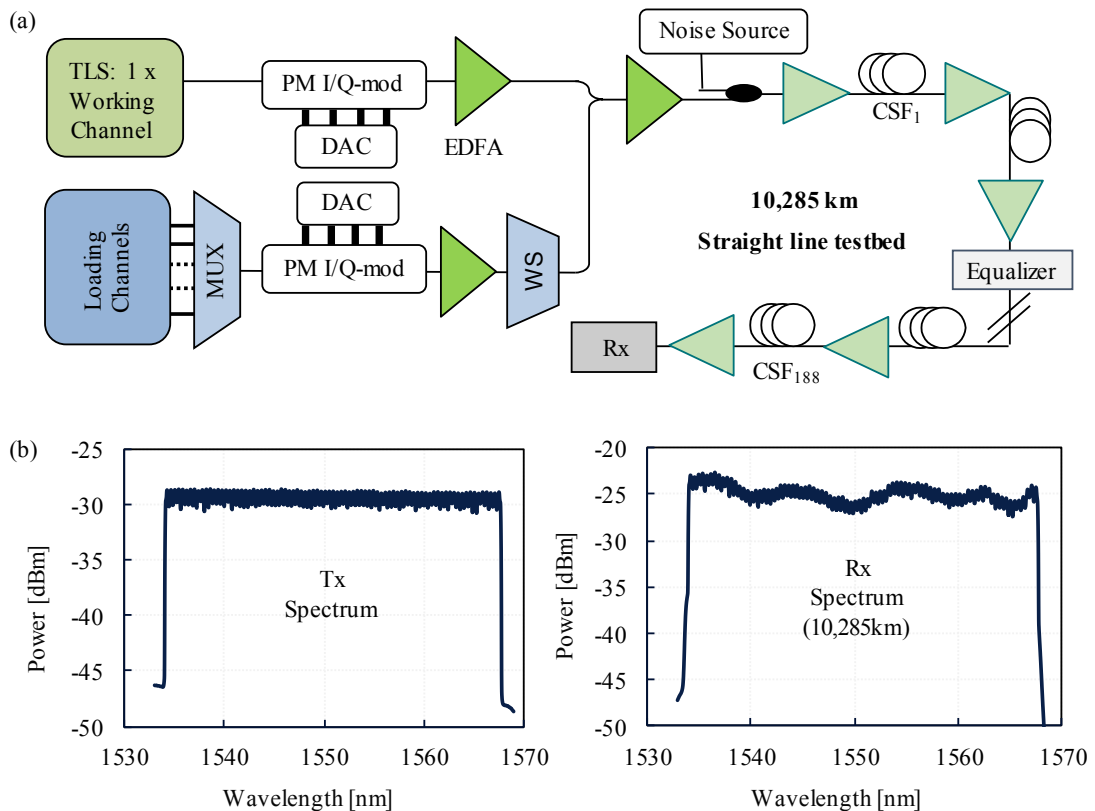


Fig. 4.1: (a) Experimental set-up, (b) optical spectrum at the transmitter and after 10,285km. DAC: digital-to-analog convertor, IQ-mod: IQ-modulator, TLS: tunable laser source, WS: wave shaper, CSF: coherent submarine fiber.

At the receiver side, the signal is sampled by an 80 Gsamples/s real-time sampling scope with 33 GHz analog bandwidth. The sampled signals are recorded and processed offline. Conventional digital coherent receiver signal processing is performed. The DSP blocks consists of CD compensation, carrier frequency and phase estimation, 1% pilot aided cycle slips

removal, and least-mean square adaptive post equalization. To process the PCS signals, a pre-convergence CMA followed by 1% pilot aided MMA are used for polarization demultiplexing as shown in Sec. 3.1. After DSP processing, the SNR and GMI (corrected for pilot overheads) are computed for each waveform. Then SC-LDPC FEC decoding is carried out.

We start by characterizing the system performance versus channel launched power in terms of both SNR and GMI at 6,209 km and 10,285 km. We consider 64QAM, PCS-64QAM of [30] and our customized TPCS-64QAM. Pre-emphasis is performed by varying the power of 8 channels situated in the middle of the band, and measuring SNR and GMI for the center channel (1550.92nm). Fig. 4.2a shows the pre-emphasis curves at 6,209 km for 64QAM and PCS-64QAM of [30], while Fig. 4.2b corresponds to 10,285 km for 64QAM and our designed TPCS-64QAM.

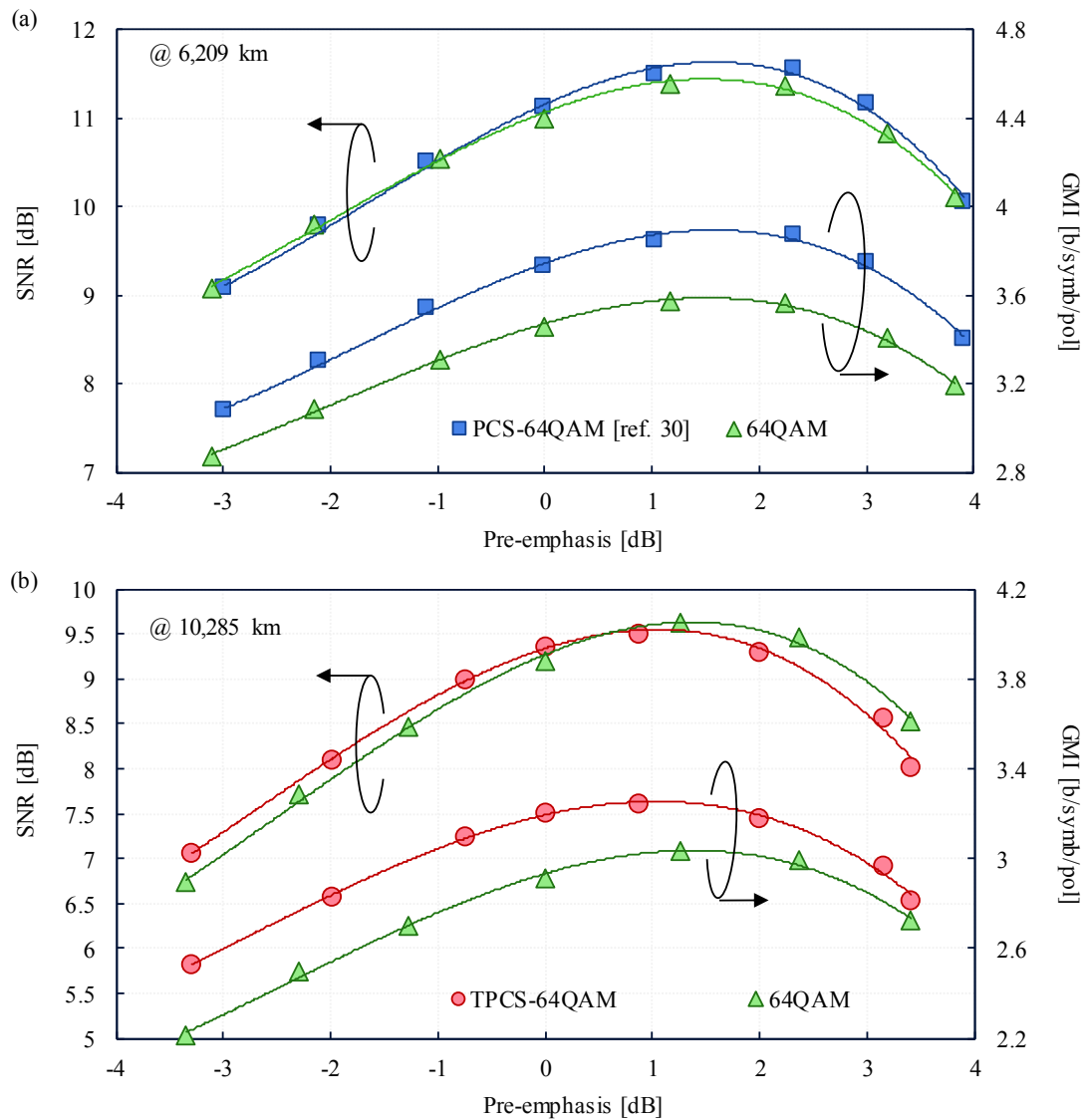


Fig. 4.2: SNR and GMI versus channel pre-emphasis for 64QAM, PCS-64QAM of [30] and TPCS-64QAM, at (a) 6,209 km and (b) 10,285 km.

Fig. 4.2 shows that the operating point of our system is 1 dB below the NLT. However, increasing the EDFAs output power above 16.6 dBm is not possible due to their limited output power range. As will be seen, this will limit the achievable gain provided by NLC algorithms. At 6,209 km, PCS-64QAM of [30] outperforms 64QAM in terms of GMI by 0.25 b/symb/pol, which is in agreement with Fig. 3.12. In terms of SNR, both formats achieve the same performance. At 10,285 km, our optimized TPCS-64QAM outperforms 64QAM by 0.25 b/symb/pol. Please note again that this gain is decreased in the nonlinear regime, as the contribution of the fourth and sixth moments of the more Gaussian like TPCS-64QAM to nonlinear variance is higher than that of 64QAM.

Considering a pre-emphasis of 0 dB, we then investigate the performance over different distances ranging from 1,500 km to 10,285 km. Fig. 4.3a shows the measured SNR and GMI versus distance for the three modulation formats. Each point is the result of averaging the SNR and GMI over 5 different wavelength channels distributed across the C band.

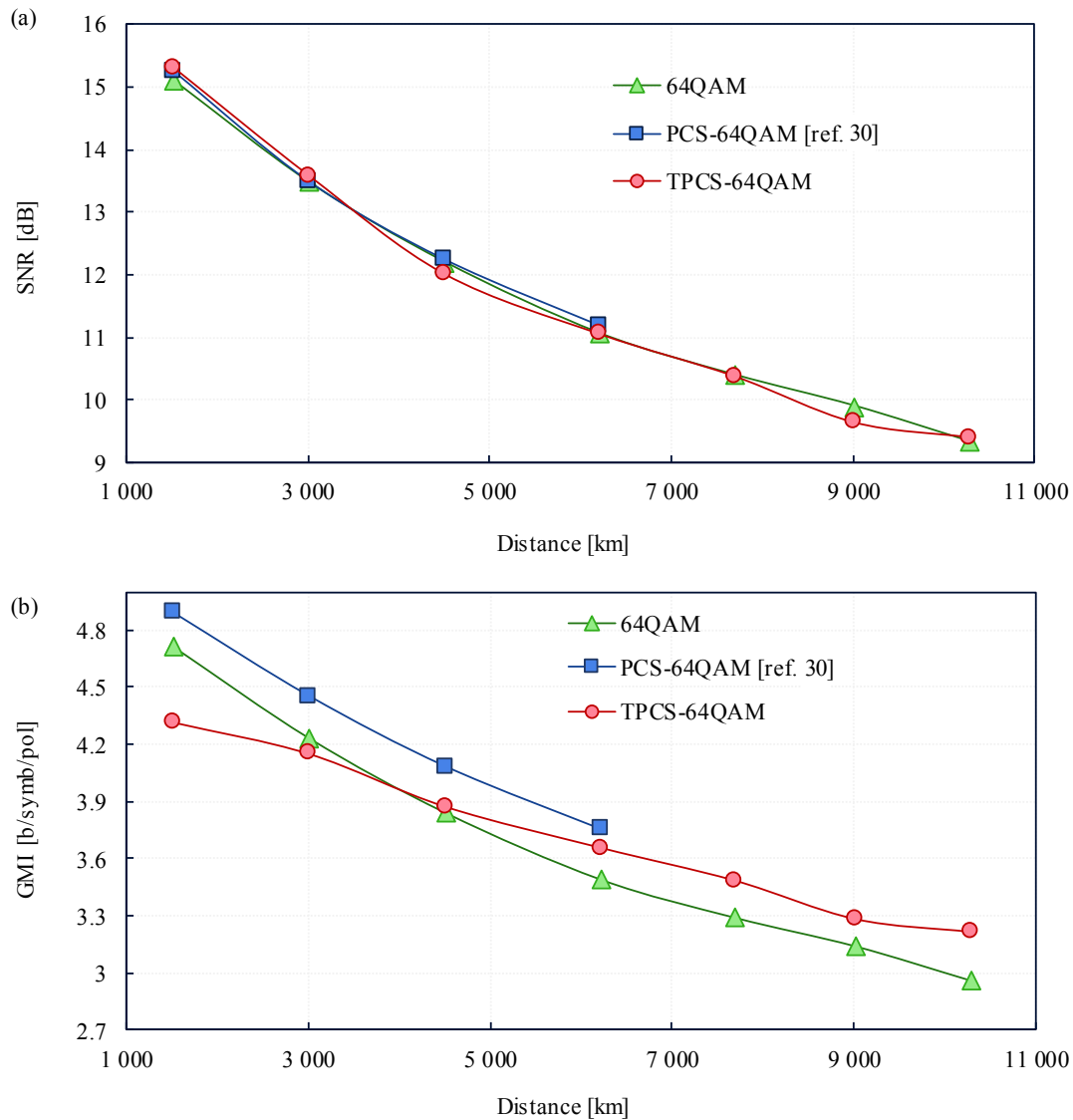


Fig. 4.3: (a) SNR and (b) GMI versus distance for 64QAM, PCS-64QAM and TPCS-64QAM.

In terms of SNR, all three formats achieve similar results. In terms of GMI, PCS-64QAM outperformed 64QAM and TPCS-64QAM up to a distance of 6,200 km (11 dB to 16 dB SNR region). After this distance, the GMI for PCS-64QAM decreased below 3.4 b/symb/pol which is its limit of operation considering a minimum allowed FEC rate of 2/3. For trans-Pacific distances (>10,000km), TPCS-64QAM outperforms 64QAM with a mean GMI of 3.2 b/symb/pol.

Next, we fix the distance at 10,285 km and perform transmission of all 84 channels. Fig. 4.4a shows the measured SNR ranging from 8.9 dB to 9.9 dB.

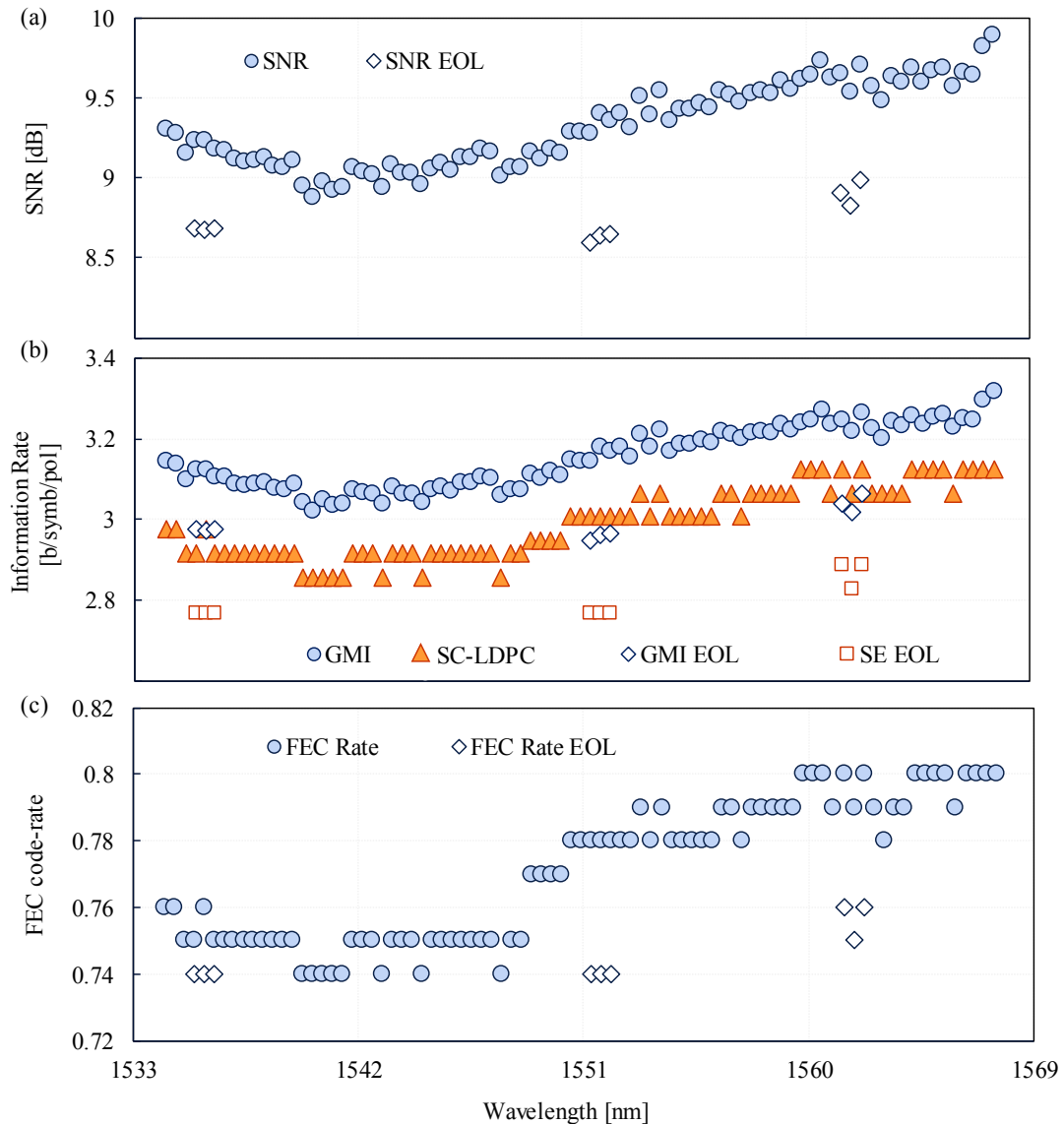


Fig. 4.4: Performance of the 84 TPCS-64QAM channels, (a) SNR, (b) GMI and SE, (c) necessary FEC code rate to achieve error free decoding.

The average value is found to be 9.3 dB. In the same manner, Fig. 4.4b shows R in terms of GMI and after our SC-LDPC FEC decoding, both corrected for 1% pilot use. The average R after FEC is 3 b/symb/pol, leading to 5.9 b/s/Hz spectral efficiency and 24.62 Tb/s total

throughput. Fig. 4.4c shows the 7 different FEC code rates used to decode each channel. We also investigate the achievable system throughput considering EOL conditions. To do so, we degrade the received OSNR by 1dB by adding ASE noise at the transmitter side as shown in Fig. 4.1a. The results are shown in Fig. 4.4 in blank markers. The SNR is degraded 0.6 dB in average, which corresponds to 6.7% decrease on system throughput which reached 23.1 Tb/s. Please note that the measured OSNR does not account for fiber Kerr nonlinear distortions, such that the relation between OSNR and SNR is nonlinear. A degradation of the system OSNR will lead to a lower degradation in SNR near the NLT.

Finally, we study the achievable gains provided by NLC based on FDBP. In this section, we consider only DBP/FDBP applied at the receiver side by replacing the CD compensation block. Fig. 4.5a shows the TPCS-64QAM pre-emphasis curve of Fig. 4.2b but with and without high resolution DBP ($N_{steps} = 20$).

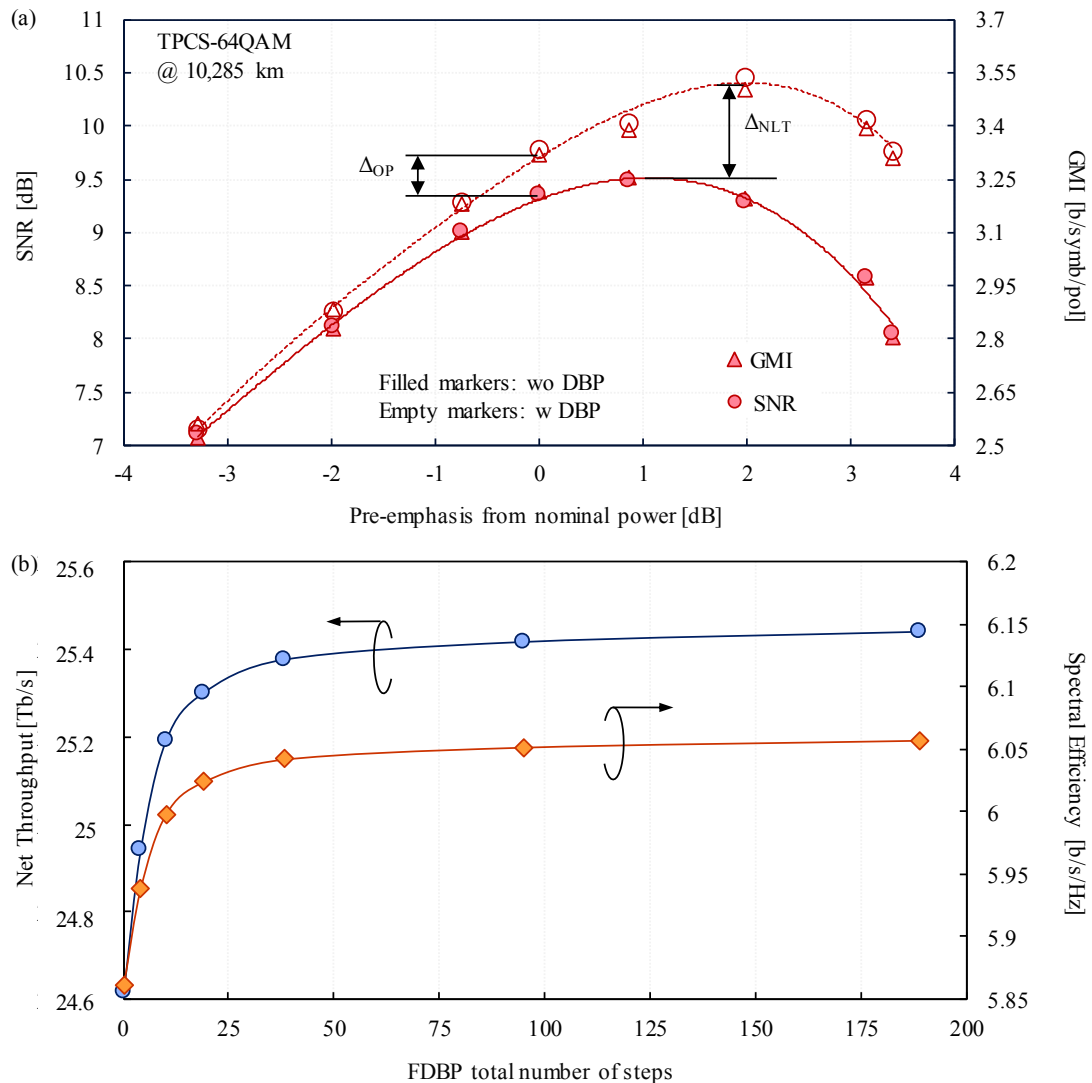


Fig. 4.5: (a) TPCS-64QAM pre-emphasis curve with and without DBP, (b) net throughput and total spectral efficiency versus number of FDBP steps.

As already mentioned, the power operating point of our transmission line is 1 dB below the optimum when no DBP is applied, and 2 dB below the optimum point when DBP is applied. This imposes a strong limitation on the achievable gain provided by DBP. At the operating point (0 dB pre-emphasis) the achievable gain is limited to $\Delta\text{SNR}_{\text{0dB}} = 0.4$ dB ($\Delta\text{GMI}_{\text{0dB}} = 0.11$ b/symb/pol), while the peak-to-peak gain is $\Delta\text{SNR}_{\text{0dB}} = 1$ dB ($\Delta\text{GMI}_{\text{0dB}} = 0.3$ b/symb/pol). Please note that the already mentioned achievable gains are slightly over-estimated, as the pre-emphasis curves are obtained by varying the power of only 8 channels within the WDM comb.

In order to study the achievable NLC gain of the entire system versus the low-complexity FDBP algorithm, we now process all 84 channels with different number of FDBP steps. The nominal channel optical power is -2.64 dBm (84 channels with 16.6 dBm total EDFA output power); however, to account for the non-flat WDM power profile and power uncertainties, we optimize the channel power within the FDBP algorithm. Fig. 4.5b shows the total throughput and the spectral efficiency versus the total FDBP steps. The maximum increase in system throughput is found to be 830 Gb/s for a total of 25.48 Tb/s, corresponding to a spectral efficiency of 6.06 b/s/Hz.

Finally, we compare the obtained results with already installed commercial systems based on 8QAM tributaries. We transmit 84 real time 8QAM channels at 150 Gb/s using industrial tributaries with a channel spacing of 50 GHz over the 10,285 km deployed testbed. All channels were decoded error free with 0.5 dB margin above our 25% SD-FEC Q^2 -factor threshold (5.4 dB). The achieved net throughput was 12.6 Tb/s corresponding to 3 b/s/Hz spectral efficiency. Compared to commercial 8QAM tributaries, the solution based on 49 GBd channels employing TPCS-64QAM and multi-rate FEC have the potential of doubling the throughput of existing trans-Pacific networks [136].

4.2 HIGH SYMBOL-RATE TRANSOCEANIC TRANSMISSION

There is a clear trend in the industry to increase the per-channel bit rate of PM-WDM coherent transmission systems. The main drive for this trend is coping with the ever-increasing throughput requirements while curbing the cost per bit via reducing the component count. Thanks to the coherent receiver technology, the feasible bit rate per wavelength of single-carrier (SC) transceivers over transoceanic distances has dramatically increased from 40 Gb/s (0.8 b/s/Hz) in 2008 to 400 Gb/s (6 b/s/Hz) in 2014 [23, 137-139]. As the bandwidth of the state-of-the-art RX technology usually takes a lead on the TX technology, dual-carrier (DC) TX design detected by a single wideband receiver may be employed to reduce the component count at the RX side. DC 400 Gb/s transmission over 9,200 km was demonstrated in [27].

In this section, we employ the capacity achieving PCS-QAM and digital NLC based on DBP, together with the cutting-edge CMOS technology available for DAC, and an advanced 70 GHz

wideband receiver, to demonstrate new per-channel transmission records over transoceanic distances beyond 400 Gb/s using high symbol-rate channels above 60 GBd.

4.2.1 Single-carrier Experiments

Our first goal is to increase the per-channel bit rate using a SC configuration. To do so, we first need to optimize the PCS-64QAM source entropy according to the SNR region of interest. We target a trans-Atlantic distance of 6,600 km for which the SNR region is ~ 12 dB, and a trans-Pacific distance of 13,200 km with a target SNR of ~ 9 dB.

In Sec. 3.2, we designed the TPCS-64QAM with source entropy of 4.3 b/symb/pol for a target SNR of 9 dB, including FEC implementation penalties. However, the PCS-64QAM designed in [30] and used in the last sections targeting a SNR of 12 dB was optimized to reduce the gap to capacity in terms of GMI, and FEC penalties were not taken into consideration. Therefore, we reoptimized PCS-64QAM targeting a SNR region of ~ 11 -13 dB as done for TPCS-64QAM. The resulting optimum PCS-64QAM source entropy is found to be $H = 4.9$ b/symb/pol.

Fig. 4.6 illustrates the information rate, R , in terms of the GMI (solid lines), and after applying SC-LDPC FEC codes (dashed lines), of the two custom shaped constellations optimized for trans-Atlantic and trans-Pacific distances.

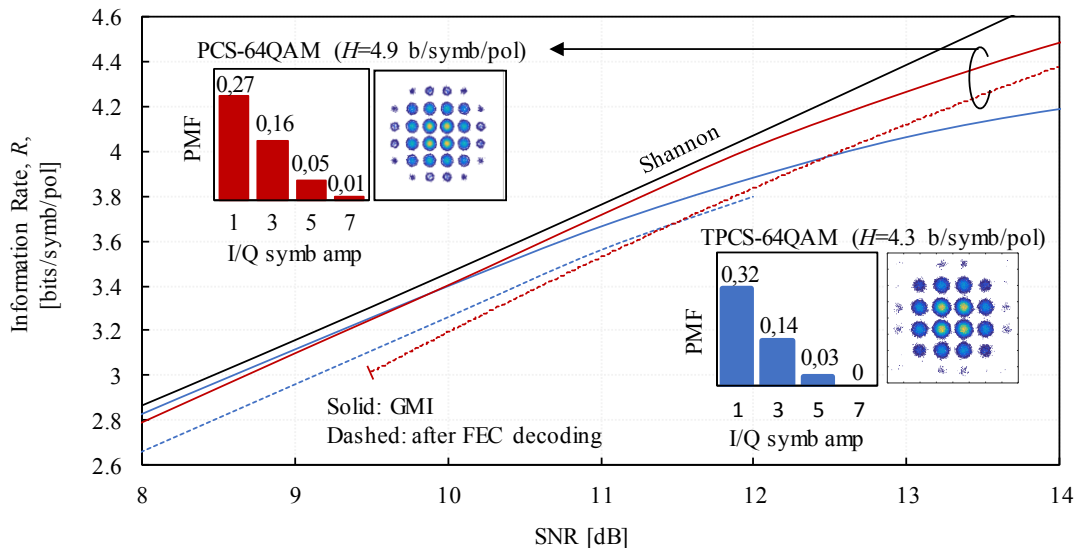


Fig. 4.6: Information rate, R , of the two custom shaped constellations.

The minimum supported SNR considering FEC implementation penalties for the PCS-64QAM with $H = 4.9$ b/symb/pol is 9.5 dB and minimizes the gap to capacity in the SNR region between 11.5 dB and 13.5 dB.

Once the source entropy of the PCS-64QAM formats have been set, we now optimize the symbol-rate. We fix the format to PCS-64QAM with source entropy of 4.9 b/symb/pol, and fix the OSNR to 19 dB which corresponds to the end-of-link OSNR of our transmission line after 6,600 km. We then sweep the channel symbol-rate and calculate the achievable net bit rate. Fig. 4.7 shows the results.

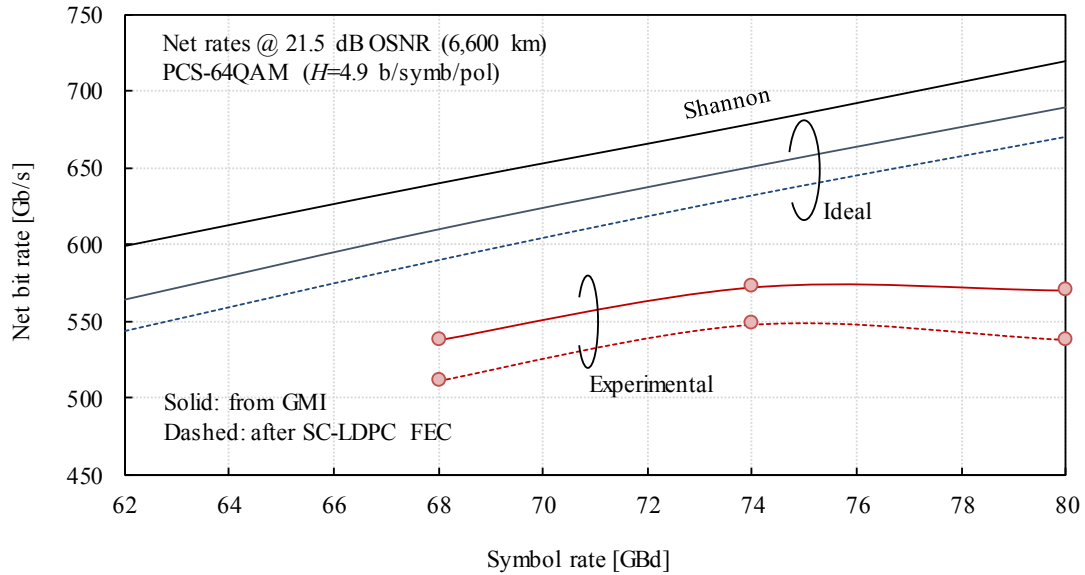


Fig. 4.7: Symbol-rate optimization for single-carrier 6,600 km transmission.

We observed that for our 88 Gsamples/s DAC, the SC symbol-rate that maximizes the net bit rate is 74 GBd. While the ideal bit rate linearly increases with symbol-rate, practical implementation penalties coming from TX impairments also increase with symbol-rate such that the performance is degraded beyond 74 GBd.

Having optimized the modulation formats and symbol-rate, we proceed to perform transmission measurements. The WDM signal is composed of three rails: one test group consisting of a single TLS, one loading group consisting of 7 TLS, and a final group consisting of 8 DFB. Using a reconfigurable WSS, the test group is inserted inside the TLS loading group, which is at the same time placed amid the DFB loading group, as shown in Fig. 4.8a. Each group is modulated by a dedicated DAC programmed with a different random sequence. We use RRC pulse shapes with roll-off 0.01. The single-wavelength TLS test channel and the 7-wavelength TLS loading group are modulated with 74 GBd signals spaced at 75 GHz, while the 8-wavelength DFB loading channels surrounding the TLS sources are modulated by 49 GBd signals at 50 GHz. The total WDM transmission bandwidth is 1 THz. Fig. 4.8b illustrates the WDM spectrum of the transmitted signal used in SC measurements.

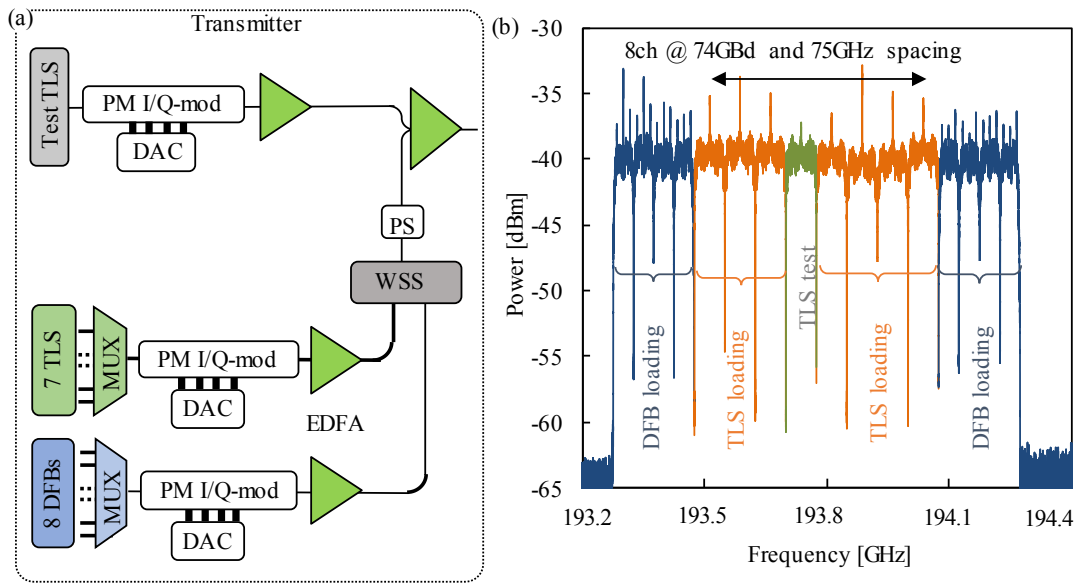


Fig. 4.8: (a) Transmitter set-up for single-carrier configuration, and (b) single-carrier transmitted spectrum.

The transmission testbed used in this work is the same as in Fig. 2.10 without any extra polarization element in the link. It consists of a recirculation loop composed of 12 spans of 55 km Corning Vascade EX3000 spans. At the output of the recirculation loop, the signal is input to a polarization-diverse coherent receiver, and is sampled and recorded by a 70 GHz scope operating at 200 GSamples/s.

The test channel is swept across the loading TLS wavelengths, leading to 8 measured wavelengths channels. Each channel is measured 5 times. The DSP chain consists of either CD compensation or single-channel DBP, followed by pilot-assisted MMA polarization demultiplexing, carrier frequency and phase recovery and least-mean square symbol-spaced blind equalization. As previously, we use 1% pilots for polarization demultiplexing and for cycle-slip removal. Finally, the received symbols are processed by our family of SC-LDPC codes, and the maximum code rate resulting in error free transmission is determined for each channel.

Fig. 4.9a shows the five SNR values per channel acquisition (circles), the average information rate (squares) based on the GMI, and the one achieved after FEC decoding (diamonds) for SC transmission over 6,600 km. The total optical power is set to 13 dBm which was found to be the optimum power in the presence of DBP. Contrary to the previous sections where we used low-complexity NLC, here we employ high-resolution DBP with 20 steps per span in order to achieve the maximum rate after transmission. It is observed that all channels transport more than 560 Gb/s net bit rate. Fig. 4.9b illustrates similar results while transmitting over 13,200 km. In this case all channels transport more than 430 Gb/s net bit rate.

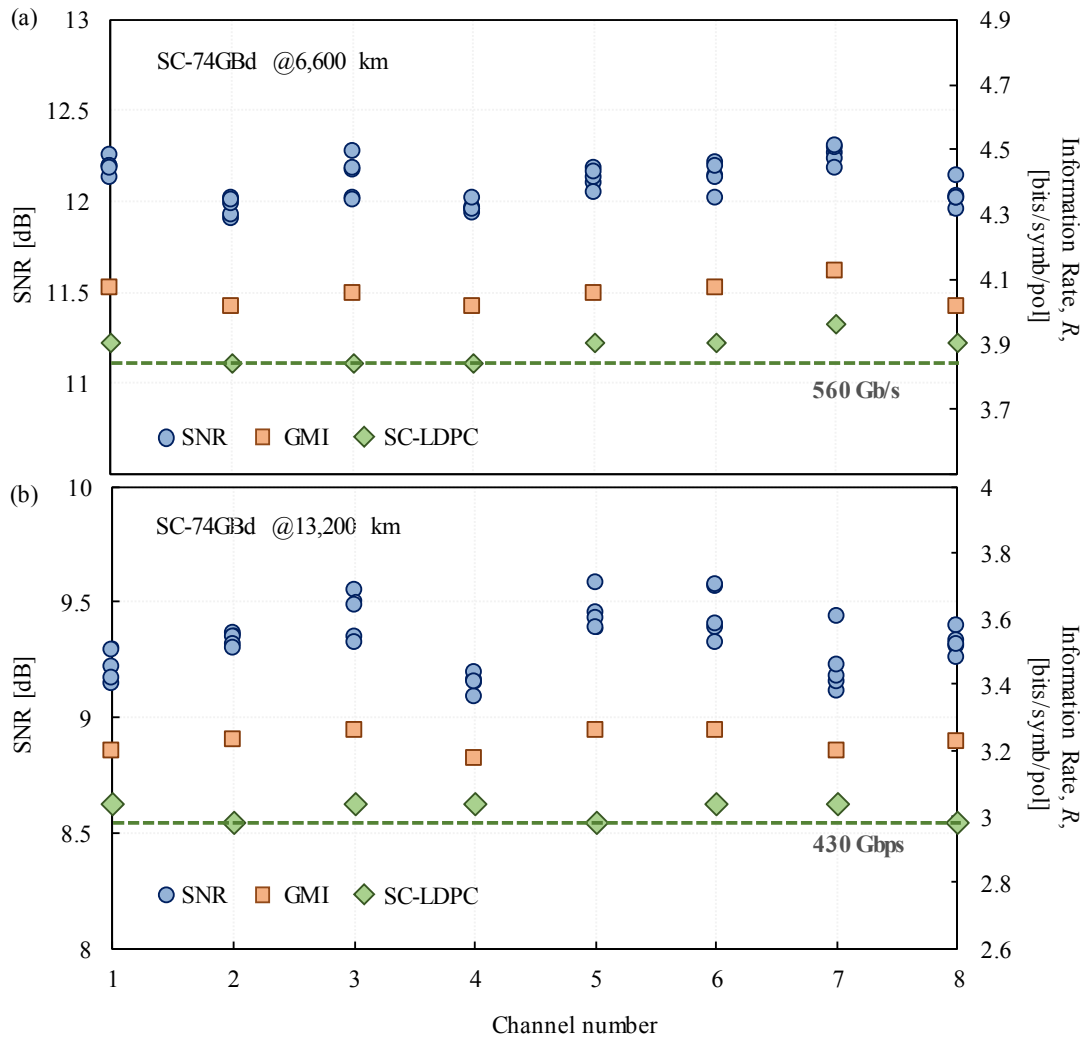


Fig. 4.9: (a) single-carrier results with DBP over (a) 6,600 km with DBP, and (b) 13,200 km.

4.2.2 Dual-carrier Experiments

As increasing the SC symbol-rate beyond 74 GBd degrades the overall system performance due to TX impairments, we now switch to a DC TX architecture to completely fill out the RX bandwidth. We design a DC test super-channel consisting of two 68 GBd PCS-64QAM subcarriers at 69.4 spacing. Fig. 4.10 illustrates the measured signal spectra at the TX output, as well as the amplitude and the phase response of our wideband RX. For the reference, the SC is also shown.

It is observed that the amplitude and phase response of the scope present oscillations after a 30 GHz bandwidth, which will be translated into some degradation in performance for the DC configuration.

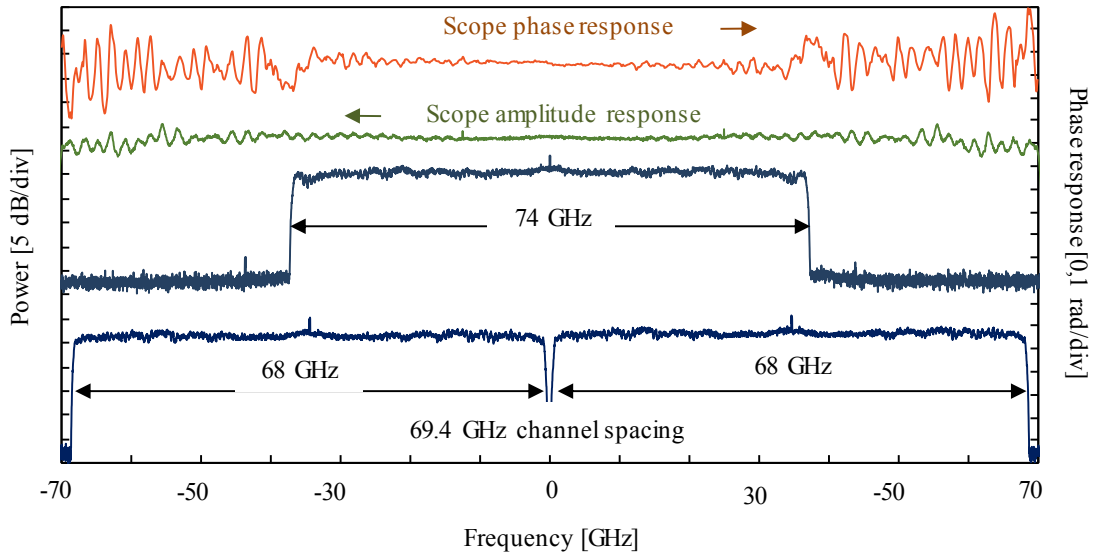


Fig. 4.10: Single-carrier 74 GBd and dual carrier 68 GBd measured signal spectra at TX output, and scope amplitude and phase responses.

To better compare the performance in B2B configuration of the SC and DC configurations, Fig. 4.11 shows the B2B curves considering 100% and 1% pilot aided DSP, both using the PCS-64QAM optimized for 6,600 km, ($H = 4.9$ b/symb/pol). For a SNR target of 12 dB, the B2B OSNR penalty for the SC configuration at 74 GBd is ~ 2.2 dB, which is increased to ~ 4.1 dB for the DC configuration at 68 GBd.

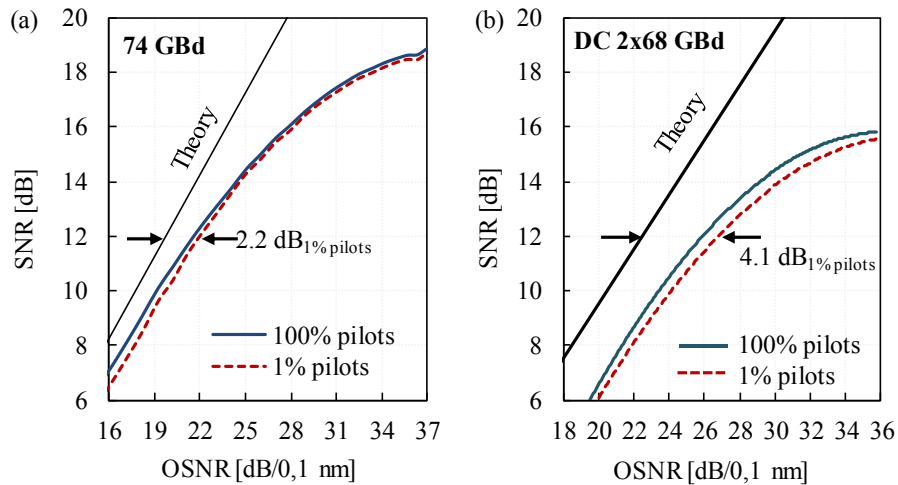


Fig. 4.11: B2B curves for (a) single-carrier, and (b) dual-carrier configurations.

For transmission experiments, the DC super-channel is surrounded by two 68 GBd TLS loading channels on each side, while the rest of the transmission bandwidth is filled with 49 GBd DFB loading channels at 50 GHz spacing. The total transmission bandwidth is 1 THz, as in the single-carrier experiments.

Taking advantage of the large RX bandwidth allowing us to simultaneously recover the two 68 GBd subcarriers for joint DSP processing, we employ DBP to jointly compensate for inter-subcarrier, and intra-subcarrier nonlinearities. The optimum total launched power with joint DBP is found to be 13 dBm. We measure only the central super channel at various distances. Fig. 4.12 illustrates the achievable net bit rate of the DC super-channel vs. distance with joint DBP (diamonds), and without NLC (squares). The number of DBP steps per span was set to 20 as in the SC measurements.

It is observed that the use of joint DBP, allows reaching net 850 Gb/s at 6,600 km, and 1 Tb/s transmission over 3,960 km, corresponding to the highest reported transmission using terabit-class super-channels. The joint DBP results in a transmission reach increase of ~20%.

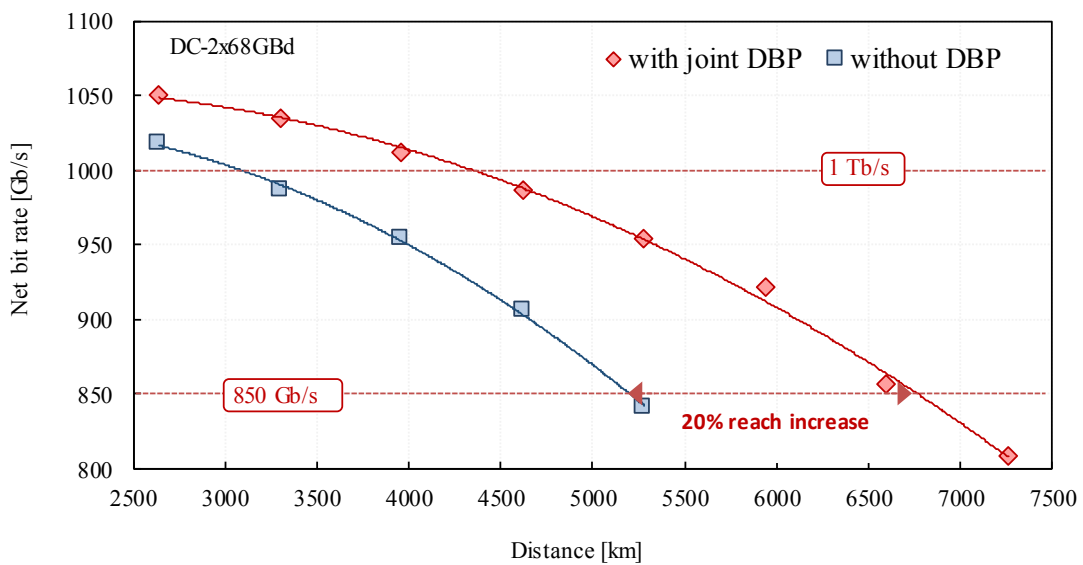


Fig. 4.12: Dual-carrier net rate versus distance with (diamonds) and without (squares) joint DBP.

Finally, Fig. 4.13 summarizes the various transmission records demonstrated in this section, and compares them against previously published records.

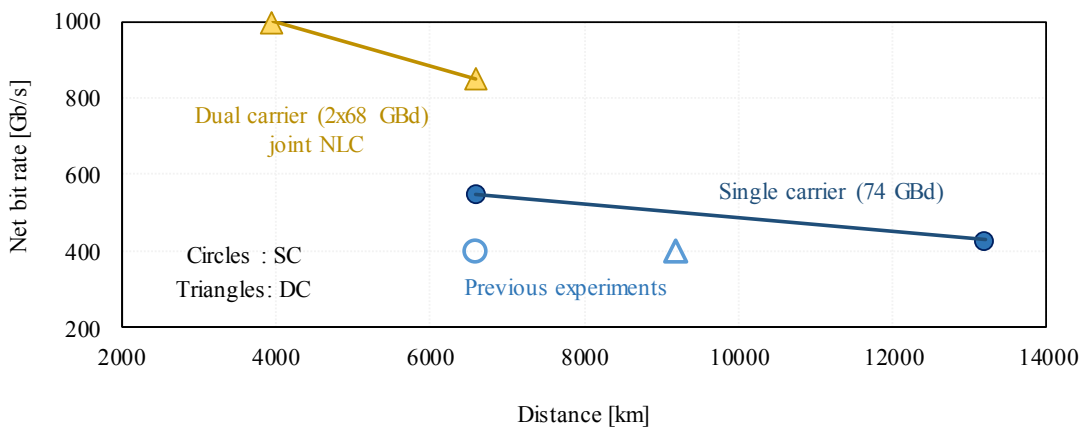


Fig. 4.13: Summary of main achieved transmission records.

4.3 65 TB/S LEVERAGED BY PCS-64QAM

In this section, we use the PCS-64QAM shown in Sec. 3.1 with a source entropy of 5.4 b/symb/pol to demonstrate a full C+L-band 6,600 km transoceanic transmission achieving a record net data rate of 65 Tb/s, with a SE of 7.3 b/s/Hz. The average per-channel net bit rate is 363.1 Gb/s [30].

4.3.1 Experimental Set-up

Fig. 4.14a shows the C-band transmitter setup. We employ a single TLS as a test channel modulated with a dedicated PM IQ-mod, and surrounded by 87 loading channels divided into even and odd rails, modulated with distinct modulators. Each modulator is driven by a dedicated DAC loaded with different randomly-generated sequences operating at 88 Gsamples/s. The sequence length is 36492 symbols. Pulse shaping is performed using RRC pulses with roll-off 0.01. Loading channels are coupled through a WSS to the measured channel. A polarization scrambler is placed at the WSS output to further decorrelate wavelength channels. The same configuration is used for the L-band transmitter, although the number of loading channels is 90, leading to a total number of 179 C+L channels.

The recirculating loop sketched in Fig. 4.14b. It consists of 12 spans of 55 km ultra low loss Corning Vascade EX3000 fiber, with C and L-band EDFAs completely compensating for span loss. The output power of all EDFAs is set to 19 dBm corresponding to NLT+1 dB to achieve maximum gain after NLC. The transmitted signal is received after 10 loops by a real-time scope with 33 GHz bandwidth, sampling at 80 Gsamples/s. DSP blocks are the same as in Chap. 3, where a 1% pilot-aided MMA is employed for PCS-64QAM signals.

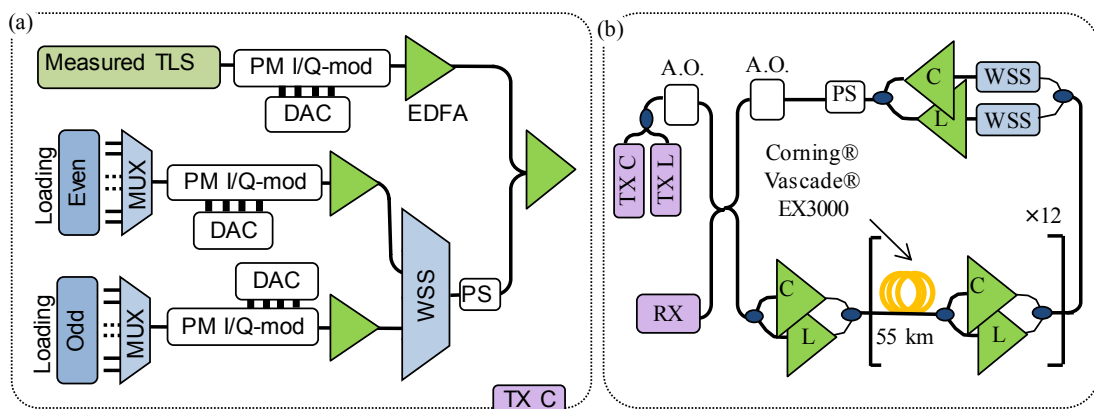


Fig. 4.14: (a) C-band transmitter, and (b) recirculating loop. DAC: digital-to-analog convertor, PM IQ-mod: polarization multiplexed IQ-modulator, TLS: tunable laser source, DFB: distributed feedback laser, PS: polarization scrambler, WSS: wavelength selective switch, A.O: acousto optic switch.

4.3.2 Experimental Results

We perform transmission of all 179 channels. We apply high-resolution DBP with 10 steps per span, where the reference channel power within the DBP algorithm has been optimized to account for the non-flat spectrum power profile. Fig. 4.15a illustrates the measured SNRs and GMIs before and after applying DBP. The mean SNR over C + L bands after NLC is ~ 12 dB, leading to a mean GMI of ~ 8 b/symb.

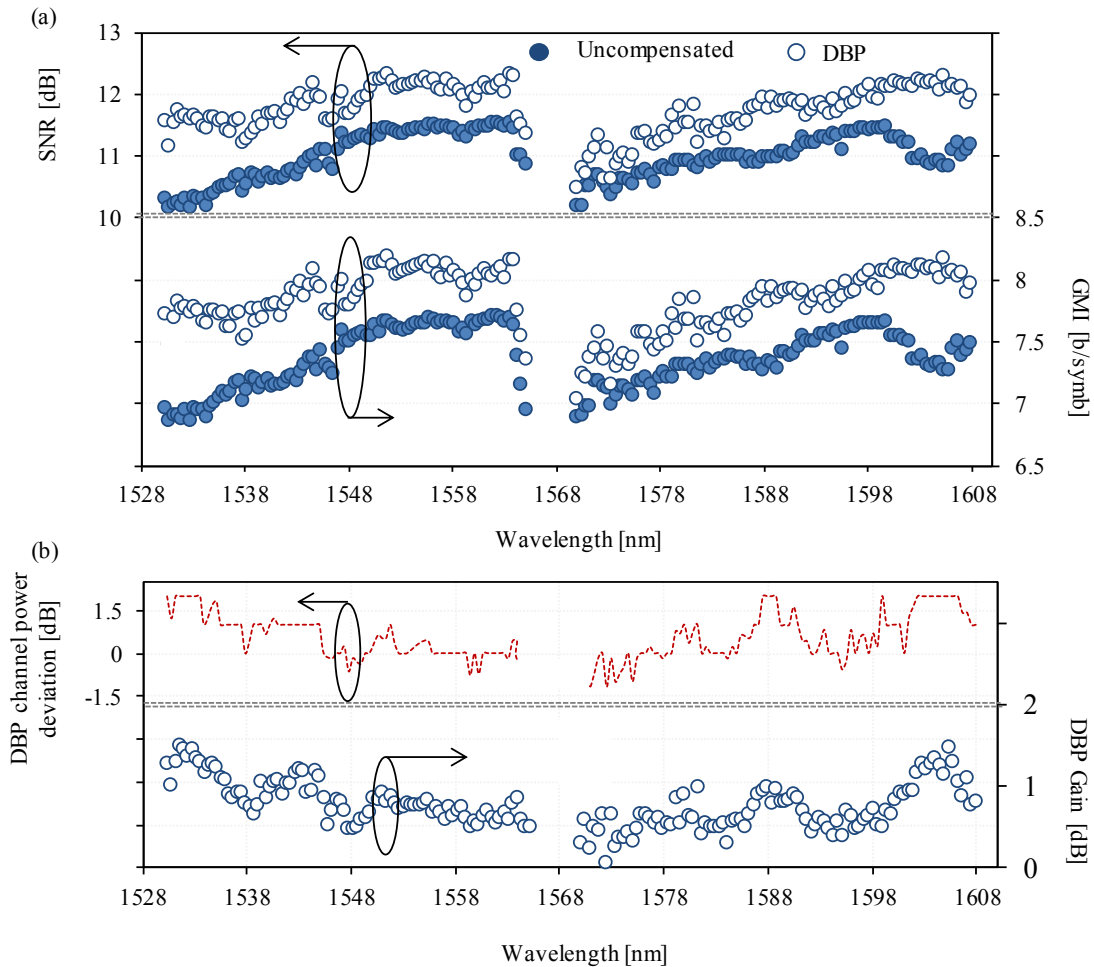


Fig. 4.15: (a) PCS-64QAM SNR and GMI of all channels, with and without NLC, and (b) DBP channel power deviation from nominal (up), and DBP SNR gain vs wavelength.

The upper part of Fig. 4.15b shows the power deviation between the channel power used within the DBP algorithm to maximize the gain and the nominal channel power per band, while the bottom part shows the DBP gain for all WDM channels. It is observed that there is a clear correlation between the DBP channel power deviation and the NLC gain. Channels that are operating more deeply in the nonlinear regime (positive DBP channel power deviation) enjoy more DBP NLC gain, while the gain is reduced for channels operating more in the linear regime (negative deviations).

In this sense, channels lying at C-band left edge operate more deeply in the nonlinear regime than the other channels, but the power-adaptive DBP provides more gain in processing C-band left edge, such that the compensated SNR distribution is more uniform than the uncompensated SNR.

Finally, we apply our family of SC-LDPC codes to all channels, and compute the net system throughput corrected for pilot use. The WDM channels are divided into a given number of groups depending on their performance. The optimal set of FEC rates that maximize the throughput are found using the optimization algorithm presented in [29]. Fig. 4.16a shows the net throughput versus the number of allowed FEC code rates. With 6 optimized rates, we achieve the net throughput of 65 Tb/s after 6,600 km. Fig. 4.16b gives an overview of the high capacity transoceanic lab demonstrations at the time of the experiment, including the current work.

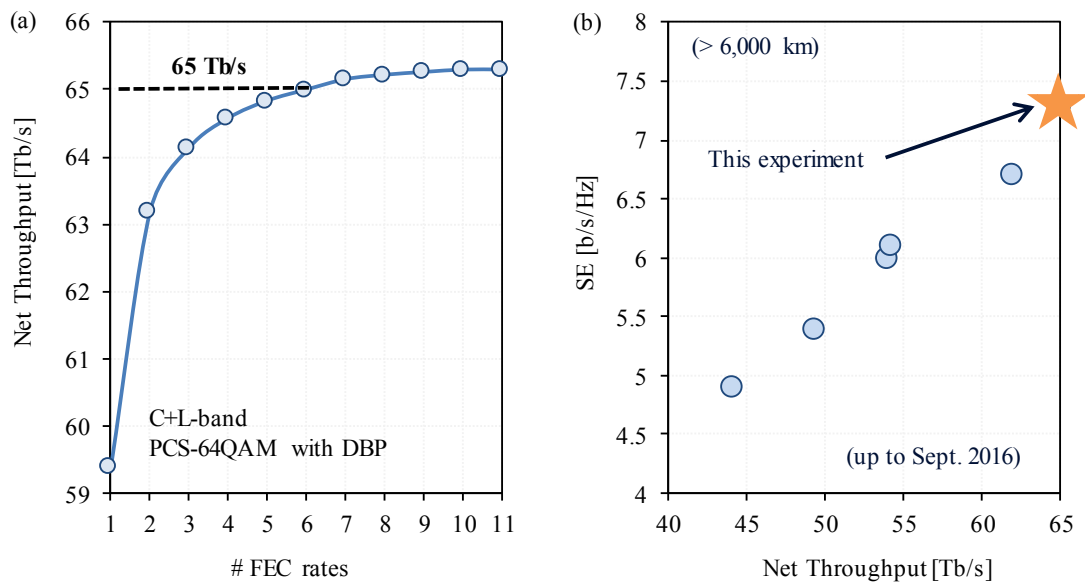


Fig. 4.16: (a) Net throughput vs. number of optimized code rates, and (b) summary of C+L-band transoceanic demonstrations at the time of this experiment.

4.4 SUMMARY

In the first part of this chapter, we demonstrated the achievable benefits of PCS, NLC and multi-rate SC-LDPC codes to increase the system throughput of current trans-Pacific optical fiber links. We employed the truncated PCS-64QAM (TPCS-64QAM) designed for a target SNR region of 8-10 dB, and experimentally compared it with standard 64QAM format. The proposed solution achieved a gain of 0.25 b/symb/pol over 64QAM. We reported a C-band EDFA-only trans-Pacific transmission using 84 channels of 49 GBd TPCS-64QAM and 7 SC-LDPC codes

to achieve a net throughput of 24.6 Tb/s and a spectral efficiency of 5.9 b/s/Hz after 10,285 km straight line. Moreover, we investigated the gain provided by low-complexity FDBP. Since we operated in the linear regime, the throughput increase due to NLC was limited to ~4%, leading to 25.4 Tb/s and a spectral efficiency of 6.06 b/s/Hz.

In the second part we demonstrated new per channel-rate transmission records for transoceanic distances thanks to cutting-edge DAC's technology and wideband receivers, optimum transceiver design leveraging PCS-64QAM and digital NLC. In particular, we demonstrated single-carrier 550 Gb/s, over 6,600 km, and 430 Gb/s over 13,200 km. We also demonstrated dual-carrier 850 Gb/s after 6,600 km, and dual-carrier 1Tb/s after 3,960 km.

Finally, in the third part we used PCS-64QAM, together with DBP and adaptive multi-rate SC-LDPC FEC codes to achieve a record of 65 Tb/s net system throughput after 6,600 km fiber transmission, with spectral efficiency of 7.3 b/s/Hz.

All the above demonstrations correspond to transmission records at the corresponding time of their realizations.

5 CONCLUSIONS AND PERSPECTIVES

Submarine optical fiber transmission systems represent the backbone of high-capacity global telecommunications. With the ever-growing demand on worldwide data traffic, new and disruptive technologies are required to continue increasing their transmission throughput. These systems have been greatly influenced by the advent of coherent detection technology, which in conjunction with advances in high-speed integrated circuits, have allowed the use of advanced modulation formats and DSP techniques to maximize the transmission spectral efficiency.

Mitigation of fiber linear effects and TX-RX impairments is a common practice in current commercial systems, such that system performance rests limited by fiber Kerr nonlinear effects. While single channel NLC is still not present in commercial systems, it will be most likely implemented in future generation systems. On the other hand, capacity approaching modulation formats as PCS-QAM have been recently introduced for the fiber channel, being a good candidate for commercial implementation.

The first part of this thesis was devoted on discussing the current status and trends of transoceanic submarine optical fiber systems, followed by describing the fundamental notions of digital telecommunication systems and transoceanic optical fiber systems.

In the second part of this thesis, I investigated the performance and achievable benefits of low-complexity DSP-based NLC techniques for transoceanic distances. The FDBP algorithm has been proposed in the literature to reduce the high computational complexity of the well-known DBP. Either its lower computation complexity, FDBP involves an exhaustive optimization of two parameters which have to be a priori optimized for every link under study. Following this, I first studied by means of numerical simulations the dependency of these two parameters on different system variables as: channel count, launched power, symbol-rate, and fiber coefficients. I showed that the FDBP parameters depend mainly on the pulse broadening per

FDBP step, and we have derived simple semi-analytical formulae for their computation. The obtained results were then validated by a trans-Atlantic experiment, where the maximum achievable gains were also compared to theoretical predictions based on perturbation theory. Moreover, the aforementioned semi-analytical formulae were further validated along this thesis, showing that even when a more rigorous theoretical study can be performed to completely understand the dependency of these parameters on system variables, they are valid over a wide range of practical system configurations and can be used to avoid complex and time consuming exhaustive optimization.

I then studied the impact of stochastic effects as PMD and PDL on the performance of FDBP and the novel PNLC algorithm. If DSP-based NLC techniques are to be adopted in commercial systems, they need to be robust against stochastic effects that are typically not considered in their implementation. While it has been shown that stochastic effects severely reduce the performance of fine resolution multi-channel DBP, it was demonstrated that low-complexity single-channel NLC algorithms which are more practical and close to implementation are less impacted by stochastic effects. The impact of PMD and PDL on FDBP and PNLC was experimentally studied by introducing PMD and PDL elements into our submarine transmission line. I performed massive transmission experiments processing 2,400 different waveforms to correctly account for PMD and PDL statistics. It was found that for a practical fully loaded C-band system composed of 32 GBd PM-16QAM channels, DGD values as large as 150 ps barely impact the performance of FDBP, while a small degradation of ~ 0.1 dB was found for PNLC. Considering PDL, it was found that values as large as 9 dB lead to a degradation in achievable gain of ~ 0.2 dB. As the PMD and PDL values introduced into the link are well in excess of modern commercial systems, it can be concluded that both FDBP and PNLC are robust to the studied stochastic effects.

With practical implementation in mind, I then studied the achievable gains provided by FDBP and PNLC for different algorithm complexities for transoceanic distances by means of numerical simulations. Two system configurations were considered; the first one based on 32 GBd PM-16QAM channels with 37.5 GHz spacing, and the second one based on 64 GBd channels at 75 GHz spacing. Thanks to the use of GPU cards, a total WDM signal bandwidth of 4 THz corresponding to a fully-loaded C-band system was simulated. Contrary to terrestrial systems where it has been shown that the maximum theoretical gain is around 0.5 dB, submarine systems enjoy more NLC gain in excess of 1 dB; making NLC more interesting for ultra-long-haul applications. However, these maximum theoretical gains are degraded due to the considered low-complexity NLC architectures, and also due to linear noise impacting their performance when placed at the receiver side. For practical OSNR regimes, PNLC can achieve gains up to 0.7 dB for systems employing 32 GBd channels, and up to 1.1 dB when 64 GBd channels are used. In the case of FDBP, the maximum gains are increased to ~ 1 dB and ~ 1.3 dB respectively. It was also shown that linear noise equally affects both FDBP and PNLC, and

that the degradation is independently of the algorithm complexity. These results show that considerable gains can be achieved by low-complexity NLC in transoceanic systems.

Besides NLC techniques, the spectral efficiency of optical fiber systems can be increased by the use of more sophisticated modulation formats aiming to reduce the gap between the constrained and the Shannon capacity. In the third part of this work, I investigated the achievable gains of the novel PCS-QAM over regular QAM formats. First, I experimentally compared the performance of four modulation formats for transoceanic distances, *i.e.*, 32QAM, 64QAM, 64APSK, and PCS-64QAM, addressing four issues: theoretical gap to the linear Shannon capacity, nonlinear performance at optimum launch power, B2B implementation penalties due to limited DAC and ADC resolutions, and DSP challenges. Even when PCS-64QAM achieves theoretical values of GMI close to capacity and outperforms all other formats, it presents new DSP challenges that if are not well addressed can lead to higher implementation penalties. Compared to regular QAM formats, the convergence of the polarization demultiplexing and phase estimation algorithms is greatly reduced for PCS-64QAM when working in low SNR regimes. In practice, in order to improve algorithm convergence, a pilot-assisted polarization demultiplexing is required, and the pilot rate has to be properly optimized. In the nonlinear fiber regime, the “Gaussian-like” constellation of PCS-64QAM results in higher penalties compared to regular QAM formats due to an enhanced nonlinear noise. Despite the nonlinear penalties and considering an optimized DSP, PCS-64QAM can achieve practical gains of ~ 0.25 bits/symb/pol with respect to regular QAM formats, making it a good candidate for future generation systems.

Then I moved to the design of a PCS-64QAM targeting trans-Pacific distances. The resulting format was referred as TPCS-64QAM since it was created using a truncated Maxwell-Boltzman distribution. The TPCS-64QAM had an entropy of 4.3 b/symb/pol and minimized the gap to capacity over the SNR region of 7 to 11 dB, while at the same time considering FEC implementation penalties.

Finally, in the last part of this work, PCS-QAM, and NLC were employed with state-of-the-art DACs, wide-band receivers and multi-rate FECs to demonstrate new transoceanic transmission records. First, the achievable benefits in terms of system throughput increase by applying the previously designed TPCS-64QAM, multi-rate SC-LDPC codes, and NLC based on FDBP were demonstrated. In particular, a spectral efficiency of 5.9 b/s/Hz (net 24.6 Tb/s) after 10,285 km straight-line transmission was demonstrated. The achievable gains provided by FDBP for different algorithm complexities were also addressed, showing that the spectral efficiency can be increased to 6.06 b/s/Hz (net 25.4 Tb/s). Compared to actual systems operating with 150 Gb/s 8QAM tributaries, the proposed solution based on TPCS-64QAM has a promising potential of doubling the throughput of existing trans-Pacific networks.

Afterwards, following the industry trend to increase the per-channel bit rate to reduce the cost per bit, new per-channel bit rate using single-carrier (74 GBd) and dual-carrier (2x68 GBd)

configurations together with PCS-QAM and NLC were demonstrated. The first single-carrier 550 Gb/s over 6,600 km, and 430 Gb/s over 13,200 km were shown, while the first dual-carrier 850 Gb/s after 6,600 km, and 1Tb/s after 3,960 km were also demonstrated.

One key point to maximize the throughput of submarine systems is to employ both C + L bands to double the throughput per single-mode optical fiber cable. In the last part of this work, a record of 65 Tb/s over 6,600 km employing the novel PCS-64QAM was demonstrated for the first time. Together with DBP and adaptive multi-rate SC-LDPC FECs, a spectral efficiency of 7.3 b/s/Hz over both C+L bands with EDFA-only amplification was achieved.

Perspectives

In this work, I presented the practical achievable gains of single channel NLC for transoceanic transmission systems. It was shown that considerable gains can be obtained with relative low-complexity NLC architectures. The effectiveness of NLC techniques relies on the level of accuracy to correctly model the optical fiber channel. The presence of stochastic effects and link uncertainties will directly impact the achievable gains of NLC techniques. While PMD, PDL, and ASE noise were already studied in this work, the impact of in-line filtering, and uncertainties in the link power profile and fiber coefficients could still be a subject of research. Moreover, adaptive NLC approaches to blindly estimate the channel parameters could also be further investigated.

It is worth mentioning that even with a perfect knowledge of the channel, the maximum achievable gains are still limited by the number of WDM available for NLC. For the transoceanic systems studied in this work, the maximum achievable gains considering ideal single channel NLC can reach up to ~1.5 dB (~35% reach increase). Multi-channel NLC could be used to further increase performance. However, the main problem behind multi-channel NLC is that apart from being more impacted by stochastic effects, it is still uncertain if the extra gain justifies the associated increase in computational complexity. The study of the practical achievable gains of multi-channel NLC versus added complexity could be performed.

Regarding PCS-QAM, it was shown that the gain in the achievable transmission rate is accompanied by different DSP challenges that need to be addressed to avoid implementation penalties. A more profound study on the convergence speed of the polarization demultiplexer and phase estimation needs to be carried out.

REFERENCES

- [1] J. Bray, *Innovation and the Communications Revolution: From the Victorian Pioneers to Broadband Internet*, London, United Kingdom: The Institution of Engineering and Technology, 202.
- [2] M. Guarneri, "The Conquest of the Atlantic," *IEEE Industrial Electronics Magazine*, pp. 53-67, March 2014.
- [3] J. Chesnoy, *Undersea Fiber Communication Systems*, 2nd Edition, Academic Press, 2015.
- [4] J. Hecht, "The Evolution of Optical Amplifiers," *Optics & Photonics News*, pp. 36-39, August 2002.
- [5] R. J. Mears, L. Reekie, I. M. Jauncey and D. N. Payne, "High-gain rare-earth-doped fiber amplifier at 1.54 μm ," in *OFC*, Reno, Nevada, 1987.
- [6] E. Desurvire and C. R. Giles, "Saturation-Induced crosstalk in high-speed erbium-doped fiber amplifiers at $\lambda = 1.53 \mu\text{m}$," in *OFC*, Texas, 1989.
- [7] TeleGeography, "Submarine Cable Map," TeleGeography, 2017. [Online]. Available: <https://www.submarinecablemap.com/>. [Accessed 16 October 2017].
- [8] S. Bergano, C. R. Davidson, C. J. Chen, B. Pedersen, M. A. Mills, N. Ramanujam, H. D. Kidorf, A. B. Puc, M. D. Levonas and H. Abdelkader, "640 Gb/s Transmission of Sixty-four 10 Gb/s WDM Channels Over 7200km With 0.33 (bits/s)/Hz Spectral Efficiency," in *Optical Fiber Communication Conference*, 1999.
- [9] C. R. Davidson, C. J. Chen, M. Nissov, A. Pilipetskii, N. Ramanujam, H. D. Kidorf, B. Pedersen, M. A. Mills, C. Lin, M. I. Hayee, J. X. Cai, A. B. Puc, P. C. Corbett, R. Menges, H. Li, A. Elyamani, C. Rivers and N. S. Bergano, "1800 Gb/s Transmission of One Hundred and Eighty 10 Gb/s WDM Channels over 7,000 km using the Full EDFA C-Band," in *Optical Fiber Communication Conference*, 2000.
- [10] G. Vaille, F. Pitel and J. F. Marcereou, "3Tbit/s (300x11.6Gbit/s) Transmission Over 7380 km Using C+L Band with 25GHz Channel Spacing and NRZ Format," in *Optical Fiber Communication Conference*, 2001.
- [11] H. Sugahara, K. Fukuchi, A. Tanaka, Y. Inada and T. Ono, "6,050km transmission of 32 x 42.7 Gb/s DWDM signals using Raman-amplified quadruple-hybrid span configuration," in *Optical Fiber Communications Conference*, 2002.
- [12] G. Charlet, "One hundred WDM channel transatlantic transmission experiment at 43 Gbit/s using Raman repeaters with large 65 km spacing," in *European Conference on Optical Communications*, Rimini, 2003.
- [13] G. Charlet, E. Corbel, J. Lazaro, A. Klekamp, R. Dischler, P. Tran, W. Idler, H. Mardoyan, A. Konczykowska, F. Jorge and S. Bigo, "WDM transmission at 6 Tbit/s capacity over transatlantic distance, using 42.7Gb/s Differential Phase-Shift Keying without pulse carver," in *Optical Fiber Communication Conference*, 2004.
- [14] H. Masuda, E. Yamazaki, A. Sano, T. Yoshimatsu, T. Kobayashi, E. Yoshida, Y. Miyamoto, S. Matsuoka, Y. Takatori, M. Mizoguchi, K. Okada, K. Hagimoto, T. Yamada and S. Kamei, "13.5-Tb/s (135 x 111-Gb/s/ch) no-guard-interval coherent OFDM transmission over 6,248 km using SNR maximized second-order DRA in the extended L-band," in *Optical Fiber Communications Conference*, San Diego, CA, 2009.

-
- [15] M. Salsi, H. Mardoyan, P. Tran, C. Koebele, E. Dutisseuil, G. Charlet and S. Bigo, "155×100Gbit/s coherent PDM-QPSK transmission over 7,200km," in *European Conference on Optical Communications*, Vienna, 2009.
- [16] J. Cai, Y. Cai, C. Davidson, A. Lucero, H. Zhang, D. Foursa, O. Sinkin, W. Patterson, A. Pilipetskii, G. Mohs and N. Bergano, "20 Tbit/s Capacity Transmission Over 6,860 km," in *Optical Fiber Communication Conference*, 2011.
- [17] M. Salsi, A. Ghazisaeidi, P. Tran, R. Rios-Muller, L. Schmalen, J. Renaudier, H. Mardoyan and P. Brindel, "31 Tb/s transmission over 7,200 km using 46 Gbaud PDM-8QAM," in *OptoElectronics and Communications Conference*, 2013.
- [18] A. Ghazisaeidi, L. Schmalen, I. Fernandez de Jauregui Ruiz, P. Tran, C. Simonneau, P. Brindel and G. Charlet, "52.9 Tb/s Transmission over Transoceanic Distances using Adaptive Multi-Rate FEC," in *European Conference on Optical Communications*, Cannes, 2014.
- [19] A. Ghazisaeidi, L. Schmalen, I. Fernandez de Jauregui Ruiz, P. Tran, C. Simonneau, P. Brindel and G. Charlet, "Transoceanic Transmission Systems Using Adaptive Multirate FECs," *Journal of Lightwave Technology*, vol. 33, no. 7, pp. 1479-1487, 2015.
- [20] S. Zhang, F. Yaman, Y. K. Huang, J. D. Downie, D. Zou, W. A. Wood, A. Zakharian, R. Khrapko, S. Mishra, V. Nazarov, J. Hurley, I. B. Djordjevic, E. Mateo and Y. Inada, "Capacity-approaching transmission over 6375 km at spectral efficiency of 8.3 bit/s/Hz," in *Optical Fiber Communications Conference*, Anaheim, CA, 2016.
- [21] A. Ghazisaeidi, I. Fernandez de Jauregui Ruiz, R. Rios-Muller, L. Schmalen, P. Tran, P. Brindel, A. Carbo Meseguer, Q. Hua, F. Buchali, G. Charlet and J. Renaudier, "65Tb/s Transoceanic Transmission Using Probabilistically-Shaped PDM-64QAM," in *European Conference on Optical Communications*, Dusseldorf, Germany, 2016.
- [22] J. X. Cai, H. G. Batshon, M. Mazurczyk, O. Sinkin, D. Wang, M. Paskov, W. Patterson, C. R. Davidson, P. Corbett, G. Wolter, T. Hammon, M. Bolshtyansky, D. Foursa and A. Pilipetskii, "70.4 Tb/s Capacity over 7,600 km in C+L Band Using Coded Modulation with Hybrid Constellation Shaping and Nonlinearity Compensation," in *Optical Fiber Communications Conference*, Los Angeles, CA, 2017.
- [23] R. Rios-Müller, J. Renaudier, P. Brindel, C. Simonneau, P. Tran, A. Ghazisaeidi, I. Fernandez de Jauregui Ruiz, L. Schmalen and G. Charlet, "Optimized spectrally efficient transceiver for 400-Gb/s single carrier transport," in *European Conference on Optical Communications*, Cannes, 2014.
- [24] I. Fernandez de Jauregui Ruiz, A. Ghazisaeidi, P. Brindel, R. Rios-Müller, A. Arnould, H. Mardoyan, O. Ait Sab, J. Renaudier and G. Charlet, "Record 560 Gb/s Single-Carrier and 850 Gb/s Dual-Carrier Transmission over Transoceanic Distances," in *Optical Fiber Communication Conference*, San Diego, 2018.
- [25] P. Schvan, D. Pollex, S. C. Wan, C. Falt and N. Ben-Hamida, "A 22GS/s 5b ADC in 0.13µm SiGe BiCMOS," in *International Solid-State Circuits Conference*, Ottawa, 2006.
- [26] K. Schuh, "100 GSa/s BiCMOS DAC Supporting 400 Gb/s Dual Channel Transmission," in *Proc. ECOC*, 2016.
- [27] H. Zhang, J. X. Cai, H. G. Batshon, M. Mazurczyk, O. V. Sinkin, D. G. Foursa, A. Pilipetskii, G. Mohs and N. S. Bergano, "200 Gb/s and dual-wavelength 400 Gb/s transmission over transpacific distance at 6 b/s/Hz spectral efficiency," in *Optical Fiber Communication Conference*, Anaheim, CA, 2013.
- [28] M. Salsi, R. Rios-Muller, J. Renaudier, P. Tran, L. Schmalen, A. Ghazisaeidi, H. Mardoyan, P. Brindel, G. Charlet and S. Bigo, "38.75 Tb/s transmission experiment over transoceanic distance," in *European Conference on Optical Communications*, London, 2013.
- [29] A. Ghazisaeidi, I. Fernandez de Jauregui Ruiz, L. Schmalen, P. Tran, C. Simonneau, E. Awwad, B. Uscumlic, P. Brindel and G. Charlet, "Submarine transmission systems using digital nonlinear compensation and adaptive rate forward error correction," *Journal of Lightwave Technology*, vol. 34, no. 8, p. 1886–1895, 2016.
- [30] A. Ghazisaeidi, I. Fernandez de Jauregui Ruiz, R. Rios-Muller, L. Schmalen, P. Tran, P. Brindel, A. Carbo Meseguer, Q. Hu, F. Buchali, G. Charlet and J. Renaudier, "Advanced C+L Band Transoceanic Transmission Systems Based on Probabilistic Shaped PDM-64QAM," *Journal of Lightwave Technology*, vol. 35, no. 7, p. 1291, 2017.
- [31] J. X. Cai, M. Mazurczyk, H. Zhang, Y. Sun, O. V. Sinkin, D. G. Foursa and A. Pilipetskii, "64QAM based coded modulation transmission over transoceanic distance with >60 Tb/s capacity," in *Optical Fiber Communications Conference*, Los Angeles, CA, 2015.
- [32] J. Cho, X. Chen, S. Chandrasekhar, G. Raybon, R. Dar, L. Schmalen, E. Burrows, A. Adamiecki, S. Corteselli, Y. Pan, D. Correa, B. McKay, S. Zsigmond, P. Winzer and S. Grubb, "Trans-Atlantic Field Trial Using Probabilistically Shaped 64-QAM at High Spectral Efficiencies and Single-Carrier Real-Time 250-Gb/s 16-QAM," in *Optical Fiber Communications Conference*, Los Angeles, CA, 2017.
- [33] L. Schmalen, F. Buchali and A. Leven, "A generic tool for assessing the soft-FEC performance in optical transmission experiments," *IEEE Photonics Technology Letters*, vol. 24, no. 1, p. 40–42, 2012.
- [34] L. Schmalen, V. Aref, J. Cho, D. Suikat, D. Rosener and A. Leven, "Spatially coupled soft-decision error correction for future lightwave systems," *Journal of Lightwave Technology*, vol. 33, no. 5, p. 1109–1116, 2015.

-
- [35] L. Schmalen, D. Suikat, D. Rosener and V. Aref, "On the design of capacity-approaching unit-memory spatially coupled LDPC codes for optical communications," in *European Conference on Optical Communications*, 2016.
- [36] E. Ip and J. M. Kahn, "Compensation of Dispersion and Nonlinear Impairments Using Digital Backpropagation," *Journal of Lightwave Technology*, vol. 26, no. 20, p. 3416–3425, 2008.
- [37] X. Li, X. Chen, G. Goldfarb, E. Mateo, I. Kim, F. Yaman and G. Li, "Electronic post-compensation of WDM transmission impairments using coherent detection and digital signal processing," *Optics Express*, vol. 16, no. 2, p. 880–888, 2008.
- [38] L. B. Du and A. J. Lowery, "Improved single channel backpropagation for intra-channel fiber nonlinearity compensation in long-haul optical communication systems," *Optics Express*, vol. 18, pp. 17075–17088, 2010.
- [39] Y. Gao, J. H. Ke, K. P. Zhong, J. C. Cartledge and S. H. Yam, "Assessment of Intrachannel Nonlinear Compensation for 112 Gb/s Dual-Polarization 16QAM Systems," *Journal of Lightwave Technology*, vol. 30, no. 24, p. 3902–3910, 2012.
- [40] A. Ghazisaeidi and R. J. Essiambre, "Calculation of Coefficients of Perturbative Nonlinear Pre-Compensation for Nyquist Pulses," in *European Conference on Optical Communications*, Cannes, 2014.
- [41] J. X. Cai, H. G. Batshon, M. V. Mazurczyk, O. V. Sinkin, D. Wang, M. Paskov, C. R. Davidson, W. W. Patterson, M. A. Bolshtyansky and D. G. Foursa, "51.5 Tb/s Capacity over 17,107 km in C+L Bandwidth Using Single Mode Fibers and Nonlinearity Compensation," in *European Conference on Optical Communications*, Gothenburg, 2017.
- [42] C. E. Shannon, "A mathematical theory of communication," *Bell Syst. Tech. J.*, vol. 27, pp. 379–423 and 623–656, 1948.
- [43] R. J. Essiambre, G. Kramer, P. J. Winzer, G. J. Foschini and B. Goebel, "Capacity Limits of Optical Fiber Networks," *Journal of Lightwave Technology*, vol. 28, no. 4, pp. 662–701, 2010.
- [44] J. Cho, L. Schmalen and P. J. Winzer, "Normalized generalized mutual information as a forward error correction threshold for probabilistically shaped QAM," in *European Conference on Optical Communications*, Gothenburg, Sweden, 2017.
- [45] G. Böcherer, "Achievable rates for probabilistic shaping," *arXiv:1707.01134v3*, 2017.
- [46] A. Leven and L. Schmalen, "Status and Recent Advances on Forward Error Correction Technologies for Lightwave Systems," *Journal of Lightwave Technology*, vol. 32, no. 16, pp. 2735–2750, 2014.
- [47] M. Cover and J. A. Thomas, *Elements of Information Theory*, Hoboken NJ, USA: Wiley, 1991.
- [48] G. D. Forney Jr and L. F. Wei, "Multidimensional constellations—Part I: Introduction, figures of merit, and generalized cross constellations," *IEEE J. Select. Areas Commun*, vol. 7, p. 877–892, 1989.
- [49] G. D. Forney Jr, "Multidimensional constellations—Part II: Voronoi constellations," *IEEE J. Select. Areas Commun*, vol. 7, p. 941–958, 1989.
- [50] G. Böcherer, F. Steiner and P. Schulte, "Bandwidth efficient and rate-matched low-density parity-check coded modulation," *IEEE Trans. Commun.*, vol. 63, no. 12, p. 4651–4665, 2015.
- [51] F. Buchali, F. Steiner, G. Bocherer, L. Schmalen, P. Schulte and W. Idler, "Rate adaptation and reach increase by probabilistically shaped 64-QAM: An experimental demonstration," *Journal of Lightwave Technology*, vol. 34, no. 7, pp. 1599–1609, 2016.
- [52] Z. Liu, Q. Xie, K. Peng and Z. Yang, "APSK constellation with gray mapping," *IEEE Commun. Letters*, vol. 15, no. 12, pp. 1271–1273, 2011.
- [53] I. Fernandez de Jauregui Ruiz, A. Ghazisaeidi, R. Rios-Muller and P. Tran, "Performance comparison of advanced modulation formats for transoceanic coherent systems," in *Opt. Fiber Commun. Conf*, Los Angeles, 2017.
- [54] J. Cho, C. Xie and P. J. Winzer, "Analysis of soft-decision FEC on non-AWGN channels," *Optics Express*, vol. 20, no. 7, pp. 7915–7928, 2012.
- [55] J. Cho, L. Schmalen and P. J. Winzer, "Normalized Generalized Mutual Information as a Forward Error Correction Threshold for Probabilistically Shaped QAM," in *ECOC*, Gothenburg, 2017.
- [56] A. Alvarado, E. Agrell, D. Lavery, R. Maher and P. Bayvel, "Replacing the Soft-Decision FEC Limit Paradigm," *Journal of Lightwave Technology*, vol. 33, no. 20, pp. 4338–4352, 2015.
- [57] T. Yoshida, M. Karlsson and E. Agrell, "Performance Metrics for Systems with Soft-Decision FEC and Probabilistic Shaping," *arXiv:1705.03736v4*, 2017.
- [58] A. Alvarado, "Information rates and post-FEC BER prediction in optical fiber communications," in *Optical Fiber Communications Conference*, Los Angeles, California, 2017.
- [59] Fujitsu, [Online]. Available: <http://www.fujitsu.com/cn/en/products/devices/semiconductor/fsp/asic/asic/ipmacro/networkingsips/>. [Accessed 09 2017].
- [60] J. Renaudier, A. Carbo Meseguer, A. Ghazisaeidi, P. Tran, R. Rios Muller, R. Brenot, A. Verdier, F. Blache, K. Mekhazni, B. Duval, H. Debregeas, M. Achouche, A. Boutin, F. Morin, L. Letteron, N. Fontaine, Y. Frignac and G. Charlet, "First 100-nm Continuous-Band WDM Transmission System with 115Tb/s

-
- Transport over 100km Using Novel Ultra-Wideband Semiconductor Optical Amplifiers," in *ECOC*, Gothenburg, 2017.
- [61] A. Ghazisaeidi, "A Theory of Nonlinear Signal-Noise Interactions in Wavelength Division Multiplexed Coherent Systems," *arXiv*, no. arXiv:1704.06461v1, 2017.
- [62] A. Mecozzi and R. J. Essiambre, "Nonlinear Shannon Limit in Pseudolinear Coherent Systems," *Journal of Lightwave Technology*, vol. 30, no. 12, pp. 2011-2024, 2012.
- [63] P. Poggiolini, A. Carena, V. Curri, G. Bosco and F. Forghieri, "Analytical Modeling of Nonlinear Propagation in Uncompensated Optical Transmission Links," *IEEE Photon. Technol. Lett.*, vol. 23, no. 11, pp. 742-744, 2011.
- [64] A. Carena, V. Curri, G. Bosco, P. Poggiolini and F. Forghieri, "Modeling of the Impact of Nonlinear Propagation Effects in Uncompensated Optical Coherent Transmission Links," *IEEE Journal of Lightwave Technology*, vol. 30, no. 10, pp. 1524-1539, 2012.
- [65] P. Poggiolini, G. Bosco, A. Carena, V. Curri, Y. Jiang and F. Forghieri, "The GN-Model of Fiber Non-Linear Propagation and its Applications," *IEEE Journal of Lightwave Technology*, vol. 32, no. 4, pp. 694-721, 2014.
- [66] P. Johannisson and M. Karlsson, "Perturbation Analysis of Nonlinear Propagation in a Strongly Dispersive Optical Communication Systems," *IEEE Journal of Lightwave Technology*, vol. 31, no. 8, pp. 1273-1282, 2013.
- [67] A. Splett, C. Kurzke and K. Petermann, "Ultimate transmission capacity of amplified optical fiber communication systems taking into account fiber nonlinearities," in *ECOC*, 1993.
- [68] A. Mecozzi, C. B. Clausen and M. Shtaif, "System impact of intrachannel nonlinear effects in highly dispersed optical pulse transmission," *IEEE Photon. Technol. Lett.*, vol. 12, no. 12, pp. 1633-1635, 2000.
- [69] R. Dar, M. Feder, A. Mecozzi and M. Shtaif, "Properties of nonlinear noise in long dispersion-uncompensated fiber links," *Optics Express*, vol. 21, no. 22, pp. 25685-25699, October 2013.
- [70] R. Dar, M. Feder, A. Mecozzi and M. Shtaif, "Accumulation of nonlinear interference noise in fiber-optic systems," *Optics Express*, vol. 22, no. 12, pp. 14199-14211, May 2014.
- [71] R. Dar, M. Feder, A. Mecozzi and M. Shtaif, "Inter-Channel Nonlinear Interference Noise in WDM Systems: Modeling and Mitigation," *IEEE Journal of Lightwave Technology*, vol. 33, no. 5, pp. 1044-1053, March 2015.
- [72] R. Dar, M. Feder, A. Mecozzi and M. Shtaif, "Pulse Collision Picture of Inter-Channel Nonlinear Interference in Fiber-Optic Communications," *IEEE Journal of Lightwave Technology*, vol. 34, no. 2, pp. 593-607, January 2016.
- [73] A. Carena, G. Bosco, V. Curri, Y. Jiang, P. Poggiolini and F. Forghieri, "EGN model of non-linear fiber propagation," *Optics Express*, vol. 22, no. 13, pp. 16335-16362, May 2014.
- [74] P. Serena and A. Bononi, "An Alternative Approach to the Gaussian Noise Model and its System Implications," *IEEE Journal of Lightwave Technology*, vol. 31, no. 22, pp. 3489-3499, November 2013.
- [75] P. Serena and A. Bononi, "A Time-Domain Extended Gaussian Noise Model," *IEEE Journal of Lightwave Technology*, vol. 33, no. 7, pp. 1459-1472, April 2015.
- [76] P. Serena, "Nonlinear SignalNoise Interaction in Optical Links With Nonlinear Equalization," *IEEE Journal of Lightwave Technology*, vol. 34, no. 6, pp. 1476-1483, March 2016.
- [77] A. Carena, V. Curri, G. Bosco, P. P. and F. Forghieri, "Modeling of the Impact of Nonlinear Propagation Effects in Uncompensated Optical Coherent Transmission Links," *Journal of Lightwave Technology*, vol. 30, no. 10, pp. 1524-1539, 2012.
- [78] L. E. Nelson and R. M. Jopson, "Introduction to polarization mode dispersion in optical systems," *Journal of Optical and Fiber Communications Reports*, vol. 1, no. 4, p. 312-344, 2004.
- [79] N. Rossi, A. Ghazisaeidi and P. Ramantanis, "Stochastic Nonlinear Interference in Dispersion Managed Coherent Optical Links," in *European Conference on Optical Communications*, Düsseldorf, 2016.
- [80] A. Mecozzi and M. Shtaif, "The Statistics of Polarization-Dependent Loss in Optical Communication Systems," *IEEE Photonics Technology Letters*, vol. 14, no. 3, pp. 313-315, 2002.
- [81] E. Awwad, Y. Jaouen and G. Rekaya, "Polarization-Time Coding for PDL Mitigation in Long-Haul PolMux OFDM Systems," *Optics Express*, vol. 21, pp. 22773-22790, 2013.
- [82] C. Zhu, B. Song, B. Corcoran, L. Zhuang and A. J. Lowery, "Improved Polarization Dependent Loss Tolerance for Polarization Multiplexed Coherent Optical Systems by Polarization Pairwise Coding," *Optics Express*, vol. 23, pp. 27434-27447, 2015.
- [83] T. Xu, G. Jacobsen, S. Popov, M. Forzati, J. Mårtensson, M. Mussolin, J. Li, K. Wang, Y. Zhang and A. T. Friberg, "Frequency-Domain Chromatic Dispersion Equalization Using Overlap-Add Methods in Coherent Optical System," *Journal of Optical Communications*, vol. 32, no. 2, pp. 131-135, 2011.
- [84] S. J. Savory, "Digital filters for coherent optical receivers," *Optics Express*, vol. 16, no. 2, p. 804-817, 2008.
- [85] F. N. Hauske, M. Kuschnerov, B. Spinnler and B. Lankl, "Optical Performance Monitoring in Digital Coherent Receivers," *Journal of Lightwave Technology*, vol. 27, no. 16, pp. 3623-3631, 2009.

-
- [86] M. Selmi, C. Gosset, M. Noelle, P. Ciblat and Y. Jaouën, "Block-Wise Digital Signal Processing for PolMux QAM/PSK Optical Coherent Systems," *Journal of Lightwave Technology*, vol. 29, no. 20, pp. 3070-3082, 2011.
- [87] M. S. Faruk and S. J. Savory, "Digital Signal Processing for Coherent Transceivers Employing Multilevel Formats," *Journal of Lightwave Technology*, vol. 35, no. 5, pp. 1125 - 1141, 2017.
- [88] P. Petropoulos, F. Parmigiani, K. R. H. Bottrill, S. Yoshima, Y. Sun and D. J. Richardson, "Multi-channel all-optical signal processing based on parametric effects," in *Optical Fiber Communications Conference*, Anaheim, CA, 2016.
- [89] S. Yoshima, Y. Sun, K. R. H. Bottrill, F. Parmigiani, P. Petropoulos and D. J. Richardson, "Nonlinearity mitigation through optical phase conjugation in a deployed fibre link with full bandwidth utilization," in *European Conference on Optical Communication*, Valencia, 2015.
- [90] I. Sackey, F. Da Ros, J. K. Fischer, T. Richter, M. Jazayerifar, C. Peucheret, K. Petermann and C. Schubert, "Kerr Nonlinearity Mitigation: Mid-Link Spectral Inversion Versus Digital Backpropagation in 5×28-GBd PDM 16-QAM Signal Transmission," *Journal of Lightwave Technology*, vol. 33, no. 9, pp. 1821-1827, 2015.
- [91] X. Liu, A. R. Chraplyvy, P. J. Winzer, R. W. Tkach and S. Chandrasekhar, "Phase-conjugated twin waves for communication beyond the Kerr nonlinearity limit," *Nat. Photonics*, vol. 7, no. 7, pp. 560-568, 2013.
- [92] S. L. I. Olsson, B. Corcoran, C. Lundström, T. A. Eriksson, M. Karlsson and P. A. Andrekson, "Phase-Sensitive Amplified Transmission Links for Improved Sensitivity and Nonlinearity Tolerance," *Journal of Lightwave Technology*, vol. 33, no. 3, p. 710–721, 2015.
- [93] T. A. Eriksson, A. Lorences-Riesgo, P. Johannisson, T. Fehenberger, P. A. Andrekson and M. Karlsson, "Achievable rates comparison for phase-conjugated twin-waves and PM-QPSK," in *OptoElectronics and Communications Conference*, 2016.
- [94] Y. Tian, Y. K. Huang, S. Zhang, P. R. Prucnal and T. Wang, "Demonstration of digital phase-sensitive boosting to extend signal reach for long-haul WDM systems using optical phase-conjugated copy," *Optics Express*, vol. 21, no. 4, pp. 5099-5106, 2013.
- [95] L. Li, Z. Tao, L. Dou, W. Yan, S. Oda, T. Tanumura, T. Hoshida and C. J. Rasmussen, "Implementation efficient nonlinear equalizer based on correlated digital backpropagation," in *Optical Fiber Communications Conference*, Los Angeles, CA, 2011.
- [96] D. Rafique, M. Mussolin, M. Forzati, J. Martensson, M. N. Chugtai and A. D. Ellis, "Compensation of intra-channel nonlinear fibre impairments using simplified digital backpropagation algorithm," *Optics Express*, vol. 19, no. 10, pp. 9453-9460, 2011.
- [97] E. Ip, N. Bai and T. Wang, "Complexity versus performance tradeoff for fiber nonlinearity compensation using frequency-shaped, multi-subband backpropagation," in *Optical Fiber Communications Conference*, 2011.
- [98] A. Napoli, Z. Maalej, V. A. J. M. Sleiffer, M. Kuschnerov, D. Rafique, E. Timmers, B. Spinnler, T. Rahman, L. D. Coelho and N. Hanik, "Reduced Complexity Digital Back-Propagation Methods for Optical Communication Systems," *Journal of Lightwave Technology*, vol. 32, no. 7, p. 1351–1362, 2014.
- [99] Z. Tao, L. Dou, W. Yan, L. Li, T. Hoshida and J. C. Rasmussen, "Multiplier-Free Intrachannel Nonlinearity Compensating Algorithm Operating at Symbol Rate," *Journal of Lightwave Technology*, vol. 29, no. 17, p. 2570, 2011.
- [100] Y. Gao, J. C. Cartledge, A. S. Karar and S. S.-H. Yam, "Reducing the Complexity of Nonlinearity Pre-compensation Using Symmetric EDC and Pulse Shaping," in *European Conference on Optical Communications*, London, 2013.
- [101] G. Liga, T. Xu, A. Alvarado, I. R. Killey and P. Bayvel, "On the performance of multichannel digital backpropagation in high-capacity long-haul optical transmission," *Optics Express*, vol. 22, no. 24, pp. 30053-30062, 2014.
- [102] F. Frey, L. Molle, R. Emmerich, C. Schubert, J. K. Fischer and R. F. H. Fischer, "Single-step Perturbation-based Nonlinearity Compensation of Intra- and Inter-Subcarrier Nonlinear Interference," in *ECOC*, Gothenburg, 2017.
- [103] O. V. Sinkin, R. Holzlohner, J. Zweck and C. R. Menyuk, "Optimization of the Split-Step Fourier Method in Modeling Optical-Fiber Communications Systems," *Journal of Lightwave Technology*, vol. 21, no. 1, pp. 61-68, 2003.
- [104] F. Matera, A. Mecozzi, M. Romagnoli and M. Settembre, "Sideband instability induced by periodic power variation in long-distance fiber links," *Optics Letters*, vol. 18, no. 18, pp. 1499-1501, 1993.
- [105] F. Forghieri, "Modeling of wavelength multiplexed lightwave systems," in *Optical Fiber Communications Conference*, Dallas, Tx, 1997.
- [106] G. Bosco, A. Carena, V. Curri, R. Gaudino, P. Poggiolini and S. Benedetto, "Suppression of Spurious Tones Induced by the Split-Step Method in Fiber Systems Simulation," *IEEE Photonics Technology Letters*, vol. 12, no. 5, pp. 489-491, 2000.
- [107] E. Ip, "Nonlinear Compensation Using Backpropagation for Polarization-Multiplexed Transmission," *Journal of Lightwave Technology*, vol. 28, no. 6, pp. 939-951, 2010.

-
- [108] D. Rafique, M. Mussolin, M. Forzati, J. Mårtensson, M. N. Chugtai and A. D. Ellis, "Compensation of intra-channel nonlinear fibre impairments using simplified digital back-propagation algorithm," *Optics Express*, vol. 19, no. 10, p. 9453–9460, 2011.
- [109] Y. Gao, J. C. Cartledge, J. D. Downie, J. E. Hurley, D. Pikula and S. S.-H. Yam, "Nonlinearity Compensation of 224 Gb/s Dual-Polarization 16-QAM Transmission Over 2700 km," *IEEE Photonics Technology Letters*, vol. 25, no. 1, pp. 14–17, 2013.
- [110] G. Gao, X. Chen and W. Shieh, "Influence of PMD on fiber nonlinearity compensation using digital back propagation," *Optics Express*, vol. 20, no. 13, pp. 14406–14418, 2012.
- [111] K. Goroshko, H. Louchet and A. Richter, "Fundamental Limitation of Digital Back Propagation due to Polarization Mode Dispersion," in *Asia Communications and Photonics Conference*, Hong Kong, 2015.
- [112] G. Liga, C. B. Czegledi, T. Xu, E. Agrell, R. I. Killey and P. Bayvel, "Ultra-Wideband Nonlinearity Compensation Performance in the Presence of PMD," in *European Conference and Exhibition on Optical Communications*, Düsseldorf, 2016.
- [113] K. Goroshko, H. Louchet and A. Richter, "Overcoming Performance Limitations of Digital Back Propagation due to Polarization Mode Dispersion," in *International Conference on Transparent Optical Networks*, Trento, 2016.
- [114] C. B. Czegledi, G. Liga, D. Lavery, M. Karlsson, E. Agrell, S. J. Savory and P. Bayvel, "Polarization-Mode Dispersion Aware Digital Backpropagation," in *European Conference and Exhibition on Optical Communications*, Düsseldorf, 2016.
- [115] B. C. Czegledi, G. Liga, D. Lavery, M. Karlsson, E. Agrell, S. J. Savory and P. Bayvel, "Modified Digital Backpropagation Accounting for Polarization-Mode Dispersion," in *Optical Fiber Communications Conference*, Los Angeles, 2017.
- [116] M. Bertolini, N. Rossi, P. Serena and A. Bononi, "Do's and Don't's for a Correct Nonlinear PMD Emulation in 100Gb/s PDM-QPSK Systems," *Optical Fiber Technology*, vol. 16, no. 5, pp. 274–278, 2010.
- [117] A. Steinkamp, S. Vorbeck and E. I. Voges, "Polarization mode dispersion and polarization dependent loss in optical fiber systems," *Proc. SPIE, Optical Transmission Systems and Equipment for WDM Networking III*, vol. 5596, 2004.
- [118] G. Bosco, R. Cigliutti, E. Torrenzo, A. Carena, V. Curri, P. Poggiolini and F. Forghieri, "Joint DGD, PDL and Chromatic Dispersion Estimation in Ultra-Long-Haul WDM Transmission Experiments with Coherent Receivers," in *European Conference on Optical Communications*, Torino, 2010.
- [119] P. Serena, N. Rossi and A. Bononi, "Nonlinear Penalty Reduction Induced by PMD in 112 Gbit/s WDM PDM-QPSK Coherent Systems," in *European Conference on Optical Communications*, Vienna, 2009.
- [120] X. Liu and F. Buchali, "Intra-symbol frequency-domain averaging based channel estimation for coherent optical OFDM," *Optics Express*, vol. 16, no. 26, pp. 21944–21957, 2008.
- [121] T. Duthel, C. R. Fludger, J. Geyer and C. Schülten, "Impact of Polarisation Dependent Loss on Coherent POLMUX-NRZ-DQPSK," in *Optical Fiber Communications Conference*, San Diego, CA, 2008.
- [122] O. Vassilieva, T. Hoshida, X. Wang, J. Rasmussen, H. Miyata and T. Naito, "Impact of Polarization Dependent Loss and Cross-Phase Modulation on Polarization Multiplexed DQPSK Signals," in *Optical Fiber Communications Conference*, San Diego, 2008.
- [123] O. Bertran-Pardo, J. Renaudier, G. Charlet, P. Tran, H. Mardoyan, M. Bertolini, M. Salsi and S. Bigo, "Demonstration of the benefits brought by PMD in polarization-multiplexed systems," in *European Conference on Optical Communications*, Torino, 2010.
- [124] P. Serena and A. Bononi, "Nonlinear Phase Noise Mitigation by Polarization Mode Dispersion in Dispersion Managed coherent PDM-QPSK Systems," in *European Conference on Optical Communications*, Vienna, 2009.
- [125] O. Vassilieva, I. Kim and T. Naito, "Systematic investigation of interplay between nonlinear and polarization dependent loss effects in coherent polarization multiplexed systems," in *European Conference on Optical Communications*, Torino, 2010.
- [126] Z. Tao, L. Li, T. Hoshida and J. Rasmussen, "Interaction between PDL and intra-channel nonlinearity in dual polarization systems," in *Opto-Electronics and Communications Conference*, Kaohsiung, 2011.
- [127] O. Vassilieva, I. Kim and M. Sekiya, "Statistical analysis of the interplay between nonlinear and PDL effects in coherent polarization multiplexed systems," in *European Conference on Optical Communications*, Amsterdam, 2012.
- [128] O. Vassiliev, S. Oda, T. Hoshida, J. Rasmussen and M. Sekiya, "Experimental investigation of the statistics of the interplay between nonlinear and PDL effects in coherent polarization multiplexed systems," in *Optical Fiber Communications Conference*, Anaheim, CA, 2013.
- [129] N. Rossi, P. Serena and A. Bononi, "Polarization-Dependent Loss Impact on Coherent Optical Systems in Presence of Fiber Nonlinearity," *Photonics Technology Letters*, vol. 26, no. 4, pp. 334–337, 2014.
- [130] R. Dar and P. J. Winzer, "Nonlinear Interference Mitigation: Methods and Potential Gain," *Journal of Lightwave Technology*, vol. 35, no. 4, pp. 903–930, 2017.
- [131] R. Dar and P. J. Winzer, "On the Limits of Digital Back-Propagation in Fully Loaded WDM Systems," *IEEE Photonics Technology Letters*, vol. 28, no. 11, pp. 1253–1256, 2016.

-
- [132] L. Beygi, N. V. Irukulapati, E. Agrell, P. Johannisson, M. Karlsson, H. Wymeersch, P. Serena and A. Bononi, "On nonlinearly-induced noise in single-channel optical links with digital backpropagation," *Optics Express*, vol. 21, no. 22, pp. 26376-26386, 2013.
- [133] D. Rafique and A. D. Ellis, "Impact of signal-ASE four-wave mixing on the effectiveness of digital backpropagation in 112 Gb/s PM-QPSK systems," *Optics Express*, vol. 19, no. 4, p. 3449-3454, 2011.
- [134] N. I. Irukulapati, H. Wymeersch, P. Johannisson and E. Agrell, "Stochastic Digital Backpropagation," *IEEE Transactions on Communications*, vol. 62, no. 11, pp. 3956-3968, 2014.
- [135] R. Rios-Müller and B. I. Bitachon, "Maximum Likelihood Carrier Phase Estimation Based on Monte Carlo Integration," in *European Conference on Optical Communications*, Gothenburg, 2017.
- [136] V. Kamalov, L. Jovanovski, V. Vusirikala, E. Mateo, Y. Inada, T. Ogata, K. Yoneyama, P. Pecci, D. Seguela, O. Rocher and H. Takahashi, "FASTER Open Submarine Cable," in *European Conference on Optical Communications*, Gothenburg, 2017.
- [137] G. Charlet, M. Salsi, H. Mardoyan, P. Tran, J. Renaudier, S. Bigo, M. Astruc, P. Sillard, L. Provost and F. Cerou, "Transmission of 81 channels at 40Gbit/s over a transpacific-distance erbium-only link, using PDM-BPSK modulation, coherent detection, and a new large effective area fibre.," in *European Conference on Optical Communications*, Brussels, 2008.
- [138] G. Charlet, M. Salsi, P. Tran, M. Bertolini, H. Mardoyan, J. Renaudier, O. Bertran-Pardo and S. Bigo, "72×100Gb/s transmission over transoceanic distance, using large effective area fiber, hybrid Raman-Erbium amplification and coherent detection," in *Optical Fiber Communications Conference*, San Diego, 2009.
- [139] M. Salsi, O. Bertran-Pardo, J. Renaudier, W. Idler, H. Mardoyan, P. Tran, G. Charlet and S. Bigo, "WDM 200Gb/s single-carrier PDM-QPSK transmission over 12,000km," in *European Conference on Optical Communications*, Geneva, 2011.
- [140] A. Bakhshali, W.Y. Chan, J. C. Cartledge, M. O'Sullivan, C. Laperle, A. Borowiec, and Kim Roberts, "Frequency-Domain Volterra-Based Equalization Structures for Efficient Mitigation of Intrachannel Kerr Nonlinearities," *Journal of Lightwave Technology*, vol. 34, pp. 1770-1777, 2016.
- [141] P. Pecci, S. Dupont, S. Dubost, S. Ruggeri, O. Courtois, and V. Letellier, "Experimental characterization of submarine "open cable" using Gaussian-Noise model and OSNRWET parameter," in *Optical Fiber Communication Conference*, Los Angeles, 2017.

PUBLICATIONS

AS FIRST AUTHOR

- [I] I. Fernandez de Jauregui Ruiz, A. Ghazisaeidi, G. Charlet, "Optimization Rules and Performance Analysis of Filtered Digital Backpropagation", Proc. European Conference on Optical Communications, We.4.6.3, Valencia, (2015).
- [II] I. Fernandez de Jauregui Ruiz, A. Ghazisaeidi, P. Tran, G. Charlet, "Impact of Polarization Mode Dispersion on Digital Nonlinear Compensation Algorithms in Dispersion Unmanaged Systems", Proc. Optical Fiber Communications Conference, Th.3.D.3, Anaheim, (2016).
- [III] I. Fernandez de Jauregui Ruiz, A. Ghazisaeidi, E. Awwad, P. Tran, G. Charlet, "Polarization Effects in Nonlinearity Compensated Links", Proc. European Conference on Optical Communications, Tu.3.B.5, Dusseldorf, (2016).
- [IV] I. Fernandez de Jauregui Ruiz, A. Ghazisaeidi, R. Rios-Muller, P. Tran, "Performance Comparison of Advanced Modulation Formats for Transoceanic Coherent Systems", Proc. Optical Fiber Communications Conference, Th.4.D.6, Los Angeles, (2017).
- [V] I. Fernandez de Jauregui Ruiz, A. Ghazisaeidi, O. Ait Sab, P. Plantady, A. Calsat, S. Dubost, L. Schmalen, V. Letellier, J. Renaudier, "25.4 Tb/s Transmission over Trans-Pacific Distances Using Truncated Probabilistically Shaped PDM-64QAM", Journal of Lightwave Technology, vol. 36, no. 5, (2018)
- [VI] I. Fernandez de Jauregui Ruiz, A. Ghazisaeidi, P. Brindel, R. Rios-Müller, A. Arnould, H. Mardoyan, O. Ait Sab, J. Renaudier, G. Charlet, "Record 560 Gb/s Single-Carrier and 850 Gb/s Dual-Carrier Transmission over Transoceanic Distances", Proc. Optical Fiber Communications Conference, M2C.2, San Diego, (2018)

AS CO-AUTHOR

- [VII] A. Ghazisaeidi, L. Schmalen, I. Fernandez de Jauregui Ruiz, P. Tran, C. Simonneau, P. Brindel, G. Charlet, "52.9 Tb/s Transmission over Transoceanic Distances using Adaptive Multi-Rate FEC", Proc. European Conference on Optical Communications, PD.3.4, Cannes, (2014).
- [VIII] R. Rios-Muller, J. Renaudier, P. Brindel, C. Simonneau, P. Tran, A. Ghazisaeidi, I. Fernandez de Jauregui Ruiz, L. Schmalen, G. Charlet, "Optimized Spectrally Efficient Transceiver for 400-Gb/s Single Carrier Transport", Proc. European Conference on Optical Communications, PD.4.2, Cannes, (2014).
- [IX] A. Ghazisaeidi, L. Schmalen, I. Fernandez de Jauregui Ruiz, P. Tran, C. Simonneau, P. Brindel, G. Charlet, "Transoceanic Transmission Systems Using Adaptive Multirate FECs", Journal of Lightwave Technology, Vol. 33, no. 7, pp. 1479 - 1487, (2015).

-
- [X] R. Rios-Muller, J. Renaudier, P. Brindel, A. Ghazisaeidi, I. Fernandez de Jauregui Ruiz, P. Tran, C. Simonneau, L. Schmalen, G. Charlet, "Spectrally-Efficient 400-Gb/s Single Carrier Transport Over 7200 km", *Journal of Lightwave Technology*, Vol. 33, No. 7, (2015).
- [XI] A. Ghazisaeidi, I. Fernandez de Jauregui Ruiz, L. Schmalen, P. Tran, C. Simonneau, E. Awwad, B. Uscumlic, P. Brindel, G. Charlet, "Submarine Transmission Systems Using Digital Nonlinear Compensation and Adaptive Rate Forward Error Correction", *Journal of Lightwave Technology*, Vol. 34, No. 8, (2016).
- [XII] A. Ghazisaeidi, I. Fernandez de Jauregui Ruiz, R. Rios-Muller, L. Schmalen, P. Tran, A. Carbo Meseguer, Q. Hu, F. Buchali, G. Charlet, J. Renaudier, "65Tb/s Transoceanic Transmission Using Probabilistically-Shaped PDM-64QAM", PDP. European Conference on Optical Communications, Th.3.C.4, Dusseldorf, (2016).
- [XIII] A. Ghazisaeidi, I. Fernandez de Jauregui Ruiz, R. Rios-Muller, L. Schmalen, P. Tran, A. Carbo Meseguer, Q. Hu, F. Buchali, G. Charlet, J. Renaudier, "Advanced C+L-Band Transoceanic Transmission Systems Based on Probabilistically-Shaped PDM-64QAM", *Journal of Lightwave Technology*, vol. 35, no 7, pp. 1291-1299, (2017).
- [XIV] O. Ait Sab, A. Ghazisaeidi, P. Plantady, A. Calsat, I. Fernandez de Jauregui Ruiz, S. Dubost, P. Pecci, J. Renaudier, V. Letellier., "376 Pb/sxkm Transmission Record over 13,419 km Using TPCS-64QAM and C-Band EDFA-Only," *Proc. Asia Communications and Photonics Conference*, Su2B. 2, Guangzhou (2017).
- [XV] O. Ait Sab, I. Fernandez de Jauregui Ruiz, A. Ghazisaeidi, P. Plantady, A. Calsat, S. Dubost, L. Schmalen, J. Renaudier and V. Letellier., "Near Capacity 24.6 Tb/s Transmission over 10,285km Straight Line Testbed at 5.9 b/s/Hz Spectral Efficiency Using TPCS-64QAM and C-Band EDFA-Only," *Proc. European Conference on Optical Communications*, Tu.1.E.2, Gothenburg (2017).
